Universidad del País Vasco
Euskal Herriko Unibertsitatea
Materials Physics Center
Centro de Física de Materiales

Bright Shining Single-Chain Nanoparticles: Advanced Applications in Photocatalysis and Photodynamic Therapy

By Davide Arena
Supervised by Prof. José A. Pomposo and Dr. M. Ester Verde
Donostia – San Sebastián, 2024

Bright Shining Single-Chain Nanoparticles: Advanced Applications in Photocatalysis and Photodynamic Therapy

by Davide Arena

Supervised by Prof. José A. Pomposo and Dr. M. Ester Verde

Donostia - San Sebastián, 2024

Acknowledgements

Firstly, I sincerely acknowledge my thesis directors Prof. José A. Pomposo and Dr. M. Ester Verde. With wise guidance and daily support, you both made me grow as a researcher and as a person.

I gratefully acknowledge the Material Physics Center and the Polymers, Soft Matter & Sustainable Materials Group for giving me the opportunity to carry out my doctoral studies in a scientifically stimulating environment. I would like to especially acknowledge Prof. Arantxa Arbe and Dr. Amaia Iturrospe for the continue dedication and support with the SAXS characterization.

I would like express deep gratitude to Dr. Magali Gary-Bobo, not only for giving me the opportunity to work on an essential part of this work at the Université de Montpellier, but also for the kindest welcoming and continuous support. I would also like to extend my most sincere gratitude to Dr. Christophe Nguyen, your teachings are, in a word, irreplaceable. Thank you to all the Glyco and Nanovectors for Therapeutic Targeting Group, Lamiaa, Laure, Mariana, Nadir, Alain, Denis, Kamel, Marie, Khaled, Melanie, for transforming my stay in such a meaningful and enriching experience.

I would also like to gratefully acknowledge Prof. Fabienne Dumoulin, Prof. Zoraida Freixa, Dr. Ane Izaskun Aranburu Leiva and Dr. Iván Rivilla, for their crucially important contributions and support to the work which is now condensed in this thesis.

I would like to thank my family and Daniel, for understanding and always being there, believing in me, bringing inextinguishable light to my life. This project would have not been possible without you.

Finally, thank to my brother, this thesis is dedicated to you, for the time that, with my absence, I stole you.

Summary

Keywords: Single-Chain Nanoparticles, Photochemistry, Photocatalysis, Photodynamic Therapy, Functional Polymers.

With the work which we present in this thesis, we aimed to establish a link between single-chain nanoparticle (SCNP) technology and photocatalysis, finding novel and advanced applications of next-generation, light-harvesting SCNPs. In particular, we focused on employing the opportunities offered by SCNP unique topology to enable advanced applications of photocatalysis in aqueous and complex environments such as for organic photocatalysis and photodynamic therapy (PDT) of cancer. The present thesis' structure comprises two first Chapters, in which basic concepts and recent literature on both SCNPs technology and organic photocatalysis are briefly reviewed, opening the discussion for the experimental results disclosed in Chapter III and IV.

Specifically, in Chapter I the definition of SCNPs is given and the relevant synthetic aspects for their preparation are illustrated. Namely, the synthesis of the polymeric precursors *via* reversible-addition fragmentation reaction (RAFT) polymerizations and the main strategies for chain folding / collapse reported in literature are discussed. In conclusion to the first Chapter we delineated the main aims of the present work, and finally outlined some major contributions to the fields of catalysis and nanomedicine involving SCNPs-based systems.

In Chapter II, we introduce the definitions, the fundamental concepts of photocatalysis, with a special focus on organic photocatalyzed reactions and the major constraints presented by the use of water as solvent to carry out such kind of valuable transformations. Apart from first, seminal reports at the infancy of Organic Chemistry, in which water was commonly used as reaction medium, the aqueous environment quickly disappeared amongst the common practice of synthetic organic chemists over the course of the past century. Considering the growing demand for increasingly low-impact processes, both from an economic and ecological point of view, the use of water to replace flammable, often toxic and expensive organic solvents in industrially relevant processes, *e.g.* the valuable small organic molecules preparation, recently gained back interest amongst the scientific community. For this reason, in Chapter II we put special attention on how supramolecular approaches have been recently applied to address the issues associated with the use of water as solvent for photo-induced organic transformations.

In Chapter III, we continue the discussion reporting the preparation of a novel class of versatile SCNP capable of efficiently carry out photocatalytic organic reactions in water. We designed an amphiphilic polymeric precursor of defined molecular weight and dispersity exploiting the amphiphilic polymeric scaffold of the Poly[(olygoethylene glycol)monomethylether methacrylate]-*r*-Poly(acetoacetoxyethyl methacrylate), Poly(OEGMA)-*r*-Poly(AEMA), which was prepared by RAFT copolymerization of the commercially available monomers OEGMA and AEMA. The obtained copolymeric precursor was then functionalized and given of photocatalytic activity by decoration with an iridium(III)-based cyclometalated complex though a mild post-polymerization functionalization approach, exploiting the rich β-ketoester chemistry of the hydrophobic comonomer AEMA. The prepared photoactive amphiphile copolymer resulted to efficiently self-assemble in aqueous solution by folding / collapse into a SCNP structure as revealed by dynamic light scattering (DLS) techniques and as confirmed by UV-Visible spectrophotometry. Interestingly, the water soluble, iridium(III)-containing SCNPs, which we called artificial photosynthase (**APS**) allowed the observation of an enhancement in the photoluminescence (PL) in water with respect of the organic solvent solutions, suggesting the arising of

aggregation-induced emission phenomena arising from the locally compact hydrophobic pockets of the SCNP.

With the **APS** in hand, we subsequently tested their ability to perform a variety of organic reactions. Specifically, we were able to observe efficient visible-light induced photocatalytic activity for two unprecedently reported organic reactions in water, namely the photo[2+2]cycloaddition of vinyl arenes and the α-arylation of arylamines, as well as the oxidation of 9-substituted anthracenes and the β-sulfonylation of styrene-like compounds. Due to the similarities of these **APS** to enzymes, kinetics data of the photo[2+2]cycloaddition of vinyl arenes "*in water*" photocatalyzed by **APS** were analyzed in terms of the traditional Michaelis-Menten model. The apparent values of k_{cat} and K_M obtained were 2.6 s^{-1} and 4.6 × 10^{-2} M, respectively, values which are comparatively and significantly close to what reported for some biotic enzymes (Chymotrypsin shows k_{cat} = 0.14 s^{-1} and K_M = 1.5 × 10^{-2} M, Pepsin k_{cat} = 0.50 s^{-1} and K_M = 3.0 × 10^{-4} M, and tRNA synthetase k_{cat} = 7.6 s^{-1} and K_M = 9.0 × 10^{-4} M).

In summary, in Chapter III we describe and report a first generation of **APS**, broadening the possibilities for performing challenging "*in water*" organic transformations via **APS**-mediated visible-light photocatalysis.

In Chapter IV, we report the design and synthesis of a polymeric precursors to enhance the PDT efficiency of a novel, long-wavelength absorbing zinc(II)-phthalocyanine (**ZnPc**). For this, we took advantage of the well-known self-assembly capability of anthracene molecules, we prepared anthracene-based amphiphilic copolymers from the commercially available hydrophobic monomer 9-anthracenylmethyl methacrylate (AnMA) and the hydrophilic OEGMA *via* RAFT copolymerization. The prepared Poly(AnMA)-*co*-Poly(OEGMA)s resulted to be both capable of self-assembly in water and of efficiently encapsulating the far-red-responsive complex **ZnPc**, yielding stable, water soluble, red-light reactive SCNPs, which we called artificial photo-oxidases (**APO**), mainly due to their ability to induce oxidative stress in cell upon exposure to light and for their ultra-small dimensions (< 20 nm). The nano-objects were characterized both by DLS and SAXS, which revealed

the effect of the **ZnPc** encapsulation on the steric hindrance of the SCNPs core through the measurement of the radius of gyration in presence and / or absence of **ZnPc**. Interestingly, the readily prepared nano-assemblies showed different photoluminescent properties in the red region depending on the overall anthracene molar fraction in the polymeric precursor. In particular, the extent of either broadening or quenching of Q-band transitions of **ZnPc** increased upon decreasing the anthracene molar fraction in the nanocarrier. Analogously, a pronounced quenching (λ^{exc} = 650 nm) of the **ZnPc** emission in the far red is observed upon decreasing the anthracene content, though allowing the tunability of the degree of aggregation within the hydrophobic core of the nanocarrier.

We finally tested **APO-ZnPc** against human breast cancer cell MDA-MB-231 lines to assess their PDT efficiency. Having observed outstanding performance for one of the selected formulations, we finally proved their PDT activity in zebrafish embryo xenografts as a more accurate human cancer model.

In conclusion, in the present thesis, the development of novel systems based on SCNPs for advanced applications in photocatalyzed organic reactions and photodynamic therapy has been studied and carried out, demonstrating that the technology of single-polymeric chains folding can be exploited for the fabrication of artificial nano-objects with protein-resembling structure of tailored photocatalytic activity.

Resumen

Palabras clave: *Single-Chain Nanoparticles*, Fotoquímica, Fotocatálisis, Fototerapia Dinámica, Polímeros Funcionales.

Mediante el presente trabajo, se pretende establecer una conexión entre la tecnología de nanopartículas poliméricas unimoleculares (SCNP, del inglés *single-chain nanoparticles*) y la fotocatálisis, encontrando aplicaciones novedosas y avanzadas para las SCNP de nueva generación capaces de utilizar la luz como fuente de energía. En concreto, se ha tratado de aprovechar las características topológicas de las SCNP para implementar aplicaciones avanzadas de fotocatálisis en ambientes acuosos y complejos, con el objetivo de emplearlas en casos como la fotocatálisis orgánica y la terapia fotodinámica (PDT, del inglés *photodynamic therapy*) del cáncer. La estructura de la presente tesis consta de dos primeros capítulos, en los que se revisan brevemente los conceptos básicos y la bibliografía reciente tanto de la tecnología de las SCNPs como de la fotocatálisis orgánica, abriendo la discusión para los resultados experimentales expuestos en los capítulos III y IV.

Concretamente, en el Capítulo I se da la definición de SCNPs y se ilustran los principales aspectos sintéticos para su preparación. En concreto, se discute la síntesis de los precursores poliméricos mediante polimerizaciones por adición, fragmentación y transferencia reversible (RAFT, del *inglés reversible addition-fragmentation transfer*) y las principales estrategias para el plegamiento / colapso de cadenas descritas

en la literatura. A modo de conclusión del primer capítulo, se han delineado los principales objetivos del presente trabajo y, por último, se han enumerado algunas contribuciones importantes a los campos de la catálisis y la nanomedicina que implican sistemas basados en SCNPs.

El Capítulo II, consta de los conceptos fundamentales de la fotocatálisis, haciendo énfasis en las reacciones orgánicas foto-catalizadas y las principales limitaciones que presenta el uso del agua como disolvente para llevar a cabo este tipo de transformaciones valiosas. A excepción de los inicios de la Química Orgánica, en los que el agua se utilizaba comúnmente como medio de reacción, el medio acuoso desapareció rápidamente de la práctica común de los químicos orgánicos sintéticos en el transcurso del siglo pasado. Teniendo en cuenta la creciente demanda de procesos con menor impacto, tanto desde el punto de vista económico como ecológico, el uso del agua para sustituir a disolventes orgánicos inflamables, a menudo tóxicos y caros en procesos de relevancia industrial, como por ejemplo la preparación de pequeñas moléculas orgánicas, ha vuelto a despertar recientemente el interés de la comunidad científica. Por este motivo, en el Capítulo II se presta especial atención a cómo se han aplicado recientemente estrategias de química supramolecular para abordar los problemas asociados al uso del agua como disolvente en las transformaciones orgánicas foto-inducidas.

En el Capítulo III, se continua con la discusión reportando la preparación de una nueva clase de SCNPs capaces de llevar a cabo eficientemente reacciones orgánicas fotocatalíticas en agua. Se diseñó un precursor polimérico anfifílico de peso molecular y dispersidad definidos, aprovechando las propiedades del Poli[(oligoetilenglicol)monometilétermetacrilato]-*r*-Poli(acetoacetoxietil metacrilato), Poli(OEGMA)-*r*-Poli(AEMA), que se sintetizó mediante copolimerización RAFT de los monómeros comerciales OEGMA y AEMA. El precursor polimérico obtenido se funcionalizó con un complejo ciclometalado basado en iridio (III), dotándolo de actividad fotocatalítica mediante su decoración, explotando la versatilidad de los β-cetoésteres del comonómero hidrofóbico AEMA. El copolímero anfifílico fotoactivo preparado resultó ser capaz de autoensamblarse en disolución acuosa plegándose /

colapsándose en una estructura SCNP, como revelaron las técnicas de dispersión dinámica de la luz (DLS) y espectrofotometría UV-Visible.

Curiosamente, las SCNPs solubles en agua que contienen iridio(III), que denominamos *fotosintasas artificiales* (**APS**, del inglés *artificial photosynthases*), permitieron observar un aumento de la fotoluminiscencia (PL) en agua con respecto a las soluciones de disolventes orgánicos, lo que sugiere la aparición de fenómenos de emisión inducidos por agregación, derivados de la formación de dominios hidrofóbicos localmente compactos dentro de las nanopartículas.

Una vez obtenidos las **APS**, se comprobó su capacidad para llevar a cabo diversas reacciones orgánicas. En concreto, se observó una eficiente actividad fotocatalítica inducida por luz visible para dos reacciones orgánicas en agua, de las que no se había reportado nada anteriormente, dichas reacciones eran la foto[2+2]cicloadición de arenos vinílicos y la α-arilación de arilaminas, así como la oxidación de antracenos 9-sustituidos y la β-sulfonilación de compuestos estirénicos. Debido a las similitudes de las APS con las enzimas, los datos cinéticos de la fotocicloadición [2+2] de vinil arenos «en agua» fotocatalizada por APS se analizaron mediante el modelo tradicional de Michaelis-Menten. Los valores aparentes de k_{cat} y K_M obtenidos fueron 2.6 s^{-1} y 4.6 × 10^{-2} M, respectivamente, valores que son comparativa y significativamente cercanos a los reportados para algunas enzimas bióticas (la quimotripsina muestra k_{cat} = 0.14 s^{-1} y K_M = 1.5 × 10^{-2} M, la pepsina k_{cat} = 0.50 s^{-1} y K_M = 3.0 × 10^{-4} M, y la tRNA sintetasa k_{cat} = 7.6 s^{-1} y K_M = 9.0 × 10^{-4} M).

En resumen, en el Capítulo III describimos y presentamos una primera generación de **APS**, que amplía las posibilidades de realizar transformaciones orgánicas «en agua» mediante fotocatálisis con luz visible.

En el Capítulo IV, reportamos el diseño y síntesis de precursores poliméricos para mejorar la eficacia de la PDT de la ftalocianina de Zn(II) encapsulada (**ZnPc**). Para ello, aprovechando la conocida capacidad de autoensamblaje de las moléculas de antraceno, se prepararon copolímeros anfifílicos basados en antraceno a partir del monómero hidrofóbico comercial 9-antracenilmetilmetacrilato (AnMA) y el hidrofílico OEGMA mediante copolimerización RAFT. Los Poli(AnMA)-*co*-

Poli(OEGMA)s preparados resultaron ser capaces tanto de auto-ensamblarse en agua como de encapsular eficientemente el complejo **ZnPc**, dando lugar a SCNPs estables, solubles en agua y reactivas a la luz roja, que denominamos foto-oxidasas artificiales (**APO**, del inglés *artificial photo-oxidades*), debido principalmente a su capacidad de inducir estrés oxidativo en la célula tras la exposición a la luz. Los nano-objetos se caracterizaron mediante DLS y SAXS, que revelaron el efecto de la encapsulación de **ZnPc** en el impedimento estérico del núcleo de las SCNPs mediante la medición del radio de giro en presencia y / o ausencia de **ZnPc**. Curiosamente, los diferentes nano-agregados preparados mostraron distintas propiedades fotoluminiscentes en la región roja dependiendo de la fracción molar de antraceno en el precursor polimérico. En concreto, el grado de ensanchamiento de las transiciones de la banda Q del **ZnPc** aumentaba al disminuir la fracción molar de antraceno en el nano-transportador. De forma análoga, se observó un decrecimiento pronunciado (λ^{exc} = 650 nm) de la emisión de **ZnPc** en el rojo lejano al disminuir el contenido de antraceno, permitiendo, de esta forma, la customización del grado de agregación dentro del núcleo hidrofóbico del nano-transportador.

Por último, ensayamos **APO-ZnPc** contra líneas celulares de cáncer de mama humano MDA-MB-231 para evaluar su eficacia PDT. Tras observar el excelente rendimiento de una de las formulaciones seleccionadas, finalmente se probó su actividad PDT en *xenografts* de embriones de pez cebra como modelo más preciso de cáncer humano.

En conclusión, en la presente tesis, se ha estudiado y realizado el desarrollo de novedosos sistemas basados en SCNPs para aplicaciones avanzadas en reacciones orgánicas fotocatalizadas y terapia fotodinámica, demostrando que la tecnología de plegamiento de cadenas poliméricas simples puede ser explotada para la fabricación de nano-objetos artificiales con una estructura similar a la proteína de actividad fotocatalítica customizada.

Table of Contents

List of Abbreviations

$[Ir(ppy)_2OH]_2$	Dihydroxotetrakis[2-(2-pyridinyl)phenyl]diiridium-(III) dimer
°C	Celsius degree / degrees
µL	Microliter / microliters
µmol	Micromole / micromoles
^1S_n	Singlets excited states
2-CNIPB	2-chloro-N,N-diisopropylbenzamide
Å	Angstrom / angstroms
AA	α-Arylation of arylamines
ABA	4-acetoxybenzaldehyde
AcOEt	Ethyl acetate
AEE	Aggregation enhanced emission
AEMA	4-acetoacetoxyethyl methacrylate
AFM	Atom-force microscopy
AgCl	Silver chloride
AgOTf	Silver(I) trifluoromethansulfonate
AIBN	Azobisisobutyronitrile
APS	Artificial photosynthase
ATRP	Atom-transfer radical polymerization
AuNP	Gold nanoparticle
BHT	Butylated hydroxytoluene
BODIPY	4,4-difluoro-4-bora-3a,4a-diaza-s-indacenes
c%	Conversion
CA	[2+2] Cycloaddition of vinyl arenes
cal	Calory / calories
$CDCl_3$	Deuterated chloroform
CH_2Cl_2	Methylene chloride
$CHCl_3$	Chloroform
cm	Centimeter / centimeters

COSY	Homonuclear correlation spectroscopy
CPADB	4-cyano-4-(thiobenzoylthio)pentanoic acid
CRP	Controlled radical polymerizations
CTA	Chain-transfer agent
CTAB	Cetrimmonium bromide
d	intra-particle photocatalytic unit density
Đ	Dispersity
Da	Daltons (u.m.a.)
DCB	1,4-dicyanobenzene
DEPT	Distortionless enhancement by polarization transfer
D_h	Hydrodynamic diameter
DLS	Dynamic light scattering
DMA	Dimethylacetamide
DMEM	Dulbecco's Modified Eagle's Medium
DMF	N,N-dimethylformammide
DMSO	Dimethyl sulfoxide
DP	Degree of polymerization
DPBF	1,3-diphenylisobenzofuran
DRI	Differential refractive index
E^*_{ox}	Excited state's oxidation potential
E^*_{red}	Excited state's reduction potential
E_{ox}	Oxidation potential
EPR	Enhanced permeability and retention
E_{red}	Reduction potential
E_T	Energy transfer
Et_2O	Diethyl ether
EtOH	Ethanol
FRET	Förster resonance energy transfer
FT-IR	Fourier transform infrared
GPC	Gel permeation chromatography
h	Hour / hours
HPAM	N-(2-hydroxypropyl)acrylamide
HPLC	High pressure liquid chromatography
HS	α-Styrene β-hydroxysulfonylation
HSQC	Heteronuclear single quantum coherence spectroscopy
IONP	Iron oxide nanoparticle
IR	Infrared
$Ir(ppy)_2(acac)$	Bis(2-phenylpyridine)-(acetylacetonate)iridium(III)
$Ir(ppy)_2(meacac)$	bis[2-(2-pyridinyl-N)phenyl-C](methyl acetoacetato)iridium(III)

$IrCl_3$	Iridium(III) trichloride
Irsppy	fac-tris[2-(5'-sulfonatophenyl)pyridine]iridate(III)
ISC	Inter-system crossing
IUPAC	International Union of Pure and Applied Chemistry
J	Joule / joules
JNPs	Janus nanoparticles
K_2CO_3	Potassium carbonate
$k_{cat,app}$	Apparent catalytic constant
kDa	Kilodalton / kilodaltons
$K_{M,app}$	Apparent Michaelis-Menten constant
kV	Kilovolt / kilovolts
L	Liter / liters
LAM	Less activated monomer
LED	Light-emitting diodes
L^{Ir}	iridium loading
M	Molarity / molar
m	Meter / meters
MA	Methyl acrylate
mA	Milliampere / milliamperes
MALDI	Mass analysis laser desorption ionization
MALS	Multi-angle laser light scattering
MAM	More activated monomer
MDO	2-methylene-1,3-dioxepane
MeOH	Methanol
mg	Milligram / milligrams
$MgSO_4$	Magnesium sulfate
MHz	Megahertz
min	Minute / minutes
mL	Milliliter / milliliters
mm	Millimeter / millimeters
MMA	Methyl methacrylate
M_n	Number average molecular weight
mol	Mole / moles
MPEG	Poly(ethylene glycol ether) methyl ether
MTT	4,5-dimethylthiazol-2-yl)-2,5-diphenyltetrazolium bromide
M_w	Weighted average molecular weight
mW	Milliwatt / milliwatts
$Na_2HPO_4 \cdot nH_2O$	Sodium phosphate dibasic n-hydrate
NaCl	Sodium chloride
NaOAc	Sodium acetate

NaOH	Sodium hydroxide
NBD	Nitrobenzoxadiole
NHSMA	N-hydroxysuccinimide ester
nm	Nanometer / nanometers
NMP	Nitroxide-mediated polymerization
NMR	Nuclear magnetic resonance
NVC	N-vinyl carbazole
NVP	N-vinyl pyrrolidone
OA	Oxidation of 9-substituted anthracenes
OD	Optical density
OEGMA	(Oligoethylene glycol monomethyl ether) methacrylate
PC	Photocatalyst
PC*	Photocatalyst excited state
PC-SCNP	Photocatalytic single chain nanoparticles
PDI	Polydispersion index
PDMEAMA	Poly(dimethylaminoethylmethacrylate)
PDT	Photodynamic therapy
PEG	Polyethylene glycol
PL	Photoluminescence
PMAA	Poly(methacrylic acid)
PN	Phenoxazine
PNIPAM	Poly(N-isopropylacrylamide)
ppm	Parts per million
PS	Photosensitizer
PVBC	Poly(vinylbenzylchloride)
PVP	Polyvinylpirrolidone
r.t.	Room temperature
RAFT	Reversible-addition-fragmentation chain-transfer
RDRP	Reversible-deactivation radical polymerization
R_g	Radius of gyration
R_g	Radius of gyration
R_h	Hydrodynamic radius
ROS	Reactive-oxygen species
rROP	Radical ring opening polymerization
SAPC	Supramolecular assembly photocatalyst
SAXS	Small-angle X-ray scattering
SCE	Saturated calomel electrode
SCNP	Single-chain nanoparticles
SDS	Sodium dodecyl sulfate
SEC	Size exclusion chromatography

SET	Single-electron transfer
SLA	Star-like aggregates
Sty	Styrene
TEA	Triethylamine
THF	Tetrahydrofuran
TLC	Thin layer chromatography
TMS	Tetramethylsilane
TOF	Time of flight
UPy	2-ureidopyrimidinone
UV	Ultraviolet
V	Volt / volts
VAc	Vinyl acetate
WA	Wenreib amide
$Zn(OAc)_2$	Zinc diacetate
$\lambda^{exc}{}_{max}$	Maximum excitation wavelenght
λ_{max}	Maximum wavelength
ν	Size scaling exponent

1. Chapter I

1.1. Introduction

Despite the nanometer (nm) being an extremely small unit of length – thousand million (10^{-9}) of a meter – the manipulation of matter with dimensions sized from 1 to 100 nanometers is a deeply investigated branch of the technology we now dispose of, namely, the nanotechnology. Covering from medicine, molecular biology, energy storage, chemistry, semiconductor physics, just to cite a few, nanotechnology includes all kinds of scientific research, having possibly gained place at the center of the attention of the scientific community worldwide, in the nanotechnology era it has already been demonstrated how powerfully our daily life can be facilitated by its application. The remarkably fascinating pictures presented in Figure 1.1 gives us a bite of how extensively the nanotechnology is infusing our scientific culture and life.

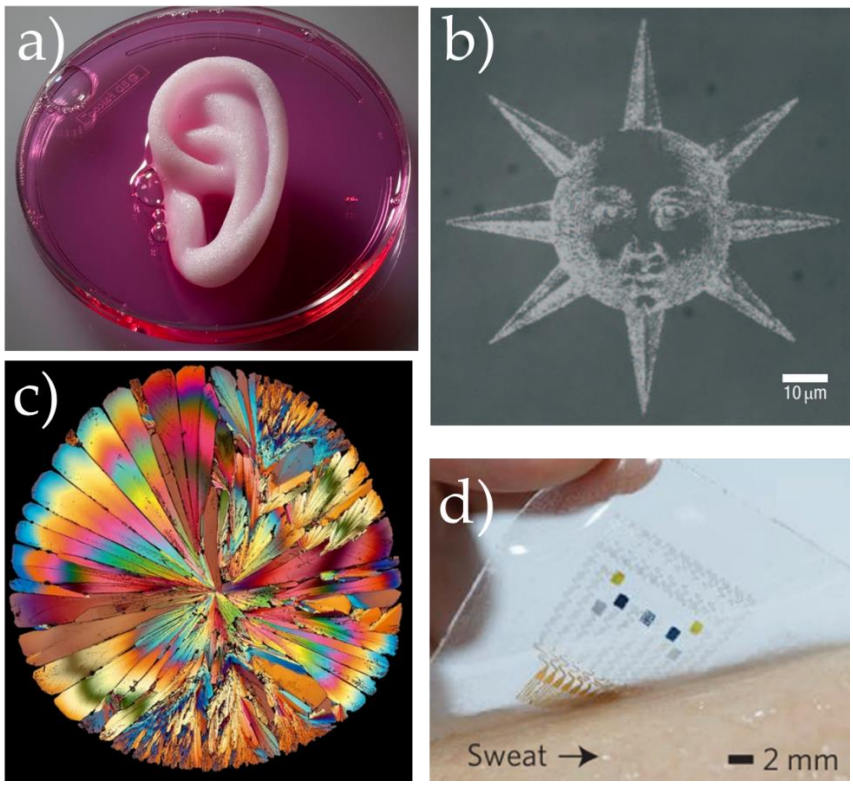

Figure 1.1. a) A synthetic ear, produced by nanostructured tissue scaffolding, is being bathed in cartilage-producing cells. Photograph by Rebecca Hale. National Geographic. **b**) Optical micrograph of a sun composed of about 20000 individiual 60 nm Au nanoparticles, reproduced with permission.[1] Copyright 2007, Springer Nature. **c**) Optical micrograph (image lenght 0.0035 mm) of a one-month-old drop of Aperol, here photographed fully crystalized. Photograph by Bernardo Cesare, University of Padua. **d**) Photograph of an integrated wearable diabetes monitoring and therapeutic device array on sweating human skin, reproduced with permission.[2] Copyright 2016, Springer Nature.

Nanotechnology is ultimately advised by nature, which often delight us with plenty of inspirational architectures. The never-ending dialogue between supramolecular scientists and the natural world resulted in a variety of molecular scaffolds, which aim to mimic the structural complexity and functions of naturally occurring materials. The preparation of both *hard* and *soft* nano-systems - spanning from macrocyclic compounds, star and linear polymers, dendrimers, micelles, lyposomes, polymersomes, quantum dots and metal nanoclusters – is now possible and

already found a plethora of applications in our daily life. Nevertheless, the possibility of achieve such control on polymer-based soft nano-objects only started to emerge by the beginning of the XXI century, partly fueled by the noticeable advances and opportunities offered by the controlled radical polymerizations (CRP) over the preparation of well-defined, functional polymers. The combination of such techniques with taylor-made polymer post-polymerization functionalization chemistries paved the way to the reliable production of what we now call single-chain nanoparticles (SCNPs). In this Chapter, we will give the definition of SCNP, as well as reviewing some recently reported fabrication methodologies. Finally, a brief overview on recent SCNPs advanced applications in the fields of catalysis and nanomedicine will be given.

1.2. Single-Chain Nanoparticles.

This emerging class of nanoparticles, as suggested by the name, consist of nano-objects produced by means of the folding / collapse of an individual polymeric chain on itself, a manner which often resembles natural proteins (Figure 1.2).

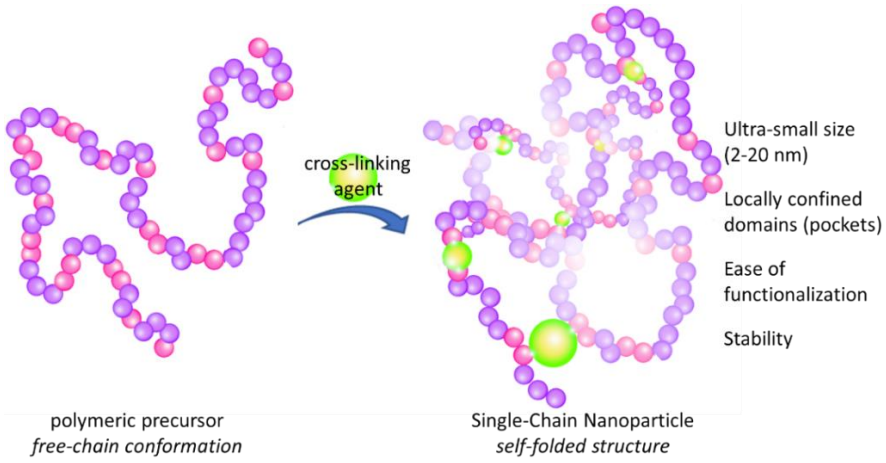

Figure 1.2. Schematic representation of the folding / collapse process by means of the compaction of the polymeric precursor in its open-chain configuration, yielding the more compact, self-folded SCNPs architecture.

As the nature of SCNPs is intrinsically related to a matter of macromolecular conformations, multiple analytical tools are generally required to confirm the successfull formation of SCNPs. To reveal the change in configuration of a certain polymeric chain is not a trivial task in most of the cases, especially considering experimental constraints as extreme sample dilution and stability which are commonly faced in laboratory practice when working with SCNPs. The techniques selected to investigate such nano-objects should be then sensitive enough to detect changes in parameters such as radius of giration (R_g) or hydrodynamic radius (R_h) in very diluted conditions - *e.g.* size exclusion chromathography (SEC), dynamic light scattering (DLS) and nuclear magnetic resonance (NMR) are spreadily adopted as techniques of election for routinary investigation of SCNPs formation.

The uniqueness of SCNPs partly relies on the fact that naturally occurring proteins, the natural counterpart of SCNPs, still represent undefeated examples of the greatness of molecular machinery precision. Enzymes' performances are, in most of the cases, of incomparable efficiency to common synthetic supramolecular catalysts in terms of, *e.g.*, efficiency, stability in aqueous media, selectivity and complexity. Their peculiarity is directly related to the stuctural precision with which compartmetalization occurs: in example, many enzymes in their native conformations exhibit hydrophobic nanocavities, which in conjunction with the global globular state of the enzyme, provide a local environment for catalytically active sites where biochemical transformations can take place. In analogy to their natural counterparts, SCNPs present ultra-small sizes (2-20 nm), are easily chemically modified allowing the formation of locally confined domains within the nanoparticle and usually present an extra stabilization towards dilution in comparison to multi-molecular assemblies, all features which make SCNPs candidates of election for advanced applications, even in complex media. In the present section, we will review some recent literature concerning SCNPs, with the aim of highligthitng principal aspects thereof, more specifically the distinct modes of preparation available to the date and relevant applications of SCNPs in the fields of catalysis and nanomedicine.

1.3. Synthetic Methods

The fabrication of well-defined SCNPs mainly relies on three fundamental steps: (i) the synthesis of the polymer precursor, as both the precursor length and cross-linkable units density determine the size of the final nanoparticle, (ii) the functionalization of the polymer, which permits to embed the macromolecular chains with tailor-made, varied chemistries enabling the folding / collapse and (iii) the actual intra-chain folding step. While designing a functional SCNP, all these three steps influence the others in a compenetrating fashion, as in the surfaces of a Penrose paradoxical triangle represented in Figure 1.3.

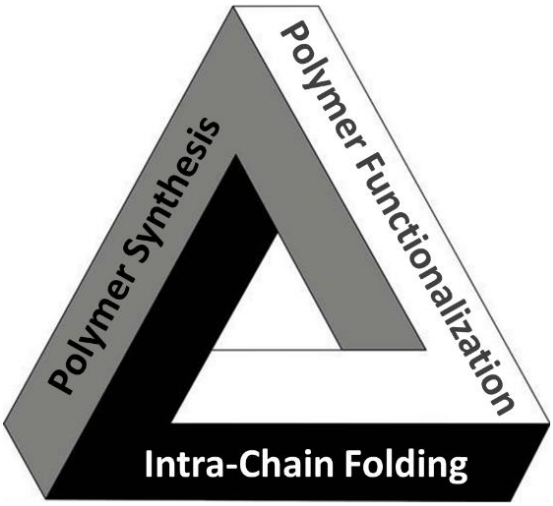

Figure 1.3. Pictorial representation of the three steps involved in the preparation of a SCNP. The polymeric precursor synthesis, its functionalization and intra-molecular chain folding / collapse all mutually influence each other in nanoparticles design.

1.3.1. Synthesis of the Polymeric Precursor

To obtain a precursor of controlled chemical structure is of utmost importance for accessing SCNPs of well-defined structure and, by that, confer functions to the final material. In this sense, the invention of CRPs techniques probably contributed the most, to the point that is often considered a "revolution" in the now 104 years old field of polymer chemistry.[3] CRPs, also referred as Reversible-Deactivation Radical Polymerizations (RDRPs), permits to tune molecular weight, dispersity (*Đ*), composition and architecture of the final polymeric product.

Generally speaking and regardless of the initiation modality, which can either be thermal, redox, or photo-induced[4] depending on the primary source of radicals employed in the particular reaction, a chain-growth radical polymerization mechanistically involves four fundamental steps, which are initiation, propagation, chain transfer and termination (Scheme 1.1), with the two latter being usually responsible of the undesired deviations from molecular architectures and broadening

of *Đ*. When a chain-growth polymerization is not controlled, *e.g.* in the case of free-radical polymerizations, the events of chain termination and chain transfer are very likely to occur extensively, resulting in poor *Đ* (*Đ* >> 1) and lack of structural definition of the final product.

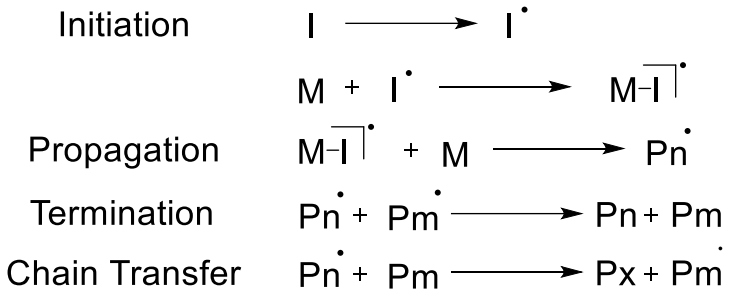

Scheme 1.1. Main mechanistic events involved in a radical polymerization.

On the contrary, in a CRP, the termination step is a reversible chemical reaction, allowing the chains to grow at almost constant and very low concentration of the highly reactive, propagating species (radicals). As a common feature, termination events and chain transfer are kept to a minimum, thanks to the fast equilibration between active (growing) chains and the inactive (dormant) species. The mechanistic fundamental aspects on which CRPs rely are illustrated in Scheme 1.2, in which is shown how the abovementioned equilibrium is displaced to the dormant species. For this, the concentration of active, growing radicals ($P_n^{\cdot}$) is maintained low over the duration of the entire polymerization, ensuring a low probability for dimerization-induced terminations (formation of P_n-P_m) and termination by disproportion (formation of P_n, P_m).

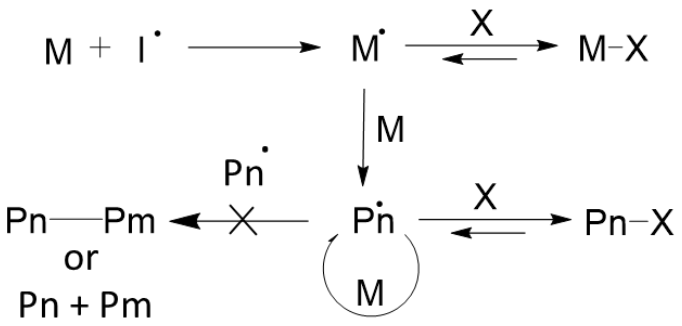

Scheme 1.2. Equilibria between radicals and dormant species in the controlled radical polymerizations.

At the present day, several CRP techniques are available, each relying on different chemistries, most famously Atom Transfer Radical Polymerization (ATRP),[5] Nitroxide-Mediated Polymerization (NMP)[6] and Reversible-Addition Fragmentation Chain-Transfer Polymerization.[7] While of extreme importance for synthetic applications, to exhaustively report all the mechanistic aspects of CRPs is far beyond the scope of the present work, for this, in the following discussion only the main features RAFT polymerization will be mentioned, being this latter the more extensively CRP technique employed for the works that constitute this thesis, as it will be disclosed in the next chapters, for the fabrication of next-generation, functional SCNPs.

As anticipated above, RAFT polymerization is one of the most versatile and powerful tools for the construction of polymeric materials of complex architecture, defined molecular weights and low dispersity.[8] RAFT is a robust technique, showing great versatility to a wide range of monomers and tolerance towards many functional groups. Notably RAFT does not require the use of metals, which is very desirable in terms of overall process economy, purification protocols and end-use in biology and electronic applications, allowing to get closer to milder reaction conditions which are more typical of uncontrolled radical polymerizations.[4,9]

RAFT polymerization requires the presence of a radical initiator and a chain transfer agent (CTA), commonly a thiocarbonyl-based compound (Figure 1.4).

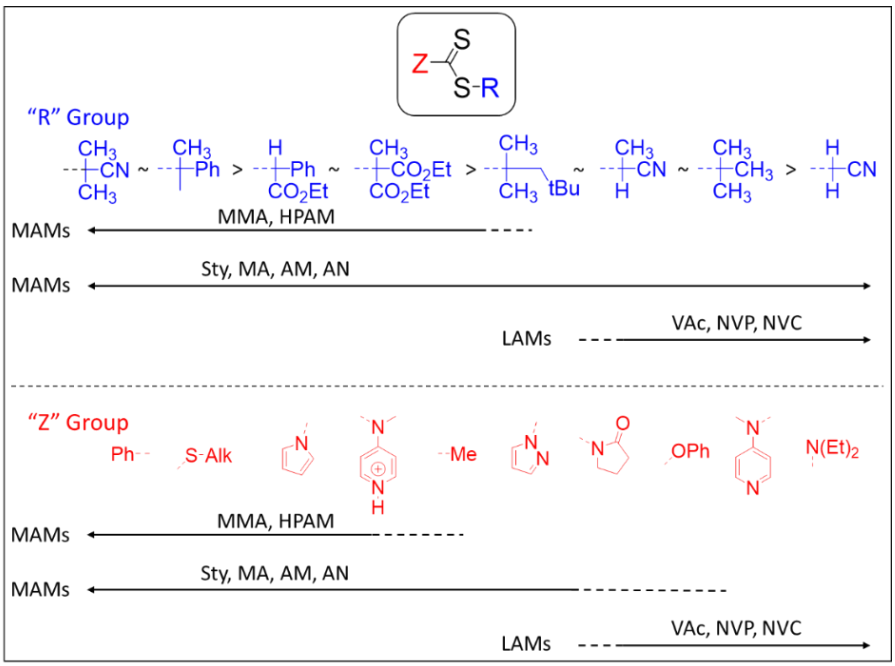

Figure 1.4. Effect of the substituent R and Z of commonly employed CTAs on the polymerization of commercially available monomers. Continuous arrow indicates high to good compatibility, dotted arrow low compatibility and no line scarce to no compatibility.[4] See text for monomers complete names (MMA, HPAM, Sty etc.).

As mentioned above, the RAFT process offers a wide tolerability towards different polymerizable monomers and, for that to be achieved, CTAs should be chosen in relation to experimental conditions,[10] as the nature of the Z and R groups of the RAFT agent (CTA) is fundamental and can be varied accordingly to the type of the selected monomers. In Figure 1.4, a schematized selection guide for CTA-monomer pairing is presented.[4] The monomer species that can be used in this type of polymerization are conventionally divided into more activated monomers (MAMs) and less activated monomers (LAMs). The first group includes monomers with vinyl groups conjugated to aromatic rings (as styrene, Sty) double bonds, carbonyl or nitrile groups such as acrylates and methacrylates (*e.g.* methyl methacrylate, MMA; and methyl acrylate, MA) dienes, or methacrylamides (*e.g.* N-(2-hydroxypropyl)acrylamide HPAM), which can be controlled using dithioesters /

dithiobenzoates or trithiocarbonates as CTAs. On the other hand, commonly employed LAMs are vinyl acetates (VAc), vinyl chlorides and 1-alkenes which have double bonds adjacent to atoms of oxygen, nitrogen, halogens or saturated carbons (*e.g. N*-vinyl pyrrolidone, NVP; *N*-vinyl carbazole, NVC).

As illustrated in Scheme 1.3, in the RAFT reaction mechanism an initiator generates a radical species that is readily added to a monomer M, thus forming a P_n polymer chain.

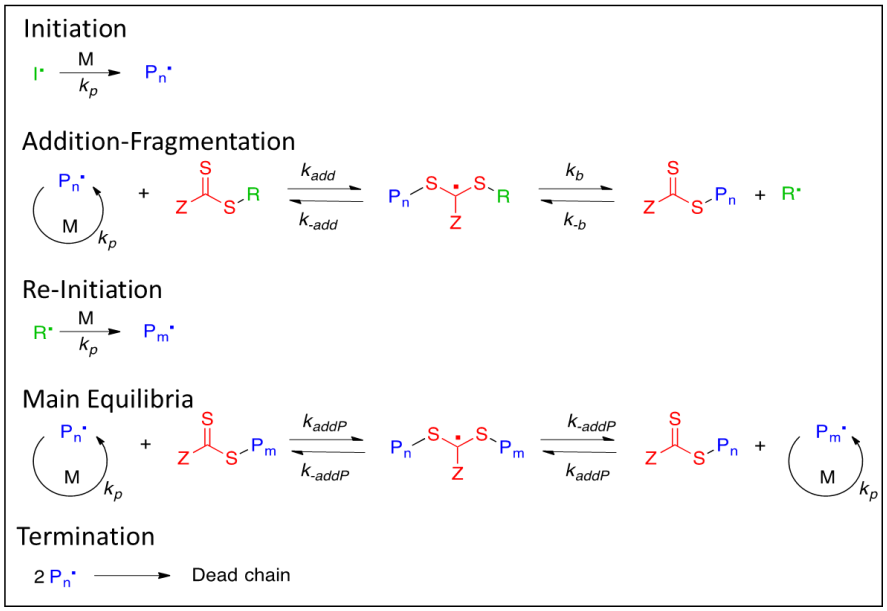

Scheme 1.3. RAFT polymerization mechanism.

This is followed by the addition-fragmentation stage in which the propagating chains are added to the CTA, releasing a new radical species R·, capable of initiating a new chain (re-initiation process). Then, in a typically short time with respect to the decomposition of the initiator, an equilibrated exchange is established between *dormant* species, which are illustrated as S=CS-P_n and contribute to the controlled character of the RAFT process, and *active* chains. In an analogy to what illustrated in Scheme 2, the intermediate radical, P_n-SĊ(Z)S-P_m, can split in both directions,

providing all polymer chains with the same chance to grow. Termination occurs, as with any radical polymerization, through coupling and disproportion mechanisms. Is worth noting that the radical species that are formed remain constant throughout the course of the reaction. This results in a uniform distribution of molecular weights and a Đ close to unity and, for this to occur, the propagation speed should always be maintained much lower than that of the addition-fragmentation stage, ensuring that a single monomeric unit is incorporated, on average, after few activation cycles, thus generating chains of similar polymerization degree. The small percentage of termination reactions, which leads to the formation of *dead* chains, is related to the number of radicals generated in the initial stage according to Equation 1.1.[9]

$$\%_{dead\ chain} = \frac{1}{\frac{[CTA]}{2f[I]_0(1-e^{-kt})}+1}10^2 \qquad \text{Equation 1.1}$$

with [CTA] equal to the concentration of the chain transfer agent in solution, $[I]_0$ equal to the concentration of initiator present in solution at the beginning of the reaction, k kinetic constant of the initiator decomposition rate in the selected experimental conditions and *f* is the decomposition rate of the initiator.

Notably, at the end of the process, each RAFT (non-dead) chain will have a carbonylthioylthio (Z-C(C=S)S) group and an R group at the polymer chain extremities, which is an essential feature for the fabrication of block copolymers and for site-specific post-polymerization modifications.[11] Despite the robustness of the RAFT technique, it should be emphasized that thiocarbonyl moieties are subject to undesirable reactions in the presence of nucleophilic species such amine impurities, which must be strictly absent in the reaction environment or, similarly, it is necessary to protect any amino functions if present in the monomers used, as polar chemical reactions as aminolysis of the Z-C(C=S)S group irreversibly terminate the chain polymerization.

The ratio between the concentration of CTA and radical initiator [CTA] / $[I]_0$ is therefore an important parameter to consider for controlling the final properties of

the synthesized material. It is usually greater than one, so that the number of molecules of the RAFT agent in solution is always maintained greater than the free radical species. While the concentration of free radicals in the system is related to the rate of decomposition of the initiator, the number of chains is, indeed, determined by the amount of CTA.[12] An increase in the concentration of RAFT agent leads to the formation of polymers with lower molecular weight and lower Đ. Conversely, decreasing the [CTA]/[I] ratio leads to a higher conversion rate but worse control over the final molecular weight, increasing the likelihood of irreversible termination reactions. For this reason, while optimizing different reaction conditions for RAFT polymerizations, it is commonly a good practice to maintain a low [CTA] / [I] to achieve better control over the final molecular weight distributions of the product. It is worth noting that, to achieve a certain desired molecular weight is possible also by stopping the polymerization reaction at defined reaction times. The degree of polymerization DP_{th}, in fact, is given by the following equation.

$$DP_{th} = \frac{[M]_0 - [M]_t}{[CTA]_0 + df([I]_0 - [I]_t)} \qquad \text{Equation 1.2}$$

where $[M]_0$ and $[M]_t$ are the monomer concentrations at the beginning of the reaction and at time t, respectively; $[CTA]_0$ is the initial concentration of chain transfer agent, $[I]_0$ is equal to the concentration of initiator present in solution at the beginning of the reaction, $[I]_t$ is equal to the concentration of initiator present in solution at the time t, d is the fraction of chains resulting from coupling reactions, and f is the efficiency of the initiator.

As a first approximation, with almost unitary efficiency of the initiator and a low incidence of termination reactions, the equation can be simplified to the following.

$$DP_{th} = \frac{[M]_0 - [M]_t}{[CTA]_0} \qquad \text{Equation 1.3}$$

This control allows the synthesis of virtually any desired polymer architecture: multi-block, star, graft, statistical, alternating, and gradient copolymers, just to cite a few (Figure 1.5).[9]

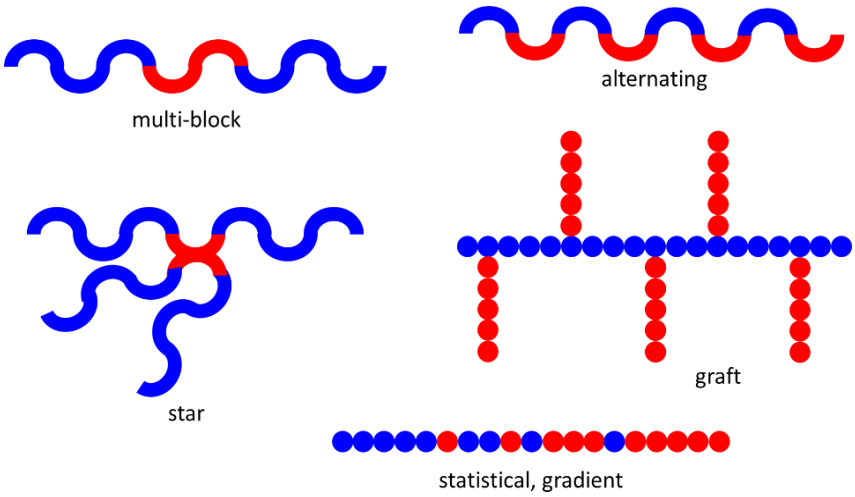

Figure 1.5. Examples of different architectures which can be achieved by RAFT copolymerization.

1.3.2. Strategies for SCNP Compaction

To facilitate the intramolecular crosslinking, a wide range of functional groups has been explored, utilizing for example photochemistry, metal-complexation or non-covalent interactions, as highlighted by several review articles in which vast collections of techniques for SCNPs folding have been reported.[13] Herein, three main strategies available for polymer single-chain compaction will be briefly mentioned, namely (i) covalent cross-linking, (ii) metal-induced cross-linking and (iii) non-covalent cross-linking, by retracing some representative and recent literature examples in the field.

(i) Covalent cross-linking.

Thanks to the high dissociation energies of the covalent range of chemical bonds, folding a polymer molecule into a single-chain nanoparticle via covalent chemistry is usually a way to ensure durability, morphology stability and compactness

of the final product. SCNPs which are obtained by means of covalent chemistries are more stable than their non-covalent counterparts, therefore facilitating their analysis via common chromatography techniques and reducing irreversible aggregation phenomena upon crowding.

Starting from the thermal dimerization of benzocyclobutene units of a single-polymeric chain,[14] milder and more controlled methodologies of fabrication of covalent SCNPs have been investigated, as amide[15] and urea formation,[16] as well as thiol-Michael utilizing diacrylate moieties in the lateral polymeric chain as electrophiles for the cross-linking, which was successfully carried out both in organic solvents and in water for different functional copolymers.[17-19] 1,3-dipolar cycloadditions have also been utilized for the formation of SCNPs, either exploiting two complementary functional monomers within the same polymeric precursor or with the introduction of a crosslinker.[20-23]

Several strategies have already been reported in this sense,[24-27] amongst which the photochemically induced collapse reported by Thanneeru *et al.* is worth mentioning.[28] In their work on tadpole-shaped SCNPs, the authors demonstrated the use of intermolecular photo-crosslinking of amphiphilic polyacrylates co-polymethacrylates block copolymers, which were efficiently converted into tadpole-shaped SCNPs of various morphologies thanks to the photo[2+2]cycloaddition of the cinnamoyl moieties present in the lateral chains of the precursors. Interestingly, different morphologies were achieved depending both on the solvent used for the photo cross-linking reaction and the position of the cinnamoyl moieties in the main chain, within the hydrophilic block or in the hydrophobic section (Figure 1.6).

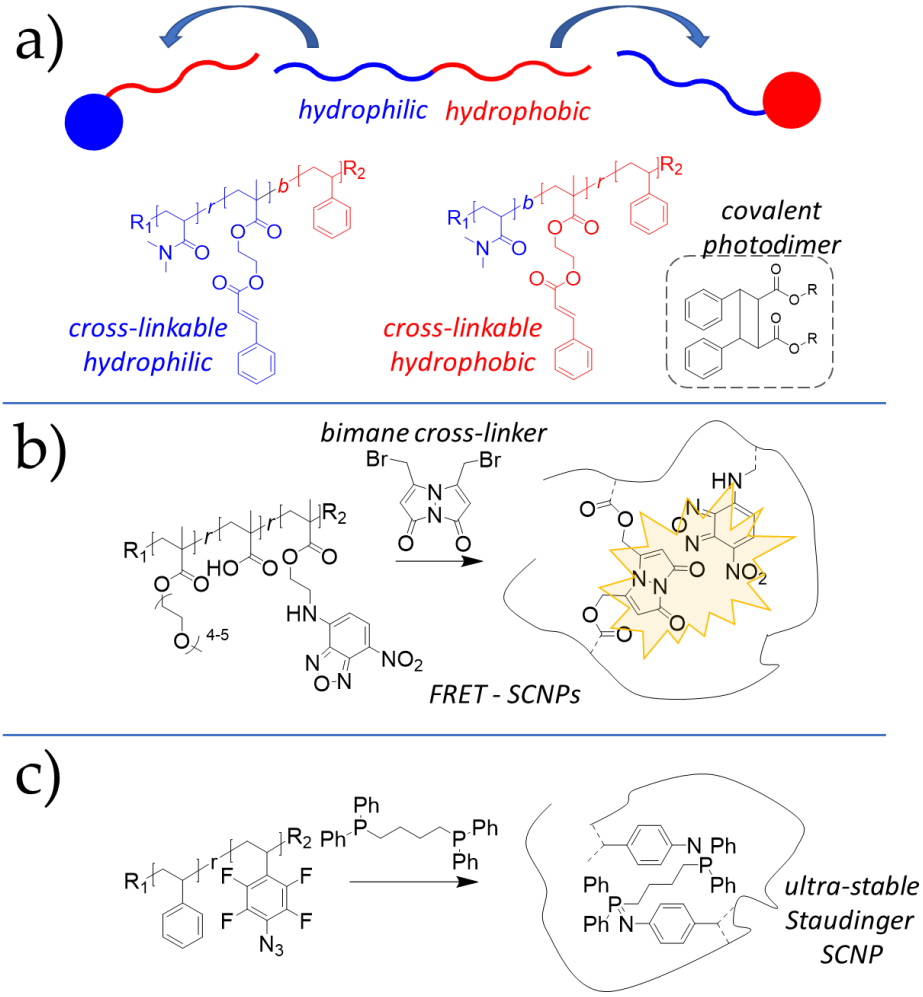

Figure 1.6. a) Tadpole-shaped, amphiphilic SCNPs of different morphologies upon switching precursors' cross-linkable units position, obtained *via* photo[2+2]cycloaddition of cinnamoyl moieties.[28] **b**) FRET-SCNPs synthesisez by Maag *et al*. *via* reaction with the dibromo bimane cross-linker.[29] **c**) Reaction scheme of the reaction of diazaylide bond formation for the preparation of the ultra-stable "Staudinger" SCNPs.[30]

In an analogous work, Zhang *et al.* report the folding of a linear polymer *via* photodimerization of cyanostilbene moieties pendants, favored by self-organization of the polymeric precursor *via* the non-covalent π-π stacking forces,[31] displays how the concomitant use of intramolecular non-covalent interactions and photochemically induced covalent bond formation can lead to reliable SCNPs of defined morphology.

The formation of amide and ester bonds for the chain collapse reaction in the fabrication of SCNPs is another reliable strategy which have been recently employed, as demonstrated by Maag *et al.*, the collapsed, highly packed polymeric structure exhibiting Förster resonance energy transfer was achieved by reacting a linear polymeric precursor bearing nitrobenzoxadiole (NBD) units and free carboxylic moieties with the fluorescent reactant dibromobimane (Figure 5).[29]

In the work published by Jackson *et al.*, stimuli-degradable SCNPs were obtained through folding of a polymeric precursor, which was obtained *via* radical ring-opening polymerization (rROP) of 2-methylene-1,3-dioxepane (MDO) and methacrylic acid *N*-hydroxysuccinimide ester (NHSMA) and subsequently cross-linked by condensation reaction with a diamino-cross-linker.[17] As anticipated, covalently cross-linked SCNPs are especially desirable when stability, either thermal or chemical, is required for a specific application, for this, the preparation of novel systems as the ultra-robust "Staudinger" SCNPs was recently reported, for which the authors took advantage of a pentafluorophenyl-bearing styrenic copolymer, which was azidated as showed in Figure 1.6 and subsequently covalently cross-linked by reaction with a diphosphine cross-linker, to give the stable azaylide bonds, as showed in Figure 1.6.[30]

(ii) Metal-mediated folding / collapse.

Metal-organic compounds present a rich chemistry, which is often present in naturally occurring proteins and exploited by enzymes not only for the ultimate catalytic purposes, but with structural functions as well, the "zinc finger" is a representative phenomenon, being a recurrent structural motif in a plenty of abundant proteins of living organisms.[32] Analogously, the formation of metal-organic complexes have been employed for the fabrication of SCNPs, as in the case of the preparation of the heterobimetallic SCNPs reported by Knöfel *et al.*[13] The authors exploited a bifunctional terpolymer precursor, synthesized by NMP, containing two orthogonal ligand moieties, phosphines and phosphine oxide which allowed the facile and selective incorporation of the two metals Pt(II) and Eu(III) respectively, as showed in Figure 1.7.

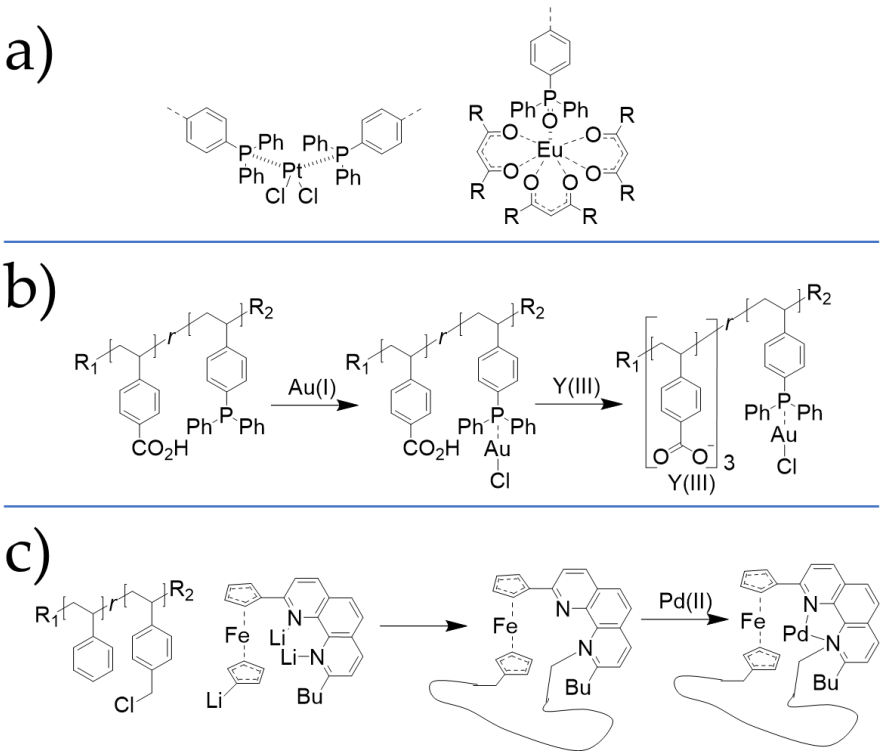

Figure 1.7. a) Orthogonal complexation modalities employed for heterobimetallic metal-induced SCNP collapse.[33] **b**) Sequential and orthogonal metal insertions within the structure of a metal-folded SCNP.[34] **c**) SCNPs embedded with a ferrocene-unit, allowing the subsequent introduction of Pd(II) ions within the nanoparticle.[35]

In an analogous work, heterobimetallic Au(I) / Y(III)-SCNPs were prepared taking advantage of the orthogonal chemistries of triphenylphosphines and carboxylate anions.[34] In this latter work, the introduction of the first metal, Au(I), though complexation with phosphines in the lateral chains of a functionalized polystyrene (Figure 1.7) did not involve the collapse of the polymeric chains, which was instead induced only by introduction of the second metal, Y(III), *via* complexation with three carboxylate anion pendants of the same polymeric chain.

A third example of heterobimetallic SCNPs is provided by the work of Reith *et al.*, in which a method of folding / collapse of the polymeric chains to SCNPs based

on the complexation of Ni(II) and Cu(II) ions by chelation of picolyl moieties.[36] In addition, this approach allowed to study the influence of the initial polymeric sequence to the final nanoparticles' morphology.

Similarly, Fe(II)-folded SCNPs have been constructed through the cooperation of intrachain Fe(II)-oxazoline coordination and hydrophobic interactions in the work published by Wang *et al*.[37] Another possible use of iron ions for SCNPs fabrication was recently reported by Gillhuber *et al.*, in which it was demonstrated that single polymeric chains can be folded on themselves *via* ferrocene formation, as well as combining SCNP-collapse with the concomitant introduction of additional ligands for other metals (Pd(II)) complexation, yielding heterobimetallic ferrocene SCNPs.[35]

(iii) Supramolecular interactions.

Although the use of either covalent or dynamic / covalent chemistries allow the preparation of reliable and more stable SCNPs, it is also true that the formed intramolecular connections are often irreversible, meaning that chains are freezed in a particular folded state. This latter is in contradiction with what exhibited by Nature when designing its unrivalled SCNPs: proteins. Biotic proteins often present advanced and specific properties, such as highly efficient catalytic specificity, molecular recognition etc., mainly due to conformational flexibility. Catalytic activity of an enzyme is, in example, lost upon disruption (denaturation) of its native, folded state, indicating that function and folding of the protein polymeric chain are intimately connected. In addition, such folding mostly relies on non-covalent, supramolecular interactions, such as hydrogen bonding, hydrophobic interactions and steric hindrance effects and only rarely tertiary and quaternary structures of a functional proteins are based on covalent interactions (the native state of a typical globular protein is favored by only∼5 kcal/mol ΔG° relative to the unfolded state near room temperature).[38] In this sense, to endow functional materials with supramolecular interactions seem to be a sound strategy towards advanced applications.

A first report of supramolecular forces-induced chain collapse described the capability of primary amide-bearing polymethacrylates of self-assembling into SCNPs when put in contact with toluene,[39] but it was only after the seminal contributions from

Berda, Meijer and Foster that supramolecular chemistry definitely entered as a new, powerful tool for SCNPs design.[10] In their work, the authors employed polymethacrylates-based nanoparticles containing 2-ureidopyrimidinone (UPy) pendant units, whose intrinsic H-bond based self-associating capability permitted the observation via atom-force microscopy (AFM) techniques of the formation of supramolecular, discrete SCNPs of well-defined morphology for the first time. From then on, different strategies relying on noncovalent forces, the use of host-guest interactions as described by Sherman *et al.*,[40] but a special attention to hydrogen bonds, for polymeric chain folding / collapse have been have been put in the investigation in this sense -spanning from systems based on benzamides, aryl tricarboxamides,[41] urea, and UPy analogues-[42] suggesting that, also amongst supramolecular chemists in the field of SCNPs, still remain the undefeated strategy towards the fabrication of noncovalent, self-assembled functional nanoparticles. Tadpole-like SCNPs were also obtained by means of electrostatic-mediated intramolecular crosslinking, which was induced through the introduction of imidazolium moieties, resulting in individual folding / collapse of polymeric chains as reported by Shao *et al.*[43] Notably, the fabrication of SCNPs with this methodology allowed the synthesis at relatively concentrated polymer solutions, up to 40 mg mL^{-1}.

SCNPs can ultimately be prepared by the sole solvophobic interactions occurring between the polymeric chains and the selected solvent, with this being especially true in the case of amphiphilic polymeric precursors in water. When a monomer-selective solvent is used, the polymeric chains tend to collapse on itself to spontaneously reach the more energetically economic conformation, resulting in self-folded nano objects in solution. In a work described by Guazzelli *et al.* this latter has been efficiently investigated both through small-angle X-ray scattering SAXS and DLS techniques, in which a polymeric precursor containing amphiphilic tetrafluoroethylene monomers bearing a polyethylene glycol (PEG) chain in the para position sowed to self-assemble / collapse into noncovalent SCNPs conformations when dissolved into water / methanol mixtures or pure water. A property which was reversibly lost in THF or DMF solutions, in which conventional random coils were obtained instead.[44] An analogous behavior was reported by Terashima *et al*. in two independent works on

amphiphilic copolymers, consisting of hydrophilic PEG pendants and a hydrophobic backbone, which resulted to self-organize in water in a spontaneous manner into SCNPs conformations.[45, 46] The authors referred to these self-assembled nano object as "unimer micelles", reporting that such entities were providing a hydrophobic compartment, spontaneously generated via hydrophobic forces upon contact with the solvent and within the collapsed structure, a feature which was completely lost upon addition of methanol.

1.4. Recent Advanced Applications of SCNPs.

A defined copolymer sequence is a powerful way to exploit supramolecular interactions to meet diverse chemical challenges. As demonstrated by Nature, the variety of structure and function displayed by biological macromolecules is unrivalled; such complexity is in fact achieved by virtue of the major biopolymer backbones, namely proteins, ribonucleic acids, and polysaccharides. Different biological functions, including molecular recognition, information storage, and catalysis, come from the precise conformation adopted by biopolymers, ultimately controlled by the self-folding of their primary structures.[47]

As described in the previous sections, the folding individual synthetic polymer chains at high dilution by means of multiple intra-chain (reversible or irreversible) bonding interactions produces SCNPs. Even following an imperfect folding process and despite there is only a rough analogy between the process of SCNP formation and the precise, specific folding of a polypeptide chain to its native, functional state, the conformational degrees of freedom in SCNPs are restricted, giving rise to local domain formation.[48] Notably, such chain compaction-related effects are beneficial for the construction of efficient enzyme-mimetic catalysts, improved drug delivery nanosystems and innovative sensing nanomaterials[49]

1.4.1. Catalysis

Enzymes are biological catalysts, which are not only responsible of the acceleration of all biochemical reactions in living organisms, but which can be selected and used for industrial purposes, often as irreplaceable, efficient catalysts for a wide collection of reactions running in water and close to room temperature, or as highly performative sensors.[50] The hypothesis of the evolutionary pressure being the driving force toward the maximal catalytic performance of enzymes is, indeed, strongly supported by the observed high reaction rates, unrivalled when compared to their uncatalyzed counterparts. Despite the recent scientific effort, still little information is available on the possible parameters and constraints which could have shaped natural enzymes, therefore hiding to synthetic scientists the secrets to design artificial enzymes outperforming biotic catalytic proteins.[51]

SCNPs are posed as perfect candidates for the development of artificial nano-enzymes, as resemble natural proteins in many aspects, which can ultimately be optimized and tuned, offering many possibilities towards novel, soft-matter based catalytic systems -*e.g.*, large surface-to-volume ratio, presence of multiple small "local pockets" for the catalytic process to occur, resistance to dilution *etc*.[52] Several applications of SCNPs for catalytic purposes have already been described and the topic has been reviewed extensively in recent years,[47,48] demonstrating the great potential of these materials in this sense. Amongst the results published over the last four years and concerning catalytically active SCNP, very noticeably stand out the works from Zimmermann *et al*. on biorthogonal approaches to SCNPs-mediated catalysis. In a first work, the authors developed a copper-containing, amphiphilic SCNPs-based catalyst which was able to operate selectively on small substrates, the ones capable of diffusion in the polymeric corona, performing azido-alkyne couplings. Having observed that the SCNPs which were decorated with surface ammonium groups resisted to cell internalization, the authors reported that these nano-objects were capable of performing extracellular catalysis in cell culture media in a biorthogonal fashion.[53] In a second work by Zimmermann's group, the authors report a second metal-containing, amphiphilic SCNP-based system, manufactured by means of click-reaction between a

cyclometalated ruthenium complex bearing alkyne groups and azide-bearing, water-soluble copolymer precursor. The obtained Ru-SCNPs were able to efficiently reduce azido groups in the corresponding amine, as in the reported case of the preparation of rhodamine from its azido-analogue.[54] Notably, the Ru-SCNPs were able to act as enzyme carriers, facilitating the uptake of a particular protein into the cells. Specifically, the Ru-SCNPs complexed the enzyme βGal and delivered it to endosomes, without altering its catalytic activity nor the enzyme one.[54]

Barner-Kowollik *et al.* recently described the preparation of visible-light photocatalytic amphiphilic SCNPs, easily fabricated by compaction of a poly(ethylene glycol) methyl ether methacrylate and glycidyl methacrylate by means of thiol-epoxide reaction with rose Bengal, which allowed the observation of the photocatalytic oxidation of long-chain fatty acids in water.[55]

Another innovative application of SCNPs in catalysis is given by the preparation of bottlebrush-colloid Janus nanoparticles JNPs, fabricated by flexible modification of a metal-containing SCNP, which SCNP was achieved in large scale by electrostatic-mediated intramolecular crosslinking of Poly(vinylbenzylchloride)-*b*-Poly(methacrylic acid), PVBC-*b*-PMAA, in concentrated solution *via* metallic coordination. The derived magnetic / pH-/ thermo-responsive bottlebrush-colloid, JNPs, obtained by grafting with Poly(N-isopropylacrylamide) and coprecipitated with a Poly(dimethylaminoethylmethacrylate), PVBC-*g*-PNIPAM-cPMAA@Co-PDMEAMA, appeared to serve as a solid emulsifier to stabilize emulsions in a way that made emulsions manipulated by adjusting pH and temperature. The bottlebrush-colloid JNPs also demonstrated high catalytic efficiency with good turnovers in hydrogenation reactions at the oil / water emulsion interface.[56]

Xu *et al.* recently demonstrated that a SCNP-based system was able to catalyze the synthesis of micro-structured composites acting as polymerization catalyst in a polymerizable matrix. Notably, the polymerization occurred inwardly, in a stepwise manner, allowing the achievement of a multi-shelled or core-shell structure.[57]

Being far easier to synthesize than their biological counterparts, the enzymes, SCNPs are posed as innovative and unique catalyst of great potential for a variety of

applications. Also, thanks to the wide array of methodologies to generate SCNPs from linear polymers, to the possibility to manipulate and tune the morphology of the final nanoparticle and diverse functionalization, including the incorporation of metal complexes, SCNPs are conquering more and more space in the field of advanced catalysis, a particularly interesting feature when thinking about bio-orthogonal applications, both for industrial and clinical purposes.

1.4.2. Nanomedicine

Nanomedicine is the application of nanotechnology and nanoscience to the prevention and treatment of human illnesses. The research in the field of nanomedicine notably impelled the development of novel nanomaterials and nanotherapeutics, leading to improvements in diagnostics and growingly sophisticated medical devices.[58] A main advantage offered by nanotherapeutics in comparison to traditional, small-molecule drugs is that the first often exhibit greater therapeutic efficacy due to their size (10–100 nm). Nanotherapeutic formulations also generally present lower toxicity, improved bioavailability, enhanced pharmacokinetics and therapeutic effect.[58] Liposome-based drug delivery systems, protein-based nanotherapeutics, inorganic nanoparticles and synthetic polymers are some of the major families of compounds currently employed for nanomedicine applications, having already reached the marked as in the notable cases of liposome-based anticancer formulations with cis-platin, paclitaxel, irinotecan and docetaxel.[59] Polymer-derived nanoparticles and nanofiber-based scaffolds can exhibit improved safety levels for the application on the human body through precise bioimaging, tissue regeneration and drug delivery applications with enhancement of the drug distribution and bioavailability, and minimized adverse effects of the treatment. Amongst the different opportunities provided by polymer-based scaffolds, SCNPs are posed as perfect candidates for applications in nanomedicine and, although the investigation in this sense is still sparse, early indications regarding in vivo behavior of SCNPs has already been reported.[60]

The tumor targeting capability and the clearance studies of SCNPs have been evaluated in xenograft mouse models for different kinds of human tumors, and zebrafish embryos.[60,61] SCNPs have also been recently tested for targeting for specific cells, a crucial challenge in biomedical applications to step forward drug selectivity for various diseases treatments. *E.g.* Kröger *et al.* glucose-based SCNPs which, after anchoring on nanodiamonds scaffolds, showed efficient selective macrophages imaging capability in vitro.[62] Specific receptor targeting was also utilized by Baij *et al.* for cell labeling and imaging of human breast cancer (SK-BR-3) cells.[63]

Another opportunity provided by SCNPs for nanomedicine applications is the encapsulation of active compounds, both for imaging and therapeutic purposes. The encapsulation abilities of SCNPs have been investigated for different systems, both covalently and non-covalently formed SCNPs. Kröger *et al.* reported a SCNP system that is able to encapsulate both hydrophobic and hydrophilic small drug molecules.[64]

To conclude, SCNPs have shown promise in in vitro studies and in preliminary in vivo observations. The investigated systems usually maintain good cell viabilities and the facile access to different functional groups allowed the preparation of selective, ultra-small nano-objects which presented good malignant cell targeting behavior. Despite the encouraging results, systematic investigations of biocompatibility, biodistribution and behavior of the SCNPs in their biological applications are required to unravel the full potential of SCNPs for nanomedical purposes.

1.5. Main Aims and Structure of the Thesis

The principal objective of this work consisted in building a bridge, both conceptual and empirical, between SCNP-based technology and photocatalysis. In particular, the present thesis focused on employing the opportunities offered by SCNP topology to enable photocatalysis in aqueous environments.

In Chapter II, we aimed at introducing the definitions, fundamental concepts and major constraints presented by organic photocatalyzed processes in aqueous solutions, with special attention on how supramolecular approaches have been recently

applied to address the issues associated with the use of water as solvent for photo-induced organic transformations.

These concepts put the basis for what we subsequently reported in Chapter III, in which we aimed to prepare a novel class of versatile SCNP capable of efficiently carry out photocatalytic organic reactions in water. The solvent selected by Nature for performing biochemical transformation is, indeed, water, a strategy which often relies on the exploitation of the hydrophobic interactions between the nano-catalysts, the enzymes, and substrates. For this, we designed an amphiphilic polymeric precursor of ultra-high molecular weight and low dispersity, which was embedded with photocatalytic activity by decoration with an iridium(III)-based cyclometalated complex though a post-polymerization functionalization approach. The readily prepared photoactive amphiphile, which resulted to efficiently self-assemble in aqueous solution by folding / collapse into a SCNP structure, was subsequently tested for its capability of performing two unprecedently reported organic reactions in water, namely the photo[2+2]cycloaddition of vinyl arenes and the α-arylation of arylamines, as well as the oxidation of 9-substituted anthracenes and the β-sulfonylation of α-styrene.

In Chapter IV we decided to further exploit the opportunities provided by SCNP towards photocatalytic applications, proving their suitability as efficient photosensitizer nanocarriers for photodynamic therapy (PDT) applications. For this, we developed a facile protocol for the encapsulation of a synthesized, long-wavelength absorbing zinc(II)-phthalocyanine (**ZnPc**) within the core of a novel, self-aggregating generation of amphiphilic copolymers. Taking advantage of the well-known self-assembly capability of anthracene molecules, we prepared anthracene-based amphiphilic copolymers both capable of self-assembly in water and of efficiently encapsulating the far infrared-responsive complex **ZnPc**, yielding stable, water soluble, red-light reactive SCNPs, as confirmed by SAXS characterization. We then tested this long-wavelength reactive amphiphilic SCNPs against human breast cancer cell MDA-MB-231 lines to assess their PDT efficiency. Having observed outstanding

performance for one of the selected formulations, we finally tested their PDT activity in Zebrafish embryo xenografts as a more accurate human cancer model.

Finally, the conclusions to the present thesis will be delineated in Chapter V.

1.6. References

(1) Kraus, T.; Malaquin, L.; Schmid, H.; Riess, W.; Spencer, N. D.; Wolf, H. Nanoparticle printing with single-particle resolution. *Nat. Nanotech*. **2007**, 2, 570-576.

(2) Lee, H.; Choi, T. K.; Cho, H. R.; Ghaffari, R.; Wang, L.; Choi, H. J.; Chung, T. D.; Lu, N.; Hyeon, T.; Choi, S. H.; Kim, D.-H. A graphene-based electrochemical device with thermoresponsive microneedles for diabetes monitoring and therapy. *Nat. Nanotech.* **2016**, 11, 566-572.

(3) Parkatzidis, K.; Wang, H. S.; Truong, N. P.; Anastasaki, A. *Chem* **2020**, 6, 1575-1588.

(4) Nitti, A.; Carfora, R.; Assanelli, G.; Notari, M.; Pasini, D. Single-chain polymer nanoparticles for addressing morphologies and functions at the nanoscale: a review. *ACS Appl. Nano Mater.* **2022**, 5, 10, 13985-13997.

(5) Matyiaszewski, K.; Xia, J. Atom transfer radical polymerization. *Chem. Rev.* **2001**, 101, 2921-2990.

(6) Hawker, C. J.; Bosman, A. W.; Harth, E. New polymer synthesis by nitroxide mediated living radical polymerizations. *Chem. Rev.* **2001**, 101, 3661-3688.

(7) Moad, G.; Rizzardo, E.; Thang, S. H. Living radical polymerization by the RAFT process-a third update. *Aust. J. Chem.* **2012**, 65, 985-1076.

(8) Moad, G.; Chiefari, J.; Krstina, J.; Postma, A.; Mayadunne, R. T. A.; Rizzardo, E.; Thang, S. H. Living free radical polymerization with reversible addition fragmentation chain transfer (the life of RAFT). *Polym. Int.* **2000**, 49, 993–1001.

(9) Handbook of RAFT polymerization. Edited by Christopher Barner-Kowollik. **2008** WILEY-VHC Verlag GmbH & Co. KGaA, Weinheim.

(10) Berda, E. B.; Foster, E. J.; Meijer, E. W. Toward controlling folding in synthetic polymers: fabricating and characterizing supramolecular single-chain nanoparticles. *Macromolecules* **2010**, 43, 1430-1437.

(11) Willcock, H.; O'Reilly, R. End group removal and modification of RAFT polymers. *Polym. Chem.* **2010**, 1, 149-157.

(12) a) Artar, M.; Terashima, T.; Sawamoto, M.; Meijer, E. W.; palmans, A. R. A. Understanding the catalytic activity of single-chain polymeric nanoparticles in water. *J. Polym. Sci. A Polym. Chem.* **2014**, 52, 12-20. b) Abdouni, Y.; ter Huurne, G. M.; Yilmaz, G.; Monaco, A.; Redondo-Gómez, C.; Meijer, E. W.; Palmans, A. R. A.; Becer, C. R. Self-assembled multi- and single-chain glyconanoparticles and their lectin recognition. *Biomacromol.* **2021**, 22, 661-670. c) Liu, Y.; Turunen, P.; de Waal,

B. F. M.; Blank, K. G.; Rowan, A. E.; Palmans, A. R. A.; Meijer, E. W. Catalytic single-chain polymeric nanoparticles at work: from ensemble towards single-particle kinetics. *Mol. Syst. Des. Eng.* **2018**, 3, 609-618. d) Deng, L.; Albertazzi, L.; Palmans, A. R. A. Elucidating the stability of single-chain polymeric nanoparticles in biological media and living cells. *Biomacromol.* **2022**, 23, 326-338.

(13) Zhang, C.; Yan, L.; Wang, X.; Zhu, S.; Chen, C.; Gu, Z.; Zhao, Y. progress, challenges, and future of nanomedicine. *Nano Today* **2020**, 35, 101008.

(14) Harth, E.; Horn, B. V.; Lee, V. Y.; Germack, D. S.; Gonzales, C. P.; Miller, R. D.; Hawker, C. J. A facile approach to architecturally defined nanoparticles via intramolecular chain collapse. *J. Am. Chem. Soc.* **2002**, 124, 8653-8660.

(15) Sanchez-Sanchez, A.; Fulton, D. A.; Pomposo, J. A. pH-responsive single-chain polymer nanoparticles utilizing dynamic covalent enamine bonds. *Chem. Commun.* **2014**, 50, 1871-1874.

(16) Beck, J. B.; Killops, K. L.; Kang, T.; Sivanandan, K.; Bayles, A.; Mackay, M. E.; Wooley, K. L.; Hawker, C. J. Facile preparation of nanoparticles by intramolecular cross-linking of isocyanate functionalized copolymers. *Macromolecules* **2009**, 42, 5629-5635.

(17) Kröger, A. P. P.; Hamelmann, N. M.; Juan, A.; Lindhoud, S.; Paulusse, J. M. J. Biocompatible single-chain polymer nanoparticles for drug delivery – a dual approach *ACS Appl. Mater. Interfaces* **2018**, 10, 30946-30951.

(18) Kröger, A. P. P.; Boonen, R. J. E. A.; Paulusse, J. M. J. Well-defined single-chain polymer nanoparticles via thiol-Michael addition. *Polymer* **2017**, 120, 119-128.

(19) Kröger, A. P. P.; Paats, W. D.; Boonen, R. J. E. A.; Hamelmann, N. M.; Paulusse, J. M. J. Pentafluorophenyl-based single-chain polymer nanoparticles as a versatile platform towards protein mimicry. *Polym. Chem.* **2020**, 11, 6056-6065.

(20) De Luzuriaga, A. R.; Ormategui, N.; Grande, H. J.; Odriozola, I.; Pomposo, J. A.; Loinaz, I. Intramolecular click cyccloaddition: an efficient room-temperature route towards bioconjugable polymeric nanoparticles. *Macromol. Rapid Commun.* **2008**, 29, 1156-1160.

(21) Chen, J.; Wang, J.; Li, K.; Wang, Y.; Gruebele, M.; Ferguson, A. L.; Zimmerman, S. C. Polymeric "clickase" accelerates the copper click reaction of small molecules, proteins, and cells. *J. Am. Chem. Soc.* **2019**, 141, 9693-9700.

(22) Chen, J.; Li, K.; Bonson, S. E.; Zimmerman, S. C. A biorthogonal small molecule selective polymeric "clickase" *J. Am. Chem. Soc.* **2020**, 142, 13966-13973.

(23) Maiz, J.; Verde-Sesto, E.; Asenjo-Sanz, I.; Fouquet, P.; Porcar, L.; Pomposo, J. A.; de Molina, P. M.; Arbe, A.; Colmenero, J. Collective motions and mechanical response of a bulk of single-chain nano-particles synthesized by click-chemistry. *Polymers*, **2021**, 13, 50.

(24) Willenbacher, J.; Wuest. K. N. R.; Mueller, J. O.; Kaupp, M.; Wagenknecht, A.; Barner-Kowollik, C. Photochemical design of functional fluorescent single-chain nanoparticles. *ACS Macro Lett.* **2014**, 3, 574-579.

(25) Wuest, K. N. R.; Lu, H.; Thomas, D. S.; Goldmann, A. S.; Stenzel, M. H.; Barner-Kowollik, C. Fluorescent glyco single-chain nanoparticle-decorated nanodiamonds. *ACS Macro Lett.* **2017**, 6, 1168-1174.

(26) Offenloch, J. T.; Willenbacher, J.; Tzvetkova, P.; Heiler, C.; Mutlu, H.; Barner-Kowollik, C. Degradable, fluorescent single-chain nanoparticles based on metathesis polymers. *Chem. Commun.* **2017**, 53, 775-778.

(27) Offenloch, J. T.; Willenbacher, J.; Tzvetkova, P.; Heiler, C.; Mutlu, H.; Barner-Kowollik, C. Degradable, fluorescent single-chain nanoparticles based on metathesis polymers. *Chem. Commun.* **2017**, 53, 775-778.

(28) Thanneeru, S.; Li, W.; He, J.; Controllable self-assembly of amphiphilic tadpole-shaped polymer single-chain nanoparticles prepared through intrachain photo-cross-linking. *Langmuir*, **2019**, 35, 2619-2629.

(29) Maag, P. H.; Feist, F.; Frisch, H.; Roesky, P. W.; Barner-Kowollik, C. Förster resonance energy transfer within songle chain nanoparticles. *Chem. Sci.* **2024**, 15, 5218-5224.

(30) Blázquez-Martín, A.; Bonardd, S.; Verde-Sesto, E.; Arbe, A.; Pomposo, J. A. ACS Polym. Au 2024, 4, 140-148.

(31) Zhang, Y.; Xue, Y.; Gao, L.; Liao, R.; Wang, F.; Wang, F.; Merging non-covalent and covalent crosslinking: en route to single chain nanoparticles. *CChem. Lett.* **2024**, 35, 109217.

(32) Li, X.; Han, M.; Zhang, H.; Liu, F.; Pan, Y.; Zhu, J.; Liao, Z.; Chen, X.; Zhang, B. Structures and biological functions of zinc finger proteins and their roles in hepatocellular carcinoma. *Biomarker Res.* **2022**, 10, 2.

(33) Knöfel, N. D.; Rothfuss, H.; Tzuetkova, P.; Kulendran, B.; Barrner-Kowollik, C.; Roesky, P. W. Heterobimetalli Eu(III)/Pt(II) single-chain nanoparticles: a path to enlighten catalytic reactions. *Chem. Sci.* **2020**, 11, 10331-10336.

(34) Bahley, J. L.; Kulendran, B.; Roesky, P. W.; Heterobimetallic Au(I)/Y(II) single-chain nanoparticles as recyclable homogeneous catalysts. *Polym. Chem.* **2021**, 12, 4016-4021.

(35) Gillhuber, S.; Halloway, J. O.; Frisch, H.; Feist, F.; Weigend, F.; Barner-Kowollik, C.; Roesky, P. W.; Ferrocene-driven single-chain polymer compaction. *Chem. Commun.* **2023**, 59, 4672-4675.

(36) Reith, M. A.; Kardas, S.; Mertens, C.; Fossepré, M.; Surin, M.; Steinkoenig, J.; Du Prez, F. E.; Using nickel to fold discrete synthetic macromolecules into single-chain nanoparticles. *Polym. Chem.* **2021**, 12, 4924-4933.

(37) Wang, W.; Wang, J.; Li, S.; Li, C.; Tan, R.; Yin, D. Iron(II)-folded single-chain nanoparticles: a metalloenzyme mimicking sustainable catalysts for highly enantioselective sulfa-Michael addition in water. *Green Chem.* **2020**, 22, 4645-4655.

(38) Mello, C. C.; Barrick, D. An Experimentally determined protein folding energy landscape. *Proc. Natl. Acad. Sci. U. S. A.* **2004**, 101, 14102−14107.

(39) Seo, M.; Beck, B. J.; Paulusse, J. M. J.; Hawker, C. J.; Kim, S. Y.; Polymeric nanoparticles via noncovalent cross-linking of linear chains. *Macromolecules* **2008**, 41, 6413-6418.

(40) Appel, E.A.; Dyson, J.; del Barrio, J.; Walsh, Z.; Scherman, O. A. Formation of single-chain nanoparticles in water through host-guest interactions. *Angew. Chem. Int. Ed.* **2012**, 51, 4185-4189.

(41) Matsumoto, K.; Terashima, T.; Sugita, T.; Takenaka, M.; Sawamoto, M. Amphiphilic random copolymers with hydrophobic / hydrogen-bonding urea pendants: self-folding polymers in aqueous and organic media. *Macromolecules* **2016**, 49, 7917-7927.

(42) a) Hosono, N.; Gillissen, M. A. J.; Li, Y.; Sheiko, S. S.; Palmans, A. R. A.; Meijer, E. W.; orthogonal self-assembly in folding block copolymers. *J. Am. Chem. Soc*. **2013**, 135, 501-510. b) Foster, E. J.; Berda, E. B.; Meijer, E. W. Metastable supramolecular polymer nanoparticles via intermolecular collapse of single polymer chains. *J. Am. Chem. Soc.* **2009**, 131, 6964-6966. c) Foster, E. J.; Berda, E. B.; Meijer, E. W. Tuning the size of supramolecular single-chain polymer nanoparticles. *J. Polym. Sci. A Polym. Chem.* **2011**, 49, 118-126. d) Cheng, C.-C.; Chang, F.-C-; Yen, H.-C.; Lee, D.-J.; Chiu, C.-W.; Xin, Z. Supramolecular assembly mediates the formation of single-chain polymeric nanoparticles. *ACS Macro Lett.* **2015**, 4, 1184-1188. e) Cheng, C.-C.; Lee, D.-J.; Liao, Z.-S., Huang, J.-J. Stimuli-responsive single-chain polymeric nanoparticles towards the development of efficient drug delivery systems. *Polym. Chem.* **2016**, 7, 6164-6169.

(43) Shao, Y.; Wang, Y.-L.; Tang, Z.; Wen, Z.; Chang, C.; Wang, C.; Sun, D.; Ye, Y.; Qin, D.; Ke, Y.; Liu, F.; Yang, Z. Scalable synthesis of photoluminescent single-chain nanoparticles by electrostatic-mediated intramolecular crosslinking. *Angew. Chem. Int. Ed.* **2022**, 61, e202205183.

(44) Guazzelli, E.; Masotti, E.; Calosi, M.; Kriechbaum, M.; Chlig, F.; Galli, G.; Martinelli, E. Single-chain folding and self-assembling of amphiphilic polyethylene glycol-modified fluorinated styrene homopolymers in water solution. *Polymer* **2021**, 231, 124107.

(45) Terashima, T.; Sugita, T.; Fukoa, K.; Sawamoto, M. Synthesis and single-chain folding of amphiphilic random copolymers in water. *Macromolecules* **2014**, 47, 589-600.

(46) Imai, S.; Hirai, Y.; Nagao, C.; Sawamoto, M.; Terashima, T. Programmed self-assembly systems of amphiphilic random copolymers into size-controlled and thermoresponsive micelles in water. *Macromolecules* **2018**, 51, 398-409.

(47) Verde-Sesto, E.; Arbe, A.; Moreno, A. J.; Cangialosi, D.; Alegría, A.; Colmenero, J.; Pomposo, J. A. Single-chain nanoparticles: opportunities provided by internal and external confinement. *Mater. Horiz.* **2020**, 7, 2292-2313.

(48) a) Single-Chain Polymer Nanoparticles: Synthesis, Characterization, Simulations, and Applications, Edited by José Adolfo Pomposo Wiley-VCH, Weinheim, **2017**. b) Mavila, S.; Eivgi, O.; Berkovich, I.; Lemcoff, N. G. Intramolecular cross-linking methodologies for the synthesis of polymer nanoparticles. *Chem. Rev.* **2016**, 116, 878-961. c) Lyon, C. K.; Prasher, A.; Hanlon, A. M.; Tuten, B. T.; Tooley, C. A.; Frank, P. G.; Berda, E. B. A brief user's guide to single-chain nanoparticles. *Polym. Chem.* **2015**, 6, 181-197.

(49) a) Koda, Y.; Terashima, T.; Sawamoto, M.; Maynard, H. D.; Protein storage with perfluorinated PEG compartments in a hydrofluorocarbon solvent. *Polym. Chem.* **2015**, 6, 240-247. b) Latorre-Sanchez, A.; Pomposo, J. A. Recent bioinspired applications of single-chain nanoparticles. *Polym. Int.* **2016**, 65, 855-860.

(50) Robinson, P. K.; Enzymes principles and biotechnological applications. *Essays Biochem.* **2015**, 59, 1-41.

(51) Sahin, A.; Weilandt, D. R.; Hatzimanikatis, V.; Optimal enzyme utilization suggests thatconcentrations and thermodynamics determine binding mechanisms and enzyme saturations. *Nat. Commun.* **2023**, 16, 2618.

(52) Rubio-Cervilla, J.; González, E.; Pomposo, J. A.; Applications of single-chain polymer nanoparticles. *John Wiley & Sons.*: Weinheim, Germany **2017**.

(53) Chen, J.; Li, K.; Bonson, S. E.; Zimmermann, S. C. A biorthogonal small molecule selective polymeric "clickase". *J. Am. Chem. Soc.* **2020**, 142, 13966-13973.

(54) Chen, J.; Li, K.; Sean, J.; Shon, L.; Zimmermann, S. C.; Single-chain nanoparticle delivers a partner enzyme for concurrent and tandem catalysis in cells. *J. Am. Chem. Soc.* **2020**, 142, 4565-4569.

(55) Mundsinger, K.; Tuten, B. T.; Wang, L.; Neubauer, K.; Kropf, C.; O'Mara, M. L.; Barner-Kowollik, C. Visible-Light-Reactive Single-Chain Nanoparticles *Angew. Chem. Int. Ed.* **2023**, 62, e202302995.

(56) Chen, X.; Chen, Z.; Ma, L. Milti-stimuli-responsive bottlebrush-colloid Janus nanoparticles toward emulsion interfacial manipulation and catalysis. Polym. Chem. 2022, 13, 959-966.

(57) Xu, W.; Ye, Y.; Sun, D.; Yang, Z. Single-chain nanoparticles catalyzed polymerization toward composite nanoparticles. J. Polym. Scie. 2024, 62, 427-435.

(58) Hamelmann, N. M.; Paulusse, J. M. J. Single-chain polymer nanoparticles in biomedical applications. *J. Control. Release* **2023**, 356, 26-42.

(59) a) Liu, D.; He, C.; Wang, A. Z.; Lin, W. Applications of liposomal technologies for delivery of platinum analogs in oncology. *Int. J. Nanomed.* **2013**, 8, 3309-33149. b) Ko, A. H.; Tempero, M. A.; Shan, Y. S.; Su, W. C.; Lin, Y. L.; Dito,

E.; Ong, A.; Wang, Y. W.; Yeh, C. G.; Chen, L. T. A multinational phase 2 study of nanoliposomal irinotecan sucrosofate (PEP02, MM-398) for patients with gemcitabine-refractory metastatic pancreatic cancer. *Brit. J. Cancer* **2013**, 109, 920–925. c) Koudelka, S.; Turánek, J.; Liposomal paclitaxel formulations. *J. Control. Release* **2012**, 163, 322–334. d) Deeken, J. F.; Slack, R.; Weiss, G. J.; Ramanathan, R. K.; Pishvaian, M. J.; Hwang, J.; Lewandowski, K.; Subramanian, D.; He, A. R.; Cotarla, I.; A phase i study of liposomal-encapsulated docetaxel (LE-DT) in patients with advanced solid tumor malignancies. *Cancer Chemoth. Pharm.* **2013**, 71, 627-633.

(60) a) Song, C.; Lin, T.; Zhang, Q.; Thayumanavan, S.; Ren, L. pH-sensitive morphological transitions in polymeric tadpole assemblies for programmed tumor therapy. *J. Control. Release* 2019, 293, 1–9. b) Benito, A. B.; Aiertza, M. K.; Marradi, M.; Gil-Iceta, L.; Shekhter Zahavi, T.; Szczupak, B.; Jiménez-González, M.; Reese, T.; Scanziani, E.; Passoni, L.; Matteoli, M.; De Maglie, M.; Orenstein, A.; Oron-Herman, M.; Kostenich, G.; Buzhansky, L.; Gazit, E.; Grande, H.-J.; Gomez-Vallejo, V.; Llop, J.; Loinaz, I. Functional single-chain polymer nanoparticles: targeting and imaging pancreatic tumors in vivo, *Biomacromolecules* **2016**, 17, 3213–3221.

(61) Arias-Alpizar, G.; Koch, B.; Hamelmann, N. M.; Neustrup, M. A.; Paulusse, J. M. J.; Jiskoot, W.; Kros, A.; Bussmann, J. Stabilin-1 is required for the endothelial clearance of small anionic nanoparticles, *Nanomed. Nanotechnol. Biol. Med.* **2021**, 34, 102395.

(62) a) Wuest, K. N. R.; Lu, H.; Thomas, D. S.; Goldmann, A. S.; Stenzel, M. H.; Barner-Kowollik, C. Fluorescent glyco single-chain nanoparticle-decorated nanodiamonds. *ACS Macro Lett.* **2017**, 6, 1168–1174. b) Kröger, A. P. P.; Komil, M. I.; Hamelmann, N. M.; Juan, A.; Stenzel, M. H.; Paulusse, J. M. J. Glucose single-chain polymer nanoparticles for cellular targeting, *ACS Macro Lett.* **2019**, 8, 95–101.

(63) Bajj, D. N. F; Tran, M. V.; Tsai, H.-Y.; Kim, H.; Paisley, N. R.; Algar, W. R.; Hudson, Z. M. Fluorescent heterotelechelic single-chain polymer nanoparticles: synthesis, spectroscopy, and cellular imaging. *ACS Appl. Nano Mater* **2019**, 2, 898–909.

(64) Tian, X.; Xue, R.; Yang, F.; Yin, L.; Luan, S.; Tang, H. Single-chain nanoparticle-based coatings with improved bactericidal activity and antifouling properties, *Biomacromolecules* **2021**, 22, 4306–4315. b) Nguyen,] T.-K.; Lam, S. J.; Ho, K. K. K.; Kumar, N.; Qiao, G. G.; Egan, S.; Boyer, C.; Wong, E. H. H. Rational design of single-chain polymeric nanoparticles that kill planktonic and biofilm bacteria. *ACS Infect. Dis.* **2017**, 3, 237–248.

2. Chapter II

2.1. Introduction

Light is an abundant, therefore cheap, source of energy we have access to readily and almost without any time restriction from our planet. Life itself evolved through precise and intricate light-harvesting strategies to sustain its long-lasting existence in a sustainable fashion. For these simple and intuitive reasons, its use as a reactant to manipulate and control our environment fascinated humanity since ancient times.

Herein, we will give main definitions of photocatalysis, as well as briefly outline the basic concepts of its application in organic synthesis. A special attention will be put on the recent reports concerning organic photocatalysis in aqueous medium, focusing on the opportunities provided by supramolecular approaches enabling light-induced organic transformations in the aqueous medium.

2.1.1. Photocatalysis, Definitions and Fundamentals.

The change in rate of a chemical transformation caused by electromagnetic radiation is an effectively resuming sentence of what reported by most authoritative English Language dictionaries for the definition of the term *photocatalysis*.[1-3] The Oxford English Dictionary reports the earliest use of the noun photocatalysis to be dated back to the 1890s, with the first evidence of its use in the writings of C. H.

Bothamley on photography.[3] The International Union of Pure and Applied Chemistry (IUPAC), in its Compendium of Chemical Terminology, extends the definition of photocatalysis to the *change in rate of a chemical reaction or its initiation*, restricts the range of wavelengths of the electromagnetic radiation involved to *ultraviolet, visible or infrared radiation*, and simultaneously introduces the concept of photocatalyst, *a substance that absorbs light and is involved in the chemical transformation of the reaction partners.*[4] Both the linguistic and scientific points of view agree on the vastness of the term photocatalysis, which indeed is, at the date, declined in a variety of applications, spanning through light-dependent conductive materials, water purification, solar energy conversion, optoelectronics, water splitting, and carbon dioxide reduction, just to cite a few, all sharing the manipulation of matter through its interaction with either UV, visible or IR electromagnetic radiation.

The curiosity for the chemistry induced by light accompanies the history of modern science since its very beginning. The experiment of the combustion of diamond employing solar light and the apparatus shown in Figure 2.1, performed in Florence by Sir Humphry Davy and Michael Faraday in 1814, legendarily exemplifies the scientific need of thinking about light as a proper reagent.[5,6]

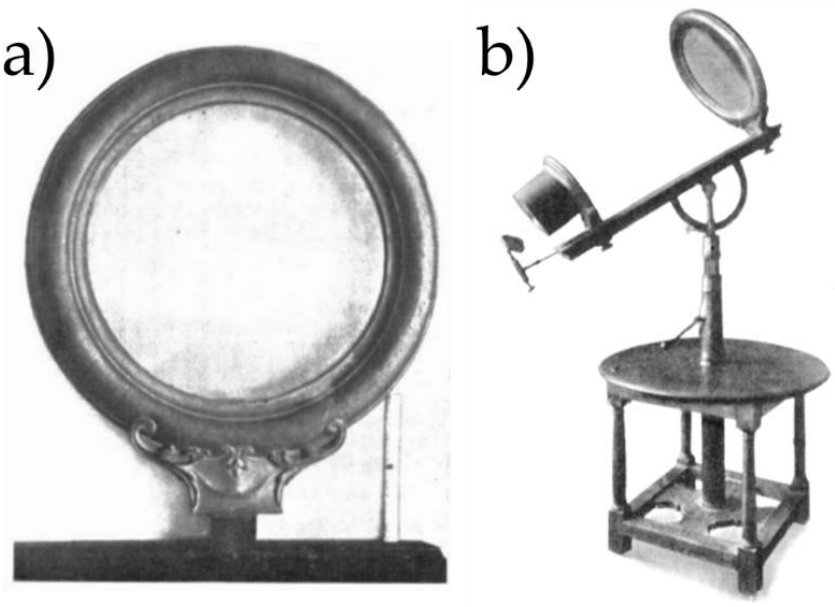

Figure 2.1. **a**) Lens, worked by Benedict Bregans and used by Sir Humphry Davy and Michael Faraday for the experiment of the combustion of the diamond. By the first decade of 1700, the same lens had already been used by Giuseppe Averani of the University of Pisa, in analogous experiments, on the combustion of precious stones.[6,7] **b**) Complete apparatus used in the experiment. Both objects are conserved in the Museo Galileo of Florence, Italy.[7]

As frequently happens with most disciplines, to establish a chronological starting point without incurring in bad mistakes can be difficult, and the same can be said not only for photocatalysis, but for *photochemistry* itself. As the name suggests, photochemistry is *the branch of chemistry concerned with the chemical effects of light (far ultraviolet, UV to infrared, IR),*[8] which is indeed a very broad definition, making the agreement on its starting point almost impossible without restricting the field. A first description of a photochemical organic reaction is reported in 1834, in the work of Hermann Trommsdorff on the chemistry of anthelmintic substances, in which a change in color and crystalline structure upon exposure to sunlight of solid α-santonin was observed (Figure 2.2).[9]

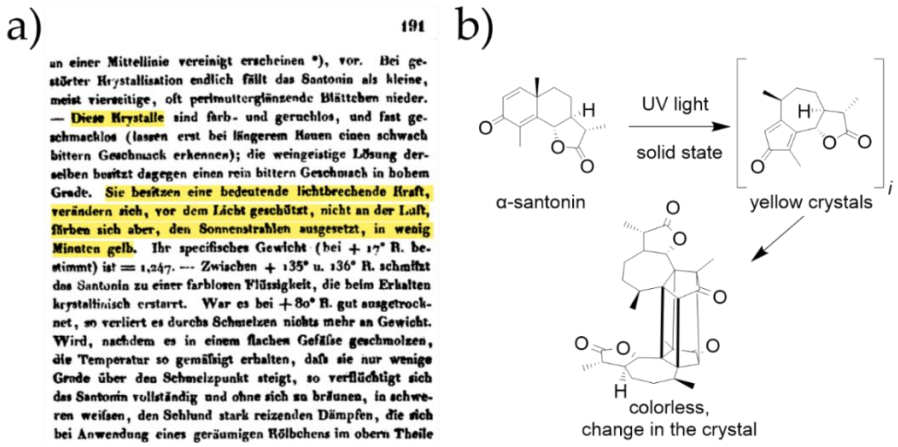

Figure 2.2. **a**) Part of the original report of Trommsdorff describing the effect of sunlight on both the and structure of α-santonin crystals.[9] **b**) Schematic representation of one of the possible transformations involved in the phenomena.[10]

Although few years later, Edmond Becquerel reported the discovery of the photovoltaic effect,[11] whose fundamental principles are intimately related to photocatalysis, this latter was first mentioned explicitly in scientific literature in 1911, in a work on the photobleaching of Prussian blue.[12] By the beginning of the past century, photochemistry and photocatalysis quickly consolidated with the development of a more systematic approach and, fueled by the pioneer work and inspiring ideas of Giacomo Ciamician, brilliantly resumed in its intervention published by Science in 1912,[13] gained increasing interest amongst experimentalists.[14] After more than a century, scientific community still agree with most of the principles stated in these seminal works.

For the contemporary understanding of photocatalytic processes, the acceleration of a certain transformation upon absorption of light by the photocatalyst can be interpreted based on molecular electronic states of the substances involved in the process. Considering the simple, thermal reaction **a**:

$$A + B \longrightarrow C \qquad \textbf{(a)}$$

For a photochemical process to take place, the first step is always light absorption of one or more reactant, as shown in the reaction **b**:

$$A + h\nu \longrightarrow A^* \qquad \textbf{(b)}$$

Where the electronic excited state of A, A*, is formed upon energy absorption. The photochemical reaction **c**, then involves A* and B as reactants.

$$A^* + B \longrightarrow C \qquad \textbf{(c)}$$

The difference between a photochemical reaction and a thermal one resides in the fact that, in the first, is the excited electronic state of a substance to react. Once a molecule undergoes to an electronic transition, the obtained electronic state is indeed a completely different species due to the altered electronic distributions geometry, though a totally different chemistry is disclosed. Light absorption promotes an electron from a lower energy to a higher energy orbital. The promoted electron can then be more easily removed, while the vacancy generated on the ground state's highest occupied molecular orbital can more easily accept electrons. As depicted in Figure 2.3, the excited state molecule is therefore a better oxidant and a better reductant simultaneously.

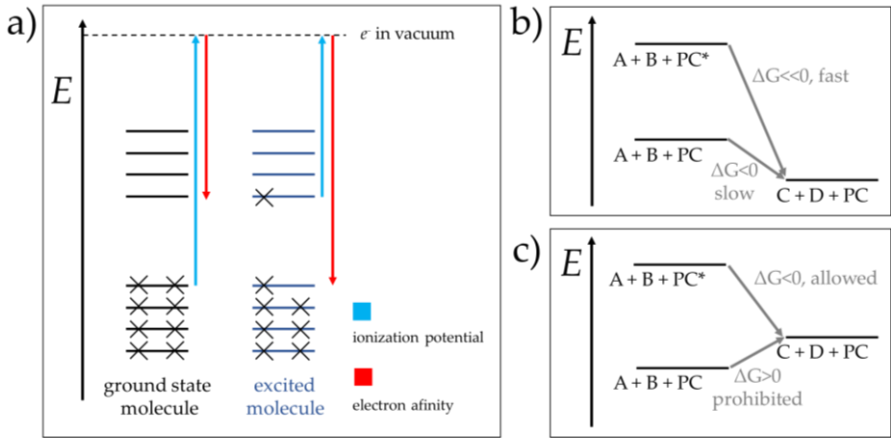

Figure 2.3. **a**) Schematic representation of the augmentation of both reduction and oxidation potential of a molecule upon electronic excitation. **b**) Thermodynamic diagram schematically displaying a thermally-allowed reaction between A and B, in presence of the photocatalyst PC, and the effect on the free Gibbs energy of the system upon photo-excitation of PC. **c**) Thermodynamic diagram illustrating the principle of light conversion into energy: a thermally-prohibited process becomes allowed upon photo-excitation of PC.

In presence of a third substance, the photocatalyst (PC), capable to absorb light and to take place in a certain process without being chemically altered, photochemical transformation can occur even between reactants which either tend not to react or do not react at all thermally. In this case, the process is said to be *photocatalyzed* by PC.

From the thermodynamic point of view, a photocatalyzed transformation can occur via two different modalities, which are schematized in Figure 2.3: in the case **b**, is described a *photosensitized* process, while the case **c** is referred to the conversion of light into chemical energy. In a photosensitized process, a thermodynamically allowed, yet slow, reaction between A and B to yield C and D, is sped up by the presence of PC, whose electronic excited state generated upon absorption of light augment the total free energy of the system. In the case of the conversion of light into chemical energy, an initially thermodynamically impossible reaction becomes allowed by the presence of the photoexcited species PC*. Both modes of action are the resultant of the contribution of the electronic excited state of PC to the total free Gibbs energy of the system.[15,16]

It is worth noting that all photocatalyzed reactions can be grouped into two main classes, according to the mechanism with which the PC enables the catalytic cycle: (i) energy transfer and (ii) photoredox catalysis. In the reaction **d** is schematized the main process of photosensitized reactions by energy transfer.

$$PC^* + A \longrightarrow PC + A^* \longrightarrow PC + \textit{products} \qquad \textbf{(d)}$$

In energy transfer catalysis, a triplet excited state T_1 of a molecule ($^3PC^*$ for the photocatalyst) is deactivated to a lower energetic state by transferring energy to a second molecule (the substrate A, the energy acceptor), which is thereby promoted to a higher energetic level, usually its triplet excited state $^3A^*$, with this latter, being capable of decaying into products (Figure 2.4).

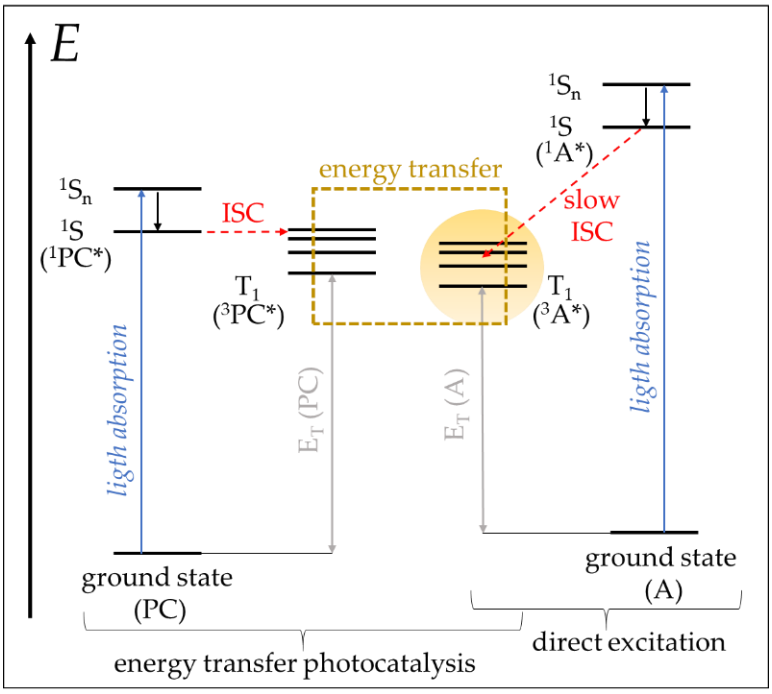

Figure 2.4. Schematic representation (Jablonski diagram) of the main electronic transitions involved in energy transfer photocatalytic processes.[17] The fine vibronic structures of the singlets excited states ^1S_n with internal relaxation thereof were omitted for pictorial clarity. The reactive triplet state of the acceptor substrate $^3A^*$, the crucial intermediate in the mechanistic pathway to products, is highlighted in yellow. The spectroscopic triplet energies E_T and the associated transitions are represented in grey.

2.1.2. Photocatalysis for Organic Reactions.

As anticipated in the previous paragraphs, to access common organic substrates' triplet states through direct excitation would generally require both short (280-315 nm) irradiation wavelengths and high light intensities, which result in unselective absorption and undesired side reactions. Efficient photocatalysts, must then exhibit high extinction coefficients and rapid inter system crossing (ISC), which in conjunction with a long-living triplet state (>100 ns), explains the prevalence of heavy-atom Ru/Ir complexes and carbonyl compounds as efficient triplet sensitizers.[18] Photocycloadditions, heterolytic bond dissociations, carbon-carbon double bonds photoisomerizations and reactions involving the formation of photosensitized singlet

oxygen are the four most commonly used classes of reactions in which the energy transfer mechanism is involved. In Figure 2.5 are shown some exemplificative applications of the abovementioned transformations.

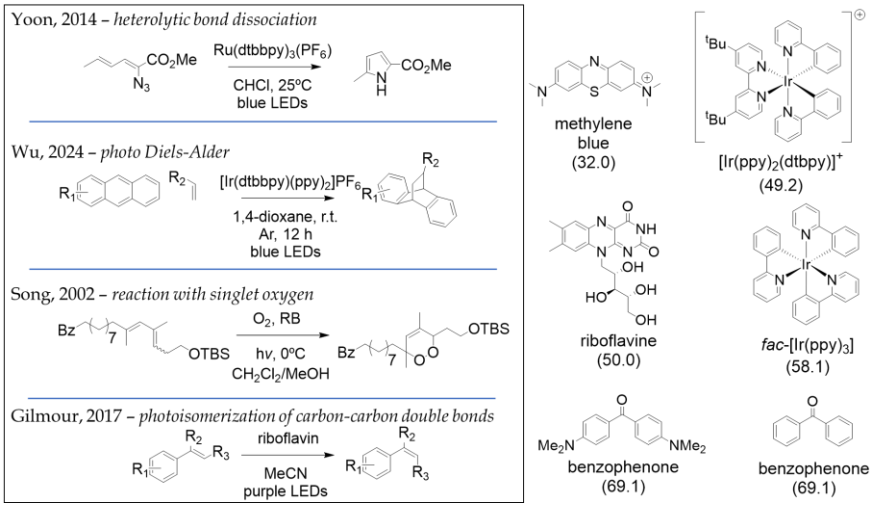

Figure 2.5. On the left, four examples of recently reported photocatalyzed reactions via energy transfer mechanism: the heterolytic bond dissociation of carbazides,[19] the regioselective photo Diels-Alder cycloadditions of anthracenes to olefins,[20] the singlet oxygen cycloaddition to dienes,[21] and the isomerization of carbon-carbon double bonds.[22] On the right, the structure of commonly used photosensitizers with their respective E_T (in parentheses) reported in kcal mol^{-1}.[18]

Regarding the second mode of action of a photocatalyzed reaction, the photoredox catalysis, the reaction mechanism involves the electron transfer between the excited photocatalyst and substrates, facilitated by the principle discussed above by which the excited states of a photocatalyst are usually both better reductants and better oxidizers.[15] If PC's excited state transfers an electron to one substrate to initiate the catalytic cycle, the mechanistic route is called reductive quenching cycle (Scheme 2.1), which is usually completed by the reduction of the oxidized intermediate of the photocatalyst via electron transfer form a second, electron donating reagent. In some cases, the redox potentials of the species involved in the cycle can undergo the opposite process, an oxidative quenching cycle, in which the photoexcited state of PC abstract an electron from a donor to initiate the catalysis (Scheme 2.1).

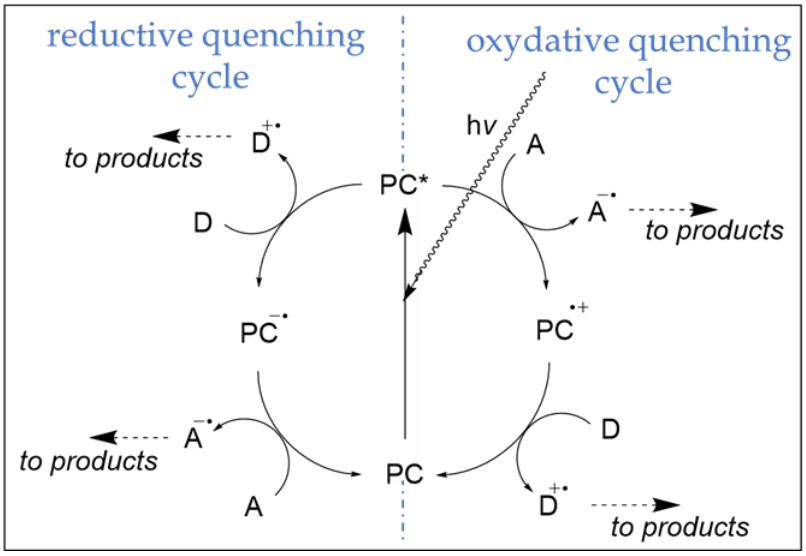

Scheme 2.1. Possible mechanisms cycles allowed for photoredox catalysis. On the right the photocatalyst PC is reduced by a donor reactant D *via* single-electron transfer (SET) after being excited upon light absorption, the reduced form of PC is oxidized by an acceptor reactant A to finally yield the regenerated PC. On the left, after being promoted to the reactive excited state upon light absorption, PC* transfers an electron *via* SET to an accepting reactant A. The ground state photocatalyst is then regenerated by a second SET step in which a donating reactant D is oxidized by the intermediate oxidized PC.

In the case of thermally-equilibrated excited states and reversible electron transfer, the redox potentials of the reactive excited state of PC (PC*) can be calculated according to Equations **1** and **2**.

$$E_{redox}(PC^{+}/PC^{*}) = E_{redox}(PC^{+}/PC) - E_{oo}(PC^{*}/PC) \qquad \text{Eq. (1)}$$

$$E_{redox}(PC^{*}/PC^{-}) = E_{redox}(PC/PC^{-}) + E_{oo}(PC^{*}/PC) \qquad \text{Eq. (2)}$$

Where $E_{oo}(PC^{*}/PC)$ is the one-electron potential corresponding to the zero-zero spectroscopic energy of the excited state and $E_{redox}(PC/PC^{-})$ and $E_{redox}(PC^{+}/PC)$ the ground state redox potentials measured for PC.[23] As a general rule, it is possible to tune

the oxidation potentials of the photocatalyst to switch from one mechanism to another, opening new synthetically valuable possibilities.[24]

Photoredox catalysis, and visible-light photoredox catalysis in particular, is an undoubtedly powerful, yet still flourishing approach to the preparation of organic molecules. First pioneering reports of photoredox catalysis were only published starting form 1979 by Kellogg,[25] followed by Fukuzumi and Tanaka,[26] Pac and Deronzier,[27] all concerning the capability of ruthenium polypyridyl complexes to accelerate a variety of organic reaction, in Figure 2.6 some significative examples are shown.

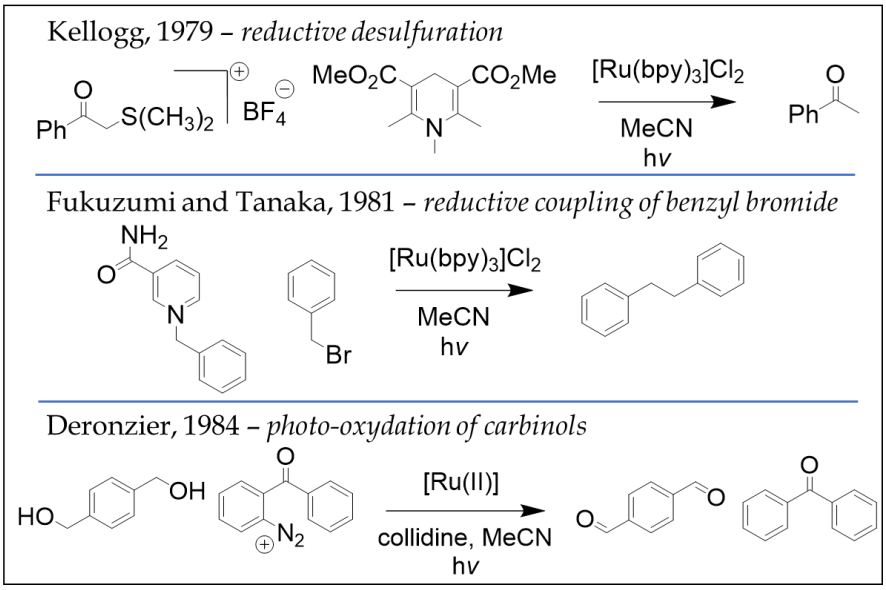

Figure 2.6. Three representative examples of historically relevant photoredox organic reaction. From the top: the light-induced acceleration of the reductive desulfuration of trialkyl sulfonium salts in presence of catalytic amounts of $[Ru(bpy)_3]Cl_2$, reported by Kellogg in 1979.[25] The light-dependent reductive coupling of benzyl bromide in presence of 1-benzyl-1,4-dihydronicotinamide and catalytic amount of $[Ru(bpy)_3]Cl_2$.[26] The photo-oxidation of benzylic alcohols to the corresponding aldehydes, mediated by polypyridyl Ru(II) complexes and using diazonium salts as sacrificial electron donors.[27]

By the beginning of this century, photoredox catalysis started its blossoming season with the works of the Nobel Laureate MacMillan and Yoon's groups on the

effect of visible light on organic reactions in presence of metal complexes.[28] From then on, photoredox catalysis now counts with a plethora of different applications and a variety of reactions, often carried out in milder conditions than their thermal analogues, have been discovered and optimized.[15] Due to the possibility to introduce structurally complex moieties in mild conditions, an increasing number of authoritative industries decide to introduce photoredox catalysis-based reactions in the synthesis and late-stage functionalization of highly-valuable molecules.[29]

Regardless the application, mostly all photochemistry and photocatalysis-based technologies have exponentially grown during the course of the past decade, a rise in development which can be easily correlated to the availability of novel, more stable and powerful light sources. Especially, related to experimental set-ups for visible-light photocatalysis practice, which traditionally relied on the use of either the sunlight or household light bulbs, the commercialization of standardized light emitting diodes (LED) permitted a net gain in terms of reaction repeatability (LEDs sources usually present narrow spectral emission) and overall performance.[30] It is also important to take in mind that light is always a proper reactant in photocatalyzed processes, which is stoichiometrically consumed, though taking part neatly in the final yield of a process and making it strictly dependent to the light intensity of the source employed.[30,31] The tendency can be visually appreciated in Figure 2.7, in which a graphic of the estimation of the number of publications with time in the fields of visible-light photocatalysis and photochemistry is reported and superimposed with three of the milestone optoelectronic inventions, which undoubtedly contributed to the revolution of the scientific community in the past decade.[32]

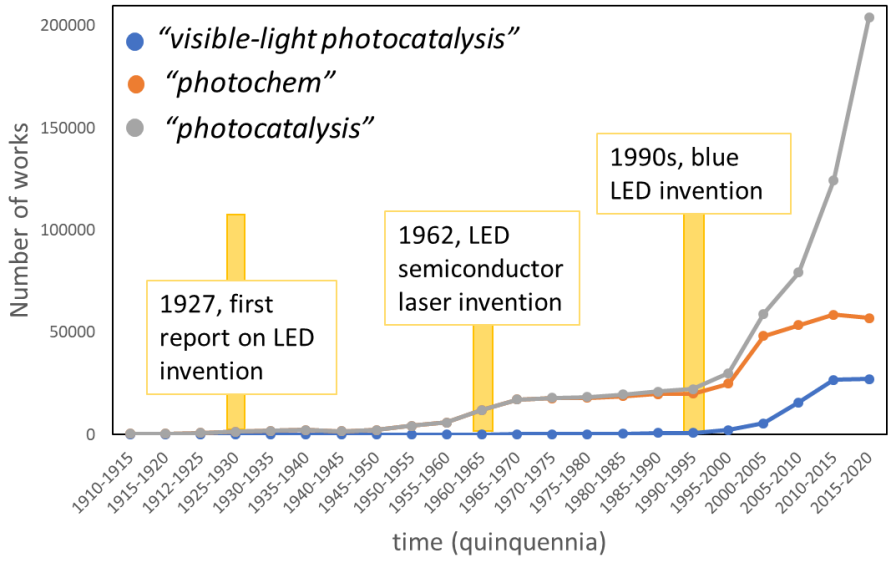

Figure 2.7. Graphic of the tendencies, given by the number of publications containing the expressions *visible-light photocatalysis*, *photochem* and *photocatalysis* per quinquennia, starting from 1910s to 2020s and derived from the digital search portal Google Scholar (14th February 2024).

2.2. Discussion

The following discussion will mainly focus on recent developments of soft-matter based photocatalytic systems, capable of carrying out organic reactions in water. The use of supramolecular scaffolds is one of the possible strategies explored by recent development in the field of photocatalysis to address, not only the major constraints of scarce solubility of catalysts and products, but which is capable of outperform natural systems in many cases. In supramolecular systems, discrete molecules interact and come together to form assembled entities. This approach, generally inspired by biological reactions which often occur in the confined pockets of enzymes, allow lowering the transition state energies of reactant molecules, which are hosted in the supramolecular assemblies' nanocavities and are facilitated to react in the microenvironment provided by the confinement.[33,34] A variety of supramolecular hosts have been developed with well-defined nanocavities to mimic enzyme activity, scientific literature is plenty of brilliant examples of how supramolecular chemists are

capable to employ weak, noncovalent interactions to build defined and discrete molecular architectures for catalysis purposes[35-39] and, notably, supramolecular hosts are, in some cases, superior to molecular catalysts in terms of higher yields and better selectivity.[40-42] Nevertheless, the application of supramolecular systems for visible-light photocatalysis of organic transformations in water still is in its infancy and, although some representative examples reported in literature already disclosed the great potential of this approach, questions and unsolved major issues remain abundant.

2.2.1. Water as Solvent in Organic Photocatalysis.

One could easily and reasonably affirm that, when thinking about photocatalysis, scientists are someway taking or took inspiration from Nature. Considering the central role that the photocatalytic process plays in the ecological homeostasis of life, the planet earth itself can be considered as a big, almost indefinitely complex photoreactor. In 1772, Joseph Priestley reported the first experiment demonstrating the production of oxygen gas by plants, while five years later Jan Ingen-Housz documented that the production of oxygen gas in plants leaves was a light-dependent process.[43] From then on, countless of scientists started the race towards the comprehension of the phenomenon, which remained covered in mystery up until the advent of cell biochemistry and modern biomolecular techniques. In this scenario, first reports of photocatalyzed reactions in water appeared. Probably aiming to simulate and unveil the processes behind plants' photosynthesis, Barker reported in 1921 the photo-induced in water synthesis of formaldehyde and carbohydrates from carbon dioxide in presence of uranium salts and colloidal iron oxides.[44] Apart from some more seminal reports concerning zinc and titanium oxides photobleaching properties in aerobic environment,[45] photocatalysis in aqueous media largely remained an uncharted challenge until the last decade.

Nevertheless, Wohler's synthesis of urea, performed by heating an aqueous solution of ammonium cyanate, was developed by the first mid of the 19th century and is commonly considered the beginning of synthetic organic chemistry. As well as for

many other transformations reported in the same period, the use of water as solvent for reaction optimization was not uncommon up until the second decade of the 20th century,[46] a tendency which have been surely inverted with the advent of Grignard reactants and the rise of petrochemical industry.[28,47] It should be pointed out that replacing hazardous solvents with safer, renewable alternatives is receiving increasing attention both in academia and industries. Almost all organic solvents, except chlorinated solvents, are flammable, chlorinated and aromatic solvents are carcinogenic, ether and chloroform have narcotic properties, high vapor pressures and form smog, just to cite few of their very undesirable characteristics.[48] Making a process greener, therefore decreasing the environmental impact and risks associated with handling and residues management, is undoubtedly linked to the use of greener solvents alternatives. The fact that water fulfills all the criteria for being an excellently green solvent is commonly agreed, as it is not only allowing the minimization of health and environmental risks, but also presents unique opportunity for producing polarity-tunable reaction media.[49,50]

In addition, when water is used as solvent, different and unexpected reactivities can be disclosed. Due to this renewed attention to sustainability, it seems logical to merge the intrinsically green features of photocatalysis to the benefits that the use of water as reaction media could provide. As highlighted by recent reviews on the topic, the same can be said for photocatalysis, still little have been reported on purely in water photocatalyzed organic reactions,[28,51] as the scarce solubility of the most potent photocatalysts and reactants is of major concern. In Figure 2.8, some significative examples of photocatalytic synthesis of organic molecules in which water is used as the sole solvent medium are schematized.

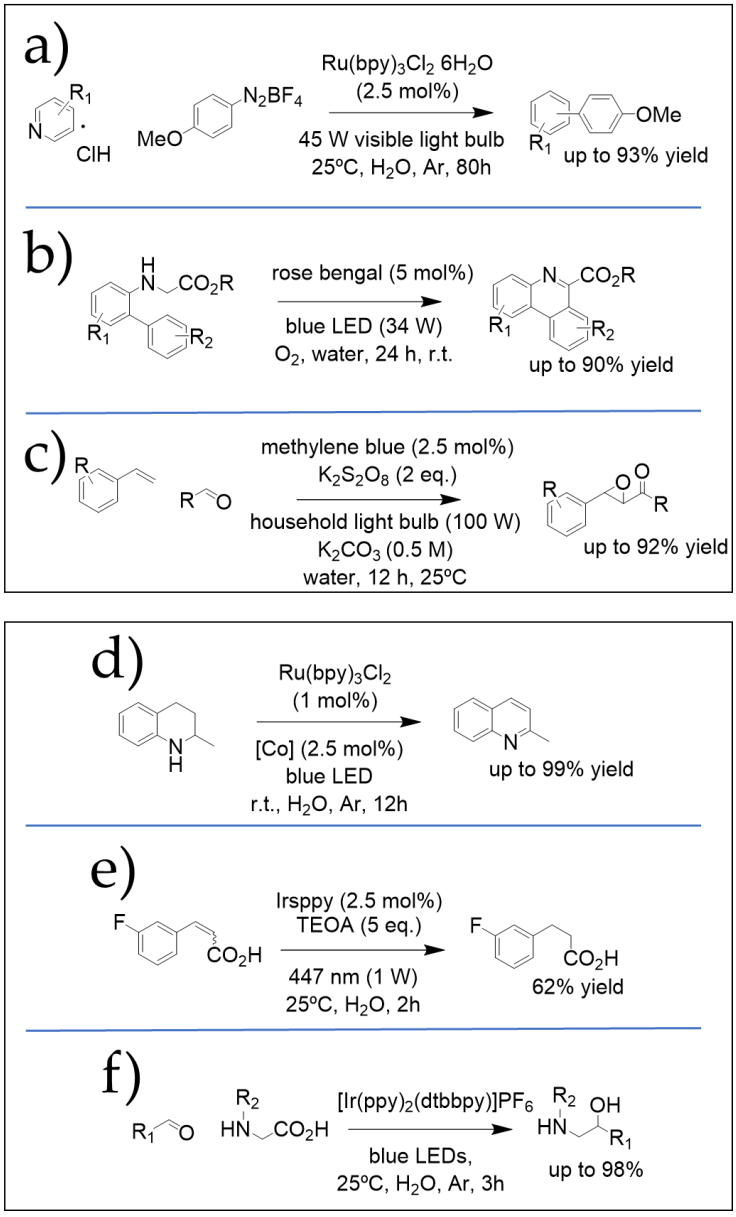

Figure 2.8. Six representative examples of light-induced photocatalytic organic reactions allowed in water: **a**) Arylation of *N*-heteroarenes with aryldiazonium salts, first reported in 2014 by Xue *et al*.[52] **b**) Visible-light-promoted oxidative radical cyclization of *N*-*N*-biarylglycines, reported by Natarajan *et al*. in 2019.[53] **c**) In water, visible light-induced acylative epoxidation of vinylarenes, reported by Salles *et al*. in 2018.[54] **d**) Aromative dehydrogenation of cyclic amines, first reported by Balaraman's group in 2019.[53] **e**) Visible-

light induced hydrogenation of aromatic alkenes in water by Wenger *et al.*, 2019.[55] **f**) Synthesis of 1,2-aminoalcohols by decarboxylative coupling of aminoacids, first reported by Zhong *et al.* in 2020.[56]

Amongst the transformations reported above, the reactions **a**, **d** and **f** demonstrate how the use of traditional transition metal catalysts in unusual conditions can lead to outstanding results. In particular the arylation of N-heteroarenes with aryldiazonium salts (**a**, Figure 2.8) resulted to proceed smoothly at room temperature and monosubstituted products were observed under title conditions, while changing the reaction solvent (e.g., employing formic acid), either a change in regioselectivity was observed. Nevertheless, even though water appeared to be the ideal solvent for the reaction, the substrate scope resulted to be limited to hydrophilic compounds, as the authors report that either the solubility of the catalyst and substrates are crucial for reaction yields (when 2, 4-dimethyl pyridine was used under title conditions, yield dropped to 55%).[52] The scheme **d** in Figure 2.8 shows the photocatalytic dehydrogenation of cyclic amines with the liberation of H_2 using water as a solvent, which resulted to proceed smoothly at room temperature and was applied by the author on a varied pool of substrates. As for the previous case, water resulted to be the solvent of election for the reaction, whose final yields dropped if carried out in methanol (MeOH) or dimethylformamide (DMF). Interestingly, this work shows how and as anticipated in the previous paragraph, when the photocatalyst and the substrates are soluble in water, mechanistic insights of the reaction can be investigated based on redox potentials considerations and cyclic voltammetry studies.[53] The synthesis of 1,2-aminoalcohols by decarboxylative coupling of amino acids (**f**, Figure 2.8), is a third example of how common transition metals photocatalysts can be employed in in water photocatalyzed processes. A reported by Zhong *et al.*,[56] it provides facile access to diverse 1,2-amino alcohols directly from readily available starting materials without any additives in good results even under sunlight and in very mild conditions. Noteworthy, this latter reaction as well resulted to be sensitive to solvent change, as yields dropped when lower dielectric organic solvents were used instead of water (*e.g.* 55% yield in 1,4-dioxane). The reaction **e** in Figure 2.8 constitutes a significative case

in which, the use of water as the reaction medium for photocatalyzed transformations, allows new, sometimes unexpected, reactivities. The use of the photocatalyst Trisodium fac-tris[2-(5'-sulfonatophenyl)pyridine]iridate(III) (**Irsppy**, Scheme 2.2), a water-soluble variant of the widely employed $Ir(ppy)_3$ photosensitizer, permitted the observation of a light-intensity dependent reactivity of *trans*-3-fluorocinnamic acid in water.[55] In particular, the saturated product was observed when a focalized blue light was used for irradiation, while the use of a non-focalized light source with the same power and wavelength yielded the isomerized alkene (Scheme 2.2).

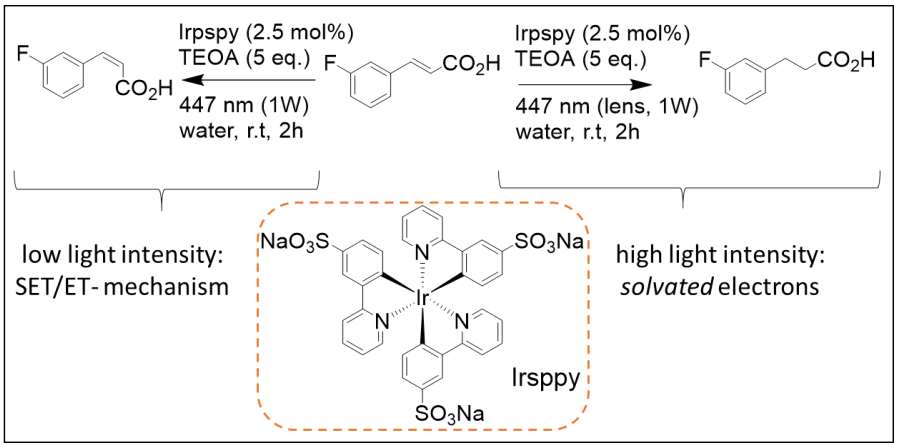

Scheme 2.2. Reaction scheme of the light intensity dependent reaction modality allowed by the use of the photocatalyst **Irsppy** in water. Namely, the *trans–cis i*somerization (left, one-photon mechanism) and hydrogenation (right, two-photon pathway) with the substrates *trans*-3-fluorocinnamic acid using the blue-light driven photocatalytic system in water.[55]

The authors hypothesized that, modulating the light intensity per area with a collimating optical element (a common lens), allowed the switching from one-photon (either triplet-triplet sensitization or SET) to two-photon (formation of *solvated* electrons) substrate activation chemistries, a phenomenon which have also been observed with the use of other water-soluble analogues of **Irsppy**.[57] Interestingly, the same water-soluble photocatalyst allowed the efficient reduction of aliphatic imines to amines by conjugating photoredox catalysis and enzymatic processes in water, which

was reported by the same group in 2018.[57] It is worth noting that the functionalization of aminoacids and peptides is currently one of the more extensively explored applications of in water organic photocatalysis. Several bio-orthogonal modifications of either biotic or abiotic peptidic systems have been successfully achieved, *e.g.* the benzylation of dehydroalanine residues in peptides and proteins,[58] The trifluoromethylation of aromatic moieties of biologically active peptides,[59] the selective arylation of cysteine,[60] the selective benzylic alkylation of tryptophan residues in peptides,[61] and decarboxylative alkylation of C-terminal sites in naturally occurring proteins,[62] just to cite a few. The author remits the reader to recently published reviews for a more comprehensive overview on the topic.[28, 63, 64]

2.2.2. Aqueous Micellar Photocatalysis.

Aqueous micellar photocatalysis, first introduced in 1970 with the main objective to help the dissolution of hydrophobic organic molecules in water,[65] is probably the chronologically older and more explored application of supramolecular systems in aqueous photocatalysis for organic reactions. As suggested by the name, micellar photocatalysis is based on the formation of micelles in the reaction medium. Micelles are in general spherical supramolecular assemblies of colloidal dimensions, loosely bound aggregates, which are formed due to solvophobic forces generated by the interactions of a variable number of molecules of the surfactant, which is the amphiphilic molecular unit, and the solvent. If the solvent is water, micelles forms as the hydrophobic region of the amphiphilic surfactant tends to escape from water, leaving exposed to the solvent only the hydrophobic moieties. For this reason, micelles formed in aqueous medium are usually spherical, flexible structures which intrinsically present a hydrophobic core, all feature which allow the solubilization and preorganization of hydrophobic substrates.[66] Based on this principle, micellar photocatalysis permits the solubilization of the photocatalytic units and the lipophilic reactants in water, accommodating the reaction partners in the confined and non-polar space of the nanoaggregate.

The recently published work by Lipshutz *et al.*[67] on the aqueous photocatalyzed β-sulfonylation of aromatic olefins is a great example indicating that this is a promising approach for expanding photocatalysis protocols into the aqueous media. The group prepared the ubiquinol-inspired amphoteric photocatalyst (**PQS-Ir**) shown in Figure 2.9, containing a hydrophilic poly(ethylene glycol ether) methyl ether (MPEG) moiety, a 50 carbon atoms-long lipophilic side chain and a photocatalytic cyclometalated iridium(III) tripyridyl complex attached through a phenoxy carboxylate linking functional group. The PQS-attached photocatalyst PQS-Ir enabled the hydroxysulfonylation of aromatic alkenes and enol acetates in excellent yields, on a rich and varied substrate pool and in absence of any organic solvents or additives, using the light of a blue LED as the only external energy source. Notably, the photocatalyst could be recycled and recovered several times before observing significant loss in catalytic activity. [67]

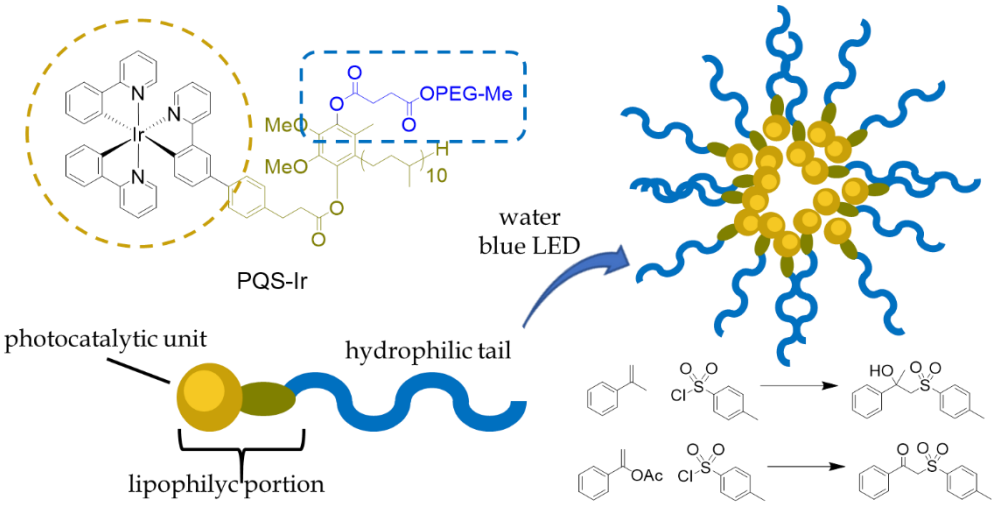

Figure 2.9. Structure of the ubiquinol-based, amphoteric photocatalyst **PQS-Ir** and the schematic representation of the self-assembled micelles in water with reaction schemes of the β-hydroxysulfonylation of aromatic alkenes and the di-functionalization of aromatic enol acetates, enabled in water via micellar photocatalysis.[67]

Giustiniano *et al*. recently reported the photocatalytic micellar reaction of *N*-methyl-*N*-alkyl aromatic amines and both aliphatic and aromatic isocyanides for the

preparation of variously functionalized amides.[68] In this case, the authors followed a readily-prepared photoactive micellar system by means of the sole mixing of photocatalyst and selected surfactants, whose structures are shown in Figure 2.10, in the aqueous medium. Interestingly, with the use of sunlight instead of blue LED light source, no change in reaction yields was observed in optimum reaction conditions. Supported by an extensive NMR study, which confirms the interactions between the photocatalyst and either the surfactant or the substrate, with a broad substrate scope and good functional group tolerance and the possibility to recycle the photocatalyst, the micellar photo-induced amide synthesis reported by Giustiniano *et al*. represents a simple, yet not trivial strategy towards a more sustainable conditions for already well-established transformations of organic reactions.

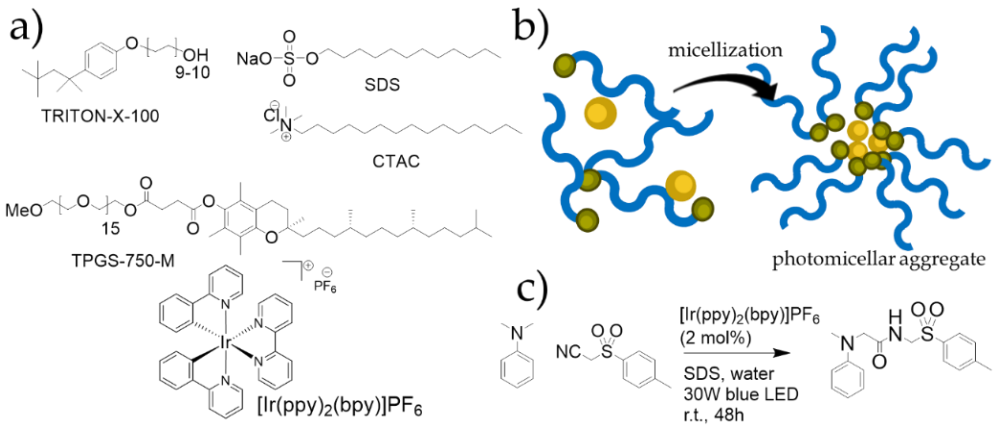

Figure 2.10. **a**) Chemical structures of the selected surfactants and photocatalyst for micellar photocatalysis by Giustiniano *et. al.*[68] **b**) Pictorial representation of the general approach to photo-micellar catalysis followed for the light-driven preparation of amides,[68] and the in water photoactivation of carbon-halide bonds.[69] **c**) Reaction scheme of the photocatalyzed synthesis of amides from *N*-methyl-*N*-alkyl aromatic amines and both aliphatic and aromatic isocyanides.[68]

With a similar approach, Giedyk *et al*. developed a controllable, micellar system-based photocatalytic strategy which allowed the activation of carbon-halides bonds in water and under mild conditions, employing the commercially available methylene blue as photocatalyst and blue LED as the light source in association with cheap and well described surfactants, e.g. sodium dodecyl sulfate (SDS) TRITON-X

and cetrimmonium bromide (CTAB).[69] The authors reported that o-chlorobenzamides as the 2-chloro-*N*,*N*-diisopropylbenzamide (2-CNIPB) can either be reduced with concomitant *N*-dealkylation or undergo to intramolecular C-H arylation, depending on the selected reaction conditions (Figure 2.11).

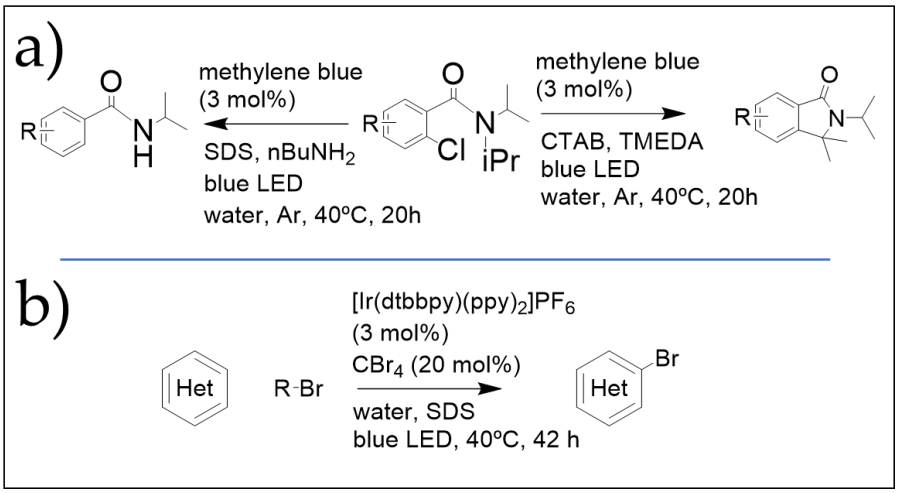

Figure 2.11. **a**) Reaction scheme of the micellar photocatalyzed activation of carbon-halide bonds, enabling controllable mechanistic switch between aromatic alkylation and dealkylative hydrogenation. **b**) Reaction scheme of the Minisci-like halogenation of inactivated heteroarenes, enabled by photo-micellar catalysis. Both the works were reported by Giedyk *et al*.[69,70]

The crucial role played by preaggregation in micellar photocatalysis was furtherly highlighted by the same group, which reported the photocatalyzed aromatic halogenation of inactivated heteroarenes schematized in Figure 2.11, which resulted to be neglected when carrying out the reaction in organic solvent instead of employing aqueous SDS.[70] This representative and recent reports contribute to demonstrate that, by taking advantage of the micellar effect and, employing or not *designer-made surfactants*, photo-micellar catalysis offers a virtually infinite number of possibilities, in terms of reaction scope, regioselectivity control and facile preparation of the reaction mixtures.[66]

2.2.3. Supramolecular Nanocapsules.

While exploring the different possibilities offered by supramolecular interactions for photocatalysis in water, it is worth reporting the use of tailor-made soft nanocapsules for the stabilization of hydrophobic photocatalyst in water. This strategy was remarkably employed by Akita *et al.* by preparing V-shaped aromatic amphiphiles, whose structure is shown in Figure 2.12, which are capable to spontaneously self-assemble in water and generate hydrophobic nanocavities, subsequently exploited to host the phenoxazine photoredox catalyst PN.[71] The authors reported that, the resulting supramolecular assembly (SAPC, Figure 2.12), composed of organic PC enclosed in the V-shaped aromatic amphiphile, resulted to efficiently catalyze the metal-free pinacol coupling in water, using blue LED light as the only external energy source. The same concept was successfully applied by the same group, which exploited the same organic V-shaped amphiphile to trap three different photocatalyst PC (Scheme 2.3), enabling a demethoxylative reductive cleavage of N-O bonds in Wenreib amides (WA, Scheme 2.3) in water, mild conditions and good yields on a reasonably large substrate pool (62 to 88% yield).[72]

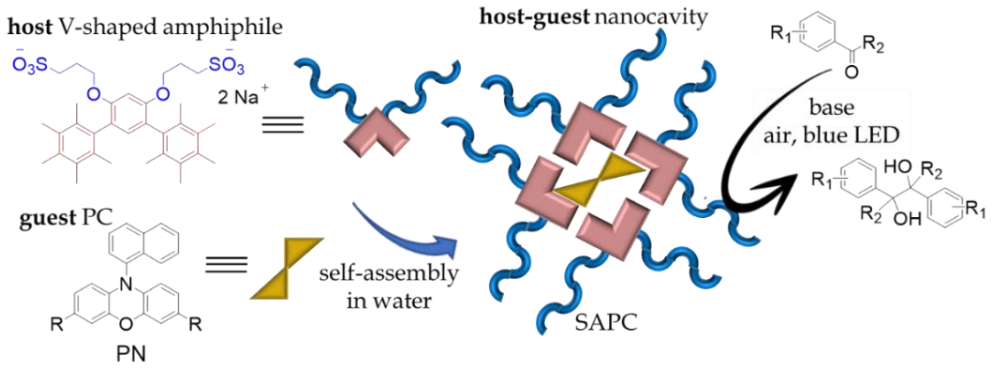

Figure 2.12. Pictorial representation of the in water self-assembly of the nanocavities prepared by Akita *et al*. The V-shaped organic amphiphile spontaneously aggregate in aqueous environment, generating hydrophobic nanocavities in which lipophilic photocatalyst as PC can be hosted.[71]

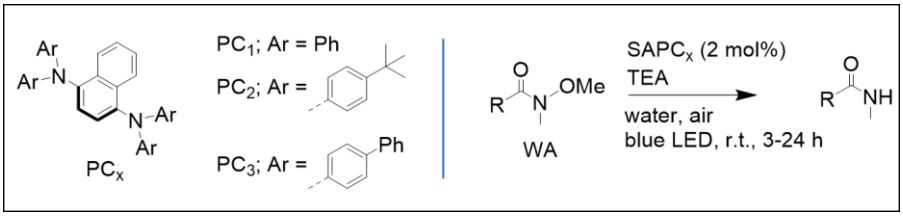

Scheme 2.3. On the left, structures of the three different organic photoredox catalysts selected by Akita *et al*. for the incorporation within the supramolecular assembly (SAPC). On the right, reaction scheme of the in water reductive cleavage of N-O bond of WA.[72]

2.2.4. Soft Polymeric Materials for Aqueous Organic Photocatalysis.

As anticipated above, in all these works in the field of photocatalysis of organic transformations in water, we observed the extensive use of supramolecular assembly to simultaneously shield the photocatalytic species from the aqueous media and to provide a confined environment in which the substrates can be hosted and undergo the desired process. While polymeric scaffold has been already widely employed for catalyst supporting, demonstrating their superiority in terms of robustness, catalyst recyclability, product selectivity enhancement and restricted catalyst leaching, still little have been described on their application in photocatalysis. Polyvinylpyrrolidone (PVP)-stabilized colloidal platinum nanoparticles in combination with a water-soluble zinc porphyrin were exploited to promote the visible-light reduction of the substrate pyruvate to lactate, enabling a photoredox-based, mild and green procedure for the preparation of a valuable raw material for the preparation of biodegradable polymeric compounds.[73]

Palmans *et al*. reported two seminal works in which water-soluble photoactive SCNPs were proven to be capable of efficiently catalyze the metal-free reduction and aromatic C-C cross-coupling reactions in water and without the use of any cosolvent.[74,75] In their reports, the authors introduce a systematic methodology for the preparation of stable, self-assembled photocatalytic SCNPs of defined structure and chemical composition. In their first work, a high-molecular weight, poly(pentafluoro phenyl) acrylate precursor was modified through a post-functionalization approach

with four different functionalities including phenothiazine pendants, ensuring both the homogeneity of the molecular weight of the polymeric precursors and to confer the photoredox properties to the material (Figure 2.13). The obtained amphiphilic copolymers resulted to spontaneously self-assemble in water to yield well-defined non-covalent SCNPs, which were exploited to perform the UV-light induced reduction of haloarenes and the cross-coupling of 2-cyanoiodobenzene and *N*-methyl pyrrole in water and in presence triethylamine (Scheme 2.4).[74]

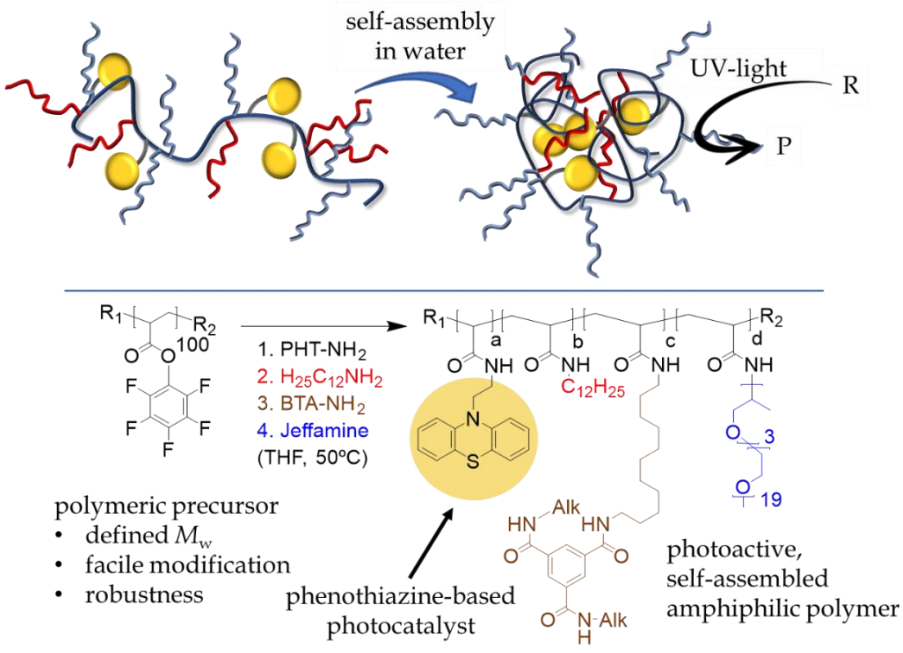

Figure 2.13. On top, the formation of non-covalent, photocatalytic SCNP upon spontaneous folding/collapse in water is depicted. The unimolecular polymeric aggregate enables the photocatalytic process to occur in its lipophilic, confined core. On the bottom, the synthetic route explored by Palmans *et al.* for the preparation of the amphiphilic photoredox SCNP polymeric precursor is shown.[74]

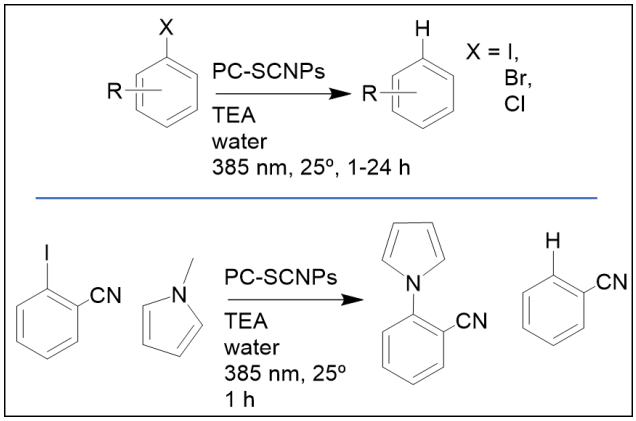

Scheme 2.4. Reaction schemes of the "in water", light-driven transformation explored by Palmans' group in their works on photocatalytic SCNPs (PC-SCNPs).[74,75] On top, the reduction of C-halogen bonds of aromatic substrates, on the bottom the cross-coupling of *N*-methyl pyrrolidone and iodoarenes.

Barner-Kowollik *et al.* recently reported a SCNPs-based photoreactor capable of performing photooxidation of fatty acid in water and under visible-light irradiation.[76] Notably, through the precise control of the folding/collapse process of the polymeric chains by means of the use of a rose Bengal derivative crosslinker, the authors were able to tune the degree of hydrophobicity of the lipophilic pockets within the core of the single-chain nanoreactor. Interestingly, the striking augment in efficiency (up to three-times) of the photocatalytic SCNP toward the photooxidation of fatty acids in comparison to the free-photosensitizer was interpreted, and supported by MD simulations, in terms of augmented polarity and high confinement in the active pockets provided by the SCNP.[76]

2.3. Conclusions.

To summarize, despite the great interest emerged amongst pure organic chemists towards visible-light photocatalysis in the last decades and considering the quick last century rise of photochemistry, the implementation of photocatalysis and

soft-matter based systems for performing valuable and challenging organic reaction still is in its infancy. With this brief overview, is in the author's hope that the importance, both academically and ecologically speaking, have been stressed out. In the next Chapters, we will try to furtherly highlight the potential of merging photocatalysis and soft-matter systems for in water applications, by means of retracing dome remarkable results in the fields of photocatalysis in water and nanomedicine.

2.4. References.

(1) “photocatalysis.” Collinsdictionary.com. 2024. https://www.collinsdictionary.com/dictionary/english/photocatalysis (06 February 2024).

(2) “photocatalysis.” Oed.com. 2024. https://www.oed.com/dictionary/photocatalysis_n (06 February 2024).

(3) “photocatalysis.” Merriam-webster.com. 2024. https://www.merriam-webster.com/medical/photocatalysis (06 February 2024).

(4) “photocatalysis” in IUPAC Compendium of Chemical Terminology, 3rd ed. *International Union of Pure and Applied Chemistry*; **2006**. Online version 3.0.1, 2019. https://doi.org/10.1351/goldbook.P04580.

(5) Some experiments on the combustion of the diamond and other carbonaceous substances by Sir Humphry Davy *Phil. Trans. R.S.* **1814**, 104, 557-570.

(6) Martin, T. The instrument used by Davy and Faraday in Florence for the combustion of diamonds. *J. Sci. Instrum.* **1931**. 8 379.

(7) https://catalogue.museogalileo.it/object/Lens.html (06 February 2024).

(8) “photochemistry” in IUPAC Compendium of Chemical Terminology, 3rd ed. *International Union of Pure and Applied Chemistry*; **2006**. Online version 3.0.1, 2019. https://doi.org/10.1351/goldbook.P04588.

(9) Trommsdorff, H. Ueber Santonin. *Annalen der Pharmacie* **1834**, 11, 190-207.

(10) a) Matsuura, T.; Sato, Y.; Ogoro, R. A novel photorearrangement of santonin in the solid state. *Tetrahedron Lett*. **1968**, 44, 4627-4630. b) Fisch, M. H.; Richards, J. H. The mechanism of the photoconversion of santonin. *J. Am. Chem. Soc*. **1963**, 85, 3029–3030. c) Chen, X.; Rinkevicius, Z.; Luo, Y.; Ågren, H.; Cao, Z. The mechanism of the photoconversion of santonin. *ChemPhysChem* **2012**, 13, 353 – 362.

(11) a) Becquerel, E. Mémoire sur les effets électriques produits sous l'influence des rayons solaires. *Comptes Rendus* **1839**, 9, 561–567. b) Becquerel, E. Mémoire sur le rayonnement chimique qui accompagne la lumière solaire et la lumière électrique. *Comptes Rendus* **1840**, 11, 702-703.

(12) a) Bruner, L.; Kozak, Z. Elektrochem. Angew. Phys. Chem. 1911, 17, 354. c) Eibner, *A. Chem.-Ztg*. **1911**, 35, 753. b) Eibner, *A. Chem.-Ztg*. **1911**, 35, 774.

(13) Ciamician, G. The photochemistry of the future. *Science* **1912**, 36, 385-394.

(14) a) Allmand, A. J. Photochemistry, 1914-1925. *Annu. Rep. Prog. Chem.*, **1925**, 22, 333-373.

(15) Megan, H.; Twilton, J.; MacMillan, D. W. C. Photoredox catalysis in organic chemistry. *J. Org. Chem.* **2016**, 81, 6898−692.

(16) Kozlowksi, M.; Yoon, T. Editorial for the special issue on photocatalysis. *J. Org. Chem.* **2016**, 81, 6895−6897.

(17) Dutta, S.; Erchinger, J., E.; Strieth-Kalthoff, F.; Kleinmans, R.; Glorius, F. Energy transfer photocatalysis: exciting modes of reactivity. *Chem. Soc. Rev.*, **2024**, 53, 1068-1089.

(18) Strieth-Kalthoff, F.; James, M. J.; Teders, M.; Pitzer, L.; Glorius, F. Energy transfer catalysis mediated by visible light: principles, applications, directions. *Chem. Soc. Rev.* **2018**, 47, 7190-7202.

(19) Farney, E. P.; Yoon, T. Visible-light sensitization of vinyl azides by transition-metal photocatalysis. *Angew. Chem. Int. Ed.* **2014**, 53, 793-797.

(20) Zhou, C.; Liu, Z.; Liang, Y.-Q.; Lei, T.; Chen, B.; Liao, R.-Z.; Tung, C.-H.; Wu, L.-Z. Regioselective Diels–Alder reactions of anthracenes with olefins via visible light photocatalysis in a homogeneous solution. *Org. Lett.* **2024**, 26, 1116-1121.

(21) a) Ghogare, A. A.; Greer, A. Using singlet oxygen to synthesize natural products and drugs. *Chem. Rev.* **2016**, 116, 17, 9994–10034. b) Jung, M.; Ham, J.; Song, J. First Total Synthesis of Natural 6-Epiplakortolide E. *Org. Lett.* **2002**, 4, 2763−2765.

(22) Metternich, J. B.; Artiukhin, D. G.; Holland, M. C.; von Bremen-Kuhne, M.; Neugebauer, J.; Gilmour, R. Photocatalytic E → Z isomerization of polarized alkenes inspired by the visual cycle: mechanistic dichotomy and origin of selectivity. *J. Org. Chem*., **2017**, 82, 9955–9977.

(23) Balzani, V.; Bergamini, G.; Ceroni, P. Photochemistry and photocatalysis. *Rend. Fis. Acc. Lincei* **2017**, 28, 125–142.

(24) Teegardin, K.; Day, J. I.; Chan, J.; Weaver, J. Advances in photocatalysis: a microreview of visible light mediated ruthenium and iridium catalyzed organic transformations. *Org. Process Res. Dev.* **2016**, 20, 1156−1163.

(25) van Bergen, T. J.; Hedstrand, D. M.; Kruizinga, W. H.; Kellogg, R. M. Chemistry of dihydropyridines. 9. Hydride transfer from 1,4-dihydropyridines to sp3-

hybridized carbon in sulfonium salts and activated halides. Studies with NAD(P)H models. *J. Org. Chem.* **1979**, 44, 4953−4962.

(26) Hironaka, K.; Fukuzumi, S.; Tanaka, T. Tris(bipyridyl)ruthenium(II)-photosensitized reaction of 1-benzyl-1,4-dihydronicotinamide with benzyl bromide. *J. Chem. Soc., Perkin Trans. 2*, **1984**, 1705-1709.

(27) Cano-Yelo, H.; Deronzier, A. Photo-oxidation of some carbinols by the Ru(II) polypyridyl complex-aryl diazonium salt system. *Tetrahedron Lett*. **1984**, 25, 5517−5520.

(28) Russo, C.; Brunelli, F.; Tron, G. C.; Giustiniano, M. Visible-light photoredox catalysis in water. *J. Org. Chem.* **2023**, 88, 6284−6293.

(29) Candish, E.; Collins, K. D.; Cook, G. C.; Douglas, J. J.; Gómez-Suárez, A.; Jolit, A.; Keess, S. Photocatalysis in the life science industry. *Chem. Rev.* **2022**, 122, 2907-2080.

(30) Gesmundo, N. J.; Shaw, M. H.; Twilton, J.; Tellis, J. C.; MacMillan D. W. C.; Nicewicz, D. A. Photoredox Catalysis Introduction, Desk Reference, and User's Guide. *Merck KGaA* **2019**

(31) Buglioni, L.; Raymenants, F.; Slattery, A.; Zondag, S. D. A.; Noël T. Technological innovations in photochemistry for organic synthesis: flow chemistry, high-throughput experimentation, scale-up, and photoelectrochemistry. *Chem. Rev.* **2022**, 122, 2752–2906.

(32) Zheludev, N. The life and times of the LED — a 100-year history. *Nature Photon.* **2007**, 1, 189-192.

(33) Vallavoju, N.; Sivaguru, J., Supramolecular photocatalysis: combining confinement and non-covalent interactions to control light initiated reactions. *Chem. Soc. Rev.* **2014**, 43, 4084-4101.

(34) Raynal, M.; Ballester, P.; Vidal-Ferran, A.; van Leeuwen, P. W. N. M., Supramolecular catalysis. Part 1: non-covalent interactions as a tool for building and modifying homogeneous catalysts. *Chem. Soc. Rev.* **2014**, 43 (5), 1660-1733.

(35) Wiester, M. J.; Ulmann, P. A.; Mirkin, C. A. Enzyme mimics based upon supramolecular coordination chemistry. *Angew. Chem., Int. Ed.* **2011**, 50, 114−137.

(36) Koblenz, T. S.; Wassenaar, J.; Reek, J. N. H. Reactivity within a confined self-assembled nanospace. *Chem. Soc. Rev.* **2008**, 37, 247−262.

(37) Brown, C. J.; Toste, F. D.; Bergman, R. G.; Raymond, K. N. Supramolecular catalysis in metal−ligand cluster hosts. *Chem. Rev.* **2015**, 115, 3012−3035.

(38) Meeuwissen, J.; Reek, J. N. H. Supramolecular catalysis beyond enzyme mimics. *Nat. Chem.* **2010**, 2, 615−621.

(39) Yoshizawa, M.; Klosterman, J. K.; Fujita, M. Functional molecular flasks: new properties and reactions within discrete, self-assembled hosts. *Angew. Chem., Int. Ed.* **2009**, 48, 3418−3438.

(40) Morimoto, M.; Bierschenk, S. M.; Xia, K. T.; Bergman, R. G.; Raymond, K. N.; Toste, F. D. Advances in supramolecular host-mediated reactivity. *Nat. Catal.* **2020**, 3, 969−984.

(41) Yoshizawa, M.; Tamura, M.; Fujita, M. Diels-Alder in aqueous molecular hosts: unusual regioselectivity and efficient catalysis. *Science* **2006**, 312, 251−254.

(42) Zhang, Q.; Catti, L.; Pleiss, J.; Tiefenbacher, K. Terpene cyclizations inside a supramolecular catalyst: leaving-group-controlled product selectivity and mechanistic studies. *J. Am. Chem. Soc.* **2017**,139,11482−11492.

(43) Govindjee, J. T. B.; Gest, H.; Allen, J. F.; Discoveries in photosynthesis. *Advances in Photosynthesis and Respiration*, **2005**.

(44) a) Baly, E. C. C.; Heilbron, I. M.; Barker, W. F.; CX.—Photocatalysis. Part I. The synthesis of formaldehyde and carbohydrates from carbon dioxide and water. *J. Chem. Soc., Trans.* **1921**, 119, 1025-1035. b) Baly, E.C.C.; Heilbron, I. M.; Stern, H.J. XXIII.—Photocatalysis. Part III. The photosynthesis of naturally occurring nitrogen compounds from carbon dioxide and ammonia. *J. Chem. Soc., Trans.* **1923**, 123, 185-197.

(45) Coronado, J. M.; Fresno, F.; Hernández-Alonso, M. D.; Portela, R. Design of advanced photocatalytic materials for energy and environmental applications. *Green Energy and Technology*, **2013**.

(46) (a) Kobayashi, S. Science of Synthesis: Water in Organic Synthesis. *Thieme Chemistry*, **2012**. (b) Lindstrom, U. M. Organic Reactions in Water; *Blackwell: Oxford*, **2007**.

(47) Kitanosono, T.; Masuda, K.; Xu, P.; Kobayashi, S. Catalytic organic reactions in water toward sustainable society. *Chem. Rev.* **2018**, 118, 679-746.

(48) Byrne, F. P.; Jin, S.; Giulia, P.; Petchey, T. H. M.; Clark, J. h.; Farmer, J. T.; Hunt, A. J.; McElroy, C. R.; Sherwood, J. Tools and techniques for solvent selection: green solvent selection guides. *Sus. Chem. Proc.* **2016**, 4, 7.

(49) Mercer, S. M.; Jessop, P. G. "Switchable water": aqueous solutions of switchable ionic strength. *ChemSusChem* **2010**, 3, 467-470.

(50) Mercer, S. M.; Robert, T.; Dixon, D. V.; Chen, C.-S.; Ghoshouni, Z.; Harjani, J. R.; Jahangiri, S.; Peslherbe, G. H.; Jessop P. G. Design, synthesis, and solution behavior of small polyamines as switchable water additives. *Green Chem.*, **2012**, 14, 832-839.

(51) Hao, Y.; Lu, Y.-L.; Jiao, Z.; Su, C.-Y. Photocatalysis meets confinement: an emerging opportunity for photoinduced organic transformations. *Angew. Chem. Int. Ed.* **2024**, DOI: 10.1002/anie.202317808.

(52) Xue, D.; Jia, Z.-H.; Zhao, C.-J.; Zhang, Y.-Y.; Wang, C.; Xiao, J. Direct arylation of N-heteroarenes with aryldiazonium salts by photoredox catalysis in water. *Chem. Eur. J.* **2014**, 20, 2960 – 2965.

(53) Natarajan, P.; Chuskit, D.; Priya, S. Metal-free, visible-light-promoted oxidative radical cyclization of N-biarylglycine esters: one-pot construction of phenanthridine-6-carboxylates in water. *Green Chem.*, **2019**, 21, 4406-4411.

(54) De Souza, G. F. P.; Bonacin, J. A.; Salles Jr, A. G. Visible-light-driven epoxyacylation and hydroacylation of olefins using methylene blue/persulfate system in water. *J. Org. Chem.* **2018**, 83, 8331-8340.

(55) Kerzig, C.; Wenger, O. S.; Reactivity control of a photocatalytic system by changing the light intensity. *Chem Sci.* **2019**, 10, 11023-1109.

(56) Pan, S.; Jiang, M.; Hu, J.; Xu, R.; Zeng, X.; Zhong, G. Synthesis of 1,2-amino alcohols by decarboxylative coupling of amino acid derived α-amino radicals to carbonyl compounds via visible-light photocatalyst in water. *Green Chem.* **2020**, 22, 336-341.

(57) Guo, X.; Okamoto, Y.; Schreier, M. R.; Ward, T. R.; Wenger, O. S. Enantioselective synthesis of amines by combining photoredox and enzymatic catalysis in a cyclic reaction network. *Chem. Sci.* **2018**, 9, 5052-5056.

(58) Von Lier, R. C. W.; de Brujin, A. D.; Roelfes, G. A water-soluble iridium photocatalyst for chemical modification of dehydroalanine in peptides and proteins. *Chem. Eur. J.* **2021**, 27, 1430-1437.

(59) Nguyen, T.-T. H.; O'Brien, C. J.; Minh, L. N. T.; Olson, S. H.; Settineri, N. S.; Prusiner, S. B.; Paras, N. A.; Conrad, J. Water soluble iridium

photoredox catalyst for the trifluoromethylation of biomolecule substrates in phosphate buffered saline solvent. *Org. Lett.* **2021**, 23, 3823-3827.

(60) Bottecchia, C.; Rubens, M.; Gunnoo, S. B.; Hessel, V.; Madder, A.; Noël, T. Visible-light mediated selective arylation of cysteine in batch and flow. *Angew. Chem. Int. Ed.* **2017**, 56, 12702-12707.

(61) Yu, Y.; Zhong, L.-K.; Buevich, A. V.; Li, G.; Tang, H.; Vachal, P.; Colletti, S. L.; Shi, Z. C. Chemoselective peptide modification via photocatalytic tryptophan β-position conjugation. *J. Am. Chem. Soc.* **2018**, 140, 6797-6800.

(62) Bloom, S.; Liu, C.; Kölmel, D. K.; Quiao, J. X.; Zhang, Y.; Poss, M. A.; Ewing, W. R.; MacMillan, D. W. C. Decarboxylative alkylation for site-selective bioconjugation of native proteins via oxidation potentials. *Nat. Chem.* **2018**, 10, 205-211.

(63) Sun, K.; Lv, Q.-Y.; Chen, X.-L.; Qua, L.-B.; Yu, B. Recent advances in visible-light-mediated organic transformations in water. *Green Chem.* **2021**, 23, 232-248.

(64) Dou, Q.; Zeng, H. Recent advances in photo-induced organic synthesis in water. *Curr. Opin. Green Sustain. Chem.* **2023**, 40, 100766.

(65) Fendler, E. J.; Fendler, J. H., Micellar catalysis in organic reactions: kinetic and mechanistic implications. *Adv. in Phys. Org. Chem., Gold, V., Ed. Academic Press* **1970**, 8, 271-406.

(66) Brüss, L.; Jeyaseelan, R.; Kürschner, J. C. G.; Utikal, M.; Naesborg, L. Micellar effects and their relevance in photochemistry and photocatalysis. *ChemCatChem* **2023**, 15, e2022011.

(67) Bu, M.-J.; Cai, C.; Gallou, F. *Green Chem.* **2018**, 20, 1233-1237.

(68) Cannalire, R.; Santoro, F.; Russo, C.; Graziani, G.; Tron, G. C.; Carotenuto, A.; Brancaccio, D.; Giustiniano, M. Photomicellar catalyzed synthesis of amides from isocyanides: optimization, scope, and NMR studies of photocatalyst/surfactant interactions. *ACS Org. Inorg. Au* **2022**, 2, 66-74.

(69) Cybularezyk-Cecotka, M.; Predygier, J.; Crespi, S.; Szczepanik, J.; Giedik, M. Photocatalysis in aqueous micellar media enables divergent C−H arylation and N-dealkylation of benzamides. *ACS Catal.* **2022**, 12, 3543-3549.

(70) Santos, M. S.; Cybularczyk-Cecotka, M.; König, B.; Giedyk, M. Minisci C-H alkylation of heteroarenes enabled by dual photoredox/bromide catalysis in micellar solutions. *Chem. Eur. J.* **2020**, 26, 15323−15329.

(71) Noto, N.; Hyodo, Y.; Yoshizawa, M.; Koike, T.; Akita, M. Transition metal-free supramolecular photoredox catalysis in water: a phenoxazine photocatalyst encapsulated in V-shaped aromatic amphiphiles. *ACS Catal.* **2020**, 10, 14283–14289.

(72) Hyodo, Y.; Takashi, K., Chitose, Y.; Abe, M.; Yoshizawa, M.; Koike, T.; Akita, M. Assemblies of 1,4-bis(diarylamino)naphtalenes and aromatic amphiphiles: highly reducing photoredox catalysis in water. *Synlett* **2022**, 33, 1184–1188.

(73) Kita, Y.; Amao, Y. pH-controlled selective synthesis of lactate from pyruvate with a photoredox system of water-soluble zinc porphyrin, an electron mediator and platinum nanoparticles dispersed by polyvinylpyrrolidone. *Sustainable Energy Fuels* **2021**, 5, 6004-6013.

(74) Eisenreich, F.; Meijer, E. W.; Palmans, A. R. A. Amphiphilic polymeric nanoparticle for photoredox catalysis in water. *Chem. Eur. J.* **2020**, 26, 10355–10361.

(75) Eisenreich, F.; Kuster, T. H. R.; van Krimpen, D.; Palmans, A. R. A. Photoredox-catalyzed reduction of halogenated arenes in water by amphiphilic polymeric nanoparticles. *Molecules* **2021**, 26, 5882.

(76) Mundsinger, K.; Tuten, B. T.; Wang, L.; Neubauer, K.; Kropf, C.; O'Mara, M. L.; Barner-Kowollik, C. Visible-light reactive single-chain nanoparticles. *Angew. Chem. Int. Ed.* **2023**, 62, e2023029.

3. Chapter III

3.1. Introduction

In Nature, only three types of enzymes carry out purely photocatalytic organic reactions.[1–3] Indeed, the design of abiotic protein nanoreactors capable of custom photoreactions requires extensive genetic engineering effort.[4–6] In organic photochemistry, the scarce solubility of reactants in aqueous media and severe catalyst deactivation are of central concern for the replacement of organic solvents with water. While several strategies have been recently proposed,[7–10] only a few works have been devoted to the use of ultrafine soft nano-objects as efficient visible-light photocatalysts of "in water" organic reactions.[11,12] Single-chain nanoparticles (SCNP) as intramolecularly self-folded synthetic polymer chains with ultra-small size (2−20 nm) are posed as perfect candidates for advanced, next-generation enzyme-mimetic catalyst preparation.[13–16] Despite the extensive use of SCNPs as nanoreactors for a plethora of organic reactions,[13–19] only a few works have disclosed the use of SCNPs for photocatalytic applications.[12,20] Herein, we report the construction of unimolecular soft nano-objects endowed with broad, manifold photocatalytic activity in water and constructed by taking advantage of the protein-mimetic architecture of polymeric SCNPs (see Scheme 3.1). These artificial photosynthases (**APS**) are used to perform a collection of four visible-light-induced transformations using water as the sole medium.

3.2. Main Aims

Herein, we report single-chain nanoparticles, SCNPs, capable of efficiently catalyzing four different "in water" organic reactions by employing visible light as the only external energy source. Specifically, we decorated a high-molecular-weight copolymer, poly(OEGMA$_{300}$-*r*-AEMA), with iridium(III) cyclometalated complex pendants at varying content amounts. The isolated functionalized copolymers demonstrated self-assembly into noncovalent, amphiphilic SCNPs in water, which enabled efficient visible-light photocatalysis of two reactions unprecedentedly reported in water, namely, [2+2] photocycloaddition of vinyl arenes and α-arylation of *N*-arylamines. Additionally, aerobic oxidation of 9-substituted anthracenes and β-sulfonylation of α-methylstyrene were successfully carried out in aqueous media. Hence, by merging metal-mediated photocatalysis and SCNPs for the fabrication of artificial photoenzyme-like nano-objects - *i.e.*, artificial photosynthases (**APS**) - our work broadens the possibilities for performing challenging "in water" organic transformations via visible-light photocatalysis.

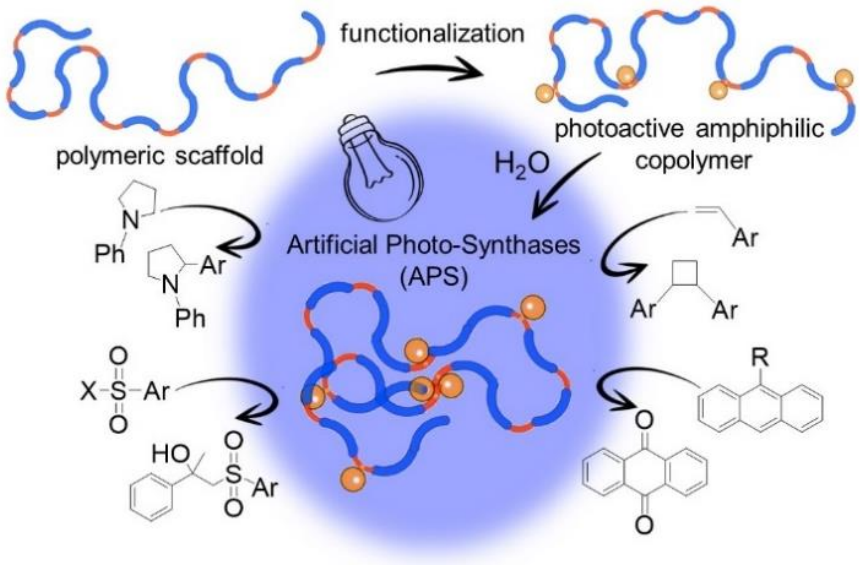

Scheme 3.1. Illustration of the preparation of an *Artificial Photo-Synthase* (**APS**) endowed with manifold photocatalytic activity towards "*in water*" reactions.

3.3. Results and Discussion

3.3.1. Preparation of the photoactive polymers

As APS precursor, we prepared the polymeric scaffold poly(OEGMA$_{300}$-*r*-AEMA) **P$_1$** of high molecular weight (>150 kDa), low dispersity (1.06), and controlled chemical composition (Table 3.1) via reversible addition−fragmentation chain transfer (RAFT) copolymerization of the monomers 4-acetoacetoxyethyl methacrylate (AEMA) and (oligoethylene glycol monomethyl ether) methacrylate (OEGMA$_{300}$).

To endow **P$_1$** with photocatalytic activity, we exploited the β-ketoester reactivity provided by the hydrophobic AEMA groups. Firstly, we prepared the reactive Ir(III) dimer dihydroxotetrakis[2-(2-pyridinyl)phenyl]diiridium-(III) dimer [Ir(ppy)$_2$OH]$_2$ **C$_1$** (Scheme 3.2) as post-polymerization functionalizing agent, starting from the commercially available iridium(III) trichloride $IrCl_3$ and adapting a procedure previously reported in literature see Experimental Techniques).[21] The choice of a dihydroxo-bridged complex was mainly dictated by the experimental necessity of working in reaction conditions as mild as possible for the post-polymerization functionalization reaction of the copolymer **P$_1$**. The experimental conditions commonly employed for the preparation of cyclometalated Ir(III) complexes bearing acetoacetates ancillary ligands are, indeed, usually involving the use of bases and refluxing solvents to go to completion and,[22] first attempts of applying such traditional synthetic methods to the polymer **P$_1$** resulted in irreversible aggregation and deterioration of the material.

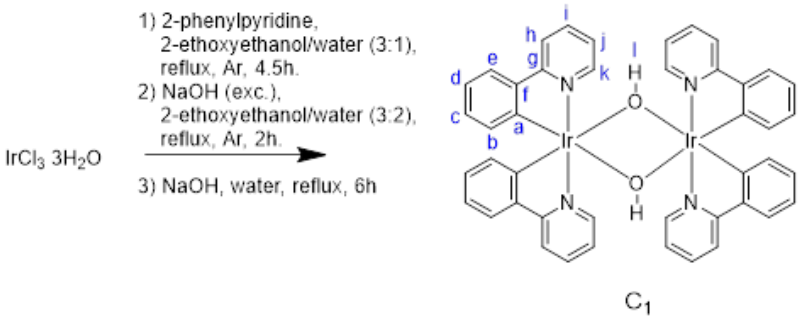

Scheme 3.2. Synthetic scheme of the preparation of the μ-dihydroxo bridged Ir(III) dimer **C$_1$**, used as reactive precursor for the functionalization of the copolymer **P$_1$**.

We then prepared Ir(III)-containing copolymers at three iridium loading ($\mathbf{L^{Ir}}$) regimes, $\mathbf{P_1{-}Ir_{10}}$, $\mathbf{P_1{-}Ir_{23}}$, and $\mathbf{P_1{-}Ir_{40}}$ ($\mathbf{L^{Ir}}$ = 10, 23, and 40 mol % with respect to AEMA units, respectively), by decorating the copolymer $\mathbf{P_1}$ through reaction with the $\mathbf{C_1}$ under very mild conditions, at room temperature and without the use of any additives (see Experimental Techniques for procedure's details).

Table 3.1. Properties of neat (P_1) and functionalized copolymers (P_1-Ir_x) synthesized in this work

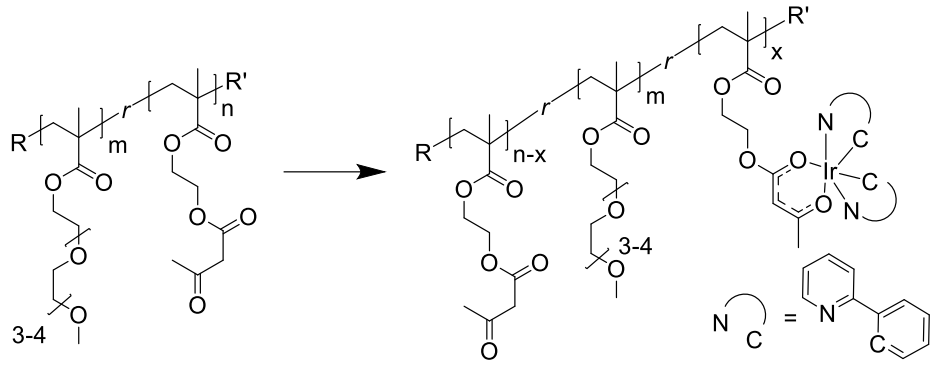

$\mathbf{P_1}$ $\mathbf{P_1\text{-}Ir_x}$

Sample	M_w (kDa)[a]	$Đ$[b]	AEMA (mol%)[c]	L^{Ir} (mol%)[d]
$\mathbf{P_1}$	169.8	1.06	20	-
$\mathbf{P_1\text{-}Ir_{10}}$	178.6	1.10	18	10
$\mathbf{P_1\text{-}Ir_{23}}$	174.5	1.13	15.4	23
$\mathbf{P_1\text{-}Ir_{40}}$	211.7	1.03	12	40

a) Weight-average molecular weight. b) Dispersity. c) Molar content of AEMA units. d) Iridium content.

A second cyclometalated complex, bis[2-(2-pyridinyl-N)phenyl-C](methyl acetoacetato)iridium(III) $Ir(ppy)_2(meacac)$ $\mathbf{C_2}$, was then prepared following a well-known literature procedure,[22] to be used as reference compound both for analytic purposes and catalysis performance comparations, as it will be discussed later. After determining the molar extinction coefficient in chloroform of the complex $\mathbf{C_2}$ (Figure 3.1), which was selected as model compound, it was possible to measure by UV-Vis

spectrophotometry of polymeric solutions in chloroform ([polymer] = 1 mg mL^{-1}) the quantity of incorporated iridium(III) in the lateral chain of the polymer, by means of its conversion into the desired species shown in Table 1.

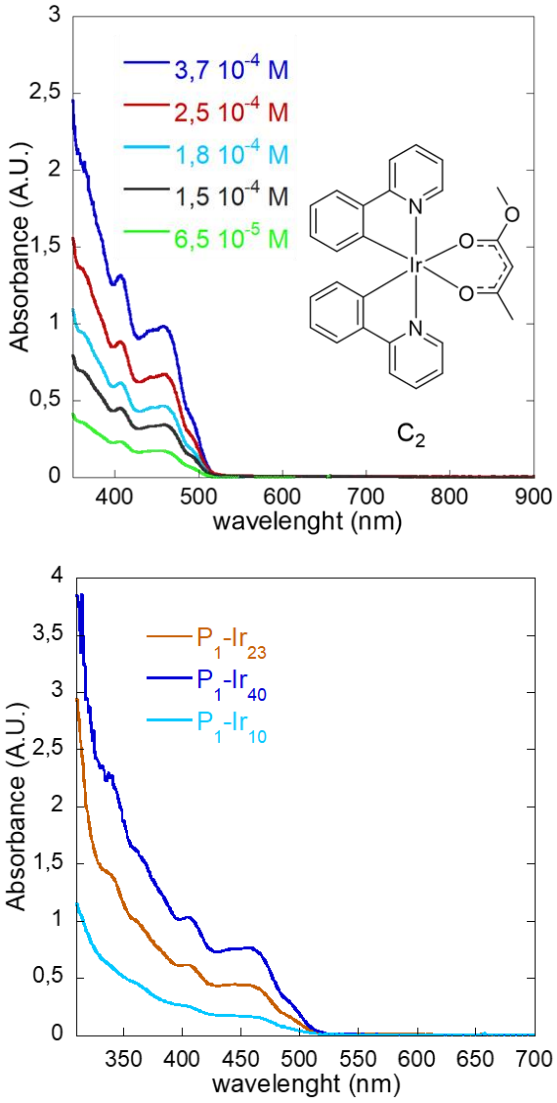

Figure 3.1. On the left, superimposed absorption spectra of the model compound **C_2** in chloroform 6.5 10^{-5} < [**C_2**] < 3.7 10^{-4} M in chloroform. On the right, superimposed absorption spectra in chloroform of the three copolymers **P_1-Ir_x** at polymer concentration of 1 mg mL^{-1}, used for incorporated iridium L^{Ir} quantification.

3.3.2. Self-assembly in aqueous solution

Thanks to their amphiphilic nature, high molecular weight (>150 kDa), and finely tuned composition, stable, self-assembled SCNPs[23,24] that we denoted as **SCNP-P$_1$**, **APS-Ir$_{10}$**, **APS-Ir$_{23}$**, and **APS-Ir$_{40}$** were obtained upon simple dissolution of **P$_1$**, **P$_1$−Ir$_{10}$**, **P$_1$−Ir$_{23}$**, and **P$_1$−Ir$_{40}$**, respectively, in water. Self-assembly was ascertained by measuring via dynamic light scattering (DLS) the difference ΔD_h between hydrodynamic diameters D_h of **P$_1$**, **P$_1$−Ir$_{10}$**, **P$_1$−Ir$_{23}$**, and **P$_1$−Ir$_{40}$** in tetrahydrofuran, THF, (good solvent for AEMA and $OEGMA_{300}$) and those of **SCNP-P$_1$**, **APS-Ir$_{10}$**, **APS-Ir$_{23}$**, and **APS-Ir$_{40}$** measured in water (selective solvent for $OEGMA_{300}$). iridium-functionalized copolymers all presented a positive ΔD_h (Table 3.2) because of the formation of a self-collapsed architecture (see Figure 3.2 and the Appendix: Section III).

Table 3.2. Hydrodynamic radii measured in THF (good solvent) and water (selective solvent)

Sample	D_h^{THF} (nm)	Sample	D_h^{water} (nm)
P$_1$	9.9	**SCNP-P$_1$**	8.7
P$_1$-Ir$_{10}$	12.3	**APS-Ir$_{10}$**	10.4
P$_1$-Ir$_{23}$	11.8	**APS-Ir$_{23}$**	9.6
P$_1$-Ir$_{40}$	10.4	**APS-Ir$_{40}$**	9.1

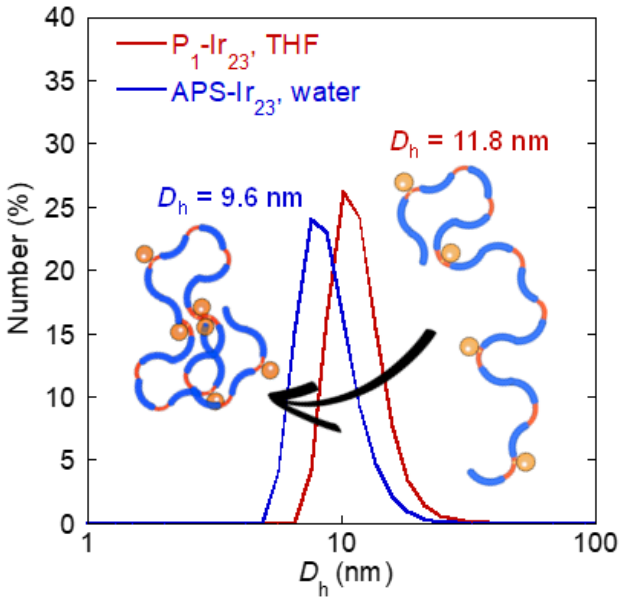

Figure 3.2. Illustration of the reduction in hydrodynamic size due to self-assembly of **P_1-Ir_{23}** (linear architecture) to **APS-Ir_{23}** (SCNP architecture) on changing from THF (good solvent) to water (selective solvent).

Additional evidence of the formation of a self-assembled conformation in **APS-Ir_{10}**, **APS-Ir_{23}**, and **APS-Ir_{40}** was obtained through photoluminescence (PL) experiments. As illustrated in Figure 3.3a, we measured the PL of eight solutions of the model compound, bis(2-phenylpyridine)(methyl acetoacetonate)iridium(III) **C_2** (see the Appendix: Sect III), in THF / water mixtures upon increase of the water content (from 0% to 70%). We observed a decrease in the PL intensity of **C_2** at high water content, which is consistent with literature data reported for the analogous complex bis(2-phenylpyridine)- (acetylacetonate)iridium(III), $Ir(ppy)_2(acac)$.[25,26] Conversely, **APS-Ir_{10}**, **APS-Ir_{23}**, and **APS-Ir_{40}** in water displayed significant PL intensity enhancement with respect to **P_1–Ir_{10}**, **P_1–Ir_{23}**, and **P_1–Ir_{40}** recorded in two different nonselective solvents (chloroform and THF) (see Figure 3.3b).

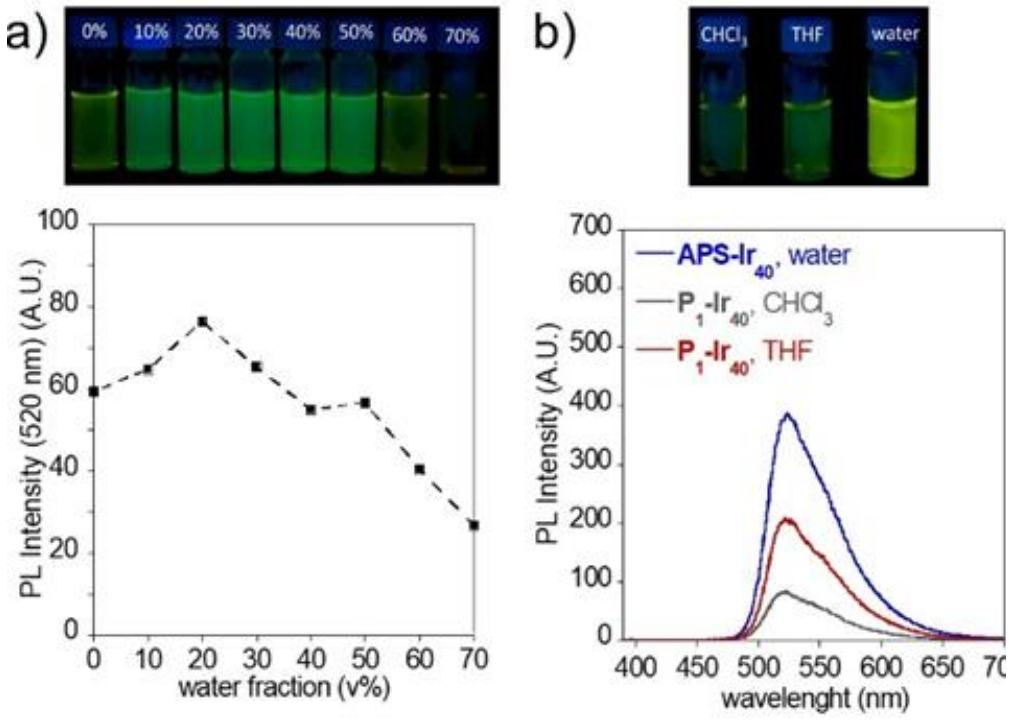

Figure 3.3. a) PL emission of model compound bis(2-phenylpyridine)(methyl acetoacetonate)iridium(III) **C2** in THF / water mixtures (from 0% to 70%) ([Ir(III)] = 3 μM, λ_{exc} = 450 nm). b) Illustration of the aggregation-enhanced emission (AEE) of **APS-Ir40** in water vs **P1–Ir40** in $CHCl_3$ and THF under LED illumination ([Ir(III)] = 3 μM, λ_{exc} = 450 nm, $\lambda_{em}{}^{max}$ = 521 nm).

These findings suggest that that confinement of the hydrophobic photocatalyst in the limited space of the self-assembled **APS-Ir10**, **APS-Ir23**, and **APS-Ir40** induces significant aggregation-enhanced emission (AEE).

3.3.3. Photocatalytic activity "in water"

With the self-assembled SCNPs in hand, we tested their suitability as artificial photosynthases (APS) for in water photocatalysis of a variety of organic transformations, which were selected from among the plethora of iridium(III) cyclometalated complex-mediated reactions in organic solvents.[27–29] Visible light has

been recently applied successfully as an energy source for [2 + 2] cycloadditions in organic solvents;[30] herein, we report an unprecedented procedure that employs water as the sole reaction medium. For instance, an **APS-Ir$_{40}$** solution was prepared by dissolving 2 mg of **P$_1$−Ir$_{40}$** in 1 mL of deionized water, which was then charged with 58 μmol of the vinylic compound **1a**, and the resulting mixture was left stirring at room temperature and under LED illumination (λ_{max} = 450 nm). After this time, the extracted crude product was analyzed *via* quantitative ^{1}H NMR (see the Appendix: Sect III) for conversion (*c*%) determination. Multiplets at 3.54 and 3.98 ppm (see Figure 3.4) indicate the formation of the 1,2-bis-substituted cyclobutane product **2a**, which was then isolated in 90% yield as a mixture of *cis* and *trans* diastereomers.

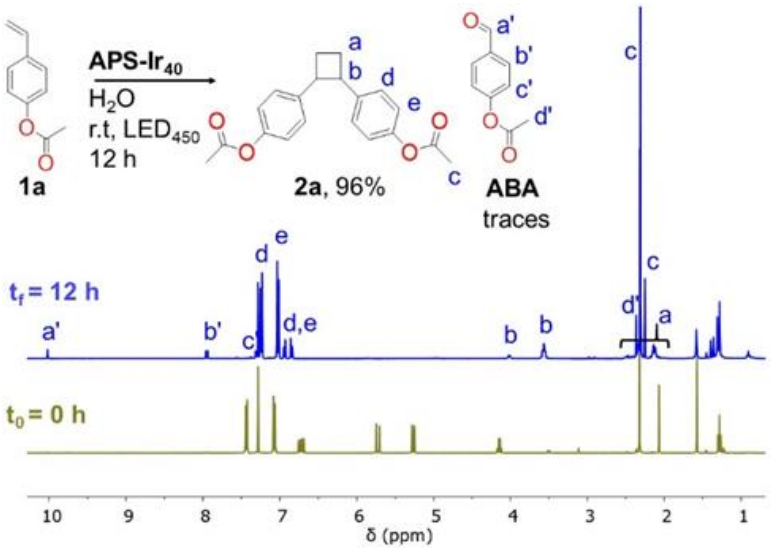

Figure 3.4. ^{1}H NMR of the crude of "*in water*" [2+2] photocycloaddition reaction of **1a** in the presence of **APS-Ir$_{40}$** (see text).

To our delight, we observed similar results when exploring a variety of substrates, as illustrated in Table 3.3. Considering typical redox potentials of vinyl arenes (*e.g.*, E_{ox} = 1.97 V vs SCE, E_{red} = −2.53 V vs SCE)[31,32] and photocatalyst excited-state potentials (*e.g.*, E^*_{ox} = 0.43 V vs SCE and E^*_{red} = −2.57 V vs SCE),[27] it seems difficult to imagine the activation of olefins **1a**−**1f** by typical single-electron transfer (SET).[33] We hypothesized that, helped by the locally hydrophobic packed environment

of the APS, these unlike processes could be allowed via an energy transfer (E_T) mechanism because of the similar triplet energies of the involved species (*e.g.*, E_T = ~60 kcal mol^{-1} for vinyl arenes, E_T = ~55 kcal mol^{-1} for **C**$_2$).[34]

Table 3. Photocatalyzed "*in water*" [2+2] cycloaddition of vinyl arenes (*CA* reaction)[a]

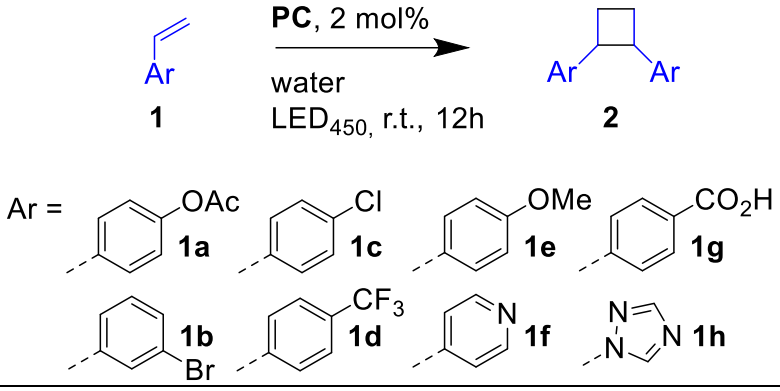

Entry	PC	Transformation	c%[b]	trans:cis[c]
1	**APS-Ir$_{40}$**	**1a → 2a**	96(90)[d]	1:0.3
2	**APS-Ir$_{23}$**	**1a → 2a**	94	1:0.3
3	**APS-Ir$_{10}$**	**1a → 2a**	96	1:0.3
4	**APS-Ir$_{40}$**	**1b → 2b**	97	1:0.2
5	**APS-Ir$_{40}$**	**1c → 2c**	96	1:0.3
6	**APS-Ir$_{40}$**	**1d → 2d**	90	1:0.3
7	**APS-Ir$_{40}$**	**1e → 2e**	60	1:0.3
8	**APS-Ir$_{40}$**	**1f → 2f**	79	1:0.3
9	**APS-Ir$_{40}$**	**1g → 2g**	n.p.[e]	-
10	**APS-Ir$_{40}$**	**1h → 2h**	n.p[e]	-
11	**No PC**	**1a → 2a**	n.p.[e]	-
12	**C$_2$**	**1a → 2a**	63	1:0.3

[a]See Experimetal Techniques for details. [b]Conversion from ^{1}H NMR. [c]Determined by ^{1}H NMR. [d]Isolated yield in parenthesis. [e]No product.

Byproducts formed in trace amounts, among which we assigned[35] the structure of 4-acetoxybenzaldehyde, ABA, to be the major constituent in agreement with the reactivity of electron-rich vinyl arenes with reactive oxygen species that may be generated during irradiation.[36] Performance of the same reaction using the model photocatalyst $\mathbf{C_2}$ dropped conversion to 63% (see the Appendix to Chapter III) with the remaining components of the crude being the reactant and byproducts. No conversion was observed by employing water-soluble substrates (**1g**, **1h**, Table 3.3), probably because of differences in the E_T values.

Interestingly, when 9-substituted anthracenes were employed as the substrate, we observed the formation of anthraquinone **4**. Since singlet oxygen and other reactive oxygen species (ROS) are generated upon excitation of $\mathbf{C_2}$ in organic solvents under aerobic conditions,[37] we surmised that **APS-Ir$_{10}$**, **APS-Ir$_{23}$**, and **APS-Ir$_{40}$** could be efficient photo-catalysts for the "in water" oxidation of 9-substituted anthracenes **3** to anthraquinone **4** *via* reaction with ROS species[38] (see Table 3.4). The formation of **4** that was confirmed by ^{1}H NMR, which is consistent with literature data,[39] resulted in being completely neglected when the complex is not confined within the SCNP (see the Appendix to Chapter III).

Table 3.4. Photocatalyzed "*in water*" oxidation of 9-substituted anthracenes (*OA* reaction)[a]

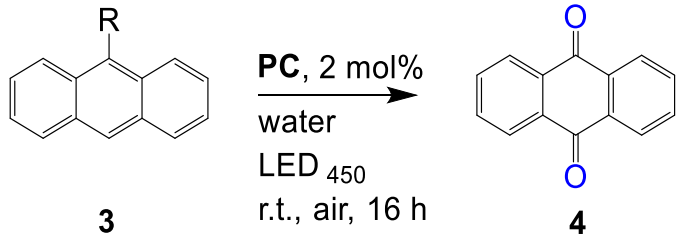

3 **4**

R = CH_2OH (**3a**), CH_2Cl (**3b**)

Entry	PC	Substrate	*c*%[b]
1	**APS-Ir$_{40}$**	**3a**	62 (58)[c]
2	**APS-Ir$_{23}$**	**3a**	21
3	**APS-Ir$_{10}$**	**3a**	19
4	**APS-Ir$_{40}$**	**3b**	59
5	**No PC**	**3a**	n.p.[d]
6	**C_2**	**3a**	n.p.[d]

[a]See Experimental Techinques for details. [b]Conversion from ^{1}H NMR. [c]Isolated yield. [d]No product.

Next, we evaluated the capability of **APS-Ir$_{10}$**, **APS-Ir$_{23}$**, and **APS-Ir$_{40}$** to catalyze visible-light-induced α-arylation of arylamines that, since its discovery reported by McMillan *et al.*,[40,41] have never been reported in water. Table 3.5, entries 1−3 show the procedure in organic solvents. To enable the photocatalytic cycle to occur in water, we prepared **APS-Ir$_{40}$** by dissolving 2 mg of **P$_1$−Ir$_{40}$** in 1 mL of degassed deionized water. We then charged the APS aqueous solution with 29 μmol of **6** and with a large excess of sodium acetate, NaOAc, (84 equiv.). The resulting mixture was deoxygenated by three consecutive vacuum / argon backfill cycles, finally 87 μmol of 5 were added and left stirring at room temperature and under blue LED (λ_{max} = 450 nm) irradiation for 12 h. Under these conditions, product **7** was obtained by using **APS-Ir$_{40}$** as photocatalyst in 57% conversion and 48% purified yield (Table 3.5, entry 5).

Table 3.5. Photocatalyzed "*in water*" α-arylation of arylamines (*AA* reaction)[a]

5 **6** **7**

Entry	PC	mol% PC	[NaOAc] M[b]	Solvent[b]	c%[c]
1	**C_2**	0.5	0.06	DMA	>95(95)[d]
2	**P_1-Ir_{40}**	0.5	0.06	DMA	>95
3	**C_2**	0.5	0.06	MeOH	8
4	**APS-Ir_{40}**	2	0.06	H_2O	n.p.[e]
5	**APS-Ir_{40}**	2	2.4	H_2O	57(48)[d]
6	**APS-Ir_{23}**	2	2.4	H_2O	22
7	**APS-Ir_{10}**	2	2.4	H_2O	21
8	**C_2**	2	2.4	H_2O	n.p.[e]
9	**APS-Ir_{40}**	2	2.4	H_2O+ DMA	33
10	**APS-Ir_{40}**	2	sat.[f]	H_2O	24
11	**No PC**	-	2.4	H_2O	n.p.[e]

[a]See Experimental Techinques for details. [b]NaOAc = sodium acetate; DMA = dimethylacetamide; MeOH = methanol. [c]Conversion of **7** from ^{1}H NMR. [d]Isolated yield of **7** in parenthesis. [e]No product. [f]Saturated in NaOAc.

Conversion was found to decrease upon reduction of the iridium loading in the **APS** photocatalyst (Table 3.5, entries 6 and 7). We attributed the striking conversion drop upon either lowering or increasing the base concentration (Table 3.5, entries 4 and 10) to the altered acidities of the reactants and additives in aqueous media with respect to the reaction conditions reported in literature for organic solvent.[40,42]

Inspired by pioneering work by Lipshutz *et al.*,[12] we finally tested **APS-Ir$_{10}$**, **APS-Ir$_{23}$**, and **APS-Ir$_{40}$** as photocatalysts for the "in water" β-hydroxysulfonylation of α-methylstyrene **8**. We carried out the photocatalytic reactions under oxygen-free conditions by charging the readily prepared APS aqueous solutions with **8** and sulfonyl halides **9**. Despite the intrinsic water-sensitive nature of these reactants, we could observe up to 67% conversion into desired product **10** (58% isolated yield) (Table 3.6, entry 2).

Table 3.6. Photocatalyzed "*in water*" α-styrene β-hydroxysulfonylation (*HS* reaction)[a]

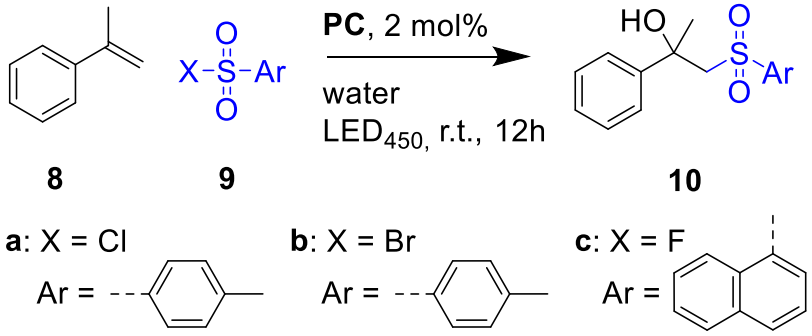

Entry	PC	Transformation	c%[b]
1	**APS-Ir$_{40}$**	**9a → 10a**	50
2	**APS-Ir$_{23}$**	**9a → 10a**	67(58)[d]
3	**APS-Ir$_{10}$**	**9a → 10a**	52
4	**APS-Ir$_{23}$**	**9b → 10b**	n.p.[e]
5	**APS-Ir$_{23}$**	**9c → 10c**	21
6	**C$_2$**	**9a → 10a**	23
7	**No PC**	**9a → 10a**	n.p.[e]

[a]See Experimental Techinques for experimental details. [b]Conversion from ^{1}H NMR. [d]Isolated yield in parenthesis. [e]No product.

As expected, a significant reduction was observed with the model compound $\mathbf{C_2}$ as a photocatalyst (Table 3.6, entry 6). For this reaction, no significant effect of iridium loading in the APS photocatalyst on conversion is observed (Table 3.6, entries 1−3).

3.3.4. Effect of APS type on conversion

To investigate the effect of APS type (*i.e.*, Ir(III)-Loading) on conversion (*c*%), we maintained fixed the overall catalyst concentration and observed the influence of the parameter ***d***, which we call the "*intra-particle photocatalytic unit density"*, as defined by Equation 3.1, on *c*%.

$$\boldsymbol{d}\ (nm^{-3}) = 3\frac{n^{PC}}{4\pi r_h^3 n^{SCNP}} \qquad \text{Equation 3.1}$$

Although for classical photocatalysis one would expect no substantial influence of ***d*** on *c%*, we observed that the dependence of *c*% on ***d*** varied with the selected reaction (Figure 3.5). We hypothesized this behavior could be due to the very different nature of the mechanisms involved, which we named as A-type or B-type. In A-type mechanism, two reactants independently interact with the photosensitizer, whereas in B-type mechanism the contact occurs either in parallel or one time only. Hence, APS showing high value of ***d*** would favor A-type mechanism (AA, OA) while B-type mechanism would be almost independent on ***d*** (CA, HS).

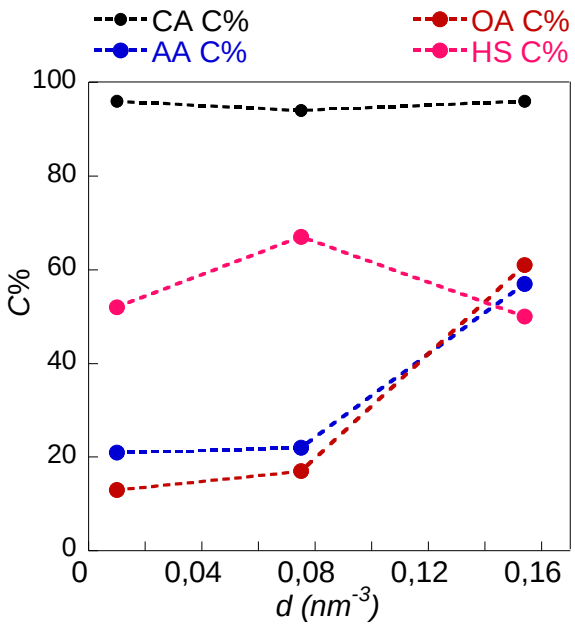

Figure 3.5. Conversion (*c*%) *vs.* "intra-particle photocatalytic unit density" (***d***) for the four kinds of reactions explored in this work. CA = [2+2] Cycloaddition of vinyl arenes. AA = α-Arylation of arylamines. OA = Oxidation of 9-substituted anthracenes. HS = α-Styrene β-hydroxysulfonylation.

We hypothesized this behavior could be due to the very different nature of the mechanisms involved, which we named as A-type or B-type. In A-type mechanism, two reactants independently interact with the photosensitizer, whereas in B-type mechanism the contact occurs either in parallel or one time only. Hence, APS showing high value of ***d*** would favor A-type mechanism (AA, OA) while B-type mechanism would be almost independent on ***d*** (CA, HS).

3.3.5. Kinetic aspects

To find the optimal experimental conditions for performing the APS catalytic turnover number estimation via initial velocities measurement, we first assessed the course of the "in water" [2+2] photocycloaddition of **1a** catalyzed by **APS-Ir$_{40}$**. Six reactions were prepared by adding to a 4 mL oven dried vial, equipped of a magnetic

stir bar, 100 µL of a stock solution of **P_1-Ir_{40}** in methylene chloride ([polymer] = 20 mg mL^{-1}). The polymer solution was then left stirring at r.t. and in the dark for 1 h, ensuring complete removal of the volatiles. Once a polymeric thin film was obtained, 1 mL of deionized water was added and the resulting mixture was then left stirring at r.t. and in the dark until a clear, pale-yellow solution of **APS-Ir_{40}** was obtained. After adding 58 µmol of **1a**, the reactions were left open and stirring at r.t. and under LED illumination (λ_{max} = 450 nm), each for the desired amount of time (t_0, t_1, t_2, t_3, t_4 and t_5 for 0 min, 30 min, 1 h, 2 h, 3 h, 6 h, respectively). After these times, the organic products were extracted by three consecutive times with 3 mL of diethyl ether each. The collected organic fractions were dried over anhydrous magnesium sulfate, filtered, and concentrated under reduced pressure. The extracted crudes were then directly diluted with 0.5 mL of $CDCl_3$ for quantitative NMR analysis (see Figures 3.6 and 3.7).

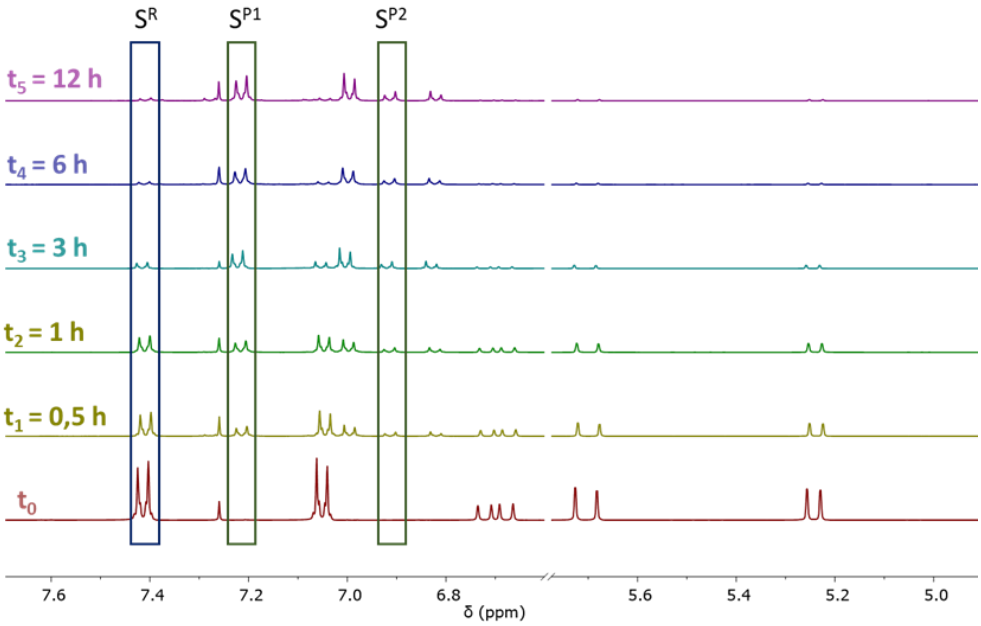

Figure 3.6. Superimposed ^{1}H NMR spectra used to follow the photoconversion of **1a** in **2a** catalyzed by **APS-Ir_{40}** over time. The highlighted portions of the figures show the signals S^{Pn} and S^R of **2a** and **1a**, respectively, used for conversion calculation (*c*% = 100 × mol **2a** / mol **1a**).

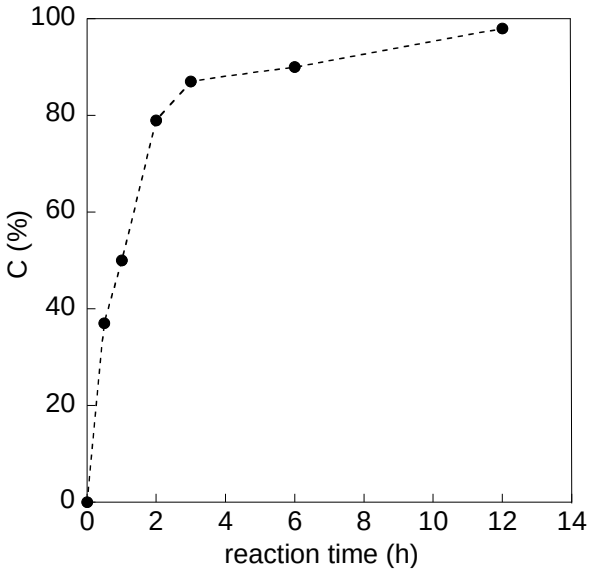

Figure 3.7. Conversion (%) vs time of the "in water" [2+2] photocycloaddition of **1a** catalyzed by **APS-Ir$_{40}$**.

For the kinetics assay, six solutions of **APS-Ir$_{40}$** were first prepared following the above standard procedure. After adding 235 µmol, or 175 µmol, or 120 µmol, or 58 µmol, or 15 µmol, or 8 µmol of vinyl arene **1a**, the reaction mixtures were left open and stirring at r.t. and under LED illumination (λ_{max} = 450 nm). Each sample reaction at fixed substrate concentration was irradiated for each of the desired amount of time (t_0, t_1, t_2, t_3 and t_4 for 0 min, 5 min, 10 min, 20 min and 30 min, respectively). After these times, the organic products were extracted by three consecutive times with 3 mL of diethyl ether each. The collected organic fractions were dried over anhydrous magnesium sulfate, filtered, and concentrated under reduced pressure. The extracted crudes were then diluted with 0.5 mL of $CDCl_3$ containing 1,4-diaminobenzene 18.4 × 10-3 M for quantitative NMR analysis. The amount of **2a** at the time t in the reaction ([**2a**]$_t$) was determined according to the Equation 3.2. The reactions corresponding to lower substrate concentrations, namely 15 mM and 8 mM, were repeated in duplicate and the respective extracted crudes were summed for quantitative calculation via NMR.

$$[\mathbf{2a}]_t(M) = \frac{n_{2a}^{i}(mol)}{V^{r}(L)} = \frac{\Sigma^{P}}{4} \times \frac{4}{I^{SI}} 9.22 \times 10^{-6} \frac{(mol)}{10^{-3}(L)}$$ Equation 3.2

where n_i **2a** is the calculated number of moles of **2a** in the NMR tube, Σ^P is the sum of the integrals of the products (*trans*-**2a** and *cis*-**2a**) at 7.23 ppm and 6.93 ppm, respectively, V_r is the volume of the reaction mixture and I^{SI} is the integrated signal of the protons of the internal standard at 6.57 ppm. After deriving the initial velocities v_0^i of the catalyzed reaction at each *i*-concentration of **2a** by linear fitting of the experimental points (see Figure 3.8), we fit the v_0^i values to a Michaelis-Menten curve (see Figure 9).

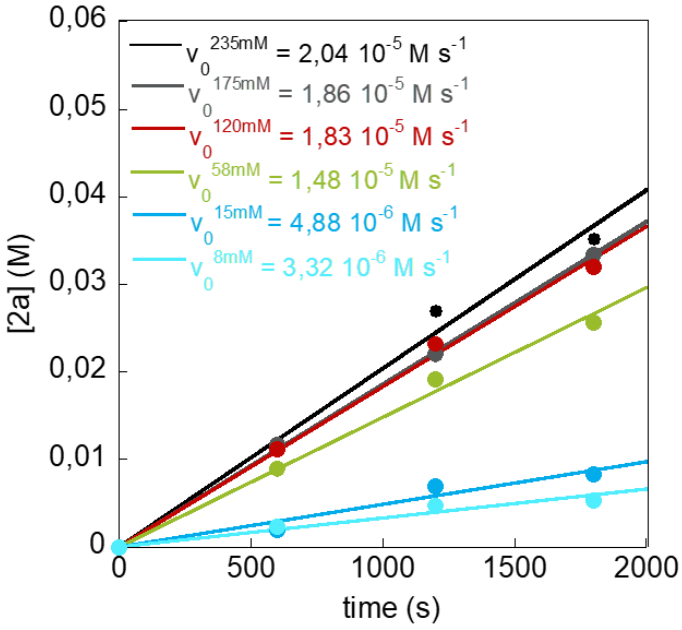

Figure 3.8. Initial velocities (^{1}H NMR) of the "in water" [2+2] photocycloaddition of **1a** catalyzed by **APS-Ir$_{40}$** in the substrate range between 0.008 M and 0.235 M.

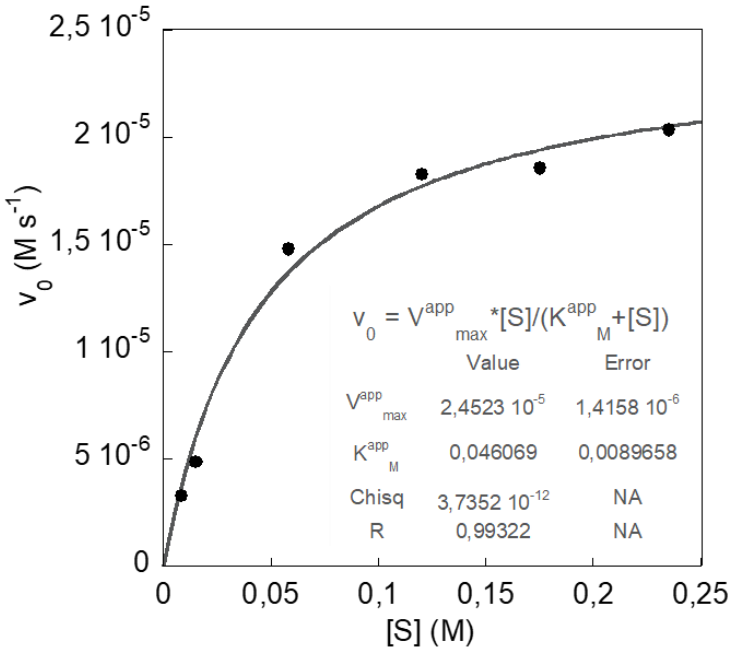

Figure 3.9. Michaelis-Menten plot of the "in water" [2+2] photocycloaddition of **1a** catalyzed by **APS-Ir$_{40}$**.

An apparent catalytic constant $k_{cat,app}$ of 2.6 s^{-1} was obtained from Equation 3.3:

$$k_{cat,app}(s^{-1}) = \frac{V_{max}}{N_T} \qquad \text{Equation 3.3}$$

where V_{max} is the maximum measured velocity of conversion of **1a** into the title product **2a** and N_T is the nanoparticle concentration employed for the catalytic reaction, calculated taking the M_w (SEC) as molecular weight. The value of the apparent Michaelis-Menten constant obtained was $K_{M,app} = 4.6 \times 10^{-2}$ M.

3.3.6. Recyclability of APS

To assess the reusability of APSs, we performed a recyclability experiment against the "*in water*" [2+2] photocycloaddition of vinyl arenes in the best conditions in terms of product yields. After a 1st "in water" [2+2] photocycloaddition reaction of

1a with **APS-Ir$_{40}$** as catalyst, the organic products were extracted by three consecutive times with 3 mL of diethyl ether each. The collected organic fractions were dried over anhydrous magnesium sulfate, filtered, and concentrated under reduced pressure. The extracted crudes were then directly diluted with 0.5 mL of $CDCl_3$ for quantitative NMR analysis. The aqueous phase was then collected and centrifuged at 4°C, the pale-yellow sediment was re-dispersed in 1 mL of deionized water by means of continuous stirring at r.t. and in the dark for 1 h. For the 2nd catalytic cycle, the resulting clear, faded-yellow solution was subsequently transferred to a 4 mL reaction vessel, charged with 58 μmol of vinyl arene **1a** and left open and stirring at r.t. and under LED illumination (λ^{max} = 450 nm) for 12 hours. After this time, the organic products were extracted by three consecutive times with 3 mL of diethyl ether each. The collected organic fractions were dried over anhydrous magnesium sulfate, filtered, and concentrated under reduced pressure. The extracted crudes were then directly diluted with 0.5 mL of $CDCl_3$ for quantitative NMR analysis. Next 3rd and 4th catalytic cycles were carried out following the same procedure as described for the 2nd one. Figure 3.10 illustrates the results of the recyclability of **APS-Ir$_{40}$** in 4 consecutive cycles.

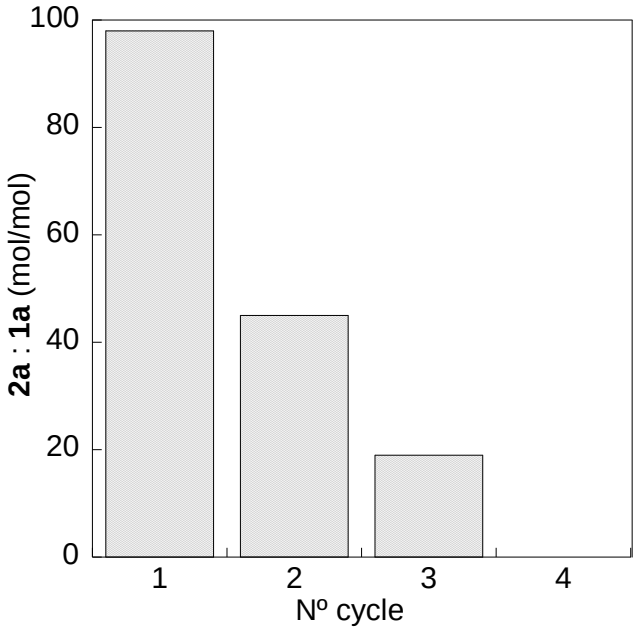

Figure 3.10. Results of the recyclability experiment of **APS-Ir$_{40}$** as catalyst of the "*in water*" [2+2] photocycloaddition of **1a**.

3.4. Experimental Techniques

3.4.1. Solvents and reagents

Unless otherwise noted, all reagents and solvents were used as received from vendors. (Oligoethylene glycol monomethyl ether) methacrylate ($OEGMA_{300}$, average molecular weight = 300 Da) (>99%) and 4-acetoacetoxyethyl methacrylate (AEMA) (>95%) were purchased from TCI Europe N.V. and were filtered over basic alumina before use. n-Hexane (96%), acetone (>99%), methylene chloride (CH_2Cl_2) (>99%, +0.2 % EtOH), n-pentane (99%), ethyl acetate (AcOEt) (>99.8) and diethyl ether (Et_2O) (>99%, +7 ppm BHT) were purchased from Scharlab. Tetrahydrofuran (THF) (>99 %, +0.025% BHT) and methanol (MeOH) (>99%) were purchased from Fisher Scientific, inhibitor-free THF was obtained by filtration over basic alumina. 1,4-Dioxane (>99%), methyl acetoacetate (99%), 2-ethoxyethanol (≥99%), sodium hydroxide (NaOH) (≥98%), chloroform (>99%, +100-200 ppm amylene), α-methyl styrene (99%), 2-naphtalenesulfonyl fluoride (95%), sodium acetate (NaOAc) (>99%), anhydrous magnesium sulfate ($MgSO_4$) (>99%), sodium chloride (NaCl) (>99%), silver(I) trifluoromethansulfonate (AgOTf) (≥98%), 4-cyano-4-(thiobenzoylthio)pentanoic acid (CPADB), 1,4-dicyanobenzene (DCB) (98%), triethylamine (TEA) (>99%), linalool (97%) and dimethylacetamide (DMA) (≥99%) were purchased from Sigma-Aldrich. p-Toluenesulfonyl chloride (99%) and p-toluenesulfonyl bromide (98%) were purchased from Sigma-Aldrich and handled under argon atmosphere. 4-Acetoxystyrene (96%), 4-chlorostyrene (99%), 3-bromostyrene (97%), 4- trifluoromethylstyrene (99%), 4-vinylpyridine (≥95%) and 1-vinyl-1,2,4-triazole (≥97%) were purchased from Sigma-Aldrich and used after filtering over basic alumina. Bis(μ-chloro)tetrakis(2- phenyl-pyridinato)diiridium(III) (98%), iridium(III) chloride trihydrate (98%), 2-phenylpyridine (>99%), 4-carboxystyrene (>99%) and 4-methoxystyrene (>99%) were purchased from BLD Pharma. Azobisisobutyronitrile (AIBN) (98%) was purchased from Fluka and recrystallized from MeOH prior use. Silica gel for column chromatography (0.035-0.07 nm 60 A) was purchased from Acros Organics. Basic alumina (0.063-0.2 mm) was purchased from Merck. N-phenylpyrrolidine (>98%) was purchased from Alpha Aesar. Deuterated chloroform ($CDCl_3$, 99.8% D, + 0.03% tretramethylsilane) for NMR

analysis was purchased from Eurisotop. Deionized water was obtained from a Thermoscientific Barnstead TII System.

3.4.2. Analytical methods and techniques

Nuclear Magnetic Resonance (NMR) Spectroscopy: ^{1}H and ^{13}C NMR spectra were recorded at room temperature (r.t.) on a Bruker spectrometer operating at 400 MHz, using $CDCl_3$ as solvent.

- Hydrophobic monomer content in the copolymer, %AEMA (mol%), was calculated according to Equation 3.4:

$$\%AEMA\ (mol\%) = \frac{S_{AEMA}^{OMe}}{S_{OEGMA}^{OMe} + S_{AEMA}^{OMe}} \times 100 \qquad \text{Equation 3.4}$$

where S^{OMe}_{AEMA} is the integrated area of the signal corresponding to the methoxylic protons of the AEMA units within the copolymer (2.29 ppm) and S^{OMe}_{OEGMA} is the integrated area of the signal corresponding to the methoxylic protons of OEGMA units (3.37 ppm).

- NMR conversion of the photo [2+2] cycloaddition reaction, *c*% (mol%), was calculated according to Equation 3.5:

$$c\%\ (mol\%) = \frac{\Sigma^{P}}{S^{R} + \Sigma^{P}} \times 100 \qquad \text{Equation 3.5}$$

where Σ^P is the sum of the normalized integrated area signals of the alkylic protons of all the isomers of the product (3.56 ppm and 4.02 ppm) and S^R is the normalized area of the signal of the vinylic proton of the reactant (5.74-5.69 ppm). The diastereomeric ratio *d.r.* was calculated using the integrated arylic proton signals of the product (7.03-7.01 ppm for the *trans* isomer and 6.86-6.83 ppm for the *cis* isomer).

- NMR conversion of the α-arylation of arylamines, *c*% (mol%), was calculated according to Equation 3.6 or Equation 3.7 when an internal standard was used:

$$c\%\ (mol\%) = \frac{S^P}{S^{Ar}_{DCB} + S^P} \times 100 \qquad \text{Equation 3.6}$$

$$c\%\ (mol\%) = \frac{S^P n^{SI}}{S^{SI} + n^P_0} \times 100 \qquad \text{Equation 3.7}$$

where S^P is the normalized area of the arylic signals of the product (7.60-7.58 ppm), S^{Ar}_{DCB} is the normalized area of the aromatic signal of the reactant 1,4-dicyanobenzene (7.79 ppm), n^{SI} is the internal standard (linalool) number of moles corresponding to the weighted amount in the tube, S^{SI} is the normalized intensity of the signal of the internal standard (5.95-5.89 ppm) and n^P_0 is the number of moles of the reactant 1,4-dicyanobenzene corresponding to the weighted amount before the reaction.

- NMR conversion of the oxidation of 9-substituted anthracenes, *c*% (mol%), was calculated according to Equation 3.8:

$$c\%\ (mol\%) = \frac{S^P}{S^R + S^P} \times 100 \qquad \text{Equation 3.8}$$

where S^P is the normalized area of the arylic signals of the anthraquinone product (7.81-7.79 ppm), S^R is the normalized area of the signal of the reactant (*e.g,*. signal at 8.04-8.01 ppm for the 9-hydroxymethyl anthracene).

- NMR conversion of the β-hydroxysulfonylation reaction, *c*% (mol%), was calculated according to Equation 3.9:

$$c\%\ (mol\%) = \frac{S^P n^{SI}}{S^{SI} + n^P_0} \times 100 \qquad \text{Equation 3.9}$$

where S^P is the normalized area of the arylic signals of the product (7.49-7.48 ppm), n^{SI} is the internal standard (1,4-dicyanobenzene) number of moles corresponding to the weighted amount in the tube, S^{SI} is the normalized intensity of the signal of the internal standard (7.79 ppm) and n^P_0 is the number of moles of the reactant α-methyl styrene corresponding to the amount before the reaction.

Size-Exclusion Chromatography (SEC): SEC measurements were performed at 30 °C on an Agilent 1200 system equipped with PLgel 5μm Guard and PLgel 5μm MIXED-C columns, and triple detection: a differential refractive index (dRI) detector (Optilab Rex, Wyatt), a multi-angle laser light scattering (MALLS) detector (MiniDawn Treos, Wyatt), and a viscosimetric (VIS) detector (ViscoStar-II, Wyatt). Data analysis was performed with ASTRA Software (version 6.1) provided by Wyatt. THF was used as eluent at a flow rate of 1 mL min^{-1}. A value of dn/dc = 0.115 mLg^{-1} was used for copolymer $\mathbf{P_1}$ and derivatives thereof.

Dynamic Light Scattering (DLS): DLS measurements were carried out at r.t. on a Malvern Zetasizer Nano ZS apparatus, using high precision quartz cells, light path 10×10 mm, provided by Hellma Analytics. Data are given as by Number as an average of at least four measurements. All the solvents for sample preparation were filtered with 2 μM Teflon filters prior use.

UV-Vis Spectroscopy (UV-Vis): UV-Vis spectra were recorded at 25 °C in an Agilent 8453A apparatus with Peltier thermostatic cell holder, T-controller 89090A, using high precision quartz cells, light path 10×10 mm, provided by Hellma Analytics.

Photoluminescence (PL) Spectroscopy: PL spectra were recorded at r.t. on an Agilent Cary Eclipse spectrometer at an excitation wavelength of 365 nm, using high precision quartz cells, light path 10×10 mm, provided by Hellma Analytics. Samples were degassed by purging argon gas for 5 consecutive minutes before each measurement.

Photocatalytic Reactions, Irradiation Set-Up: Photoreactions were carried out using a Penn PhD Photoreactor, equipped with a 450 nm LED source, purchased from Merck. LED intensity was set at 100%, and a 4 mL vial-holder was used (10 cm light path to the reaction vessel and form the light source).

3.4.3. Synthesis and characterization of compounds

*3.4.3.1. Synthesis of the Polymeric Precursor Poly(OEGMA$_{300}$-co-AEMA) (**P$_1$**)*

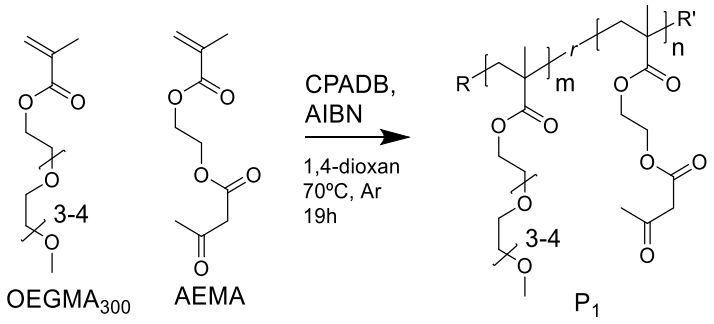

In an oven dried Schlenk flask equipped of a magnetic stir bar, 1.92 g (6.4 mmol) of OEGMA$_{300}$, 343 mg (1.6 mmol) of AEMA, 10.6 mg (38 µmol) of 4-cyano-4-(thiobenzoylthio)pentanoic acid (CPADB), 1.29 mg (7.7 µmol) of AIBN and 3.4 mL of 1,4-dioxane were added in this order. The flask was then sealed with a rubber septum and, after purging the solution with argon flow for 20 min., the reaction mixture was left stirring at 70ºC under argon atmosphere for 19 h. After this time, the reaction was quenched submerging the tube in liquid nitrogen. The crude was then precipitated in a large excess of *n*-hexane for three consecutive times, yielding the desired polymeric product **P$_1$**. M_w (kDa) = 169.8, PDI = 1.06, %AEMA (mol%) = 20, ^{1}H NMR (400 MHz, $CDCl_3$): **δ** (ppm) = 4.33 (m., CH_3COCH_2CO), 4.14 (m., $CH_2CO_2CH_2CH_2$), 4.07 (m., CH_2CO_2C), 3.65-3.54 (m., OCH_2CH_2O), 3.37 ($COCH_3$), 2.29 (s., CH_3COCH_2), 2.09-1.17 (m., CH_2CCH_3), 1.01-0.86 (m., CH_2CCH_3). ^{13}C NMR (100 MHz, $CDCl_3$): **δ** (ppm) = 30.42, 44.90, 45.26, 49.75, 59.12, 64.03, 68.58, 70.69, 72.05.

*3.4.3.2. Synthesis of the Hydroxo-Bridged Iridium(III) Dimer Tetrakis(2-phenylpyridinato-N,C2)(m-dihydroxy)diiridium(III) ([Ir(ppy)$_2$OH]$_2$) (**C$_1$**)*

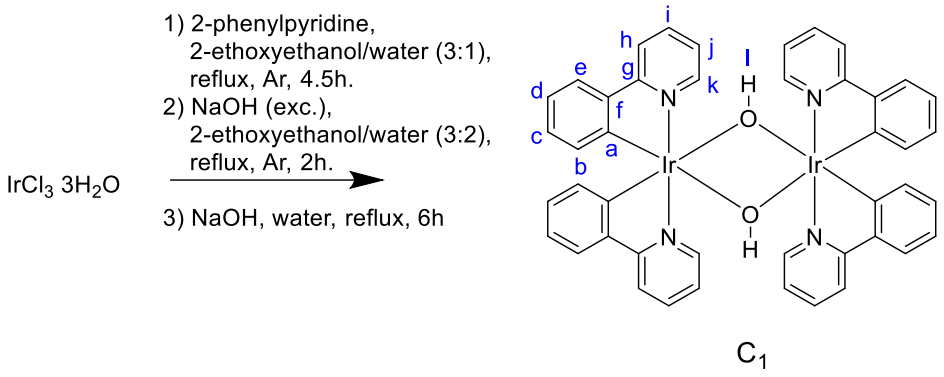

C$_1$

The dimeric complex **C$_1$** was synthesized according to a procedure reported in literature.[21] A mixture of 257 mg (0.73 mmol) of $IrCl_3$ $3H_2O$, 276 mg (1.71 mmol) of 2-phenyl-pyridine in 12 ml of a solution of 2-ethoxy-ethanol/water (3:1) was refluxed under argon for 4.5 h. After this time, an excess of NaOH (1.25 g, 30 mmol) dissolved in 12.5 mL of H_2O was added and the resulting mixture was left stirring under reflux for 2 h. After cooling to r.t., 25 mL of H_2O was added. An orange-brown precipitate was filtered off, dissolved in 15 mL methylene chloride and, subsequently, filtered. The filtrate was treated with a NaOH solution (1.68 g, 0.04 mol in 4.5 mL H_2O) at reflux for 6 h. Afterwards, the organic solvent (CH_2Cl_2) was evaporated, and H_2O (125 mL) was added. The crude product was filtered off and washed with *n*-pentane (10 mL) and diethyl ether (10 mL). Further purification was carried out by precipitation (CH_2Cl_2 solution) in *n*-pentane, yielding [Ir(ppy)$_2$OH]$_2$ (**C$_1$**) as a brown powder (295 mg, 78%). ^{1}H NMR (400 MHz, $CDCl_3$): δ (ppm) = 9.4-9.23 (m, 1H, H^k), 8.69-8.47 (m, 1H, H^h), 7.9-7.45 (m, 2H, $H^{e,i}$), 6.84-6.51 (m, 3H, $H^{c,d,j}$), 6.02-5.83 (m, 1H, H^b), –1.54 (s, 1H, H^l).

*3.4.3.3. Synthesis of the Cyclometalated Complex Bis[2-(2-pyridinyl-N)phenyl-C](methyl acetoacetato)iridium(III) (**C₂**)*

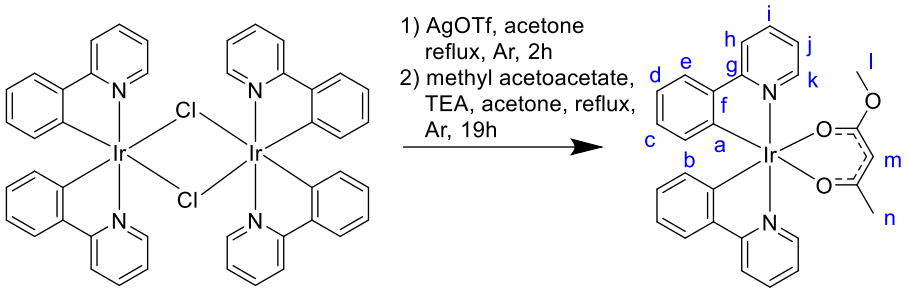

$[Ir(ppy)_2Cl]_2$ C_2

The complex **C₂** was synthesized as follows and according to a procedure for the preparation of the analogue bis[2-(2-pyridinyl-N)phenyl-C](acetylacetonato)iridium(III), which is well described in literature.[22] Specifically, 117.9 mg (0.11 mmol) of $[Ir(ppy)_2Cl]_2$ and 84 mg (0.32 mmol) AgOTf were dissolved, in this order, in 8 mL of degassed acetone and refluxed at 55ºC under nitrogen atmosphere and continuous stirring for 2 h. The solution was cooled to r.t. and filtered to remove AgCl. The filtrate was refluxed under nitrogen atmosphere for 1 h and added under inert atmosphere to a 1 h refluxed solution of methyl acetoacetate (46 µl, 0.43 mmol) and triethylamine (113 µl, 0.81 mmol) dissolved in degassed acetone (4 ml), The resulting bright-brown solution was refluxed overnight under nitrogen atmosphere. The crude was then cooled to r.t. and filtered on cotton to eliminate last residues of AgCl. The volatiles were removed and the solid was sonicated in deionized water and centrifuged for three consecutive times. The obtained solid was then dried under vacuum at r.t. for three days, affording the desired product **C₂**. Yield % (weight %): 85 %. ^{1}H NMR (400 MHz, $CDCl_3$): δ (ppm) = 8.64-8.53 (m, 2H, H^k), 7.90-7.84 (m, 2H, H^h), 7.79-7.73 (m, 2H, H^i), 7.58-7.53 (m, 2H, H^e), 7.21-7.15 (m, 2H, H^j), 6.86-6.80 (m, 2H, H^d), 6.73-6.86 (m, 2H, H^c), 6.29-6.25 (m, 2H, H^b), 4.72 (s, 1H, H^m), 3.40 (s, 3H, H^l), 1.83 (s, 3H, H^n). ^{13}C NMR (100 MHz, $CDCl_3$): δ (ppm) = 28.73, 46.67, 51.28, 83.19, 99.95, 118.10, 118.39, 119.18, 120.60, 120.69, 121.42, 121.52, 123.49, 123.87, 128.78, 132.92, 133.10, 136.75, 136.96, 148.62, 148.80, 168.73, 186.37.

*3.4.3.4. Synthesis of Iridium(III)-Decorated Copolymers at Different Iridium(III) Loadings (**P_1-Ir_{40}**, **P_1-Ir_{23}** and **P_1-Ir_{10}**)*

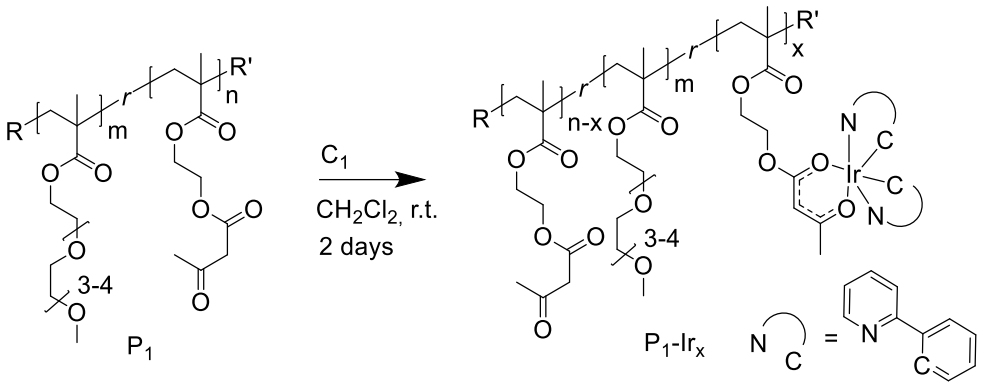

50 mg (0.707 mmol of AEMA) of polymer precursor **P_1** and 18.6 mg (17.7 µmol) of **C_1** were dissolved in 2 mL of anhydrous chloroform. The mixture was then degassed for 10 minutes and left stirring at r.t. under inert atmosphere and in the dark for 2 days. After this time, the crude was filtered and the volatiles were removed fluxing nitrogen, until a deep yellowish-brown film was obtained. **P_1-Ir_{40}**: Iridium(Ir)(III) loading, L^{Ir} (mol%) = 40, M_w (kDa) = 211.7, PDI = 1.03. **P_1-Ir_{23}** was obtained following the same procedure reported above, employing 50 mg of polymer precursor **P_1** and 9.3 mg (8.8 µmol) of **C_1**. **P_1-Ir_{23}**: L^{Ir} (mol%) = 23, M_w (kDa) = 174.5, PDI = 1.13. **P_1-Ir_{10}** was obtained following the same procedure reported above, employing 50 mg of polymer precursor **P_1** and 4 mg (3.8 µmol) of **C_1**. L^{Ir} (mol%) = 10, M_w (kDa) = 178.6, PDI = 1.10. ^{1}H NMR (400 MHz, $CDCl_3$) (**P_1-Ir_{40}**): δ (ppm) = 8.55-8.50 (m, 1 H), 7.84-7.75 (m, 1 H), 7.50 (m, 2H), 7.20 (m, 1 H), 6.77 (m, 1 H), 6.63 (m, 1 H), 6.19 (m, 1 H), 4.73 (m, 1 H), 4.31 (m., $CH_3COC\mathit{H}_2CO$), 4.13 (m., $CH_2CO_2C\mathit{H}_2CH_2$), 4.05 (m., $C\mathit{H}_2CO_2C$), 3.62-3.51 (m., $OC\mathit{H}_2C\mathit{H}_2O$), 3.34 ($COC\mathit{H}_3$), 2.27 (s., $C\mathit{H}_3COCH_2$), 2.09-1.78 (m., $C\mathit{H}_2CCH_3$), 0.99-0.85 (m., $C\mathit{H}_2CCH_3$). ^{13}C NMR (100 MHz, $CDCl_3$): **δ** (ppm) = 30.79, 45.46, 45.76, 50.30, 59.69, 64.60, 69.14, 71.25, 72.60.

*3.4.3.5. Preparation of Artificial Photo-Synthases based on Iridium(III)-Decorated Single Chain Nanoparticles in Aqueous Solutions (**APS-Ir$_{40}$**, **APS-Ir$_{23}$**, **APS-Ir$_{10}$**)*

As a general procedure, aqueous solutions of non-covalent, self-folded iridium(III) single chain nanoparticles at different metal loadings (**APS-Ir$_{40}$**, **APS-Ir$_{23}$**, **APS-Ir$_{10}$**) were obtained *via* direct dissolution of a film of the polymeric precursors (**P$_1$-Ir$_{40}$**, **P$_1$-Ir$_{23}$** and **P$_1$-Ir$_{10}$**) in water. In a typical procedure, 200 µL of a stock solution of iridium(III)-decorated copolymer (respectively **P$_1$-Ir$_{40}$**, **P$_1$-Ir$_{23}$** and **P$_1$-Ir$_{10}$**) in methylene chloride ([polymer] = 10 mg mL^{-1}) were left stirring at r.t. and in the dark for 2 h and until complete removal of the solvent, which was verified *via* gravimetry. The resulting deep-yellow polymeric film was then put in contact with a certain amount of deionized water to reach the desired final polymer concentration, and left stirring at r.t. overnight. After this time, the obtained transparent solutions were analyzed *via* DLS and UV-Vis spectrophotometry.

3.4.4. *"In Water"* [2+2] Photocycloaddition of Vinyl Arenes

General Procedure

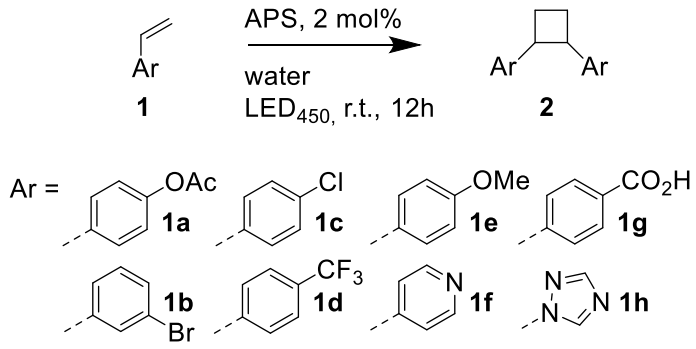

To a 4 mL oven dried vial, equipped of a magnetic stir bar, 100 µL of a stock solution of polymeric carrier **P_1-Ir_{40}** in methylene chloride ([polymer] = 20 mg mL^{-1}) was added. The polymer solution was then left stirring at r.t. and in the dark for 1 h, ensuring complete removal of the volatiles. Once a polymeric thin film was obtained, 1 mL of deionized water was added and the resulting mixture was then left stirring at r.t. and in the dark until a clear, pale-yellow solution was obtained. After adding 58 µmol of vinyl arene, the reaction was left open and stirring at r.t. and under LED illumination (λ_{max} = 450 nm) for 12 hours. After this time, 1 mL of saturated aqueous ammonium chloride was added to the mixture and the organic products were extracted by three consecutive times with 3 mL of diethyl ether each. The collected organic fractions were dried over anhydrous magnesium sulfate, filtered, and concentrated under reduced pressure. The extracted crude was then either purified via silica gel column chromatography to afford the title compound **2a** (*n*-hexane/ethyl acetate 10:1 to 1:1) or directly diluted with 0.6 mL of $CDCl_3$ for quantitative NMR analysis.

The compounds **2b**, **2c**, **2d**, **2e**, **2f**, were isolated by following the general procedure. The NMR interpretations of the extracted reaction crudes NMR spectra resulted consistent with expected products according to literature data.[3, 4, 5]

2a: Isolated yield (weight %) = 90 %. NMR conversion (mol%) = 96 %. Trans/cis ratio = 1:0.3. ^{1}H NMR (400 MHz, $CDCl_3$): δ (ppm) = 7.23-7.21 (d, 4H, CH_2CHCCH^{Ar}), 7.01-6.99 (d, 4H, $OCCH^{Ar}$), 6.93-6.90 (d, 0.66H, CH_2CHCCH^{Ar}), 6.83-6.81 (d, 0.66H, $OCCH^{Ar}$), 4.01-3.97 (m, 0.4H, CH_2CHC), 3.56-3.52 (m, 2H, CH_2CHC), 2.46-2.31 (m, 2.5H, CH_2CH_2), 2.29 (s, 6H, CH_3), 2.23 (s, 1H, CH_3), 2.11 (m, 2.2H, CH_2CH_2). ^{13}C NMR (100 MHz, $CDCl_3$): δ (ppm) = 21.29, 24.45, 26.14, 29.86, 44.85, 47.55, 120.88, 121.47, 128.96, 142.06, 149.08, 169.81.

2b: NMR conversion (mol%) = 97 %. Trans/cis ratio = 1:0.2. ^{1}H NMR (400 MHz, $CDCl_3$): δ (ppm) = 7.39-7.34 (m, 4H, $CHCBrCH$), 7.20-7.15 (m, 5H, $CHCHCC$ and *cis*-$CHCBrCH$), 7.13-83 (m, 1.1H, *cis*-$CCCHCH$), 4.02-3.98 (m, 0.7H, *cis*-$CHCC$), 3.57-3.50 (m, 2H, *trans*-$CHCC$), 2.52-2.30 (m, 3.4H, *cis*-CH_2CH_2 and *trans*-CH_2CH_2), 2.20.2.08 (m, 2H, *trans*-CH_2CH_2).

2c: NMR conversion (mol%) = 96 %. Trans/cis ratio = 1:0.3. ^{1}H NMR (400 MHz, $CDCl_3$): δ (ppm) = 7.29-7.27 (m, 4H, $CHCCl$), 7.16-7.14 (m, 2H, $ClCCHCH$), 7.11-7.09 (m, 1.2H, *cis*-$CHCCl$), 6.88-6.86 (m, 1.2H, *cis*-$ClCCHCH$), 4.01-3.97 (m, 0.6H, *cis*-$CCHCH_2$), 3.53-3.45 (m, 2H, *trans*-$CCHCH_2$), 2.54-2.28 (m, 3.3H, CH_2CH_2), 2.17-2.07 (m, 2H, CH_2CH_2).

2d: NMR conversion (mol%) = 90 %. Trans/cis ratio = 1:0.3. ^{1}H NMR (400 MHz, $CDCl_3$): δ (ppm) = 7.57-7.55 (m, 4H, *trans*-F_3CCCH), 7.36-7.30 (m, 5.2H, *cis*-F_3CCCH and *trans*-$CH^{Ar}CC$), 7.03-7.01 (m, 1.2H, *cis*-$CH^{Ar}CC$), 4.13-4.09 (m, 0.7H, *cis*-$CCHCH_2$), 3.67-3.59 (m, 2H, *trans*-$CCHCH_2$), 2.60-2.43 (m, 3.6H, CH_2CH_2), 2.42-2.14 (m, 2H, CH_2CH_2).

2e: NMR conversion (mol%) = 60 %. Trans/cis ratio = 1:0.3. ^{1}H NMR (400 MHz, $CDCl_3$): δ (ppm) = 7.17-7.15 (m, 4H, *trans*-$MeOCHCH$), 7.04-7.02 (m, 1.6H, *cis*-$MeOCHCH$), 6.93-6.91 (m, 1.6H, *cis*-$MeOCH$), 6.86-6.84 (m, 4H, *trans*-$MeOCH$), 3.92 (s, 2.1H, *cis*-OCH_3), 3.80 (s, 6H, *trans*-OCH_3), 3.46 (m, 2H, *trans*-$CCHCH_2$), 2.47-2.22 (m, 3.4H, CH_2CH_2), 2.14-2.03 (m, 3H, CH_2CH_2).

2f: NMR conversion (mol%) = 79 %. Trans/cis ratio = 1:0.3. ^{1}H NMR (400 MHz, $CDCl_3$): δ (ppm) = 8.55-8.53 (m, 4H, *trans*-NCH), 8.35-8.33 (m, 1.8H, *cis*-

NC*H*), 7.15-7.13 (m, 4H, *trans*-NCHC*H*), 6.88-6.87 (m, 18H, *cis*-NCHC*H*), 4.06 (m, 1H, cis-CC*H*CH_2), 3.59 (m, 1H, *trans*-CC*H*CH_2), 2.59-2.44 (m, 2.30H, *cis*-CH_2CH_2), 2.41 (m, 2H, *trans*-CH_2CH_2), 2.22 (m, 2H, *trans*-CH_2CH_2).

3.4.5. *"In Water"* Oxidation of 9-Substituted Anthracenes

General Procedure

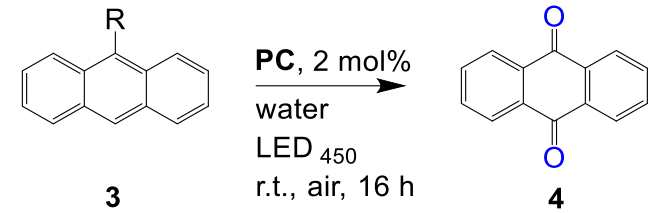

3 **4**

R = CH_2OH (**3a**), CH_2Cl (**3b**)

*Photocatalytic SCNPs-Mediated oxygenation of anthracenes in Water, general procedure (**OA-1**).* To a 4 mL oven dried vial, equipped of a magnetic stir bar, was added 100 µL of a stock solution of polymeric carrier **P_1-Ir_{40}** in methylene chloride ([polymer] = 20 mg/mL). The polymer solution was then added of 29 µmol of **3** and the resulting mixture was then left stirring at r.t. and in the dark for 2 hours and until all the volatiles were removed. After adding 1 mL of deionized water, the reaction was left open and stirring at r.t. and under LED illumination (λ_{max} = 450 nm) for 16 hours. After this time, the mixture was added of 1 mL of saturated aqueous ammonium chloride and extracted three consecutive times with 3 mL of ethyl acetate each. The collected organic fractions were dried over anhydrous magnesium sulfate, filtered, and concentrated under reduced pressure. The extracted crude was then either purified via silica gel column chromatography to afford the title compound **4** (n-hexane/ethyl acetate 2:1) or directly diluted with 0.6 mL of $CDCl_3$ for quantitative NMR analysis. Spectral data agree with literature data.[6,7,8] Isolated yield (weight %) = 58 %. Conversion NMR (mol%) = 62 %. ^{1}H NMR (400 MHz, $CDCl_3$): **δ** (ppm) = 8.35-8.31 (m, 4H, OCCCH^{Ar}), 7.83-7.79 (m, 4H, CCCH^{Ar}). ^{13}C NMR (100 MHz, $CDCl_3$): **δ** (ppm) = 127.39, 134.28

3.4.6. *"In Water"* α-Arylation of Arylamines

General Procedure

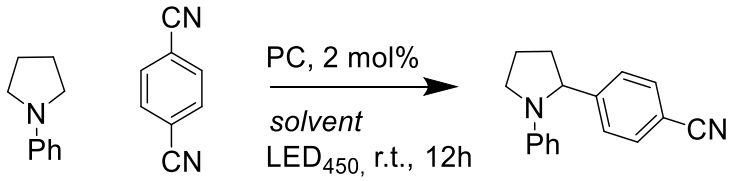

5 **6** **7**

(AA-5). To a 4 mL oven dried vial, equipped of a magnetic stir bar, was added 100 µL of a stock solution of polymeric carrier **P_1-Ir_{40}** in methylene chloride ([polymer] = 20 mg/mL). The polymer solution was then added of 3.7 mg (29 µmol) of 1,4-dicyanobenzene and 203 mg (2.47 mmol) of sodium acetate. The resulting mixture was then left stirring at r.t. and in the dark for two hours and until all the volatiles were removed, the vial was then sealed with a rubber septum. After three consecutive vacuum-evacuation/Argon backfill cycles, 1 mL of extensively degassed deionized water and 12.5 µL (87 µmol) of N-phenyl pyrrolidine were added under Argon positive pressure. The resulting mixture was left stirring at r.t. and under LED illumination (λ_{max} = 450 nm) for 12 hours. After this time, the mixture was extracted three times with 6 mL of ethyl acetate each. The collected organic fractions were dried over anhydrous magnesium sulfate, filtered, and concentrated under reduced pressure. The extracted crude was then either purified *via* silica gel column chromatography to afford the title compound **7** (n-hexane/ethyl acetate 10:1 to 2:1) or directly diluted with 6.5 mL of $CDCl_3$ for quantitative NMR analysis. Isolated yield (weight %) = 48 %. Conversion NMR (mol%) = 57 %. ^{1}H NMR (400 MHz, $CDCl_3$): **δ** (ppm) = 7.59 (2H, d., H^{Ar}), 7.34 (2H, d., H^{Ar}), 7.15 (2H, t., H^{Ar}), 6.68 (1H, t., H^{Ar}), 6.44 (2H, d., H^{Ar}), 4.74 (1H, d., NC*H*), 3.73 (1H, m., NCH_2), 3.43 (1H, m., NCH_2), 2.47-2.39 (1H, m., CHCH_2), 2.03-1.88 (3H, m., CHCH_2CH_2). ^{13}C NMR (100 MHz, $CDCl_3$): **δ** (ppm) = 23.29, 29.86, 36.03, 49.38, 62.93, 110.75, 112.58, 116.65, 119.12, 126.90, 129.29, 132.60, 146.84, 150.62 In agreement with literature data.[9, 10, 11]

AA-4 and **AA-10** were carried out according to the general procedure varying the salt amount in the reaction mixture, using 70 mg (58 µmol) or 1.2 g (14.6 mmol) of

NaOAc respectively. **AA-9** was carried out following the general procedure, using 1 mL of binary solution water/DMA (DMA 10%) as solvent.

*α-Arylation of N-Arylamines in Water. Non-supported catalyst procedure (**AA-8**).* To a 4 mL oven dried vial, equipped of a magnetic stir bar, was added 0.36 mg (0.58 µmol) of $\mathbf{C_2}$, 3.7 mg (29 µmol) of 1,4-dicyanobenzene and 203 mg (2.47 mmol) of sodium acetate. The vial was then sealed with a rubber septum. After three consecutive vacuum-evacuation/Argon backfill cycles, 1 mL of extensively degassed deionized water and 12.5 µL (87 µmol) of N-phenyl pyrrolidine were added under Argon positive pressure. The resulting mixture was left stirring at r.t. and under LED illumination (λ_{max} = 450 nm) for 12 hours. After this time, the mixture was extracted three times with 6 mL of ethyl acetate each. The collected organic fractions were dried over anhydrous magnesium sulfate, filtered, and concentrated under reduced pressure. The extracted crude was then diluted with 6.5 mL of $CDCl_3$ for quantitative NMR analysis. No conversion to the desired product was observed.

*α-Arylation of N-Arylamines in Water. Procedure in organic solvents (**AA-1, AA-2, AA-3**).* An oven-dried 15 mL vial equipped with a rubber septum and a magnetic stir bar was charged with 0.5% mol of photocatalyst (3.08 mg of $\mathbf{C_2}$ for **AA-1** and **AA-3**, 50 µL of 20 $mgmL^{-1}$ $\mathbf{P_1\text{-}Ir_{40}}$ stock solution in methylene chloride for **AA-2**), 128.1 mg (1 mmol) of 1,4-dicyanobenzene and 164,1 mg (2 mmol) of NaOAc. The Schlenk was then purged with 3 consecutive vacuum evacuation/argon backfill. Then, 4 mL of degassed solvent (DMA for **AA-1**, **AA-2**, MeOH for **AA-3**) was added under positive nitrogen pressure followed by 434 µL (3 mmol) of N-phenylpirrolidine. The reaction mixture was furtherly degassed via three cycles of vacuum evacuation/argon backfill. After degassing, the vial was sealed with parafilm and left under LED illumination (λ_{max} = 450 nm) for 12 hours. After this time, the reaction was then diluted with ethyl acetate and added to a separatory funnel containing 25 mL of a saturated Na_2CO_3 aqueous solution. The layers were separated, and the aqueous layer was extracted with EtOAc. The collected organic fractions were dried over anhydrous magnesium sulfate, filtered, and concentrated under reduced pressure. The extracted crude was then

purified *via* silica gel column chromatography to afford the title compound **7** (*n*-hexane/ethyl acetate 10:1 to 2:1).

3.4.7. *"In water"* β-Hydroxysulfonylation of *α*-Methyl Styrene

General Procedure

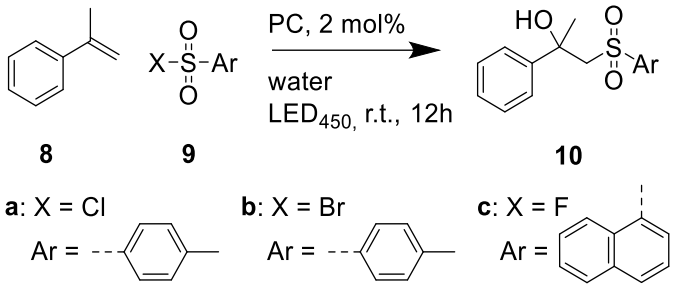

200 µL of a stock solution of polymeric carrier **P_1-Ir_{23}** in methylene chloride ([polymer] = 20 mg/mL) and 9 mg (35 µmol) of tosyl chloride were put in an oven dried 4 mL vial, previously equipped with a magnetic stir bar. After complete removal of the volatiles, the vial was sealed with a rubber septum and the resulting polymeric film was degassed via three consecutive vacuum-pump/Argon-backfill cycles. 1 mL of extensively degassed deionized water and 3.4 mg (29 µmol) of α-methyl styrene were then added under Argon positive pressure. The resulting solution was left stirring at r.t. and under LED light (λ_{max} = 450 nm) irradiation for 12 hours. After this time, the crude was extracted three times with 6 mL of ethyl acetate each. The collected organic fractions were dried over anhydrous magnesium sulfate, filtered, and concentrated under reduced pressure. After solvent removal, the crude product was either purified by column chromatography on silica gel (n-hexane/ethyl acetate 4:1) to afford the title compound **10a** or added of a known amount of 1,4-dicyanobenzene and diluted with 0.6 mL of $CDCl_3$ for quantitative ^{1}HNMR analysis. Isolated yield (weight %) = 58 %. Conversion NMR (mol%) = 67 %. ^{1}H NMR (400 MHz, $CDCl_3$): **δ** (ppm) = 7.49 (d, 2H), 7.29 – 7.27 (m, 2H), 7.18 (td, 5H), 4.63 (br.s., 1H), 3.71 – 3.57 (m, 2H), 2.39 (s, 3H), 1.71 (s, 3H). ^{13}C NMR (100 MHz, $CDCl_3$): **δ** (ppm) = 21.73, 29.85, 60.54, 62.31, 121.88, 126.38, 128.08, 128.51, 128.84, 129.65, 136.76, 142.43.

HS-1 was carried out according to the general procedure, using 100 µL of **P_1-Ir_{40}** stock solution in methylene chloride ([polymer] = 20 mg/mL). **HS-3** was carried

out according to the general procedure, using 400 µL of **P_1-Ir_{10}** stock solution in methylene chloride ([polymer] = 20 mg/mL). **HS-4** was carried out following the general procedure using 8.2 mg (35 µmol) of paratoluensulfonyl bromide in substitution of the tosyl chloride. **HS-5** was carried out following the general procedure using 7.4 mg (35 µmol) of 2-naphtalenesulfonyl fluoride in substitution of tosyl chloride.

*β-Hydroxysulfonylation of Aromatic Alkenes. Non-supported catalyst procedure (**HS-6**).* To a 4 mL oven dried vial, equipped of a magnetic stir bar, was added 0.36 mg (0.58 µmol) of **C_2**, 9 mg (35 µmol) of tosyl chloride were put in an oven dried 4 mL vial, previously equipped with a magnetic stir bar. After complete removal of the volatiles, the vial was sealed with a rubber septum and the resulting polymeric film was degassed via three consecutive vacuum-pump/Argon-backfill cycles. 1 mL of extensively degassed deionized water and 3.4 mg (29 µmol) of α-methyl styrene were then added under Argon positive pressure. The resulting solution was left stirring at r.t. and under LED light (λ_{max} = 450 nm) irradiation for 12 hours. After this time, the crude was extracted three times with 6 mL of ethyl acetate each. The collected organic fractions were dried over anhydrous magnesium sulfate, filtered, and concentrated under reduced pressure. After solvent removal, the crude product was added of a known amount of 1,4-dicyanobenzene and diluted with 0.6 mL of $CDCl_3$ for quantitative ^{1}HNMR analysis.

HS-7 was carried out following the general procedure and without adding any photocatalyst. No conversion to the desired product was observed.

3.5. Conclusions

In summary, artificial photosynthases (APS) arise by endowing enzyme-mimetic single-chain nanoparticles, SCNPs, with broad visible-light photocatalytic activity for challenging “in water” organic reactions. We introduce a first generation of APS resulting from the decoration of an amphiphilic high-molecular-weight copolymer, poly- (OEGMA$_{300}$-*r*-AEMA), with iridium(III) cyclometalated complex pendants followed by its own self-assembly in water. APS enabled efficient visible-light photocatalysis of a variety of organic transformations in an aqueous solution at room temperature and under LED illumination (λ_{max} = 450 nm). This work broadens the possibilities for performing challenging “in water” organic transformations via APS-mediated visible-light photocatalysis.

3.6. References

(1) Emmanuel, M. A.; Bender, S. G.; Bilodeau, C.; Carceller, J. M.; DeHovitz, J. S.; Fu H.; Liu, Y.; Nicholls B. T.; Ouyang, Y.; Page, C. G.; Qiao, T.; Raps, F. C.; Sorigué, D. R.,; Sun, S.-Z.; Turek-Herman, J.; Ye, Y.; Rivas-Suchet, A.; Cao, J.; Hyster, T. K. Photobiocatalytic strategies for organic synthesis. *Chem. Rev.* **2023**, *123*, 5459-5520.

(2) Alphand, V.; Van Berkel, W. J. H.; Jurkaš, V.; Kara, S.; Kourist, R.; Kroutil, W.; Mascia, F.; Nowaczyk, M. M.; Paul, C. E.; Schmidt, S.; Spasic, J.; Tamagnini, P.; Winkler, C. K. Exciting enzymes: Current state and future perspective of photobiocatalysis. *ChemPhotoChem* **2023**, *7*, e202200325.

(3) Sancar, A. Structure and function of DNA photolyase. *Biochemistry* **1994**, *33*, 2-9.

(4) Trimble, S. J; Crawshaw, R; Hardy, F. J.; Levy, C. W.; Brown, M. J. B; Fuerst, D. E.; Heyes, D. J.; Obexer, R.; Green, A. P. A designed photoenzyme for enantioselective [2+2] cycloadditions. *Nature* **2022**, *611*, 709-714.

(5) Jeong, W. J.; Lee, J.; Eom, H.; Song, W. J. A specific guide for metalloenzyme designers: introduction and evolution of metal-coordination spheres embedded in protein environments. *Acc. Chem. Res.* **2023**, *56*, 2416-2425.

(6) Fu, Y.; Huang, J.; Wu, Y.; Liu, X.; Zhong, F.; Wang, J. Biocatalytic cross-coupling of aryl halides with a genetically engineered photosensitizer artificial dehalogenase. *J. Am. Chem. Soc.* **2021**, *143*, 617-622.

(7) Russo, C.; Brunelli, F.; Tron, C. G.; Giustiniano, M. Visible-light photoredox catalysis in water. *J. Org. Chem.* **2023**, *88*, 6284-6293.

(8) Sun, K.; Lv, Q.-Y.; Chen, X.-L.; Qu, L.-B., Yu, B. Recent advances in visible-light-mediated organic transformations in water. *Green Chem.* **2021**, *23*, 232-248.

(9) Hong, D.; Shi, L.; Liu, X.; Ya, H.; Han, X. Photocatalysis in water-soluble supramolecular metal organic complex. *Molecules* **2023**, *28*, 4068.

(10) Bottecchia, C.; Noël, T. Photocatalytic modification of amino acids, peptides and proteins. *Chem. Eur. J.* **2019**, *25*, 26-42.

(11) Bu, M.-J.; Cai, C.; Gallou, F.; Lipshutz, B. H. PQS-enabled visible-light iridium photoredox catalysis in water at room temperature. *Green Chem.* **2018**, *20*, 1233-1237.

(12) Mundsinger K.; Tuten B. T.; Wang, L.; Neubaner, K.; Kropf, C.; O'Mara, M. L.; Barner-Kowollik, C. Visible-light-reactive single-chain nanoparticles. *Angew. Chem. Int. Ed.* **2023**, *62*, e202302995.

(13) Pomposo, J. Single-chain polymer nanoparticles: synthesis, characterization, and applications. *Wiley-VSH* **2017**, 978-3-527-80638-6.

(14) Rothfuss, H.; Knöfel, N. D.; Roesky, P. W.; Barner-Kowollik, C. Single-chain nanoparticles as catalytic nanoreactors. *J. Am. Chem. Soc.* **2018**, *140*, 5875-5881.

(15) Rubio-Cervilla, J.; González, E.; Pomposo, J. A. Advances in single chain nanoparticles for catalysis applications. *Nanomaterials* **2017**, *7*, 341.

(16) Verde-Sesto, E.; Arbe, A.; Moreno, A. J.; Cangialosi, D.; Alegría, A.; Colmenero, J.; Pomposo, J. A. Single-chain nanoparticles: ooportunities provided by internal and external confinement. *Mater. Horiz.* **2020**, *7*, 2292-2313.

(17) Xiong, T. M.; Garcia, E. S.; Chen, J.; Zhu, L.; Alzona, A. J.; Zimmermann, S. C. Enzyme-like catalysis by single chain nanoparticles that use transition metal cofactors *Chem. Commun.* **2022**, *58*, 985-988.

(18) Mundsinger, K.; Izuagbe, A.; Tuten, B. T.; Roesky, P. W.; Barner-Kowollik, C. Single chain nanoparticles in catalysis. *Angew. Chem. Int. Ed.* **2023**, e202311734.

(19) Chen, R.; Berda, E. 100th annyversary of macromolecular science viewpoint: re-examining single-chain nanoparticles. *ACS Macro Lett.* **2020**, *9*, 1836-1843.

(20) Spicuzza, M.; Gaikwad, S. P.; Huss, S.; Lee, A.; Craescu, C. V.; Griggs, A.; Joseph, J.; Puthenpurayil, M.; Lin, W.; Matarazzo, C.; Baldwin, S.; Perez, V.; Rodriguez-Acevedo, D. A.; Swierk, J. R.; Elaqua E. Visible-Light-Mediated Diels-Alder Reactions Under Single-Chain Polymer Confinement: Investigating the Role of the Crosslinking Moiety on Catalyst Activity. *ChemRxiv*, **2023**, 10.26434/chemrxiv-2023-zwvsq-v2.

(21) Ulbricht, C.; Becer, C. R.; Winter, A.; Schubert, U. S. RAFT polymerization meets coordination chemistry: synthesis of a polymer-based iridium(III) emitter. *Macromol. Rapid Commun.* **2010**, *31*, 827-833.

(22) Beyer, B.; Ulbricht, C.; Winter, A.; Hager, M. D.; Hoogenboom, R.; Herzer, N.; Baumann, S. O.; Kickelbick, G.; Görls, H.; Schubert, U. S. Unexpected metal-mediated oxidation of hydroxymethyl groups to coordinated carboxylate groups by bis-cyclometalated iridium(III) centers. *New J. Chem.* **2010**, *34*, 2622-2633.

(23) Pomposo, J. A.; Colmenero, J.; Kohlbrecher, J.; Arbe, A.; Sanchez-Sanchez, A. Efficient synthesis of single-chain globules mimicking the morphology and polymerase activity of metalloenzymes. *Macromol. Rapid Commun.* **2015**, *36*, 1592-1597.

(24) Robles-Hernandez, B.; González, E.; Pomposo, J. A.; Colmenero, J.; Alegría, A. Water dynamics and self-assembly of single-chain nanoparticles in concentrated solutions. *Soft Matter* **2020**, *16*, 9738-9745.

(25) Chen, Z.; Jiang, J.; Zhao, Q.; An aggregation-induced phosphorescent emission-active iridium(III) complex for fluoride anion imaging in living cells. J. *Organomet. Chem.* **2021**, *932*, 1211644.

(26) Di, L.; Xing, Y.; Yang, Z.; Qiao, C.; Xia, Z. Sens. Photostable aggregation-induced emission of iridium(III) complex realizing robust and high-resolution imaging of latent fingerprints. *Actuators B Chem.* **2023**, *375*, 132898.

(27) Twilton, J.; Le, C.; Zhang, P.; Shaw, M. H.; Evans, R. W; MacMillan, D. W. C. The merger of transition metals and photocatalysis. *Nat. Rev. Chem.* **2017**, *1*, 0052.

(28) Strieth-Kalthoff, F.; James, J J.; Teders, M.; Pitzer, L.; Glorius, F, Energy transfer catalysis mediated by visible light: principles, applications, directions. *Chem. Soc. Rev.* **2018**, *47*, 7190-7202.

(29) Shon, J.-H.; Kim, D.; Rathnayake, M. D.; Sittel, S.; Weaver, J.; Teets, T. S. Photoredox catalysis on unactivated substrates with strongly reducing iridium photosensitizers. *Chem. Sci.* **2021**, *12*, 4069-4078.

(30) a) Poplata, S.; Tröster, A.; Zou, Y.-Q.; Bach, T. Recent advances in the synthesis of cyclobutanes by olefin [2+2] photocycloaddition reactions. *Chem. Rev.* **2016**, *116*, 9748-9815. b) Du, J.; Yoon, T. P. Crossed intermolecular [2+] cycloadditions of acyclic enones via visible light photocatalysis. *Chem. Soc.* **2009**, *131*, 14604-14605. c) Pagire, S. K.; Hossain, A.; Traub, L.; Kerres, S.; Reiser, O. Photosensitized regioselective [2+2]-cycloaddition of cynnamates and related alkenes. *Chem. Commun.* **2017**, *53*, 12072-12075. d) Zhao, J.; Brosmer, J. L.; Tang, Q.; Yang, Z.; Houk, K. N.; Diaconescu, P. L.; Kwon, O. Intramolecular crossed [2+2] photocycloaddition thorugh visible light-induced energy transfer. *J. Am. Chem. Soc.* **2017**, *139*, 9807-9810. e) Lu, Z.; Yoon, T. P. Visible light photocatalysis of [2+2] styrene cycloadditions by energy transfer. *Angew. Chem., Int. Ed.* **2012**, *51*, 10329-10332. f) Tanaka, K.; Iwama, Y.; Kishimoto, M.; Ohtsuka, N.; Hoshino, Y.; Honda, K. Redox potential controlled selective oxidation of styrenes for regio- and stereoselective crossed intermolecular [2+2] cycloaddition via organophotoredox catalysis. *Org. Lett.* **2020**, *22*, 5207-5211.

(31) Roth, H. G.; Romero, N. A.; Nicewicz, D. A.; Experimental and calculated electrochemical potentials of common organic molecules for applications to single-electron redox chemistry. *Synlett* **2015**, *27*, 714-723.

(32) Prier, C. K.; Rankic, D. A.; McMillan, D. W. C. Visible light photoredox catalysis with transition metal complexes: applications in organic synthesis. *Chem. Rev.* **2013**, *113*, 5322-5363.

(33) Eady, S. C.; Maclness, M. M.; Lehnert, N. Immobilized cobalt bis(benzenedithiolate) complexes: exceptionally active heterogeneous electrocatalysts for dihydrogen production from mildly acidic aqueous solutions. *Inorg. Chem.* **2017**, *56*, 11565-11576.

(34) Montalti, M.; Credi, A.; Prodi, L.; Gandolfi, M. T.; Handbook of photochemistry. *Taylor & Francis Group, LCC* **2006**, 9780429115387.

(35) a) Kawajiri, T.; Kato, M.; Nakata, H.; Goto, R.; Aibara, S.; Ohta, R.; Fujioka, H.; Sajiki, H.; Sawama, Y. Aromatic aldehydes and acetals via pyridinium salt intermediates. *J. Org. Chem.* **2019**, 84, 3853-3870. b) Christensen, S. H.; Olsen, E. P. K.; Rosenbaum, J.; Madsen, R. Hydroformylation of olefins and reductive carbonylation of aryl halydes with syngas formed ex situ from dehydrogenative decarbonylation of hexane-1,6-diol. *Org. Biomol. Chem.* **2015**, 13, 938-945. c) Despras, G.; Zamaleeva, A. I.; Dardevet, L.; Tisseyre, C.; Magalhaes, J. G.; Garner, C.; De Waard M.; Amigorena, S.; Feltz, A.; Mallet, J.-M.; Collot, M. H-Rubies, a new family of red emitting fluorescent pH sensors for living cells. *Chem. Sci.* **2015**, 6, 5928-5937. d) Shmidt, B.; Elizarov, N.; Berger, R.; Hölter, F. Scope and limitation of the Heck-Matsuda-coupling of phenol diazonium salts and styrenes: a protecting-group economic synthesis of phenolic stilbenes. *Org. Biomol. Chem.* **2013**, 11, 3674-3691. e) Hussain, M. I.; Feng, Y.; Hu, L.; Deng, Q.; Zhang, X.; Xiong, Y. Copper-catalyzed oxidative difunctionalization of terminal unactivated alkenes. *J. Org. Chem.* **2018**, 83, 7852-7859. f) Murphy-Benenato, K. E.; Olivier, N.; Choy, A.; Ross, P. L.; Miller, M. D.; Thresher, J.; Gao, N.; Hale, M. R. Synthesis, structure, and SAR of tetrahydropyran-based LpxC inhibitors. *ACS Med. Chem. Lett.*, **2014**, 5, 1213-1218.

(36) a) Naik, A.; Meina, L.; Zabel, M.; Reiser, O. Efficient aerobic Wacker oxidation of styrenes using palladium bis(isonitrile) catalysts. *Chem. Eur. J.* **2010**, 16, 1624-1628. b) Daw, P.; Petakamsetty, R.; Sarbajna, A.; Laha, S.; Ramapanicker, R.; Bera, J. K. A highly efficient catalyst for selective oxidative scission of olefins to aldehydes: abnormal-NHC-Ru(II) complex in oxidation chemistry. *J. Am. Chem. Soc.* **2014**, 136, 40, 13987-13990. c) Xu, J.; Zhang, Y.; Yue, X.; Huo, J.; Xiong, D.; Zhang, P. Selective oxidation of alkenes to carbonyls under mild conditions. *Green Chem.* **2021**, 23, 5549-5555.

(37) a) Gao, R.; Ho, D. G.; Hernandez, B.; Selke, M.; Murphy, D.; Djurovich, P. I.; Thompson, M. E. Bis-cyclometalated Ir(III) complexes as efficient singlet oxygen sensitizers. *J. Am. Chem. Soc.* **2002**, 124, 14828-14829. b) Xu, Y.; Wang, X.; Song, K.; Du, J.; Liu, J.; Miao, Y.; Li, Y. BSA-encapsulated cyclometalated iridium complexes as nano-photosensitizers for photodynamic therapy of tumor cells. *RSC Adv.* **2021**, 11, 15323-15331. c) Jiang, X.; Peng, J.; Wang, J.; Guo, X.; Zhao, D.; Ma, Y. Iridium-based high-sensitivity oxygen sensors and photosensitizers with ultralong triplet lifetimes. *ACS Appl. Mater. Interfaces* **2016**, 8, 3591–3600. d) Ashen-Garry, D.; Selke, M. Singlet oxygen generation by cyclometalated complexes and applications. *Photochem Photobiol.* **2014**, 90, 257–274. e) McKenzie, L. K.; Sazanovich, I. V.; Baggaley, E.; Bonneau, M.; Guerchais, V.; Williams, J. A. G.; Weinstein, J. A.; Bryant, H. E. Metal complexes for two-photon photodynamic therapy: a cyclometalated iridium complex induces two-photon photosensitization of cancer cells under near-IR light. *Chem. Eur. J.* **2017**, 23, 234-238. f) Xu, Y.; Wang, X.; Song, K.; Du, J.; Liu, J.; Miao, Y.; Li, Y. BSA-encapsulated cyclometalated iridium complexes as nano-photosensitizers for photodynamic therapy of tumor cells. *RSC Adv*. **2021**, 11, 15323-15331. g) Maggioni, D.; Galli, M.; D'Alfonso, L.; Inverso, D.; Dozzi, M. V.; Sironi, L.; Iannacone, M.; Collini, M.; Ferruti, P.; Ranucci, E.; D'Alfonso, G. A luminescent poly(amidoamine)-iridium complex as new singlet-oxygen sensitizer for photodynamic therapy. *Inorg. Chem.* **2015**, 54, 544-553. h) Qin, W.-W.; Pan, Z.-Y.; Cai, D.-H.; Li, Y.; He, L. Cyclometalated iridium(III)-complexes for mitochondria-targeted combined chemo-photodynamic therapy. *Dalton Trans.* **2020**, 49, 3562. i) Zamora, A.; Vigueras, G.; Rodríguez, V.; Santana, M. D.; Ruiz, J. Cyclometalated iridium(III) luminescent complexes in therapy and phototherapy. *Coord. Chem. Rev.* **2018**, 360, 34-76.

(38) a) Zhao, J.-L.; Jiang, X.-K.; Wu, C.; Wang, C.-Z.; Zeng, X.; Redshaw, C.; Yamato, T. An unprecedented photochemical reaction for anthracene-containing derivatives. *ChemPhysChem* **2016**, 17, 3217-3222. b) Jacob, J. P.; Gopalakrishnan, R.; Mallia, R. R.; Vadakkan, J. J.; Unnikrishan, P. A.; Prathapan, S. Dramatic solvent and concentration dependence in the reaction of (anthracen-9-yl)methanamines with suitable electron-deficient acetylenes. *Phys. Org. Chem.* **2014**, 27, 884-891. c)Adam, W.; Prein, M. Diastereoselective [4+2] cycloaddition of synglet oxygen in the photooxygenation of chiral naphthyl alcohols: evidence for a hydroxy group-directing effect. *J. Am. Chem. Soc.* **1993**, 115, 3766-3767. d) Mondal, S.; Mondal, S.; Midya, S. P.; Das, S.; Mondal, S.; Ghosh, P. Merging photocatalytic C-O cross-coupling for α-oxycarbonyl-β-ketones: esterification of carboxylic acids via a decarboxylative pathway. *Org. Lett.* **2023**, 25, 184-189.

(39) a) Natarajan, P.; Vagicherla, V. D.; Vijayan, M. T.; A mild oxidation of deactivated naphthalenes and anthracenes to corresponding para-quinones by N-bromosuccinimide. *Tetrahedron Lett.* **2014**, 55, 3511-3515. b) Pankhurst, J. R.; Curcio,

M.; Sproules, S.; Lloyd-Jones, G. C.; Love, J. B. Earth-abundant mixed-metal catalysts for hydrocarbon oxygenation. *Inorg. Chem.* **2018**, 57, 5915-5298. c) Chatani, N.; Kamitani, A.; Oshita, M.; Fukumoto, Y.; Murai, S. Catalytic carbonylation reactions of benzene derivatives. *J. Am. Chem. Soc*. **2001**, 123, 12686-12687. d) Majumdar, B.; Bhattacharya, T.; Sarma, T. K. Gold nanoparticle-polydopamine-reduced graphene oxide ternary nanocomposite as efficient catalyst for selective oxidation of benzylic C(sp^3)-H bonds under mild conditions. *ChemCatChem* **2016**, 70, 8, 1825-1835. e) Dong, C.-P.; Higashiura, Y.; Marui, K.; Kumazawa, S.; Nomoto, A.; Ueshima, M.; Ogawa, A. Metal-free oxidative coupling of benzylamines to imines under an oxygen atmosphere promoted using salicylic acid derivatives as organocatalysts. *ACS Omega* **2019**, 4, 17934-17938.

(40) McNally, A.; Prier, C. K.; MacMillan, D. W. C. Discovery of an α-amino C-H arylation reaction using the strategy of accelerated serendipity. *Science* **2011**, 334, 1114-1117.

(41) Prier, C. K.; MacMillen, D. W. C.; Amine α-heteroarylation via photoredox catalysis: a homolytic aromatic substitution pathway. *Chem. Sci.* **2014**, 5, 4173-4178.

(42) a) Zhang, X.; Yeh, S.-R.; Hong, S.; Freccero, M.; Albini, A.; Falvey, D. E.; Mariano, P. S. Dynamics of .alpha.-CH deprotonation and .alpha.-desilylation reactions of tertiary amine cation radicals. *J. Am. Chem Soc.* **1994**, 116, 4211-4220. b) Yoon, U. C.; Mariano, P. S. Mechanistic and synthetic aspects of amine-enone single electron transfer photochemistry. *Acc. Chem. Res.* **1992**, 25, 233-240. c) Eckert, F.; Leito, I.; Kaljurand, I.; Kütt, A.; Klamt, A.; Diedenhofen, M. Prediction of acidity in acetonitrile solution with COSMO-RS. *J. Comp. Chem.* ***2009***, 30, 799-810.

4. Chapter IV

4.1. Introduction

Photodynamic therapy (PDT) is now a well-recognized treatment of cancer, even though it is still too often described as emerging. The first photosensitizers were approved decades ago,[1-2] but had several drawbacks in terms of characterization, tumor targeting and efficiency. Second generation-photosensitizers have since been approved or are in advanced clinical trials.[3-5] Using excitation wavelengths within the first phototherapeutic window (600-1000 nm) for PDT is advantageous for two reasons: first, it avoids exciting endogenous chromophores,[6] and second, it allows deeper light penetration into biological tissues.[7] Phthalocyanines are synthetic tetrapyrrolic molecules of the porphyrinoid family and show typically an average maximum absorption at 700 nm. In this respect, phthalocyanines are excellent photosensitizer molecular bases for anti-cancer PDT.[8-11] Many water-soluble phthalocyanines with cationic, anionic or neutral substituents have been used for PDT.[12] However, they are frequently aggregated, which is a constraint for their efficiency. Besides, excessive water-solubility of photosensitizers may be detrimental since it induces a rapid clearance from the body without having the chance to accumulate in the targeted tissues, and / or prevents cellular internalization by limiting the cellular membrane crossing. The use of hydrophobic photosensitizers overcomes these issues, but a significant drawback is that they are not biocompatible as they cannot circulate in the bloodstream. This promoted the use of various nanocarriers, either by encapsulation or by covalent grafting of the hydrophobic photosensitizer.[13] An additional advantage is that nano-formulated photosensitizers can benefit from the enhanced permeability and retention (EPR) effect, which may have some limitations[14] but is anyway a good way to deliver photosensitizers. A liposomal formulation of unsubstituted zinc

phthalocyanine has entered advanced clinical trials,[15] and several micellar formulations of phthalocyanine derivatives for PDT applications have been reported.[16-17] Conjugating a mono-hydroxylated phthalocyanine to poly-L-glutamic acid allowed to obtain polymeric nanoparticles of high efficiency,[18-19] and phthalocyanine-based organo-silica nanoparticles exhibited remarkable photodynamic efficiency.[20-21] It has been shown that the nature of the polymeric nanocarrier can greatly affect the photodynamic efficiency of a nano-photosensitizing system.[22]

Self-assembled nanocarriers such as single-chain nanoparticles (SCNPs) have proven to be efficient carriers for the delivery of hydrophobic drugs.[23-25] These works are relatively recent. Indeed, only a handful of tetrapyrrolic derivatives combined with SCNPs have been reported: a porphyrin has been grafted onto the skeleton of individual SCNPs;[26] phthalonitriles (which are the most common precursor of phthalocyanines) have been introduced on a polystyrene backbone, the subsequent intramolecular formation of the phthalocyanine moiety leading to the formation of colored single-chain polymeric nanoparticles;[27] and the axial coordination of a polymeric chain containing pyridine moieties by a cobalt phthalocyanine produced CO_2-reducing materials.[28]

Based on Nature exclusive capability of merging single-chain (protein) technology and photocatalysis, in the present Chapter, we report the preparation of an amphiphilic SCNPs of improved efficiency for PDT of cancer applications. By means of the non-covalent encapsulation of a Zn(II)-phthalocyanine within the hydrophobic, self-assembled, anthracene-based core of an amphiphilic SCNP, this novel class of compounds, which we called Artificial Photo Oxidases (**APO**), enabled high-efficiency PDT effect, both in vitro and in zebrafish xenografts models for human cancer, employing far-red excitation wavelengths.

4.1.1. Photodynamic Therapy

The use of light in treating pathological conditions of the human body counts with an almost 3500-years old history. Ancient civilizations are known to have

employed sunlight as medicament for skin illnesses as vitiligo and psoriasis, but also against mental disordes as psychosis.[29-31] The term heliotherapy has been, indeed, coined by the ancient Greek philosopher Herodotus, and was originally referred to the administration of sunlight for strengthening human body and as an agent for the restoration of health.[29] As often happens in medicinal chemistry, is of little surprise that some of the seminal works conducted at the beginning of the XX century involving light as curing agents were, in fact, inspired by the same preparations reported to be effective already in ancient times. *E.g*. the compound 8-methoxypsoralen, which can be considered one of the first molecules to be tested as effective treatment of severe psoriasis was, notably, identified and isolated in 1947 from the vegetal extract of a weed found in the Nile river, namely the Ammi maius L., a preparation already known and used by ancient Egyptians for the same purposes.[30] Nevertheless, first substantial scientific contributions to the field started to emerge only by the beginning of the past century, initiated by the studies of Oscar Raab on the lethal effect of light on infusoria in presence of the photosensitizer acridine[32] and with the works of the Nobel laureate Niels Finsen in the employment of light for treating pathological skin conditions, namely the *phototherapy*.[30] In the same years, several physicians reported independently the inflammatory effects occurring upon exposure to sunlight on skin of patients previously treated with oral eosin. The term photodynamic action itself was already reported by the end of 1903 by von Tappeneimer and A. Jesionek, which observed beneficial effects in skin cancer development in patients treated with topic eosin and subsequently exposed to white household light.[33] In Figure 4.1, a chronological list of milestone reports in the field of phototherapy and photodynamic therapy is illustrated.

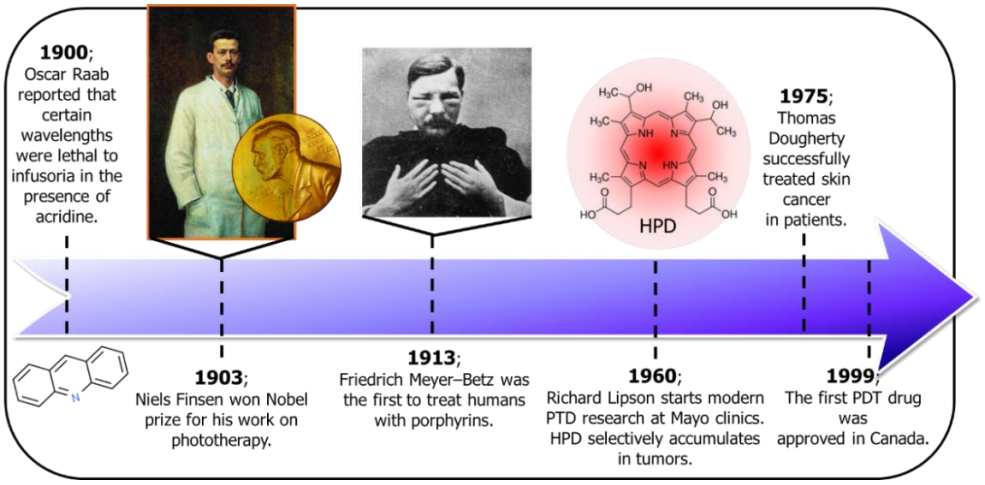

Figure 4.1. Milestones in the development of phototherapy and photodynamic therapy over the past century.[32-35]

The experiment reported by Meyer-Betz is worth mentioning, being far more than a scientific curiosity, he applied on his own skin 200 mg of hematoporphyrin and documented the extended inflammation response upon exposure to sunlight (in Figure 4.1, the picture of Friedrich Meyer-Betz captured after having a walk) is the first document describing the effects of a porphyrin system in humans: porphyrins are now the more extensively studied photosensitizers for PDT applications. These seminal and fundamental observations paved the way to what is now a consolidated field of research and, in a non-irrelevant number of cases, an approved medical treatment for a variety of malignant solid tumors.

Phototherapy is the use of light in the treatment of a disease, while photodynamic therapy (PDT), which can be considered as a specific photochemotherapy, involves a combination of the administration of a photosensitizer and the use of light to treat a certain pathological condition. More specifically, PDT can be defined as: *a therapeutic modality, which involves two individually non-toxic component (a photosensitizer and light) that are combined to induce cellular and tissue effect in an oxygen-dependent manner*.[34] PDT involved the administration, usually either oral, or topic, or intravenous, of a photosensitizer (PS) molecule, which is

biodistributed according to the biology of the organism under study and can, or not, selectively accumulate in organs of interest for the treatment. After the PS being absorbed, the application of light induces the promotion of PS ground state to its excited states and, as for every photocatalytic process, longer-living excited states (usually the triplets) induces oxidative stress within the cellule in which the PS have been internalized. This latter can be the resultant of the direct reaction of PS excited states with a substrate important for cell survival (type-I reactions), generating reactive radicals which can produce oxygenated products upon reaction with cellular oxygen. Alternatively, PS triplet state can directly react with cellular oxygen, forming singlet oxygen and reactive oxygen species (ROS), which are then capable to induce high oxidative stress in the cell, finally degenerating into cell apoptosis (type-II reactions). In Figure 4.2, the substantial different mechanistic pathways with which PDT can actuate in the cellular medium are illustrated. The proportion of these two types of reaction taking place relies on the properties of the specific PS used, in all cases, PDT is an oxygen-dependent process whose fundamental principles rely on photocatalysis in the biological, still aqueous, environment.

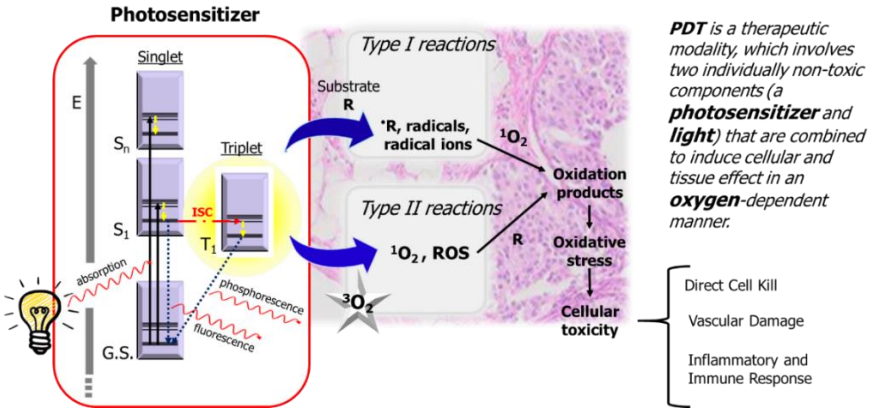

Figure 4.2. Pictorial representation of the basic principles of PDT.[34, 36, 37]

4.1.2. Traditional Photosensitizers for PDT

Ideal photosensitizers for PDT should possess a good lipophilic balance, to simultaneously ensure efficient biodistribution and accumulation in the tumoral tissues,

as well as high light absorption coefficients, preferably at as-long-as-possible wavelengths, high ISC efficiencies, negligible dark cytotoxicity and low photobleaching. At the date, different PS have been deeply investigated and widely used for therapeutic applications, and can be classified in three subgroups, or generations. Porphyrins like hematoporphyrin, whose chemical structure is shown in Figure 4.3, are first-generation photosensitizers and are traditionally natural occurring substance with high quantum yields to produce ROS.[38]

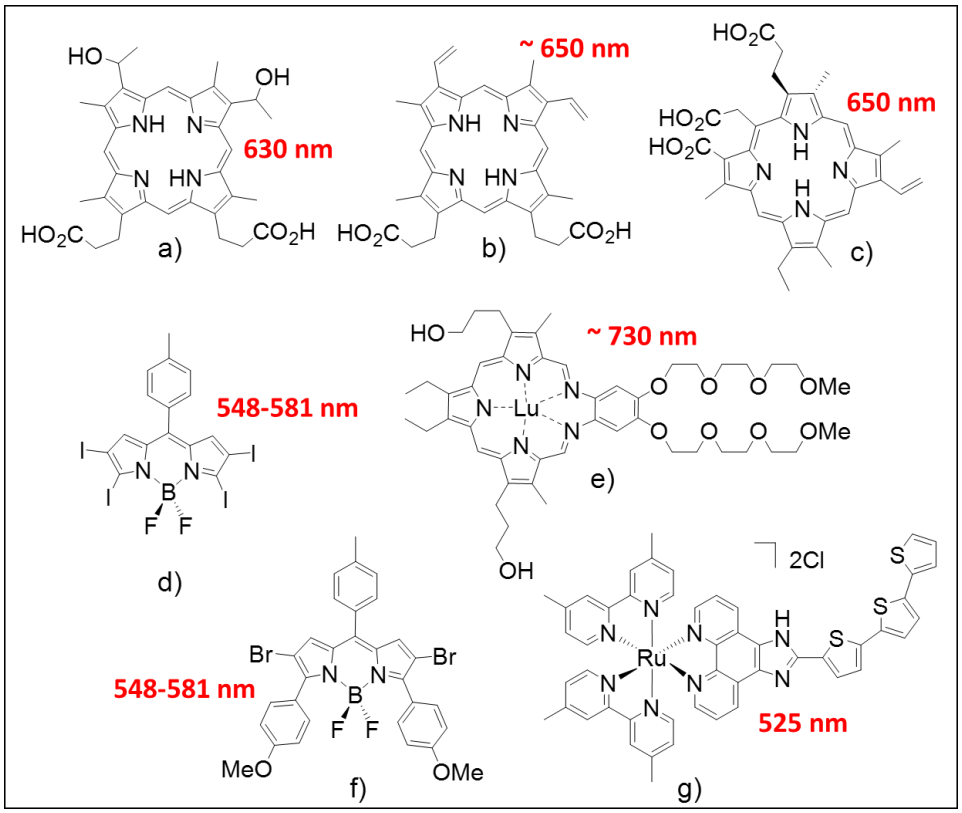

Figure 4.3. Structures of commonly employed molecular architectures for first and second-generation photosensitizer for PDT with their respective wavelength of activation. **a**) hematoporphyrin, **b**) protoporphyrin IX, **c**) chlorin e6, **d**) iodine-substituted BODIPY, **e**) Lu-texaphyrin,[39] **f**) modified aza-BODIPY, g) $Ru[(dmb)_2(IP\text{-}3T)]Cl_2$ (TLD1433).[40]

Hematoporphyrins and their analogues have been extensively reported as effective PDT agents since the very first reports on the field, however, with their

extended polycyclic aromatic structure low solubility in water usually is of central concern.[40] Second-generation PS are commonly substances designed to overcome these major issues, as for chlorin e6 and protoporphyrin IX and Lu-texaphyrin (shown in Figure 4.3), the basic structure of first-generation photosensitizers were modified to improve critical features like solubility in water, wavelength of absorbance and enhance ROS generation quantum efficiency. Completely novel molecular structures as variously functionalized 4,4-difluoro-4-bora-3a,4a-diaza-s-indacenes (BODIPYs) as well as water-soluble cyclometalated transition-metal complexes (Figure 4.3) can be classified as second-generation catalyst. In particular, BODIPY appeared to be an interesting molecular structure for their low photobleaching degrees, higher stability in biological environment, low dark-toxicity and high light absorption coefficients, however, due to the high luminescence they usually present low singlet oxygen generation quantum yields. Regarding cyclometalated transition-metal complexes, they commonly present ROS efficiency of comparable entity than that of phthalocyanine and porphyritic systems and, helped by the rich chemistry of their electronic excited states, usually manifest high phototoxcitities.[40,41] For these reasons, they have been of particular interest as systems that can enable PDT in hypoxic condition and at low oxygen tension tissues, as in the case of TLD1433, the ruthenium(II) polypyridyl complex $Ru[(dmb)_2(IP\text{-}3T)]Cl_2$ (Figure 4.3) being the first organometallic to reach human clinical trials, which exploits long-living triplet states for either singlet-oxygen sensitization and to initiate intracellular cytotoxic radical pathways.[40]

4.1.3. Nanostructures in PDT

As a general aspect, the induction of effective and selective destruction of damaged and cancerous cells while forbearing the surrounding healthy tissues is of pivotal importance for PDT. Despite the promising results and progress registered over the last century, PDT is currently an approved clinical solution only for very specific cases of tumors, which generally must be superficial and flat, or accessible with endoscopes to ensure good illumination of the affected region. PDT is not applicable to highly diffused, metastatic tumors, as is not possible to illuminate the entire body of

a patient with the technology we currently dispose of. The same can be said for solid, deep-seated tumors, in which light penetration, and so PSs activation, is of major constraint.[42] Selectivity for cancer tissue is usually achieved by taking advantage of the abnormal physiology of this latter, which commonly present either higher vascularization, poor lymphatic drainage or decreased pH, all features which can be exploited for designing smarter PSs capable of selective accumulation within the tumor. In this sense, the use of nanoparticles for PDT efficiency improvement is a particularly promising approach for several reasons. An important benefit arising from the use of a nanostructure for PSs delivery for PDT is given by the possibility of inducing enhanced permeability and retention (EPR) effect. Altered vascularization of tumoral tissue normally results in abnormal internalization of circulating species in the blood systems of the affected organisms and, when the size of the nanostructures employed for the drug delivery is appropriately selected, this abnormal physiology can lead to selective accumulation of the bigger *objects* within the tumor (retention).[43] This way, the use of nano-sized objects has been exploited to move a step forward a more selective PDT, permitting a more site-specific accumulation of the photoactive species, furtherly improving the cellular uptake, biodistribution, pharmacokinetics and minimizing the unwanted side effects arising from scarcely selective accumulation.[44] Other benefits of using nanoparticles in PDT include, large surface-to-volume ratios, which always corresponds to enhanced efficacy of the delivered species in the target cells, the premature delivery of the PSs is also prevented, with this being especially true when a non-biodegradable, inert nanoparticle is used as a passive carrier and, not less importantly, nanoparticles can be prepared in a variety of fashions, topologies, dimensions and with the possibility of almost inexhaustible ways of chemical functionalization for improving biodistribution and PSs performance.[42-45] Concerning inorganic-based systems, gold nanoparticles (AuNPs) have demonstrated to be employable as effective passive PSs nanocarriers for PDT-applications. Apart from being usually stable, hard systems which present optimal biocompatibility, with this explaining its wide use in nanomedicine more in general, AuNPs can be easily functionalized either covalently or *non*-covalently *via* the easily accessible metallic gold-thiolate chemistry. In Figure 4.4 are shown two examples of the different

approaches which can be followed for incorporating a PS into AuNPs, which can be either covalent, as reported by Russel *et al*. in the functionalization of PEGylated AuNPs with zinc(II)-phthalocyanine containing thiolate moieties,[24] or *non*-covalently, exploiting strong ionic interactions between opposite charged NPs and PS, as reported by Pérez-García *et al.* in the preparation of positively charged, water-soluble AuNPs loaded with anionic porphyrins.[46]

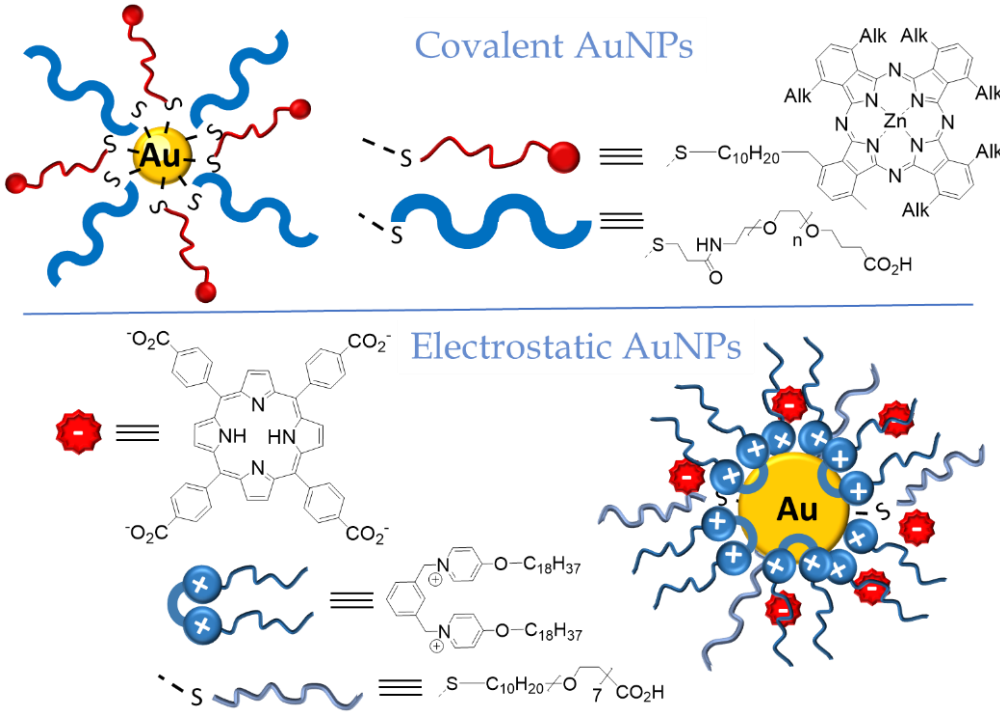

Figure 4.4. Illustration of two exemplificative strategies towards PDT-active AuNPs. On top, covalent functionalization of the surface of metallic gold nanoparticles with hydrophilic PEG-based pendants and thiolate-bearing zinc(III)phthalocyanine.[47] On the bottom, the water-soluble photoactive AuNPs system assembled via coulombic forces between pyridinium species and anionic porphyrins.[46]

Analogously, nanostructured silica also offers a plethora of possibilities in terms of its application in nanomedicine. Its derivative nanostructures are well-known for their biocompatibility and the possibility of subsequent functionalization, as well for the usually high colloidal stability of the final product. Silica-based nanoparticles

have already been applied for the fabrication of PDT-active materials, as PSs can be incorporated into mesoporous silica nanoparticles, or used for chemical modification of silica nano-objects and, notably, silica can be used to coat pre-existing nanoparticles, thanks to the possibility of layer-by-layer deposition.[48,49] Amongst the different opportunities provided by inorganic-based materials, iron oxide nanoparticles (IONPs) are worth mentioning, due to the possibility offered by the application of local magnetic fields, either static for directing to the desired site of action or alternating for inducing magnetic hyperthermia, IONPs gained special attention in nanomedicine in recent times[50,51] and, for what concerns PDT, they have already been demonstrated to expand the possibilities of multi-directed approaches (coupling PDT with magnetic induced hyperthermia) when included with PSs in liposomes and cell-mimicking structures.[52]

Nanoparticles can often guarantee augmented PSs solubilization in the complex, aqueous medium of the biological systems. *E.g.*, the use of polymeric micelles to carry strongly hydrophobic PSs by means of their *non*-covalent encapsulation within the amphiphilic nanoparticles and / or covalent anchoring into the hydrophobic core have been demonstrated in several applications, including Pluronic, PEG-based lipids, pH-responsive Poly(N-isopropyl acrylamide) (PNIPAM)-based micelles and poly-ion complex micelles, to cite a few.[53] As a general behavior, the micellar core is responsible for the drug-carrying capability of these polymeric nano-vectors, since a variety of hydrophobic drugs can be incorporated into the core by non-covalent interactions. For this reason, PS are usually incorporated into polymeric micelles through hydrophobic interactions with the segment that forms the micellar core, by means of physical entrapment. PS can also be carried through covalent bonds between functional groups of the PS and pendent group of hydrophobic segments of the polymeric scaffold used for the supramolecular assembly formation. It is worth mentioning that the stability of the physical trapping of the PS depends on the magnitude of the hydrophobic interactions between the PS and the hydrophobic part of the copolymer.[54]

Amongst all the possibilities offered by the construction of nano-objects of controlled structure and shape, single-chain polymeric nanoparticles (polymeric

SCNPs) provide an interesting scaffold for medicinal chemistry. Thanks to their defined shape, tunable morphology resembling the one of enzymes and naturally occurring proteins, as well as the ease of functionalization, good water-solubility, and ultra-small dimensions (2-20 nm), SCNPs already have been proved to be efficient nanocarriers for drug-delivery applications and imaging. Due to the by-definition unimolecular character, SCNPs are usually more dilution-resistant than micelles and liposomes, whose major constraint is indeed coalescence in the bloodstream often leading to PS aggregation, which is usually detrimental to the pharmacokinetics and PSs efficacy over time. Also due to their ultra-reduced dimensions, SCNPs are usually highly compatible with the intracellular space.[55,56] In addition, the collapse/folding of individual polymeric chains allows the formation of individual pockets in which the photoactive units can be isolated from themselves, which is generally associated with the enhancement of their optical properties, hence resulting in augmentation of ROS generation in the biological media. In a seminal, recent work reported by Meijer *et al*. the use of a novel class of porphyrin-containing, water-soluble SCNPs is proposed as innovative scaffold for aqueous photosensitizations.[57] The authors developed the photoactive single-chain nanocarrier by means of a post-polymerization functionalization of an ultra-high molecular weight polymeric precursor Poly(pentafluoro styrene), while let reacting specific amount of the porphyrin-based photosensitizer and Jeffamine, conferring water-solubility to the final product.

The readily prepared photoactive polymer resulted to self-assemble in aqueous environment into the collapsed/folded unimolecular structure were then evaluated for their feasibility in aqueous photosensitization by means of a spectrophotometric investigation, both in the UV-Vis range for the determination porphyrin aggregation-extent and infra-red (IR) emission spectroscopy for singlet-oxygen generation ability estimation.[57] In a later work, Liu *et al.* developed analogous SCPNs-based systems bearing photocatalytic porphyrins, which were successfully introduced into the lysosomal region of HeLa cells *via* endocytosis.[58] Interestingly, the authors reported no significant changes in the emission spectra of the porphyrins upon cell internalization, indicating minimal aggregation or modification of the functional unit. The porphyrin based SCPN induced significant cell death after irradiating the cells with $\lambda^{exc}_{max} = 403$

nm light, which agrees with their ability to generate cytotoxic $^1O_2$ singlet oxygen. The remarkable singlet-oxygen capability of the PS-loaded SCNP, in comparison to the free-porphyrin system, could not only be due to an augmented stabilization in water of the PS, but also to the fact that SCNPs possess a compact but rather open and flexible structure, allowing to the reactants (triplet molecular oxygen) and the products (ROS) to diffuse easily in and out the nanoparticles. To summarize, with a photoactive, porphyrin-containing SCNPs being evaluated for PDT-effect in a proper biological system, although these pioneering works demonstrate that the inclusion of a hydrophobic, highly aggregating PDT-suitable photosensitizer within the architecture of a water-soluble SCNP constitute a valid strategy for ROS-generating dyes for therapeutic applications, still a lot of effort have to be put for revealing the hidden potential of photocatalytic SCNPs to be exploited as efficient, last generation PDT-nanodrugs.

4.2. Objectives

When planning an encapsulation strategy, supramolecular approaches constitute a valid option towards the formulation of more performative PSs. The types of aggregates arising from different noncovalent interactions can confer to materials intriguing photochemical properties, very different from the single constituents taken alone.[59] In Nature, photocatalytic processes are enabled in water by aminoacidic single-chain nanoparticles, which we call proteins, whose precise folding allows the stabilization and efficient functioning of photosensitizing molecules in the chemically complex, aqueous, biological media. As it happens for the most abundant photocatalyzed reaction on Earth, the chlorophyll-based photosynthesis, the careful assemble of proteins and pigments (often hydrophobic molecules) is required for the catalytic process to take place. *E.g.*, higher plants photosystem I (PSI) is composed, amongst others, by the unique assembly of four different light-harvesting proteins (LHCI), which welcome and enclose in their folded structure a total of 165 chlorophylls and 5 additional electron-carrying cofactors as phylloquinones and Fe-S clusters, as reported in the structure shown in Figure 4.5.[60,61]

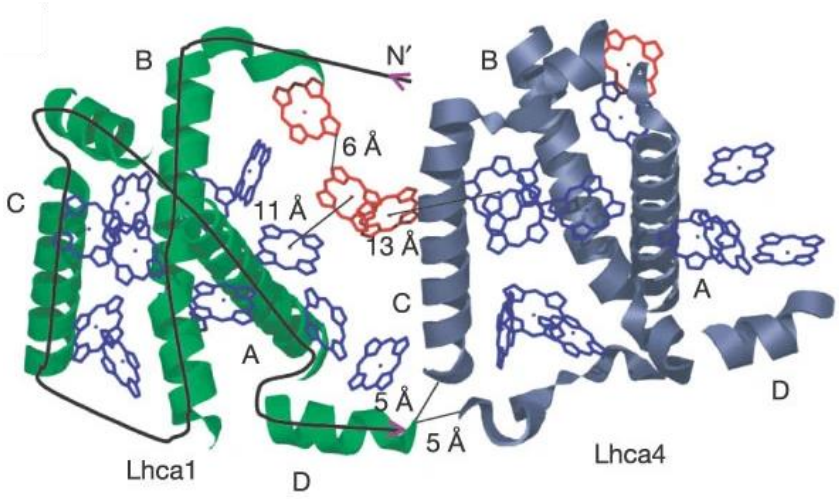

Figure 4.5. Crystal structures o part of the constitutive units of the PSI from Pisum Sativum. Specifically, the contact region of Lhca1 (green) and Lhca4 (grey) is shown. The magenta solid line follows schematically the backbone of the proteinic single-chain unit Lhca1. Enclosed chlorophylls are depicted in blue if bound to LHCA monomers, in red when present a linker function.[60]

Due to the extended electron delocalization in the tetrapyrrolic structure, it is worth noting that phthalocyanines are capable of specifically interact through π-π interactions with the aromatic ring systems of proteins, to the point that have been reported to be able of modulation of unwanted amyloid aggregation of proteins.[62] Organic chromophores like anthracene, perylene *etc.* are, in fact, knowingly prone to aggregation and, although their properties in the condensed state are difficult to predict and control, several strategies to tune their assembly are often desirable when thinking on advanced application of their optoelectronic functionalities. The use of metal organic frameworks,[63,64] co-assembly with biomacromolecules,[65] and host-guest encapsulation,[66] are some of the possible approaches toward the design of tunable-aggregation of phthalocyanine PSs-based materials.

The present work aimed at the rational design and preparation of improved amphiphilic single-chain polymer nanoparticles (SCNP) for imaging and photodynamic therapy (PDT) in zebrafish embryo xenografts. As described in the previous chapters, SCNPs are ultra-small polymeric nanoparticles with sizes similar to

proteins, making them ideal for biomedical applications. Amphiphilic SCNPs result from the self-assembly in water of isolated synthetic polymeric chains through intrachain hydrophobic interactions, mimicking natural biomacromolecules and, specially, proteins (in size and when loaded with drugs, metal ions or fluorophores also in function). Initial in vitro experiments with non-functionalized, amphiphilic SCNPs loaded with a substituted zinc phthalocyanine (zinc-1,8,15,22-tetrakis(isobutylthio)phthalocyanine, Zn**Pc**) showed promise for PDT. Herein, we disclose the preparation of improved, protein-mimetic SCNPs containing **ZnPc** as highly efficient photosensitizer encapsulated within the nanoparticle and surrounded by anthracene moieties. The amount of anthracene units and **ZnPc** molecules within each single-chain nanoparticle controls the imaging and PDT properties of these nanocarriers. Critically, based on polycyclic aromatic moieties self-aggregation capability, this work opens the way to improved PDT applications based on amphiphilic SCNPs (Figure 4.6).

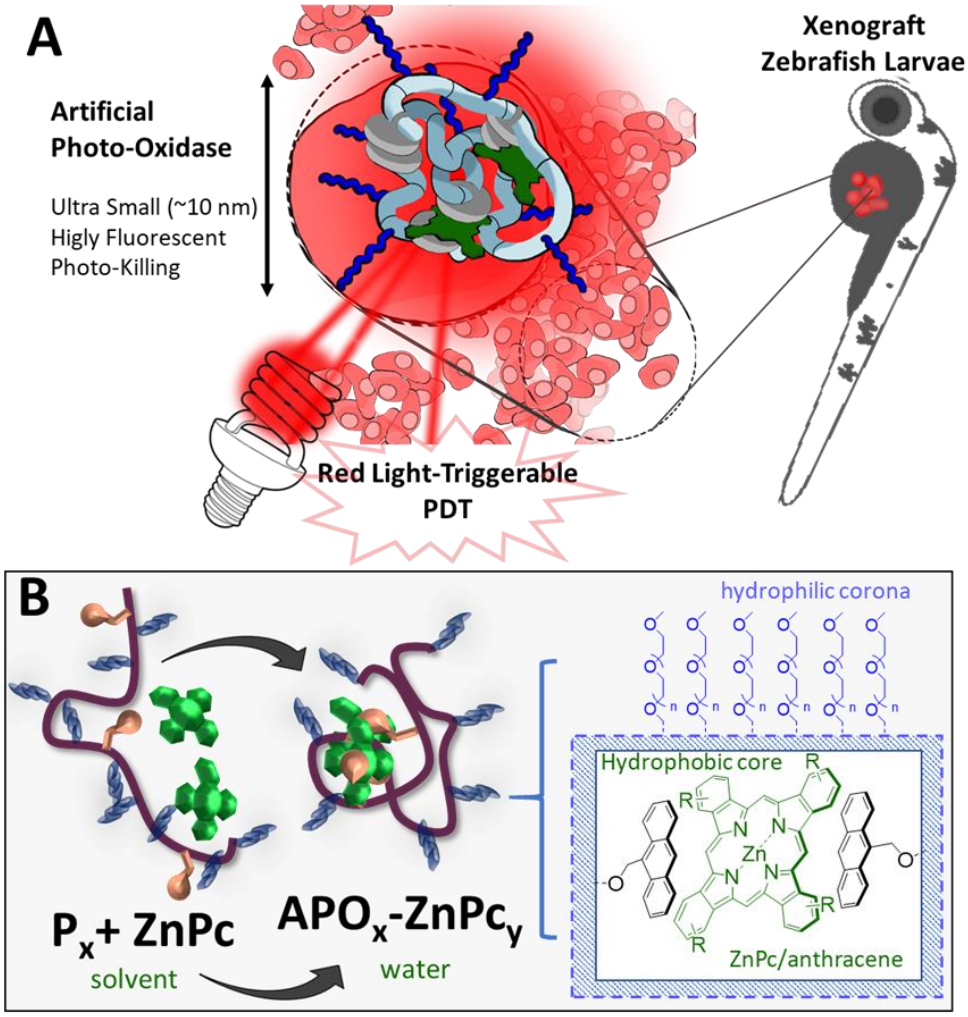

Figure 4.6. a) Ideal, long-term Artificial Photo-Oxidases endowed with excellent imaging and far-red photo-killing properties for photodynamic therapy (PDT) in Zebrafish embryo xenografts. b) Rational design of amphiphilic SCNPs containing zinc-1,8,15,22-tetrakis(isobutylthio)phthalocyanine (**Pc**) surrounded by anthracene (**P_x** = amphiphilic polymer precursor containing a defined amount of anthracene moieties; **APO_x-Pc_y** = SCNP prepared from **P_x** containing a defined amount of **Pc** encapsulated within the nanoparticle).

4.3. Results and Discussion

4.3.1. Preparation of π-π self-assembled amphiphilic SCNPs containing Zn(II)-phthalocyanine Pc

4.3.1.1. Preparation of the nanocarriers

Figure 4.7 shows the self-folding in water of an amphiphilic polymer precursor $\mathbf{P_x}$ composed of hydrophobic anthracene methacrylate (AnMA) and hydrophilic oligo(ethylene glycolmonomethyl ether) methacrylate ($OEGMA_{300}$) units. The formation of non-covalent, reversible, and self-assembled SCNPs is possible in water for amphiphilic copolymeric precursors in the appropriate range of molecular weights, hydrophilic / hydrophobic monomer ratio and dilution regimes.[67,68]

Firstly, we synthesized three well-defined poly($OEGMA_{300}$-*stat*-AnMA) random copolymers containing 31, 16 and 8 mol% of anthracene units that we denoted as $\mathbf{P_1}$, $\mathbf{P_2}$ and $\mathbf{P_3}$, respectively (Figure 4.7a). The *quasi*-randomness of the copolymers synthesized in this study was proved by measuring the incorporation rates of the two monomers used in the reaction conditions selected for the preparation of $\mathbf{P_x}$ as described follows: 177 mg (0.64 mmol) of AnMA, 450 mg (1.5 mmol) of $OEGMA_{300}$, 1.51 mg (5.4 µmol) of CPADB, 0.34 mg (2.1 µmol) of AIBN and 1.07 mL of 1,4-dioxane were added to a dark, oven-dried vial, equipped of a magnetic stir bar. After purging the mixture with an argon flow for 10 min, the vial was sealed with a rubber septum, and the reaction was left stirring at 70ºC and under inert atmosphere for 19 h. A 100 µL aliquot of crude was taken each hour and over the course of the first five hours, which were analyzed via SEC (Figure 4.7b) and ^{1}H NMR (See Appendix to Chapter IV).

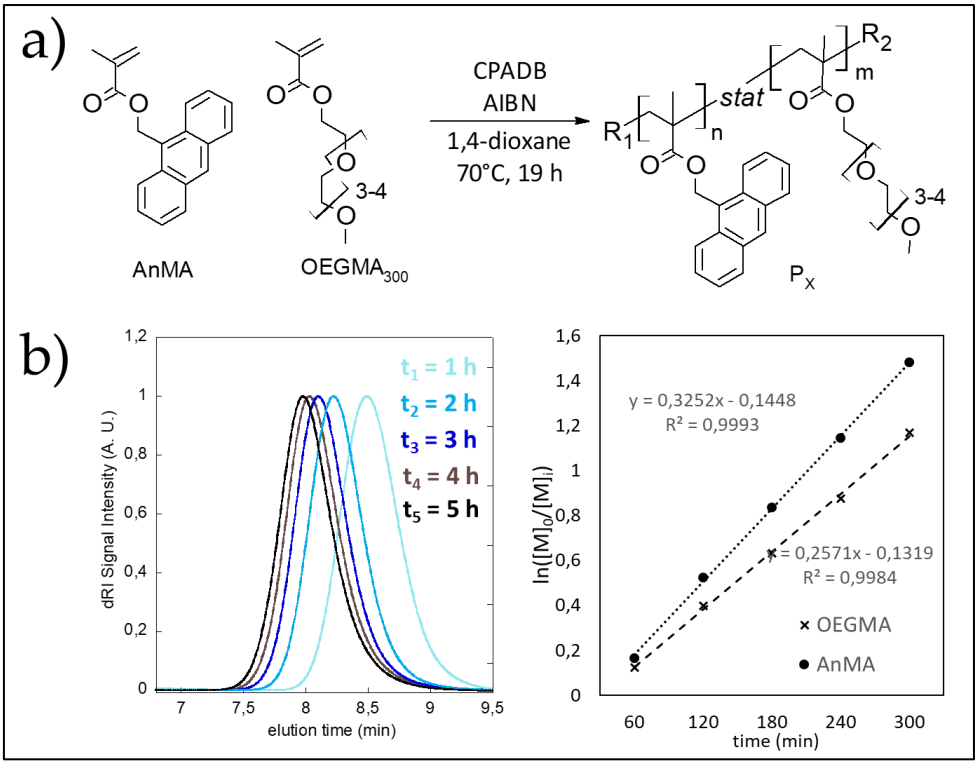

Figure 4.7. a) Reaction scheme for the RAFT copolymerization of AnMA and $OEGMA_{300}$ in the selected conditions for the preparation of the amphiphilic, self-assembled copolymer $\mathbf{P_x}$. b) On the left, GPC / SEC chromatograms of the copolymerization reactions kinetics, on the right monomers incorporations kinetics calculated via ^{1}H NMR spectroscopy showing similar addition rates to the growing polymeric chains.

In order to observe the formation of single-chain nanoparticles, solutions of $\mathbf{P_1}$, $\mathbf{P_2}$ and $\mathbf{P_3}$ in water, all at a polymer concentration of 5 mg mL^{-1}, were prepared by dissolving 10 mg of each copolymer in 2 mL of deionized water. The resulting solutions were left stirring in the dark and at room temperature (r.t.) for 24 h. After this time, the samples were analyzed via dynamic light scattering (DLS). The reversible self-folding of $\mathbf{P_x}$ to $\mathbf{SCNP_x}$ in aqueous media was confirmed via comparison of the DLS size distributions of solutions of $\mathbf{P_x}$ in tetrahydrofuran (THF) and the resulting $\mathbf{SCNP_x}$ in water, both at a polymer concentration of 5 mg mL^{-1}. A reduction of the hydrodynamic diameter (D_h) of $\mathbf{P_1}$, $\mathbf{P_2}$ and $\mathbf{P_3}$ was observed when transferred to water indicating more

compact structures of **SCNP$_1$**, **SCNP$_2$** and **SCNP$_3$** with respect to those of **P$_1$**, **P$_2$** and **P$_3$** in THF (see Figure 4.8b).

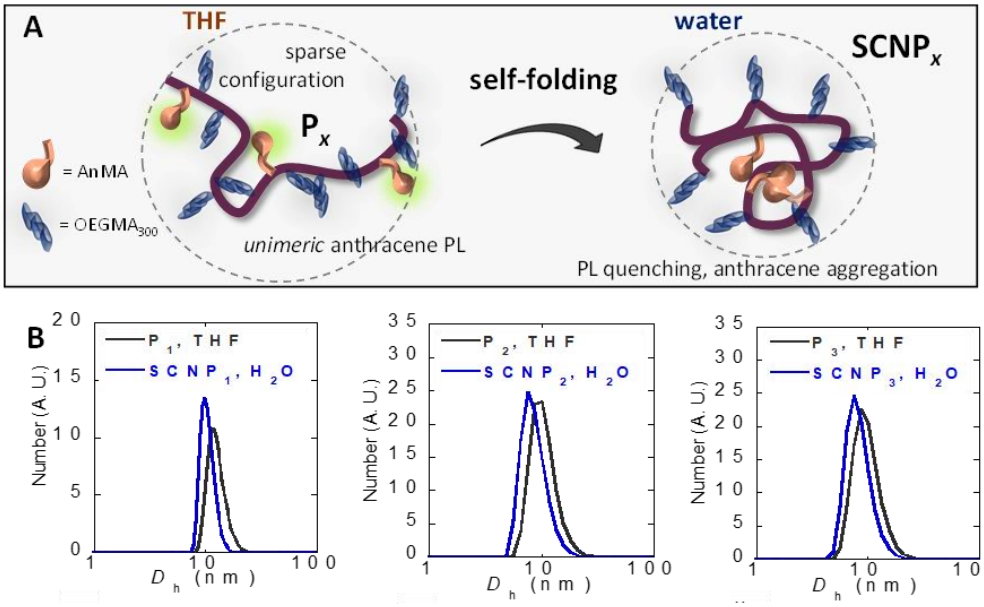

Figure 4.8. a) Depiction of the self-folding of an anthracene-containing amphiphilic precursor, **P$_x$**, which presents typical anthracene photoluminescence (PL) when in open-chain conformation in THF (good solvent for both AnMA and OEGMA$_{300}$), to the self-assembled SCNP in water (selective solvent for OEGMA$_{300}$) in which the anthracene PL is lost due to self-aggregation. b) DLS size distributions of copolymers **P$_1$** (anthracene content: 31 mol%), **P$_2$** (16 mol%) and **P$_3$** (8 mol%) showed as superimposed populations measured in THF and water (in the latter case as **SCNP$_1$**, **SCNP$_2$** and **SCNP$_3$**, respectively) [copolymer] = 5 mg mL^{-1}.

Concomitantly, the slight bathochromic shift of the UV-Visible absorbance in the range between 300 and 400 nm (see Figure 4.9a), as well as the pronounced decrease in fluorescence intensity, broadening of the emission band and its red-shifting (see Figure 4.9b) are indicative of self-aggregation, similar to that reported for anthracene solid-state phenomena such as excimer formation.[69]

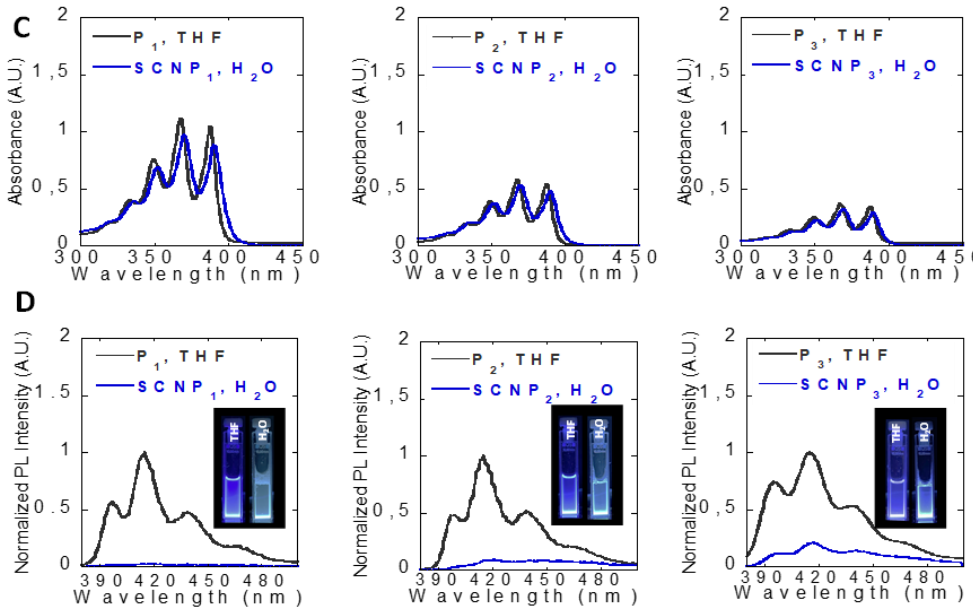

Figure 4.9. a) UV-Vis absorbance spectra of **P_1**, **P_2** and **P_3** in THF and **$SCNP_1$**, **$SCNP_2$** and **$SCNP_3$** in water, [copolymer] = 0.2 mg mL^{-1}. b) PL emission spectra of **P_1**, **P_2** and **P_3** in THF and **$SCNP_1$**, **$SCNP_2$** and **$SCNP_3$** in water, [copolymer] = 0.2 mg mL^{-1}.

Additional evidence of anthracene self-aggregation was obtained by ^1H nuclear magnetic resonance (NMR) spectroscopy showing upfield shifts of the aromatic and benzylic protons signals of **P_1**, **P_2** and **P_3** and **P_4** and **P_5**, two higher-anthracene content (50 and 100 mol%, respectively) prepared as reported in the Annexes (Section V). In particular, to a higher AnMA content in the polymer correspond a concomitant broadening and shielding towards higher fields, which can be interpreted as the resultant of an augmented self-association capability of the aromatic moieties. The same can be said for all the signals in the aromatic region (Figure 4.10).

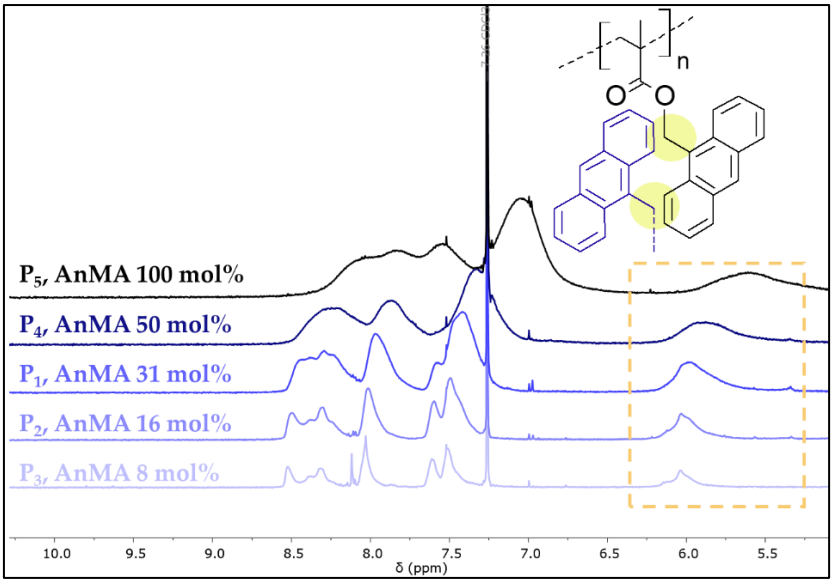

Figure 4.10. ^{1}H NMR (chloroform-d) superimposed spectra of $\mathbf{P_x}$ all recorded at 30 mg / mL. The signals between 5,5 and 6,5 ppm are assigned to the benzylic protons of the anthracenyl pendants of the polymeric chains, which are strongly influenced by the percentage of the AnMA monomer molar fraction.

4.3.1.2. Preparation of the photosensitizer ZnPc.

The photo-properties of phthalocyanines can be modulated by their substitution pattern.[70] The presence of S-alkyl substituents shifts their maximum absorption towards the red, as well as non-peripheral substitution. Bulky substituents are known to limit aggregation. Isobutyl moieties were selected to be introduced *via* thioether functions in one non-peripheral position of each of the four isoindole subunits of a Zn-phthalocyanine. As shown in Scheme 4.1, the synthesis was readily achieved in two steps. First, phthalonitrile **1** was prepared by the reaction between isobutylthiol and 3-nitrophthalonitrile, in 80 % yield. The corresponding phthalocyanine **2** was obtained by reacting phthalonitrile **1** in presence of $Zn(OAc)_2$, yielding the desired phthalocyanine in 28% yield and in rather large scale (300 mg). All analyses confirmed the proposed structure.

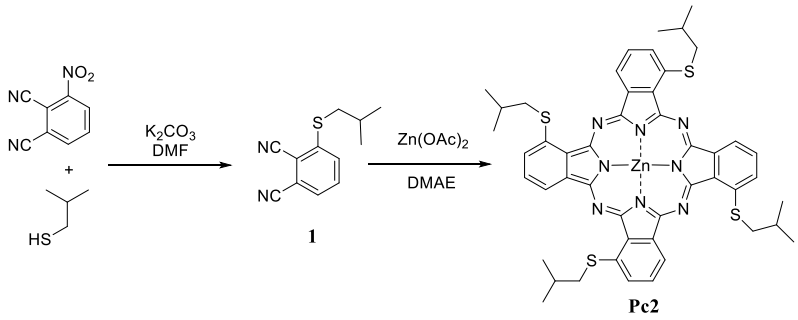

Scheme 4.1. Synthesis of phthalocyanine **ZnPc** (only one of the existing regioisomers is shown).

UV-vis spectra of **ZnPc** have been recorded in THF, DMSO and chloroform at 10 micromolar, conditions for which **ZnPc** is not aggregated. DMSO has been selected as the solvent for the next measurements to use the unsubstituted **ZnPc** as the standard, as all necessary reference data are available.[71] The maximum of the Q band is located at 717 nm, reflecting the bathochromic shift effect expected from both the non-peripheral and the alkylthio substitution (see Appendix to Chapter IV), compared to unsubstituted phthalocyanine that absorbs at 675 nm in DMSO[71] corresponding to a substantial bathochromic shift of more than 40 nm.

The fluorescence spectrum recorded in DMSO showed the expected shape and small stokes shift. The fluorescence quantum yield of **ZnPc** in DMSO was determined to be 0.07, in line with its high oxygen generation quantum yield (Φ_Δ = 0.78). All the photo-properties of **ZnPc** in DMSO are summarized in Table 4.1. All these collected data confirm the relevance of using **ZnPc** for anti-cancer PDT, both for its strong absorption at far-red wavelength and its high ability to generate singlet oxygen.

Table 4.1. Photo-properties of **ZnPc** in DMSO.

λ^{max} (nm)	logε	λ^{em} (nm)	λ^{exc} (nm)	$\Delta\lambda$ (nm)	ϕ_F	ϕ_Δ
717	**5.29**	**736**	**720**	**16**	**0.07**	**0.78**

4.3.1.3. Encapsulation of the photosensitizer ZnPc.

Having demonstrated the self-folding ability of $\mathbf{P_x}$ in water to give $\mathbf{SCNP_x}$, we envisioned the construction of improved, amphiphilic SCNPs containing zinc-1,8,15,22-tetrakis(isobutylthio)phthalocyanine, **Pc**, encapsulated within $\mathbf{SCNP_x}$ as highly performative PSs surrounded by anthracene moieties as highly-efficient nanocarriers for PDT applications.[72] Moreover, we surmised that the presence of **Pc** would endow the resulting SCNPs with useful imaging properties. For the preparation, we selected an overall $\mathbf{P_x}$ concentration in solution of 5 mg mL^{-1}. Under these conditions, $\mathbf{P_1}$, $\mathbf{P_2}$ and $\mathbf{P_3}$ allowed the preparation of different single-chain nanoparticles charged with the photoactive **Pc** at three different loadings that we denote as $\mathbf{APO_1\text{-}Pc_{60}}$, $\mathbf{APO_2\text{-}Pc_{25}}$ and $\mathbf{APO_3\text{-}Pc_{10}}$, corresponding to overall **Pc** concentrations in solution of 60, 25 and 10 µM respectively. As a general procedure for encapsulation of the **Pc** (see Figure 4.11), 25 mg of the copolymer nanocarrier were weighted in an amber glass vial and diluted with 100 µL of inhibitor-free THF.

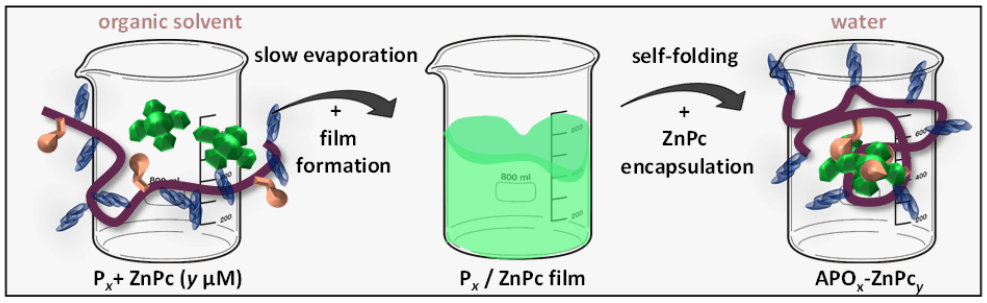

Figure 4.11. Schematic illustration of the synthetic procedure followed for the formation of self-assembled $\mathbf{APO_x\text{-}Pc_y}$.

After stirring at r.t. for 1 h, n µL of **Pc** stock solution (1 g L^{-1} in inhibitor-free THF) was added to the solution, with n selected depending on the desired final concentration of **Pc**. The resulting solution was left stirring at r.t. and in the dark for 72 h to ensure complete evaporation of the organic solvent. After this time, 5 mL of deionized water was added to the resulting polymeric film and the final mixture was left under gentle agitation at r.t. and in the dark for 24 h. The resulting clear and

transparent solutions of **APO_x-Pc_y** were analyzed via small-angle X-ray scattering (see Figure 4.12) and stored in a dark place at 4°C.

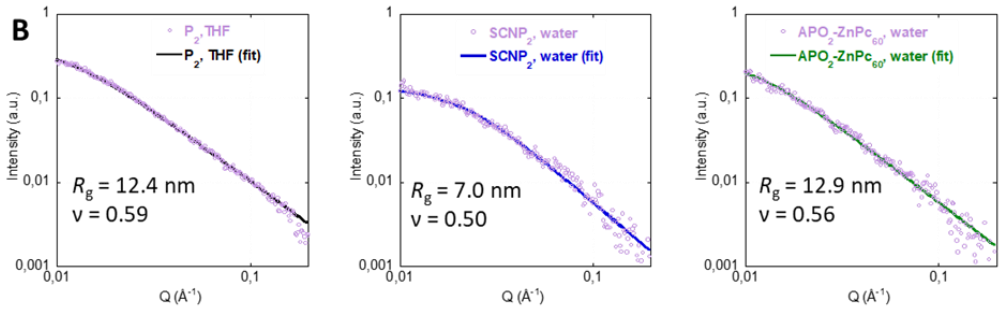

Figure 4.12. Small-angle X-ray scattering (SAXS) results (R_g is the radius of gyration, ν is the scaling exponent) revealing the compaction of **P₂** switching solvents from THF to water (**SCNP₂**), followed by an enlargement of the radius of gyration (R_g) upon **Pc** incorporation within the nanoparticle to give **APO₂-Pc₆₀**.

Considering the strong hydrophobicity of the phthalocyanine used in this work, we assumed that the total absence of any precipitate in solution is a good indication of a quantitative encapsulation of **Pc** within the hydrophobic core of the SCNP. A further confirmation was obtained by the comparison of the radius of gyration (R_g) of the single-chain nanoparticles in water prior- and post-encapsulation of the **ZnPc** (Figure 4.12). After encapsulation, the values of R_g were always higher with respect to the neat (**Pc** free) nanocarriers, which we attribute to the increased steric hindrance in the core of the nanoparticles, due to the encapsulated **Pc**. We hypothesized that changes in the anthracene content in the SCNPs could have significant effects in its photophysical properties (see Figure 4.13). As illustrated in Figure 4.13, by measuring the UV-Vis absorbance of the **APO$_x$-ZnPc$_y$** we observed a clear correlation between the molar fraction of anthracene moieties in the nanocarrier and the aggregation degree of the encapsulated phthalocyanine PS. As shown in Figure 4.13-up, left, by the comparison of the absorption in the far-red region of **APO₁-Pc₆₀**, **APO₂-ZnPc₆₀** and **APO₃-ZnPc₆₀**, the extent of either broadening or quenching of Q-band transitions increases upon decreasing the anthracene molar fraction in the nanocarrier. Analogously, a pronounced quenching (λ^{exc} = 650 nm) of the **ZnPc** emission in the far red is observed upon decreasing the anthracene content from 31 mol % (**APO₁-Pc₆₀**) to 8 mol% (**APO₃-ZnPc₆₀**) (see Figure 4.13-up, right). Consequently, this novel class of amphiphilic SCNPs not only enables the facile encapsulation of the far-red absorbing **Pc**, but also

allows the tunability of the degree of aggregation within the hydrophobic core of the nanocarrier, as depicted in Figure 4.13-bottom.

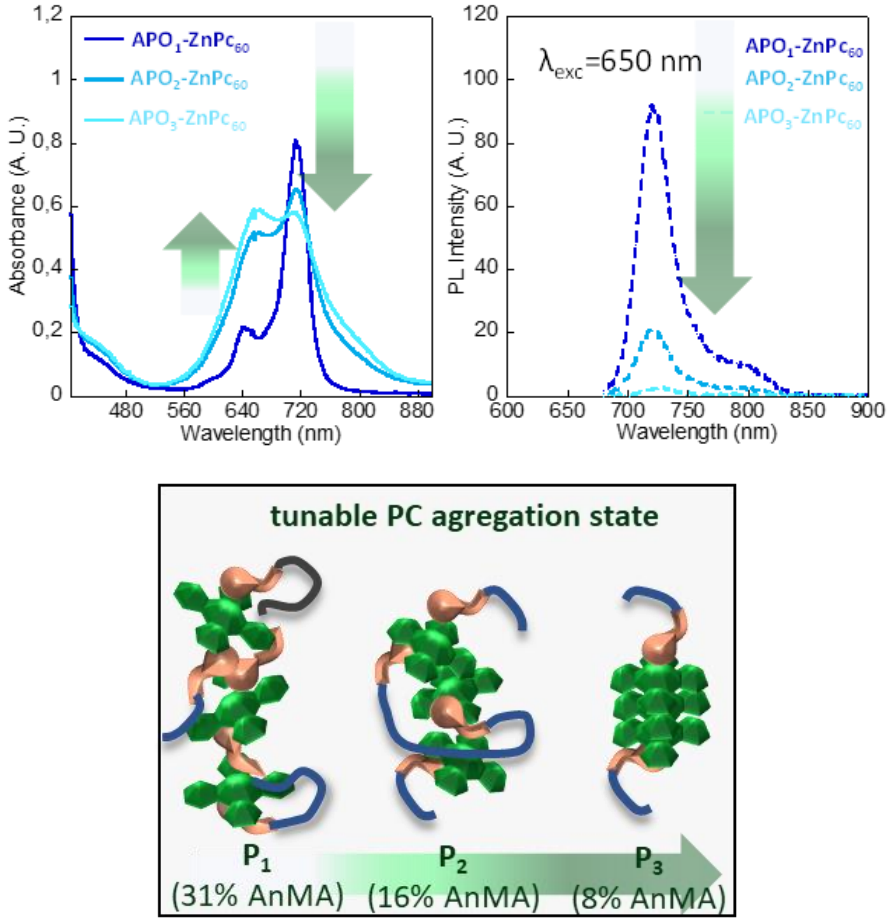

Figure 4.13. Up: On the left, UV-Vis spectra of **APO₁-Pc60**, **APO₂-Pc60** and **APO₃-Pc60** in water ([copolymer] = 0.2 mg mL^{-1}). On the right, PL emission spectra of the same solutions, recorded after oxygen displacement by argon bubbling. Bottom: Depiction of the tuning of the aggregation state of the **Pc** encapsulated within the core of the SCNP depending on the anthracene content in the polymeric nanocarrier.

4.3.2. In vitro Imaging and PDT with Amphiphilic SCNPs Containing ZnPc Molecules and Anthracene Moieties

To determine the therapeutic potential of the, we first assessed their intrinsic toxicity by means of performing cytotoxicity experiments against human breast

adenocarcinoma (MDA-MB-231) cells. In a typical experiment, the cytotoxicity against MDA-MB-231 cells was estimated after having incubated the cells with the **APO$_x$-Pc$_y$** at fixed concentrations for 72 h using the 3-(4,5-dimethyltriazol-2-yl)-2,5-diphenyltetrazolium bromide (MTT) test.[73] Figure 4.14 shows that no significant cytotoxic activity was observed when MDA-MB-231 cells were incubated in presence of **APO$_x$-Pc$_y$** at a nanoparticle concentration of up to 100 μg mL^{-1}.

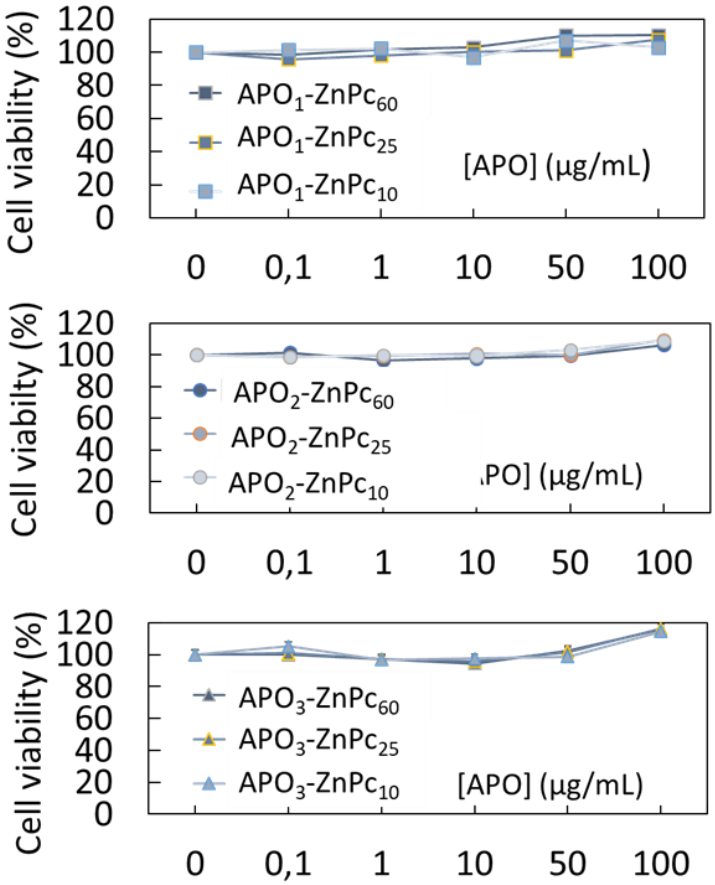

Figure 4.14. Dark cytotoxicity experiments of **APO$_x$-Pc$_{60}$** against human breast adenocarcinoma MDA-MB-231 cells, which were incubated 72 hours with increasing concentrations of **APO$_x$-ZnPc$_y$**. Values are means ± standard deviations of 3 experiments.

The good biocompatibility observed for this novel class of nanocarriers is, after all, in agreement with what reported for other PEGylated nanoparticles employed in nanomedicine applications. Next, we explored the cellular uptake of **APO$_x$-Pc$_y$** by

MDA-MB-231 cells. For these experiments, we selected the SCNPs with the higher **Pc** content, **APO_x-Pc_{60}**, as the internalization was visualized by fluorescence microscopy exploiting the intrinsic fluorescence (λ^{exc} max = 630 nm) of the encapsulated phthalocyanine. As shown in Figure 4.15a, long-wavelength emitted PL of the photosensitizer **Pc** was observed for all the three SCNP-based nano-systems. Notably, the fluorescence intensity relations measured in aqueous solutions of **APO_x-Pc_{60}** (Figure 4.13-left, up), specifically **APO_1-Pc_{60}** > **APO_2-Pc_{60}** ~ **APO_3-Pc_{60}**, was qualitatively maintained also upon internalization in MDA-MB-231 cells. Conversely, when MDA-MB-231 cells were incubated with non-encapsulated **Pc** under the same experimental conditions, no substantial internalization was observed. Consequently, encapsulation of the highly hydrophobic and self-aggregating **Pc** within the APO is essential for ensuring good bioavailability. Figure 4.15b shows confocal microscopy images of MDA-MB-231 breast cancer cells containing both **APO_2-Pc_{60}** and Hoechst dye as imaging agents, by which it was possible to visualize the distribution of the internalized **APO_2-Pc_{60}** within the cytosolic region of the tumor cells.

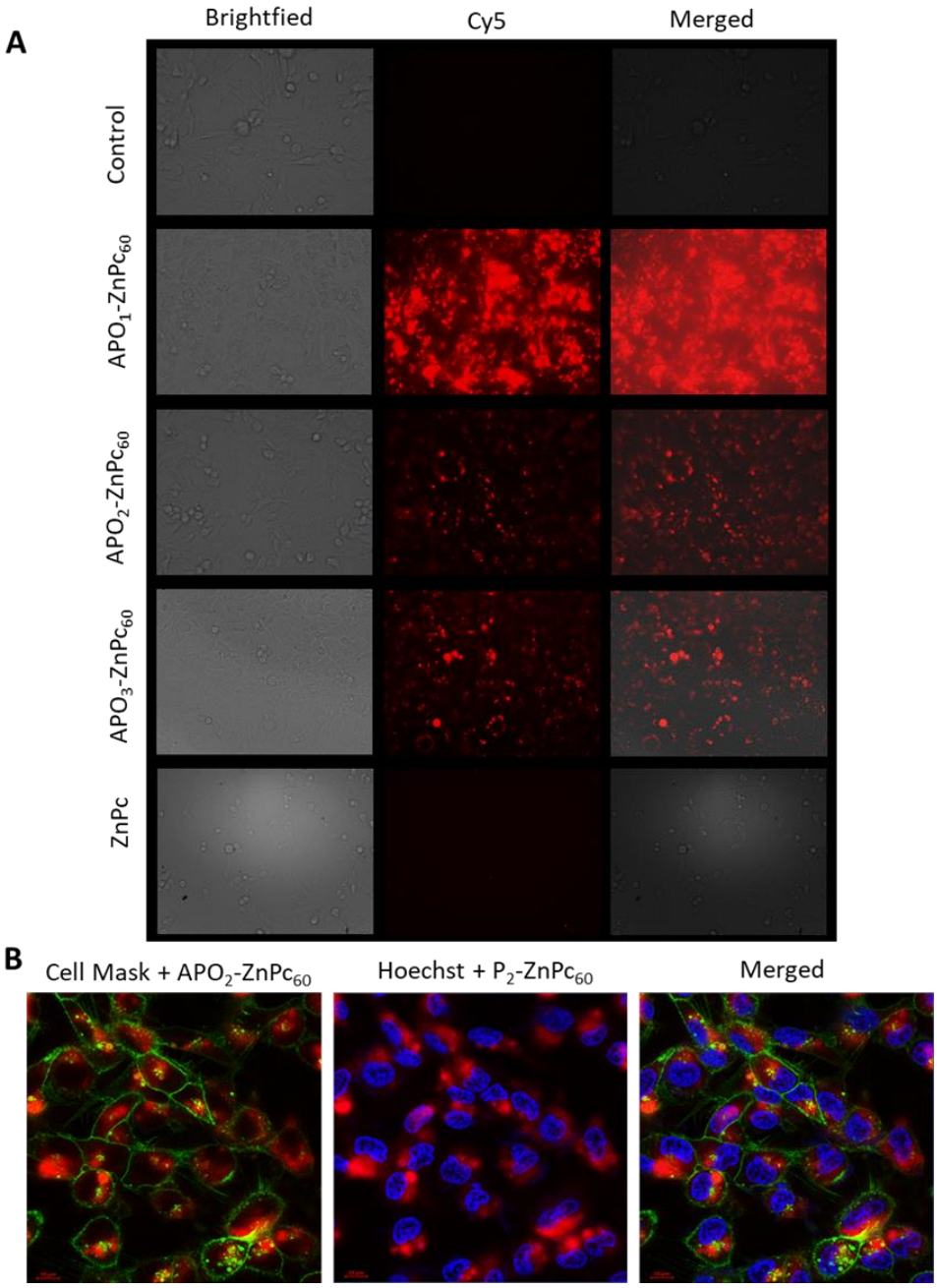

Figure 4.15. a) Fluorescence microscopy images recorded on MDA-MB-231 breast cancer cells treated either (or not) with **APO_x-Pc_{60}** at 100 µg mL^{-1} or with non-encapsulated **Pc** (1.2 µM). The fluorescence of **APO_x-Pc_{60}** is revealed using an excitation wavelength of 630 nm. b) Confocal microscopy images of MDA-MB-231 breast cancer cells incubated with **APO_2-$ZnPc_{60}$**, 100 µg mL^{-1}. Cell membranes and nuclei stained with Cell Mask (green) and Hoechst (blue), respectively.

Then, the PDT effect in cancer cells was investigated at two different irradiation wavelengths in the far-red region of the visible spectrum of light, namely at λ^{exc}_{max} = 630 nm and λ^{exc}_{max} = 730 nm. MDA-MB-231 cells were incubated for 24 h with the **APO_x-Pc_y** at an optimal concentration of 100 μg mL^{-1}, since performing the same experiments at lower SCNPs contents (25 μg mL^{-1}) resulted in a less remarkable effect. Notably, all the samples showed PDT-effect when a 630 nm light source was employed for irradiation (Figure 4.16a). All **APO_x-Pc_{60}** manifested high cell photo-killing ability, with the specific PDT effect of **APO_2-Pc_{60}** being tremendous. Interestingly, significant PDT-effect was observed when shifting to the longer irradiation wavelength (730 nm) (Figure 4.16b).

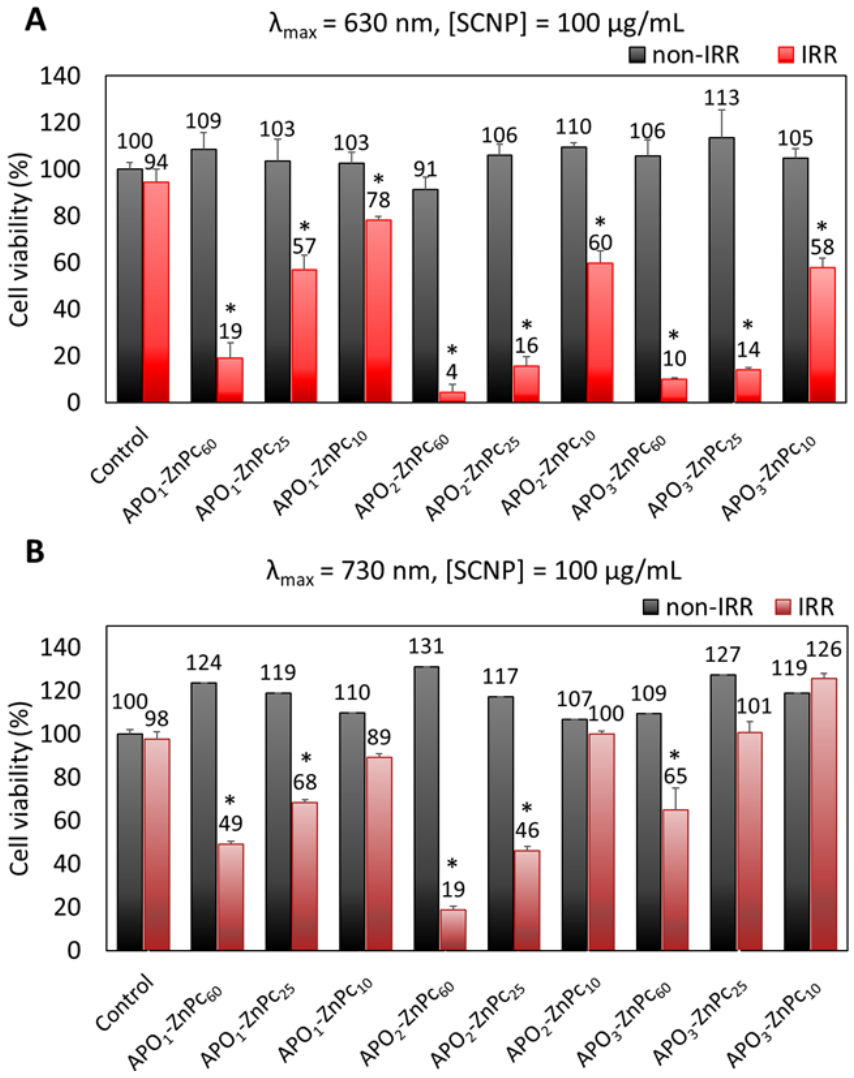

Figure 4.16. PDT-effect studies of **APO$_x$-ZnPc$_y$** incubated in MDA-MB-231 cells using an irradiation wavelength of 630 nm (A) or 730 nm (B). Values are means ± standard deviations of 3 experiments. *, p-value < 0.05, significantly different between non-IRR and IRR.

To further test the suitability of **APO$_x$-Pc$_{60}$** nanoparticles as effective PDT agents, we performed the same experiments exposing the 96-well plate at room light for 3 h, and no cytotoxicity was observed (see Appendix: Section IV). These results indicate that the confinement of the ZnPc within the core of the **APO$_x$-Pc$_y$** yields nanoaggregates with a PDT activity which is selective for long-wavelength and intense radiations, a highly desirable quality for perspective application in more complex

systems. We confirmed that the cell-killing activity of **APO_x-Pc_y** is due to a PDT mechanism by demonstrating the in vitro ROS production during light excitation. Hence, cells were incubated with the non-fluorescent reactant 2´,7´-dichlorodihydrofluorescein diacetate (DCFH-DA) for 45 min. In the presence of ROS, the molecule is straightforwardly oxidized to its fluorescent form 2´,7´-dichlorofluorescein (DCF), whose characteristic intense green luminescence was detected by fluorescence microscopy. The results shown in Figure 4.17 illustrate that, when incubated for 24 h in presence of 100 μg mL^{-1} of **APO_x-Pc_{60}**, light excitation at a maximum wavelength of 630 nm induced green fluorescence inside the tumor cells. This result qualitatively demonstrates intracellular ROS production and confirms that the cell death follows a PDT-like mechanistic pathway.

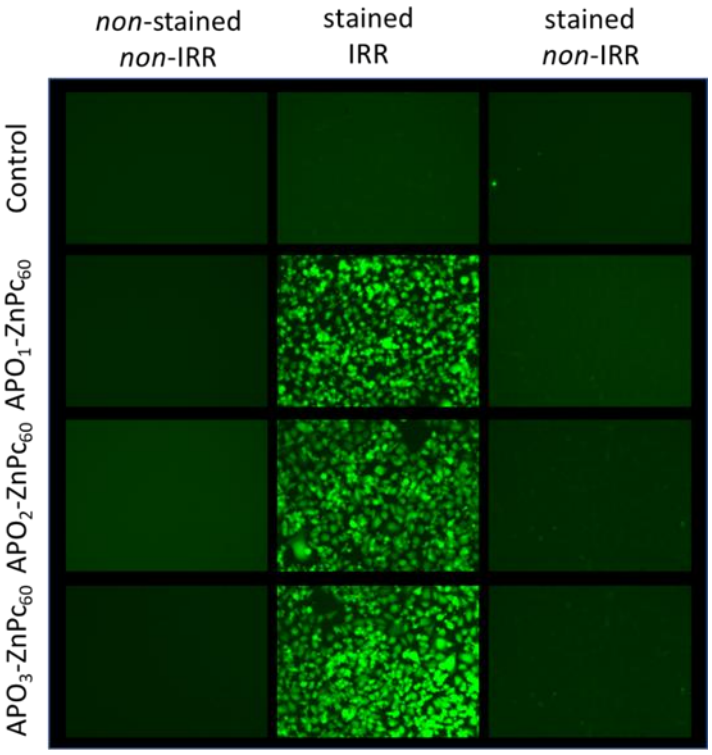

Figure 4.17. Detection of intracellular ROS in MDA-MB-231 cells treated with **APO_x-$ZnPc_{60}$** after irradiation with a 630 nm light source. Detection of intracellular ROS in MDA-MB-231 cells incubated for 24 hours with 100 μg mL^{-1} of **APO_x-$ZnPc_{60}$** and 20 μM DCFDA for 45 min and irradiated with a 630 nm light source. Green fluorescence was observed under GFP filter (λ^{exc} = 480 nm).

4.3.3. π-π self-assembled amphiphilic SCNPs containing Zn(II)-phthalocyanine Pc as imaging and far-red photo-killing agents for PDT in Zebrafish embryo xenografts

With the biomedical potential of **APO$_x$-Pc$_{60}$** for PDT assessed, we wanted to further demonstrate their employability by performing both fluorescence imaging and PDT experiments in Zebrafish embryos as integrated models for human tumors.[74] First, we assessed the **APO$_x$-Pc$_y$** capability to induce long-wavelength fluorescence in zebrafish larvae. Specifically, we injected 72 h post fertilization (hpf) zebrafish embryos with **APO$_x$-Pc$_y$** from the three different copolymer precursors **P$_1$**, **P$_2$** and **P$_3$** at their highest **Pc** loading (**APO$_x$-Pc$_{60}$**), which were administrated through intravenous (IV) injection (Figure 4.18b).

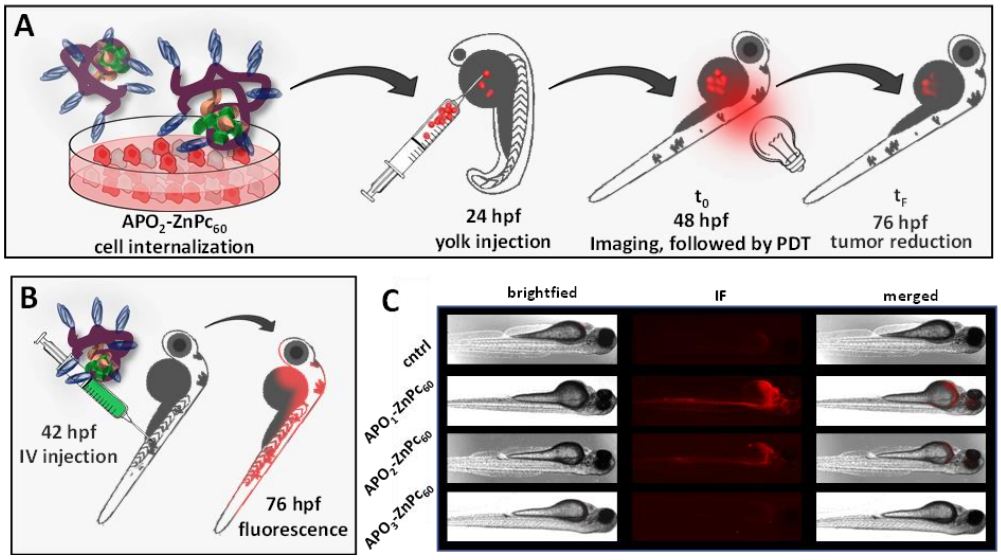

Figure 4.18. **a**) Scheme of the PDT experiment of xenograft zebrafish embryos tumor model. **b**) Scheme of the **APO$_x$-ZnPc$_{60}$**-induced fluorescence in the zebrafish. **c**) Experimental results of **APO$_x$-ZnPc$_{60}$**-induced fluorescence in zebrafish.

After letting circulating the nanoparticles in the organisms' bloodstreams for 4 h, we captured the photoluminescence by fluorescence microscopy using a maximum excitation wavelength of 630 nm. As shown in Figure 14c, the **APO$_x$-Pc$_{60}$** easily and homogeneously distributed in the vascular system of the subjects, indicating both a

good biodistribution behavior and appropriate properties of the amphiphilic SCNPs also in the chemically complex zebrafish larvae's vascular system. Interestingly, analogous PL intensity patterns (**APO_1-Pc_{60}** > **APO_2-Pc_{60}** ~ **APO_3-Pc_{60}**), already observed for in vitro experiments, were observed also upon injection in the embryos.

Encouraged by all the above-mentioned results, we finally carried out PDT experiments on Zebrafish larvae xenografts to further evaluate the potential of this novel class of ultra-small nanoparticles for PDT cancer treatment. For this, we first seeded MDA-MB-231 cells expressing the fluorescent protein Luciferase (RFP) with the nanoparticles which shown the best in vitro results, namely **APO_2-Pc_{60}** solutions, at a polymer concentration of 100 μg mL^{-1} for an incubation time of 24 h. After **APO_2-Pc_{60}** internalization, culture media were rinsed and concentrated up to reach a cell concentration suitable for intra-yolk injection (see Experimental Techniques for the detailed procedure). 72 hpf zebrafish embryos were then injected with **APO_2-Pc_{60}** -loaded (or not loaded) MDA-MB-231 Luc RFP cells via injection in the yolk, ensuring an injection of about 200-300 cells per subject. After a period of 24 h for tumor implantation, fluorescence microscopy images of all the tumors were recorded exploiting the RFP-responding luminescence of the Luciferase expressed by the tumor cells and the subjects were (or not) subsequently exposed to light irradiation (λ^{exc}_{max} = 630 nm) for a total duration of 10 minutes using the same microscope. 24 h after the irradiation, images of the tumors were captured again and under the same optical conditions, allowing the measurement of the evolution extent of the tumoral mass in each specific and different experimental condition (Figure 4.19). The resulting statistics, which was built with six individual subjects for each condition is illustrated in Figure 4.19, suggesting that **APO_2-Pc_{60}** shows a promising photo-killing effect against human tumor cells in Zebrafish larvae xenografts.

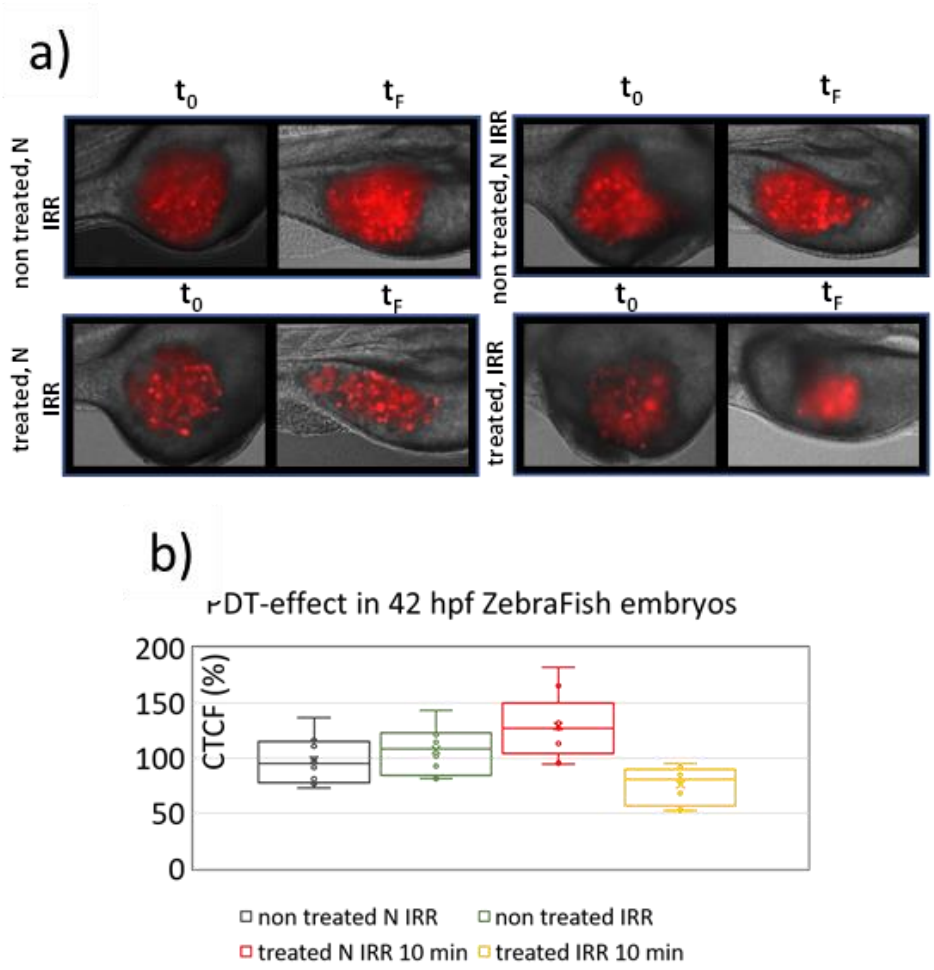

Figure 4.19. a) Fluorescence microscopy imaging of four representative cases, one for each experimental condition explored, of the PDT effect of **APO_x-$ZnPc_y$** in Zebrafish embryos. b) Statistics of the *in Zebrafish* PDT effect of **APO_2-$ZnPc_{60}$**.

While in either non-treated or treated but not irradiated subjects the tumor fluorescence showed a neat increase with respect to initial conditions, in the case of irradiated and treated ones an encouraging diminishment of tumor dimensions was observed.

4.4. Experimental Techniques

4.4.1. Materials

Unless otherwise noted, all reagents and solvents were used as received from vendors. Oligo(ethylene glycol monomethyl ether) methacrylate ($OEGMA_{300}$, average molecular weight = 300 Da) (>99%) was purchased from TCI Europe N.V. and was filtered over basic alumina before use. n-Hexane (96%), was purchased from Scharlab. Tetrahydrofuran (THF) (>99 %, +0.025% BHT as stabilizer), ethanol (EtOH) (>99%) and methanol (MeOH) (>99%) were purchased from Fisher Scientific. Inhibitor-free THF was obtained by filtration of THF (Fisher Scientific) over basic alumina. 1,4-Dioxane (>99%), 9-anthracenylmethyl methacrylate (>99%), 4-cyano-4-(phenylcarbonothioylthio)pentanoic acid (CPADB) and dimethyl sulfoxide (98%) were purchased from Sigma-Aldrich. Azobisisobutyronitrile (AIBN) (98%) was purchased from Fluka and recrystallized from MeOH prior use. Basic alumina (0.063-0.2 mm) was purchased from Merck. Deuterated chloroform ($CDCl_3$, 99.8% D, + 0.03% tretramethylsilane) for ^1H NMR analysis was purchased from Eurisotop. Deionized water was obtained from a Thermoscientific Barnstead TII System.

4.4.2. Synthesis of the photosensitizer Pc

The preparation of zinc 1,8,15,22-tetrakis(isobutylthio)phthalocyanine, **Pc**, was carried out as reported in the previous Chapter.

4.4.3. Synthesis of P_1.

177 mg (0.64 mmol) of 9- anthracenylmethyl methacrylate (AnMA), 450 mg (1.5 mmol) of oligo(ethylene glycol monomethyl ether) methacrylate ($OEGMA_{300}$), 1.51 mg (5.4 µmol) of 4-cyano-4-(phenylcarbonothioylthio)pentanoic acid (CPADB), 0.34 mg (2.1 µmol) of azobisisobutyronitrile (AIBN) and 1.07 mL of 1,4-dioxane were added to a dark, oven-dried vial, equipped of a magnetic stir bar. After purging the mixture with an argon flow for 10 min., the vial was sealed with a rubber septum, and

the reaction was left stirring at 70 ºC and under inert atmosphere for 19 h. After this time, the crude was purified via four consecutive precipitations in n-hexane. After drying under dynamic vacuum for 24 h, the obtained product was analyzed via size exclusion chromatography (SEC) and NMR. M_w (kDa) = 184.5, Đ = 1.39, AnMA (mol%) = 31. ^{1}H NMR (400 MHz, $CDCl_3$): **δ** (ppm) = 8.44-7.42 (m, 9H, H^{Ar}), 5.98 (b.s., 2H, $H_9C_{10}CH_2$), 4.08-3.99 (m, 2H, CH_2CH_2O), 3.62-3.50, (m, $(OCH_2CH_2)_n$), 3.34 (s, 3H, OCH_3), 1.74 (m, CH_2CCH_3), 1-0.83 (m, CH_2CCH_3).

4.4.4. Synthesis of P_2

98 mg (0.35 mmol) of AnMA, 600 mg (2 mmol) of $OEGMA_{300}$, 1.65 mg (5.9 µmol) of CPADB, 0.39 mg (2.4 µmol) of AIBN and 1.07 ml of 1,4-dioxane were added to a dark, oven-dried vial, equipped of a magnetic stir bar. After purging the mixture with an argon flow for 10 minutes, the vial was sealed with a rubber septum, and the reaction was left stirring at 70 ºC and under inert atmosphere for 19 h. After this time, the crude was purified via four consecutive precipitations in nhexane. After drying under dynamic vacuum for 24 h, the obtained product was analyzed via SEC and NMR. M_w (kDa) = 157.1, Đ = 1.20, AnMA (mol%) = 16. ^{1}H NMR (400 MHz, $CDCl_3$): δ (ppm) = 8.5- 7.51 (m, 9H, H^{Ar}), 6.02 (b.s., 2H, $H_9C_{10}CH_2$), 4.07 (m, 2H, CH_2CH_2O), 4.00-3.53, (m, $(OCH_2CH_2)_n$), 3.36 (s, 3H, OCH_3), 1.88 (m, CH_2CCH_3), 1.01-0.84 (m, CH_2CCH_3).

4.4.5. Synthesis of P_3

49 mg (0.175 mmol) of AnMA, 600 mg (2 mmol) of $OEGMA_{300}$, 3.3 mg (11.8 µmol) of CPADB, 0.78 mg (4.8 µmol) of AIBN and 1.07 ml of 1,4-dioxane were added to a dark, oven-dried vial, equipped of a magnetic stir bar. After purging the mixture with an argon flow for 10 min., the vial was sealed with a rubber septum, and the reaction was left stirring at 70 ºC and under inert atmosphere for 19 h. After this time, the crude was purified via four consecutive precipitations in n-hexane. After drying under dynamic vacuum for 24 h, the obtained product was analyzed via SEC and NMR.

M_w (kDa) = 132.7, Đ = 1.23, % AnMA (mol%) = 8 %. ^{1}H NMR (400 MHz, $CDCl_3$): δ (ppm) = 8.53-7.52 (m, 9H, H^{Ar}), 6.03 (b.s., 2H, $H_9C_{10}CH_2$), 4.08 (m, 2H, CH_2CH_2O), 3.74-3.54, (m, $(OCH_2CH_2)_n$), 3.37 (s, 3H, OCH_3), 1.85 (m, CH_2CCH_3), 1.26-0.88 (m, CH_2CCH_3).

4.4.6. Preparation of APO_x-Pc_y

As a general procedure for encapsulation of **Pc**, 25 mg of $\mathbf{P_x}$ was weighted in an amber glass vial and diluted with 100 µL of inhibitor-free THF. After stirring at room temperature for 1 h, n µL of a **Pc** stock solution (1 g L^{-1} in inhibitor-free THF) was added to the 19 solution, with n selected depending on the desired final y µM concentration of **Pc**. The resulting solution was left stirring at r.t. and in the dark for 72 h to ensure complete evaporation of the organic solvent. After this time, 5 mL of deionized water was added to the resulting polymeric film, and the final mixture was left under gentle agitation at r.t. and in the dark for 24 h. The resulting clear and transparent $\mathbf{APO_x\text{-}Pc_y}$ solutions were analyzed via DLS and UV-Vis spectrometry, and finally stored in a dark place at 4 °C.

4.4.7. Cell culture conditions for in vitro experiments

Human breast adenocarcinoma MDA-MB-231, the standard cell line or this expressing luciferase and red fluorescent protein (MDA-MB-231 Luc RFP) were purchased from ATCC (American Type Culture Collection, Manassas, VA). Cells were cultured in Dulbecco's Modified Eagle's Medium (DMEM), incorporating 10 % Fetal Bovine Serum and antibiotic (FBS) (2 % penicillin – streptomycin). MDA-MB-231 Luc RFP cells were maintained in the previously mentioned cell culture media compositions in addition to 5 µg mL^{-1} blasticidin as a selection antibiotic. The cell growth was performed in humidified atmosphere at 37 °C under 5% CO_2. DMEM, FBS and antibiotics were purchased from Gibco.

4.4.8. Cell viability assay

In a typical cell viability experiment, cells were seeded in a 96-well plate in 200 μL of their respective culture medium, 24 h after cell growth; at the end of each specific experiment, always corresponding to a maximum period of 4 days after first seeding, cells were incubated with 0.5 mg mL^{-1} of 3-(4,5-dimethylthyazol-2-yl)-2,5-diphenyltetrazoliumbromide (MTT). Three hours after, MTT / medium solution was removed and the precipitated dark-purple crystals were dissolved in ethanol/DMSO (1:1, v/v) solution with gentle, round shaking for 20 min. The absorbance was read at 540 nm. The percentage of living cells was calculated based on a direct correlation between the optical density (OD) and the number of living cells in the plate and was expressed as the ratio between the OD of treated cells and OD of control cells.

4.4.9. In vitro dark cytotoxicity

For a typical cytotoxicity assay, analyses were performed by using MDAMB-231 cells seeded into 96-well culture plates, ~ 2000 cells per well in 200 μL of culture medium and allowing them to grow for 24 h. The cells were then treated with different concentrations of $\mathbf{APO_xPc_y}$ ($0 < [\mathbf{APO_x\text{-}Pc_y}] < 100$ μg mL^{-1}) and, after 3 days, a colorimetric MTT assay of living cells was performed, as above mentioned.

4.4.10. In vitro phototoxicity assay

In vitro phototoxicity assays were performed with MDA-MB-231 cells seeded into 96-well plates at a concentration of ~2 × 103 cells per well in 200 μL of culture medium and allowed to grow for 24 h. The cells were then incubated for 24 h in the presence or absence of the photosensitizer employed for the particular experiment ($[\mathbf{APO_x\text{-}Pc_y}] = 100$ μg mL^{-1}). After incubation, cells were submitted, or not, to light excitation ($\lambda^{exc}_{max} = 630$ nm, 1.45 J cm^{-2} or $\lambda^{exc}_{max} = 730$ nm, 1.45 J cm^{-2}) for 10 min, using Cy5 and Cy7 light cubes, respectively) of EVOS5000 (ThermoFisher) microscope. A total of 48 h after irradiation, the cytotoxicity or phototoxicity of the

investigated substances were evaluated using an MTT assay in the abovementioned conditions.

4.4.11. Reactive oxygen species (ROS) production

The day after being seeded in a 96-well plate in 200 µL of their respective culture medium, MDA-MB-231 cells were incubated with 100 µg mL^{-1} of **APO_x-Pc_{60}** for 24 h and submitted, or not, to light excitation (λ^{exc}_{max} = 650 nm, 10 min, 1.45 J cm^{-2}). However, 45 minutes before excitation, cells were incubated with 20 µM of 2′,7′-dichlorofluorescin diacetate (DCFDA / H_2DCFDA - Cellular ROS Assay Kit-ab113851). After excitation, cells were rinsed with culture media and fluorescence emission of 2′,7′-dichlorofluorescein (DCF) (λ^{exc} = 480 nm) was collected using the camera of standard fluorescence microscope. In vitro **APO_x-Pc_{60}** fluorescence imaging: The day prior to the experiment, MDA-MB-231 cells were seeded onto bottom glass dishes (World Precision Instrument, Stevenage, UK) at a density of ~ 100 cells / cm^{-2}. Adherent cells were then washed once and incubated in 1 mL cell medium with or without **APO_x-Pc_{60}** at a concentration of 100 µg mL^{-1} for 24 h. Before visualization, cells were gently rinsed with cell media. Cells were then scanned via fluorescence microscopy exciting with Cy5 light cube of EVOS5000 microscope.

4.4.12. *Danio Rerio* embryos handling for in Zebrafish experiments

Wild-type AB zebrafish strain was purchased from Zebrafish International Resource Center (ZIRC) as embryos and were raised to adulthood in circulating aquarium system inside environmentally controlled room (28 ºC, 80 % humidity, 14 h light / 10 h dark cycle), in the lab's facilities of Molecular mechanisms in neurodegenerative dementia (MMDN), Inserm U1198, Montpellier University, Montpellier. Only fish directly from ZIRC or their F1 offspring were used as egg producers to avoid inbreeding effects. Embryos were obtained from pairs of adult fish by natural spawning and raised at 28.5 °C in tank water. At 7 h post fertilization (hpf),

embryos were examined under the microscope, and only embryos that developed normally and reached gastrula stage were selected for the study.

4.4.13. Injection, irradiation, and imaging of MDA-MB-231 in Zebrafish embryos

The MDA-MB-231 cells expressing Luc RFP were seeded in two 25 cm^2 flasks and incubated for 24 h. In one of the two flasks, the cells were treated with 100 μg mL^{-1} of **APO_x-Pc_{60}** solution. After 24 h incubation, the cells were trypsinized, centrifuged, and then resuspended in a sufficient volume of Phosphate-Buffered Saline (PBS) containing 2 % Fetal Bovine Serum to have a cell concentration of 2 × 107 cells mL^{-1}. The two cell populations, with and without **APO_x-Pc_{60}**, were kept on ice until injection. The embryos at 24 hpf were divided into three groups: control group (without any injection), treatment with MDA-MB-231 Luc RFP cells alone, and treatment with MDA-MB-231 Luc RFP cells loaded with **APO_x-Pc_{60}**. The embryos were then anesthetized with tricaine solution at 17 mg mL^{-1} for 10 minutes prior to injection. Each embryo was placed in an agar mold for the microinjection of MDA-MB-231 cells expressing Luc RFP. Needles made of borosilicate glass with an internal diameter of 0.78 mm were loaded with 4 μL of the desired cell suspension. The cells were then injected into the embryos' yolk. Each embryo received 2-4 pulses of 10 nL cell suspension of 2 × 107 cells mL^{-1} to get 200 – 400 injected cells per embryo. The embryos were then placed in a 12 well plate (1 embryo per well in 400 μL of water), incubated at 30 °C and observed regularly after injection. One day later, the embryos were imaged and 21 then submitted (or not) to light irradiation using RFP light cube of EVOS 5000 microscope. The wells were irradiated by 1 session of 10 min. of duration each. After 24 h, the effect of irradiation on the injected MDA-MB-231 cells was assessed by imaging the embryos with the same microscope. Final image analysis and visualization were performed using ImageJ-win32 software to adjust brightness and to remove out-of-focus background fluorescence. Zebrafish fluorescence imaging: Zebrafish larvae of 24 hpf were manually dechorionated and then let develop for further 42 hours in the abovementioned conditions. The 72 hpf embryos were then anesthetized

with tricaine solution at 17 mg mL^{-1} for 10 minutes prior to injection. The **APO_x-Pc_{60}** solutions at the concentration of 4.35 mg mL^{-1}, previously added of 10 % penicillin - streptomycin, were directly injected via intra-venous injections. Each embryo received a total injected volume of approximately 10 nL nanoparticle solution. Four hours later, the embryos were imaged using the Cy5 light cube of EVOS5000 microscope.

Statistical analyses: Significance was carried out using Student *t*-test to compare the pared groups of data ("irradiated" versus "non-irradiated"). A p-value < 0.05 was considered to be statistically significant.

4.5. Conclusions

In conclusion, the efficient encapsulation of zinc 1,8,15,22-tetrakis(isobutylthio)phthalocyanine, **ZnPc**, molecules within water-soluble, amphiphilic single-chain nanoparticles (SCNPs) containing hydrophobic anthracene pendants gives to promising nanocarriers for photodynamic therapy (PDT). The imaging and PDT properties of the resulting **APO_x-Pc_y** nanocarriers are ready tunable by adjusting both the amount of anthracene units and **ZnPc** molecules within each single-chain nanoparticle. All **APO_x-Pc_y** showed excellent biocompatibility as revealed by dark cytotoxicity experiments as well as very good-to-excellent PDT properties inside human breast adenocarcinoma (MDA-MB-231) cells when irradiated at 630 or 730 nm. In particular, **APO_2-Pc_{60}** shows a promising photo-killing effect against human tumor cells in zebrafish larvae xenografts. This work is expected to have a positive effect in the future, long-term development of innovative artificial photo-oxidases for biomedical applications.

4.6. References

(1) Kou, J.; Dou, D.; Yang, L. Porphyrin photosensitizers in photodynamic therapy and its applications. *Oncotarget* **2017**, *8*, 81591-81603.

(2) Kassel, D. Photodynamic Therapy: A Brief History. *J. Clin. Med*. **2019**, *8* (*10*), 1581.

(3) Frochot, C.; Mordon, S. Update of the situation of clinical photodynamic therapy in Europe in the 2003–2018 period. *J. Porphyr. Phthalocyanines* **2019**, *23*, 347-357.

(4) Penetra, M.; Arnaut, L. G.; Gomes da Silva, L. C. Trial watch: an update of clinical advances in photodynamic therapy and its immunoadjuvant properties for cancer treatment. *OncoImmunology* **2023**, *12*, 2226535.

(5) Baskaran, R.; Lee, J.; Yang, S. G. Clinical development of photodynamic agents and therapeutic applications. *Biomater. Res*. **2018**, *22*, 25.

(6) Wainwright, M. Therapeutic applications of near-infrared dyes. *Color. Technol.* **2010**, *126*, 115-126.

(7) Pucelik, B.; Sułek, A.; Dąbrowski, J. M. Bacteriochlorins and their metal complexes as NIR-absorbing photosensitizers: properties, mechanisms, and applications. *Coord. Chem. Rev.* **2020**, *416*, 213340.

(8) Lo, P.-C.; Rodriguez-Morgade, M. S.; Ng, D. K. P.; Torres, T.; Pandey, R.; Dumoulin, F. The unique features and promises of phthalocyanines as advanced photosensitisers for photodynamic therapy of cancer. *Chem. Soc. Rev.* **2020**, *49*, 1041-1056.

(9) Zhang, Y.; Lovell, J. F. Recent applications of phthalocyanines and naphthalocyanines for imaging and therapy. *WIREs Nanomed. Nanobiotechnol.* **2017**, *9*, e1420.

(10) Almeida-Marrero, V.; van de Winckel, E.; Anaya-Plaza, E.; Torres, T.; de la Escosura, A. Porphyrinoid biohybrid materials as an emerging toolbox for biomedical light management. *Chem. Soc. Rev.* **2018**, *47*, 7369-7400.

(11) Li, X.; Zheng, B.-D.; Peng, X.-H.; Li, S.-Z.; Ying, J.-W.; Zhao, Y.; Huang, J.-D.; Yoon, J. Phthalocyanines as medicinal photosensitizers: Developments in the last five years. *Coord. Chem. Rev.* **2019**, *379*,147-160.

(12) Dumoulin, F.; Durmus, M.; Ahsen, V.; Nyokong, T. Synthetic pathways to water-soluble phthalocyanines. *Coord. Chem. Rev.* **2010**, *254*, 2792-2847.

(13) Obaid, G.; Broekgaarden, M.; Bulin, A.-L.; Huang, H.-C.; Kuriakose, J.; Liu, J.; Hasan, T. Photonanomedicine: a convergence of photodynamic therapy and nanotechnology. *Nanoscale*, **2016**, *8*, 12471-12503.

(14) Wilhelm, S.; Tavares, A. J.; Dai, Q.; Ohta, S.; Audet, J.; Dvorak, H. F.; Chan, W. C. W. Analysis of nanoparticle delivery to tumours. *Nat. Rev. Mater*. **2016**, *1*, 16014.

(15) Love, W. G.; Duk, S.; Biolo, R.; Jori, G.; Taylor, P. W. Liposome-Mediated Delivery of Photosensitizers: Localization of Zinc (II)-Phthalocyanine within Implanted Tumors after Intravenous Administration. *Photochem. Photobiol.* **1996**, *63*, 656-661.

(16) Pucelik, B.; Gürol, I.; Ahsen, V.; Dumoulin, F.; Dąbrowski, J. M. Fluorination of phthalocyanine substituents: Improved photoproperties and enhanced photodynamic efficacy after optimal micellar formulations. *Eur. J. Med. Chem.* **2016**, *124*, 284-298.

(17) Pehlivan, E. G.; Ek, Y.; Topkaya, D.; Tazebay, U. H.; Dumoulin, F. Effect of PVP formulation on the in vitro photodynamic efficiency of a photosensitizing phthalocyanine. *J. Porphyr. Phthalocyanines* **2019**, *23*, 1587-1591.

(18) Kiew, L. V.; Cheah, H. Y.; Voon, S. H.; Gallon, E.; Movellan, J.; Ng, K. H.; Alpugan, S.; Lee, H. B.; Dumoulin, F.; Vicent, M. J.; Chung, L. Y. Near-infrared activatable phthalocyanine-poly-L-glutamic acid conjugate: increased cellular uptake and light-dark toxicity ratio towards an effective photodynamic cancer therapy. *Nanomed.-Nanotechnol. Biol. Med.* **2017**, *13*, 1447-1458.

(19) Cheah, H. Y.; Gallon, E.; Dumoulin, F.; Hoe, S. Z.; Japundžić-Žigon, N.; Glumac, S.; Lee, H. B.; Anand, P.; Chung, L. Y.; Vicent, M. J.; Kiew, L. V. Near-Infrared Activatable Phthalocyanine− Poly-L-Glutamic Acid Conjugate: Enhanced in Vivo Safety and Antitumor Efficacy toward an Effective Photodynamic Cancer Therapy. *Mol. Pharm.* **2018**, *15*, 2594-2605.

(20) Ekineker, G.; Nguyen, C.; Bayir, S.; Dominguez-Gil, S.; Isci, U.; Daurat, M.; Godefroy, A.; Raehm, L.; Charnay, C.; Oliviero, E.; Ahsen, V.; Gary-Bobo, M.; Durand, J.-O.; Dumoulin, F. Phthalocyanine-based mesoporous organosilica nanoparticles: NIR photodynamic efficiency and siRNA photochemical internalization. *Chem. Commun.* **2019**, *55*, 11619-11622.

(21) Mauriello-Jimenez, C.; Henry, M.; Aggad, D.; Raehm, L.; Charnay, C.; Cattoen, X.; Man, M. W. C.; Alpugan, S.; Ahsen, V.; Tarakcı, D. K.; Maillard, P.; Maynadier, M.; Garcia, M.; Dumoulin, F.; Gary-Bobo, M.; Coll, J.-L.; Josserand, V.; Durand, J.-O. Porphyrin- or phthalocyanine- bridged silsesquioxane theranostic

nanoparticles for two-photon imaging, photodynamic therapy or photoacoustic imaging. *Nanoscale* **2017**, *9*, 16622-16626.

(22) Gergely, L. P.; Yüceel, Ç.; İşci, Ü.; Spadin, F. S.; Schneider, L.; Spingler, B.; Frenz, M.; Dumoulin, F.; Vermathen, M. Comparing PVP and Polymeric Micellar Formulations of a PEGylated Photosensitizing Phthalocyanine by NMR and Optical Techniques. *Mol. Pharmaceutics* **2023**, *20*, 4165-4183.

(23) Pia, A.; Kröger, P.; Paulusse, J. M. J. Single-chain polymer nanoparticles in controlled drug delivery and targeted imaging. *J. Control. Release* **2018**, *286*, 326-347.

(24) Pia, A.; Kröger, P.; Hamelmann, N. M.; Juan, A.; Lindhoud, S.; Paulusse, J. M. J. Biocompatible Single-Chain Polymer Nanoparticles for Drug Delivery-A Dual Approach. *ACS Appl. Mater. Interfaces* **2018**, *10*, 30946-30951.

(25) Pomposo, J. A., Ed.; *Single-Chain Polymer Nanoparticles: Synthesis, Characterization, Simulations, and Applications*; John Wiley & Sons: Weinheim, Germany, **2017**.

(26) Liu, Y.; Pujals, S.; Stals, P. J. M.; Paulöhrl, T.; Presolski, S. I.; Meijer, E. W.; Albertazzi, L.; Palmans, A. R. A. Catalytically Active Single-Chain Polymeric Nanoparticles: Exploring Their Functions in Complex Biological Media. *J. Am. Chem. Soc.* **2018**, *140*, 3423-3433.

(27) Jeong, J.; Lee, Y.-J.; Kim, B.; Kim, B.; Jung, K.-S.; Paik, H.-J. Colored single-chain polymeric nanoparticles via intramolecular copper phthalocyanine formation. *Polym. Chem.* **2015**, *6*, 3392-3397.

(28) Kramer, W. W.; McCrory, C. C. L. Polymer coordination promotes selective CO_2 reduction by cobalt phthalocyanine. *Chem. Sci.* **2016**, *7*, 2506-2515.

(29) Ackroyd, R.; Kelty, C.; Brown, N.; Reed, M. The history of photodetection and photodynamic therapy. *Photochem. and Photobiol*., **2001**, 74, 656–669

(30) Hönigsmann, H. History of phototherapy in dermatology. *Photochem. Photobiol. Sci.* **2013**, 12, 16-21

(31) Algorri, J. F.; Ochoa, M.; Roldán-Varona, P.; Rodríguez-Cobo, L.; López-Higuera, J. M. Photodynamic therapy: a compendium of latest reviews. *Cancers* **2021**, 13, 4447.

(32) Raab, O. Uber die wirkung fluoreszierender stoffe auf infusorien. *Zeitung Biol.* **1990**, 39, 524-526.

(33) von Tappeiner, H.; Jesionek, A. Therapeutische versuche mit fluoreszierenden stoffen. *Muench Med. Wochenschr.* **1903**, 47, 2042–2044.

(34) Dolman, D. E. J. G. J.; Fukumura, D.; Jain, R. K. Photodynamic therapy for cancer. *Nature Rev. Cancer* **2003**, 3, 380-387.

(35) Betz, MF. Untersuchungen uber die biologisme (photodynamische) wirkung des hemotoprophyrins und anderer derivate des blut und gallenfarbstoffs. *Dtsch. Arch. Klin Med.* **1913**, 112, 476–503.

(36) Soriano, J.; Villanueva, A.; Stockert, J. C.; Cañete, M. Regulated necrosis in HeLa cells induced by ZnPc photodynamic treatment: a new nuclear morphology. *Int. J. Mol. Sci.* **2014**, 15, 22772–22785.

(37) Chen, B.; Pogue, B. W., Luna, J. M.; Hardman, R. L.; Hoopes, P. J.; Hasan, T. Tumor vascular permeabilization by vascular-targeting photosensitization: effects, mechanism, and therapeutic implications. *Clin Cancer Res* **2006**, 12, 917–923.

(38) Escudero, A.; Carrillo-Carrión, C. Castillejos, C.; Romero-Ben, E.; Rosales-Barrios, C.; Khiar, N. Photodynamic therapy: photosensitizers and nanostructures. *Mater- Chem. Front.* **2021**, 5, 3788-3812.

(39) Blumenkranz, M. S.; Woodburn, K. W.; Qing, F.; Verdooner, S.; Kessel, D.; Miller, R. Lutetium texaphyrin (Lu-Tex): a potential new agent for ocular fundus angiography and photodynamic therapy. *Am. J. of Ophtalmol.* **2000**, 129, 353-362.

(40) Monro, S.; Colón, K. L.; Yin, H.; Roque, J.; Konda, P.; Gujar, S.; Thummel, R. P.; Lilge, L.; Cameron, C. G.; McFarland, S. A. Transition metal complexes and photodynamic therapy from a tumor-centered approach: challenges, opportunities, and highlights from the development of TLD1433. *Chem. Rev.* **2019**, 119, 797-828.

(41) García-Fresnadillo, D.; Georgiadou, Y.; Orellana, G.; Braun, A. M.; Oliveros, E.; Singlet-oxygen (1Dg) production by ruthenium(II) complexes containing polyazaetherocyclic ligands in methanol and in water. *Helv. Chim. Acta*, **1996**, 79, 1222-1238.

(42) Lucky, S. S.; Soo, K. C.; Zong, Y. Nanoparticles in photodynamic therapy. *Chem. Rev.* **2015**, 115, 1990-2042.

(43) Park, J.; Choi, Y.; Chang, H.; Um, W.; Ryu, J. H.; Kwon, I. C. Alliance with EPR effect: combined strategies to improve the EPR effect in the tumor microenvironment. *Theranostics* **2019**, 9, 8073-8090.

(44) Popp, J.; Tuchin, V. V.; Chian, A. Handbook of Biophotonics Vol. 2: Photonics for Health Care, I Ed. *Wiley-VCH* **2012**.

(45) Paszko, E.; Ehrhardt, C.; Senge, M. O.; Kelleher, D. P.; Reynolds, J. V. Nanodrug applications in photodynamic therapy *Photodiagn. Photodyn. Ther*. **2011**, 8, 14.

(46) Alea-Reyes, M. E.; Soriano, J.; Mora-Espí, I.; Rodrigues, M.; Russell, D. A.; Barrios, L.; Pérez-García, L. Amphiphilic Gemini pyridinium-mediated incorporation of Zn(II)meso-tetrakis(4-carboxyphenyl)porphyrin into water-soluble gold nanoparticles for photodynamic therapy. *Colloids Surf. B.* **2017**, 158, 602-609.

(47) Camerin, M.; Moreno, M.; Marín, M. J.; Schofield, C. L.; Chambrier, I.; Cook, M. J.; Coppellotti, O.; Jori, G.; Russell, D. A.; Delivery of a hydrophobic phthalocyanine photosensitizer using PEGylated gold nanoparticle conjugates for the in vivo photodynamic therapy of amelanotic melanoma. *Photochem. Photobiol. Sci.* **2016**, 15, 618-625.

(48) Bayir, S.; Barros, A.; bankherrab, R.; Szunerits, S.; Rachm, L.; Richeter, S.; Durand, J. O. Mesoporous silica nanoparticles in recent photodynamic therapy applications. *Photochem. Photobiol. Sci.* **2018**, 17, 1651-1674.

(49) Cheng, J.; Fon, T.; Xie, Z.; zeng, L.; Xue, P.; Zheng, T.; Chen, Y.; Luo, X.; Zhong, H.; Advanced in nanomaterials for photodynamic therapy applications: status and challenges. *Biomat.* **2020**, 237, 119827.

(50) Chen, Y.; Hou, S. Recent progress in the effect of magnetic iron oxide nanoparticles on cells and extracellular vesicles. *Cell Death Disc.* **2023**, 9, 195.

(51) Frtús, A.; Smolková, B.; Uzhytchak, M.; Lunova, M.; Jirsa, M.; Kubinová, S.; Dejneka, A.; Lunov, O. Analyzing the mechanisms of iron oxide nanoparticles interactions with cells: a road from failure to success in clinical applications. *J. Control. Rel.* **2020**, 328, 59-77.

(52) a) Zhang, P.; Wu, G.; Zhao, C.; Zhou, L.; Wang, X.; Wei, S.; Magnetic stomatocyte-like nanomotor as photosensitizer carrier for photodynamic therapy based cancer treatment. *Colloids Surf. B.* **2020**, 194, 111204. b) Di Corato, R.; Béalle, G.; Kolosnjaj-Tabi, J.; Espinosa, A.; Clément, O.; Silva, A. K. A.; Ménager, C.; Wilhelm, C. Combining magnetic hyperthermia and photodynamic therapy for tumor ablation with photoresponsive magnetic liposomes. *ACS Nano*, **2015**, 9, 2904-2916.

(53) Van Nostrum, C. Polymeric micelles to deliver photosensitizers for photodynamic therapy. *Adv. Drug Deliv. Rev.* **2004**, 56, 9-16.

(54) a) Kotta, S.; Aldawasari, H. M.; Badr-Eldin, S. M.; Nair, A. B.; YT, K. *Pharmaceutics* **2022**, 14, 1636. b) Bose, A.; Roy, B.; Sikdar, B.; Patra, P. *IET Nanobiotechnol.* **2021**, 15, 19–27. c) Zhang, Y.; Huang, Y.; Li, S. *AAPS PharmSciTech* **2014**, 15, 862-871.

(55) Hamelmann, N. M.; Paats, J.-W. D.; Paulusse, J. M. J. Cytosolic delivery of single-chain polymer nanoparticles. *ACS Macro Lett.* **2021**, 10, 11, 1443–1449.

(56) Hamelmann, N. M.; Paulusse, J. M. J. Single-chain polymer nanoparticles in biomedical applications. *J. Control. Rel.* **2023**, 356, 26-42.

(57) Liu, Y.; Pauloehrl, T.; Presolski, S. I.; Albertazzi, L.; Palmans, A. R. A.; Meijer, E. W. Modular synthetic platform for the construction of functional single-chain polymeric nanoparticles: from aqueous catalysis to photosensitization. *J. Am. Chem. Soc.* **2015**, 137, 40, 13096-131105.

(58) Liu, Y.; Pujals, S.; Stals, P. J. M.; Paulöhrl, T.; Presolski, S. I.; Meijer, E. W.; Albertazzi, L.; Palmans, A. R. A. Catalitically active single-chain polymeric nanoparticles: exploring their functions in complex biological media. *J. Am. Chem. Soc.* **2018**, 140, 9, 3423–3433.

(59) Ávila-Rovelo, N. R.; Ruiz-Carretero, A. Recent progress in hydrogen-bonded π-conjugated systems displaying J-type aggregates. *Org. Mat.* **2020**, 2, 47-63.

(60) Ben-Shen, A.; Frolow, F.; Nelson, N. Crystal structure of plant photosystem I. *Nature*, **2003**, 426, 630-635.

(61) Jensen, P. E.; Bassi, R.; Boekma, E. J.; Dekker, J. P.; Jansson, B.; Leister, D.; Robinson, C.; Scheller, H. V. Structure, function and regulation of plant photosystem I. *Bioenergetics*, **2007**, 5, 335-352.

(62) Valiente-gabiond, A. A.; Miotto, M. C.; Chesta, M. E.; Lombardo, V.; Binolfi, A.; Fernández, C. O. Phthalocyanines as molecular scaffolds to block disease-associated protein aggregation. *Acc. Chem. Res.* **2016**, 49, 801-808.

(63) Haldar, R.; Mazel, A.; Kristić, M.; Zhong, A.; Jakoby, M.; Haward, I. A.; Richards, B. S.; Jung, N.; Jacquemin, D.; Diring, S.; Wenzel, W.; Odobel, F.; Wóll, C. Excitonically coupled states in crystalline coordination networks. *Nat. Commun.* **2019**, 10, 2048.

(64) Chen, H.; Martín-Gormis, L.; Xiu, Z.; Fischer, J. C.; Howard, I. A.; Herrero, D.; Sobrino-Bastán, V.; Sastre-Santos, Á.; Haldar, R.; Wöll, C. Tunable J-type aggregation of silicon phthalocyanines in a surface-anchored metal-organic framework thin film. *Phys. Chem. Chem. Phys*. **2023**, 25, 19626-19632.

(65) a) Bettini, S.; Valli, L.; Giancane, G.; Application of photoinduced phenomena in supramolecularly arranged phthalocyanine derivatives: a perspective. *Molecules*, **2020**, 25, 3742. b) Garifullin, R.; Erkal, T. S.; Tekin, S.; Ortas, B.; Gürek, A. G.; Ahsen, V.; Yaglioglu, H. G.; Elmali, A.; Guler, M. O. Encapsulation of a zinc phthalocyanine derivative in self-assembled peptide nanofibers. *J. Mater. Chem.* **2012**, 22, 2553-2559.

(66) Conte, C.; Scala, A.; Siracusano, G.; Leone, N.; Patanè, S.; Ungaro, F.; Miro, A.; Sciortino, M. T.; Quaglia, F.; Mazzaglia, A. Nanoassembly of an amphiphilic cyclodextrin and Zn(II)-phthalocyanine with the potential for photodynamic therapy of cancer. *RSC Adv.* **2014**, 4, 43903-43911.

(67) Sanchez-Sanchez, A.; Arbe, A.; Kohlbrecher, J.; Colmenero, J.; Pomposo, J. A. Efficient Synthesis of single-chain globules mimicking the morphology and polymerase activity of metalloenzyme. *Macromol. Rapid Commun.* **2015**, 36, 1592.

(68) Robles-Hernandez, B.; González, E.; Pomposo, J. A.; Colmenero, J.; Alegría, A. Water dynamics and self-assembly of single-chain nanoparticles in concentrated solutions. *Soft Matter*, **2020**, 16, 9738.

(69) Gao, Y.; Liu, H.; Zhang, S.; Gu, Q.; Shen, Y.; Ge, Y.; Yang, B. Excimer formation and evolution of excited state properties in discrete dimeric stacking of an anthracene derivative: a computational investigation. *Phys. Chem. Chem. Phys.* **2018**, 20, 12129.

(70) Idowu, M.; Nyokong, T. Photophysical and photochemical properties of zinc and aluminum phthalocyanines in the presence of magnetic fluid. *J. Photochem. Photobiol. A: Chem.* **2007**, *188* (*2-3*), 200-206.

(71) Topal, S. Z.; İşci, Ü.; Kumru, U.; Atilla, D.; Gürek, A. G.; Hirel, C.; Durmuş, M.; Tommasino, J.-B.; Luneau, D.; Berber, S., Dumoulin, F.; Ahsen, V. Modulation of the electronic and spectroscopic properties of Zn(II) phthalocyanines by their substitution pattern. *Dalton Trans.* **2014**, *43*, 6897-6908.

(72) Zou, J.; Li, L.; Zhu, J.; Li, X.; Yang, Z.; Huang, W.; Chen, X. Singlet Oxygen "Afterglow" therapy with NIR-II fluorescent molecules. *Adv. Mater.* **2021**, 33, 2103627.

(73) Dikaloy, S. I.; Harrison, D. G. Methods for detection of mitochondrial and cellular reactive oxygen species. *Antioxid. Redox Signal.* **2014**, 20, 372.

(74) White, R.; Rose, K.; Zon, L.; *Nat. Rev. Cancer* **2013**, 13, 624.

Conclusions

In conclusion, we present three different novel, water soluble, visible-light harvesting SCNPs systems, all relying on the spontaneous self-folding / collapse of the respective photoactive amphiphilic polymeric precursors. In particular, we focused on employing the opportunities offered by our easily-accessible SCNPs unique topology to enable advanced applications of **visible-light photocatalysis in aqueous media**, such as for organic photocatalysis and PDT of cancer.

In a first work, we introduced the preparation and application of artificial photosynthase (**APS**), water-soluble SCNPs endowed with manifold photocatalytic activity towards a variety of organic reactions. We designed an amphiphilic polymeric precursor of defined molecular weight and dispersity, which was subsequently decorated with an iridium(III)-based cyclometalated complex through a mild post-polymerization functionalization. The prepared photoactive amphiphile copolymer resulted to efficiently self-assemble in aqueous solution by spontaneous self-assembly into a SCNP structure, as revealed by dynamic light scattering (DLS) techniques and as confirmed by UV-Visible spectrophotometry and fluorimetry. With the **APS** in hand, we then tested their ability to perform a variety of organic reactions. Specifically, we observed efficient visible-light induced photocatalytic activity for two unprecedently reported **organic reactions in water**: the photo[2+2]cycloaddition of vinyl arenes and the α-arylation of arylamines, as well as the oxidation of 9-substituted anthracenes and the β-sulfonylation of styrenic compounds. Preliminary kinetics data of the [2+2] photocycloaddition of vinyl arenes "*in water*" photocatalyzed by **APS** showed promising result in terms of closeness to what reported for some biotic enzymes such as Chymotrypsin and Pepsin. Describing and and reporting a first generation of **APS**,

we broadened broadening the possibilities for performing challenging "*in water*" organic transformations *via* visible-light photocatalysis.

In a second approach, we endowed SCNPs with photocatalytic activity by means of non-covalent encapsulation of a tailor-made photosensitizing metal complex. We developed a facile protocol for the preparation and non-covalent encapsulation of a long-wavelength absorbing zinc(II)-phthalocyanine (**ZnPc**) within the core of a synthesized PEG-based polymethacrylate. Taking advantage of the well-known self-assembly capability of anthracene molecules via π-π stacking, we prepared anthracene-based amphiphilic copolymers both capable of self-assembly in water and of efficiently encapsulating the far infrared-responsive complex **ZnPc**, yielding stable, water soluble, red-light reactive SCNPs, which we called artificial photo-oxidase (**APO-ZnPc**), due to their ability to generate oxidative stress upon light trigger. Interestingly, the readily prepared nano-assemblies showed different photoluminescent properties in the red region, depending on the overall anthracene molar fraction in the polymeric precursor.

After characterization of the nanoaggregates by SAXS techniques, we then tested their suitability for **photodynamic therapy** (PDT) of cancer applications. After assessing that **APO-ZnPc** presented no significant intrinsic (dark) cytotoxicity against human breast cancer MDA-MB-231 cells up to a nanoparticle concentration of 100 μg mL^{-1}, we tested this long-wavelength reactive amphiphilic SCNPs against human breast cancer cell MDA-MB-231 lines to assess their PDT efficiency, which resulted in outstanding performance for especially one of the selected formulations at two different excitation wavelengths (630 and 730 nm). We finally tested their PDT activity in zebrafish embryo xenografts, as a more accurate human cancer model. Having shown a promising photo-killing effect also against human tumor cells in zebrafish larvae xenografts, this work is expected to have a positive effect in the future, long-term development of innovative artificial photo-oxidases for biomedical applications.

This thesis has contributed to the following publications

- Arena, D. Verde-Sesto, E.; Pomposo, J. A. Stars, combs and bottlebrush of elastic single-chain nanoparticles. *Polymer* **2022**, 258, 125315.

- Arena, D.; Verde-Sesto, E.; Rivilla, I, Pomposo, J. A. Artificial Photosynthases: Single-Chain Nanoparticles with Manifold Visible-Light Photocatalytic Activity for Challenging "in Water" Organic Reactions. *J. Am. Chem. Soc.* **2024**, 10.1021/jacs.4c02718.

- Arena, D.; Ümit, İ.; Onofre, M.; Nguyen, C.; Sahin, Z.; Verde-Sesto, E.; Iturrospe, A.; Arbe, A.; Gary-Bobo, M.; Pomposo, J. A.; Dumoulin, F. Topology Effects in Photodynamic Therapy with Phthalocyanine Nanocarriers. *Submitted Article.*

- Arena, D.; Nguyen, C.; Ali, L. M. A.; Verde-Sesto, E.; Iturrospe, A.; Arbe, A.; Ümit, İ.; Sahin, Z.; Dumoulin, F.; Gary-Bobo, M.; Pomposo, J. A. Amphiphilic Single-Chain Polymer Nanoparticles as Imaging and Far-Red PhotoKilling Agents for Photodynamic Therapy in Zebrafish Embryo Xenografts. *Adv. Healthc. Mater.* **2024**, 10.1002/adhm.202401683. *Accepted article in production.*

- Pomposo, J. A.; Arena, D.; Verde-Sesto, E; Maiz, J.; Malo de Molina, P.; Moreno, A. Why Single-Chain Nanoparticles From weak polyelectrolytes can be synthesized at large scale in concentrated solution? *Submitted Article.*

Appendix to Chapter III

A.III.1. SEC chromatograms.

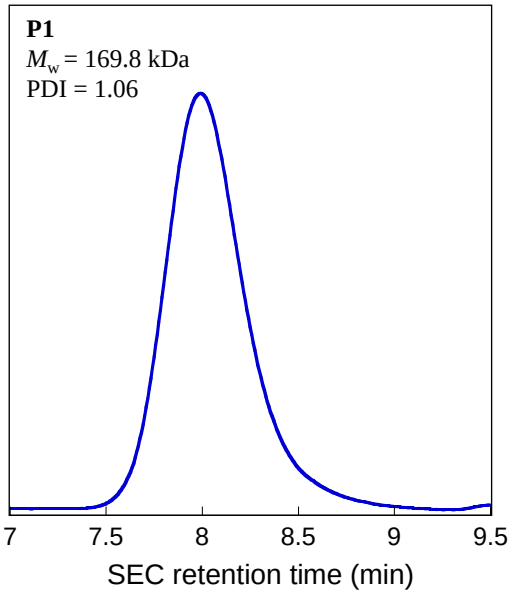

Figure A.III.1. SEC chromatogram of copolymer **P$_1$** (DRI detector, THF, 1 mL min^{-1}).

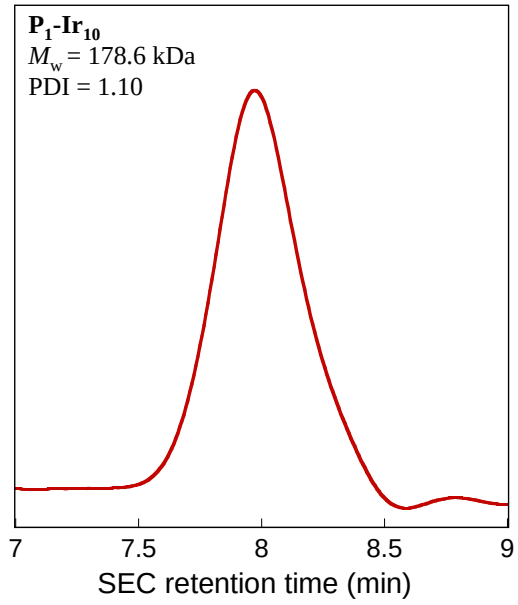

Figure A.III.2. SEC chromatogram of copolymer **P₁-Ir₁₀** (DRI detector, THF, 1 mL min^{-1}).

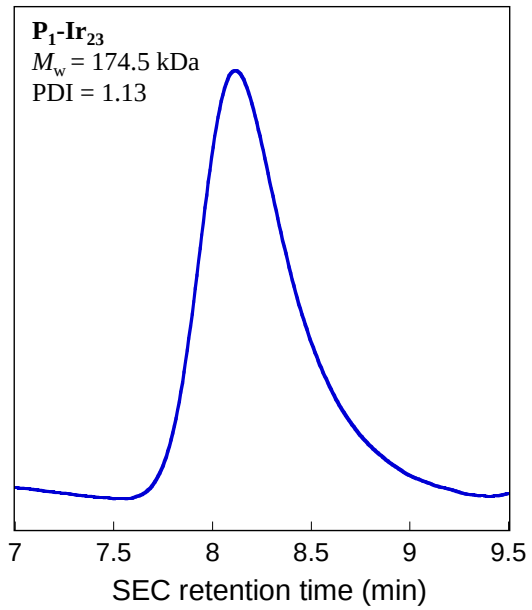

Figure A.III.3. SEC chromatogram of copolymer **P₁-Ir₂₃** (DRI detector, THF, 1 mL min^{-1}).

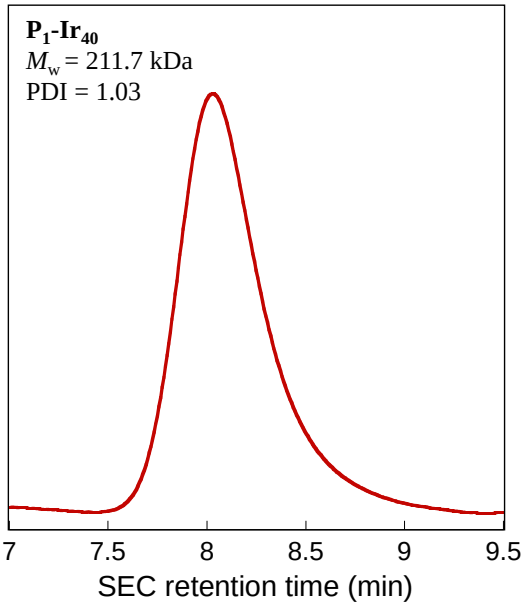

Figure A.III.4. SEC chromatogram of copolymer **P$_1$-Ir$_{40}$** (DRI detector, THF, 1 mL min^{-1}).

A.III.2. DLS Data

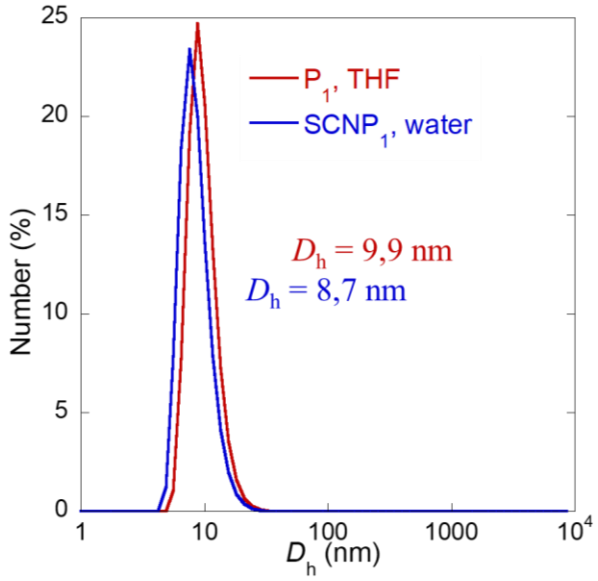

Figure A.III.5. DLS size distributions of copolymer **P_1** in THF (red line) and **SCNP-P_1** water (blue line) at a concentration of 4 mg mL^{-1}.

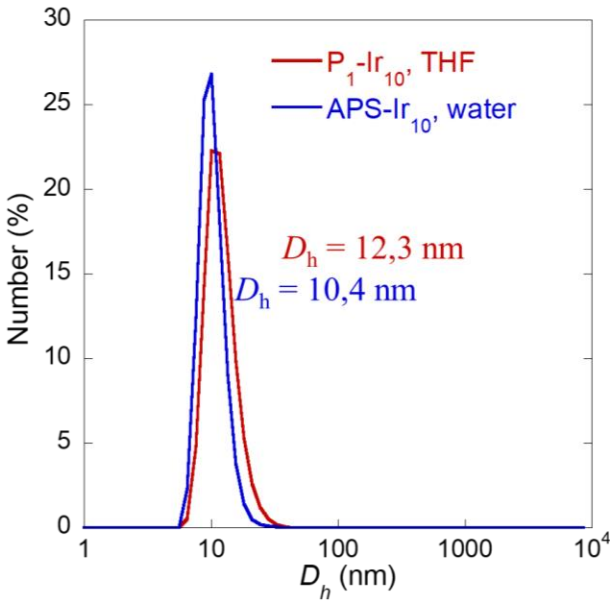

Figure A.III.6. DLS size distributions of **P_1-Ir_{10}** in THF (red line) and **APS-Ir_{10}** in water (blue line) at a concentration of 4 mg mL^{-1}.

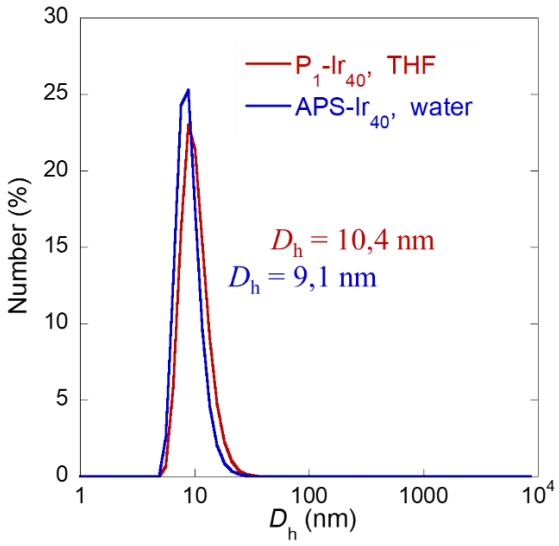

Figure A.III.7. DLS size distributions of **P_1-Ir_{40}** in THF (red line) and **APS-Ir_{40}** in water (blue line) at a concentration of 4 mg mL^{-1}.

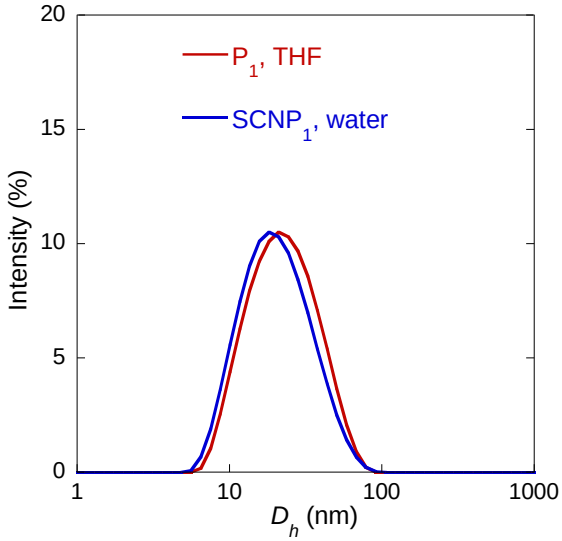

Figure A.III.8. DLS size distributions by scattered light intensity of **P_1** in THF (red line) and **$SCNP_1$** in water (blue line) at a concentration of 4 mg mL^{-1}.

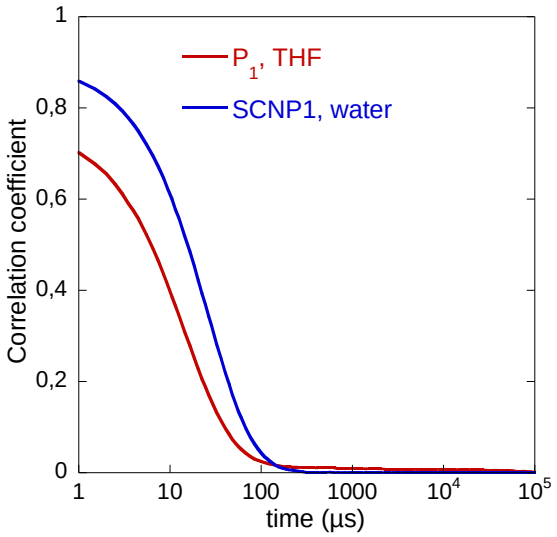

Figure A.III.9. DLS correlograms of **P₁** in THF (red line) and **SCNP₁** in water (blue line) at a concentration of 4 mg mL^{-1}.

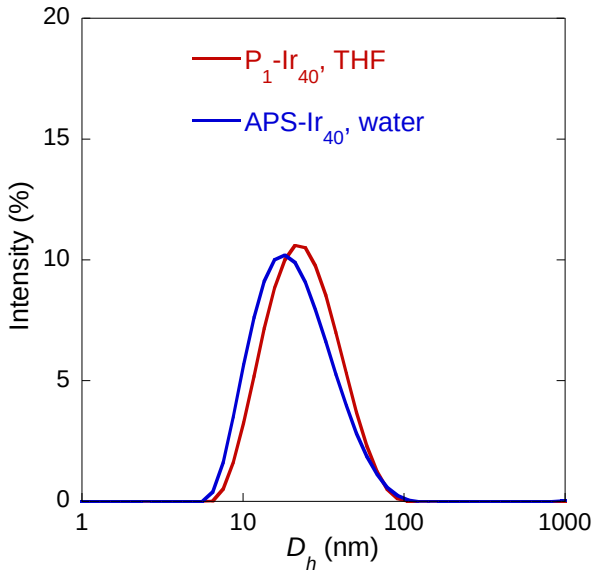

Figure A.III.10. DLS size distributions by scattered light intensity of **P₁-Ir₄₀** in THF (red line) and **APS-Ir₄₀** in water (blue line) at a concentration of 4 mg mL^{-1}.

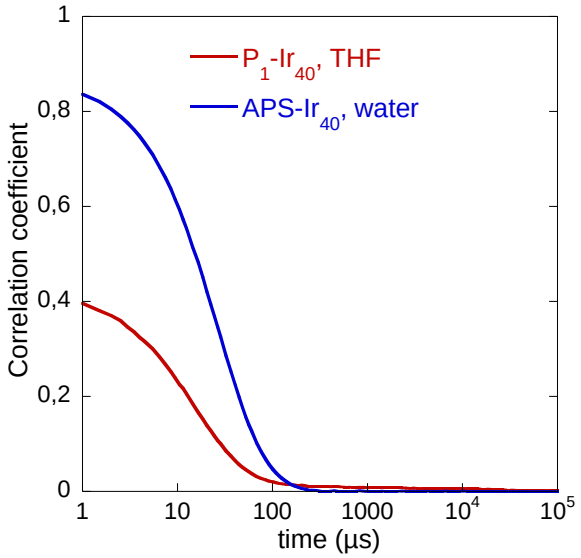

Figure A.III.11. DLS correlograms of **P₁-Ir₄₀** in THF (red line) and **APS-Ir₄₀** in water (blue line) at a concentration of 4 mg mL^{-1}.

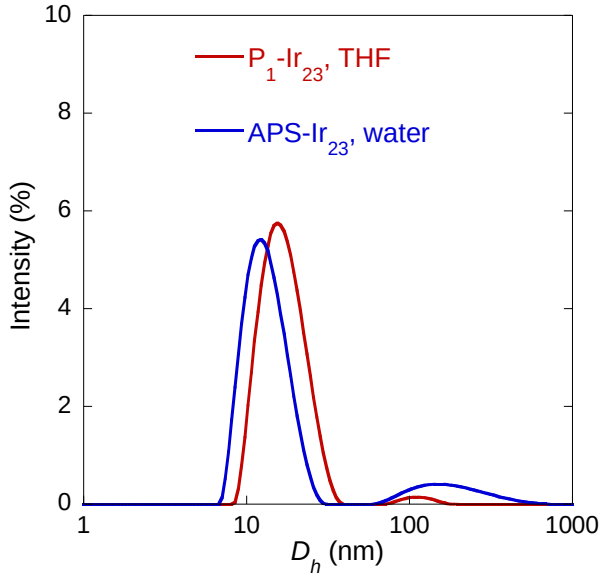

Figure A.III.12. DLS size distributions by scattered light intensity of **P₁-Ir₂₃** in THF (red line) and **APS-Ir₂₃** in water (blue line) at a concentration of 4 mg mL^{-1}.

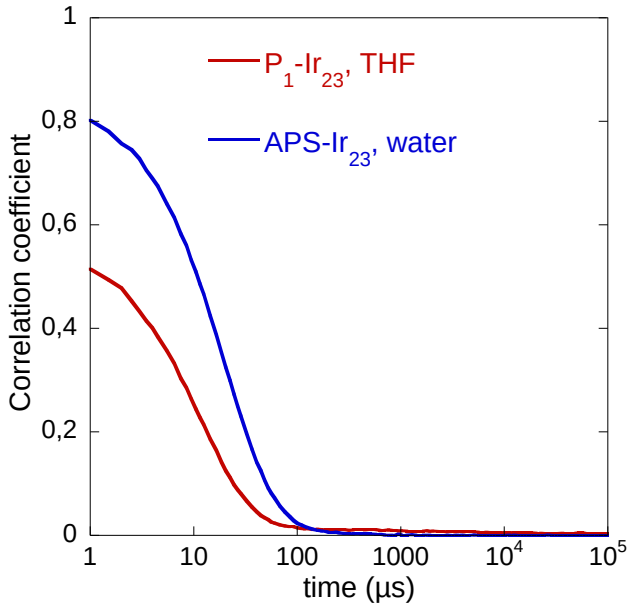

Figure A.III.13. DLS correlograms of **P₁-Ir₂₃** in THF (red line) and **APS-Ir₂₃** in water (blue line) at a concentration of 4 mg mL^{-1}.

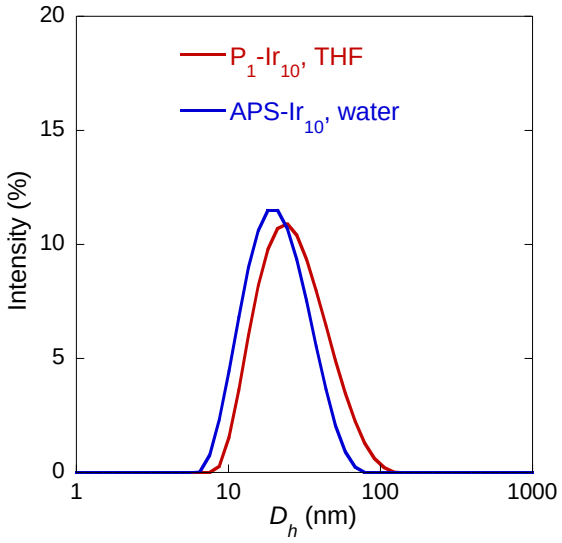

Figure A.III.14. DLS size distributions by scattered light intensity of **P_1-Ir_{10}** in THF (red line) and **APS-Ir_{10}** in water (blue line) at a concentration of 4 mg mL^{-1}.

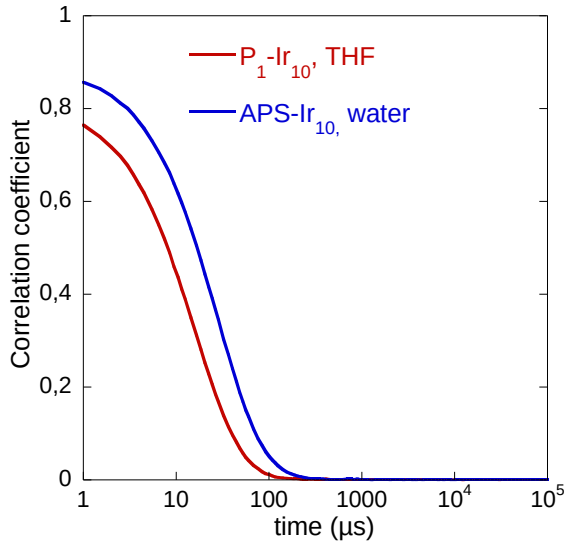

Figure A.III.15. DLS correlograms of **P_1-Ir_{10}** in THF (red line) and **APS-Ir_{10}** in water (blue line) at a concentration of 4 mg mL^{-1}.

A.III.3. Supplementary UV-Vis Spectra

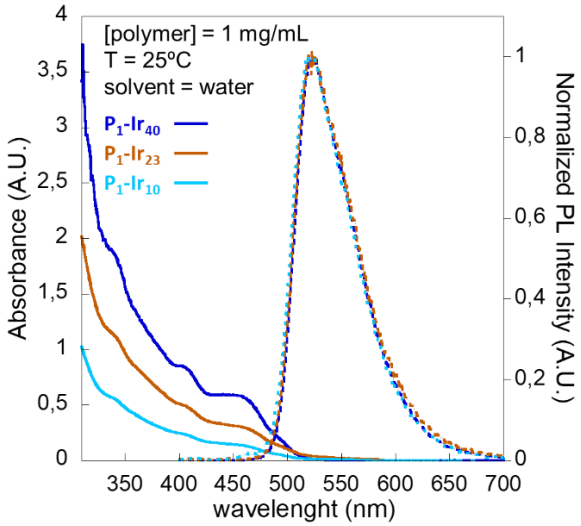

Figure A.III.16. Superimposed absorbance spectra of **P₁-Ir$_x$** in water all at a concentration of 1 mg mL^{-1} and respective normalized emission spectra, recorded with a λ_{exc} = 365 nm.

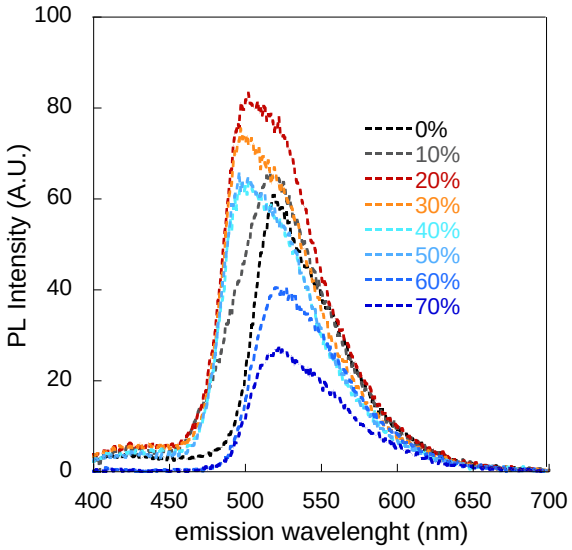

Figure A.III.17. Superimposed emission spectra of seven **C₂** ([**C₂**] = 3 µM) degassed solutions in THF at increasing water amount added (v/v%).

A.III.4. NMR Spectra

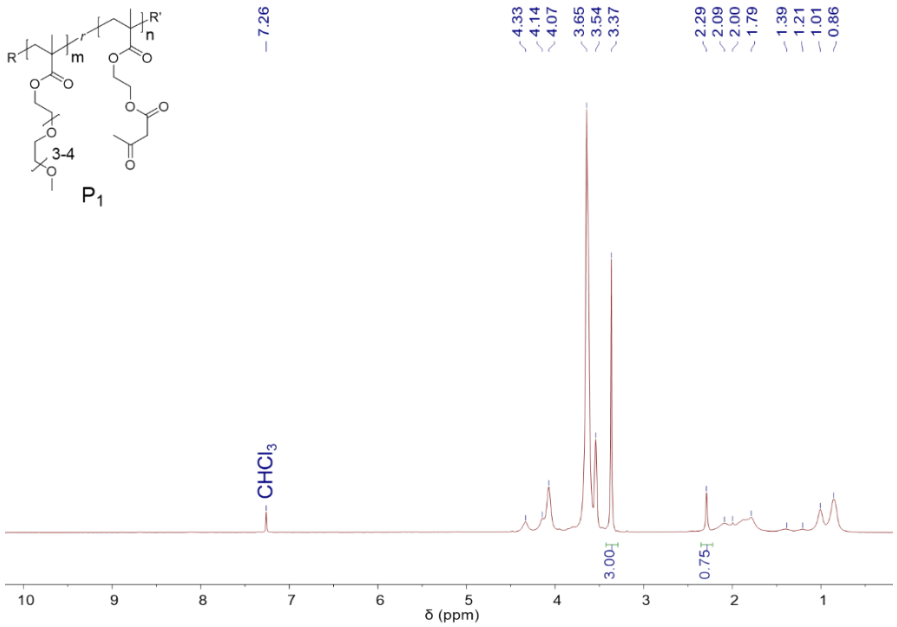

Figure A.III.18. ^{1}H NMR spectrum of **P$_1$**.

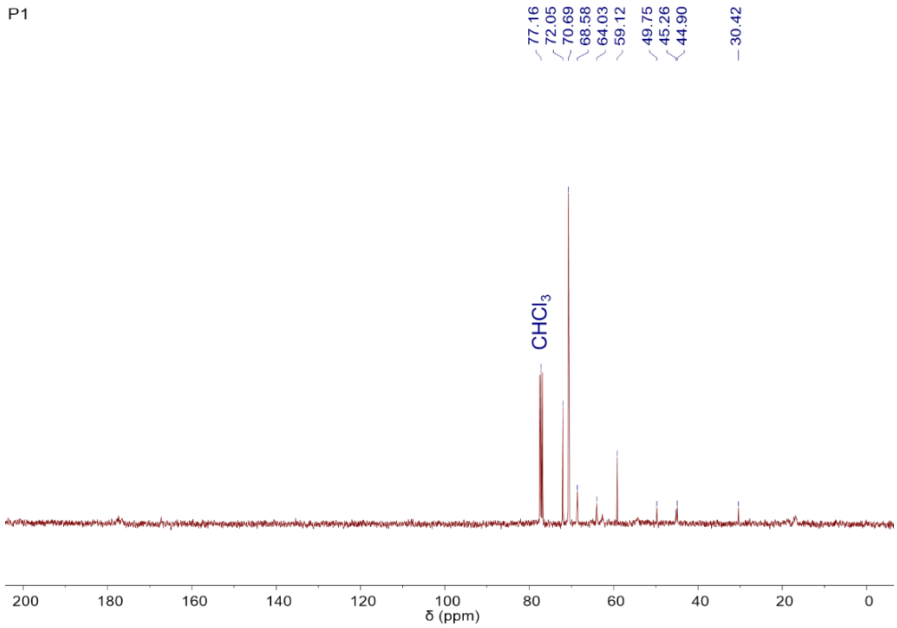

Figure A.III.19. ^{13}C NMR spectrum of **P$_1$**.

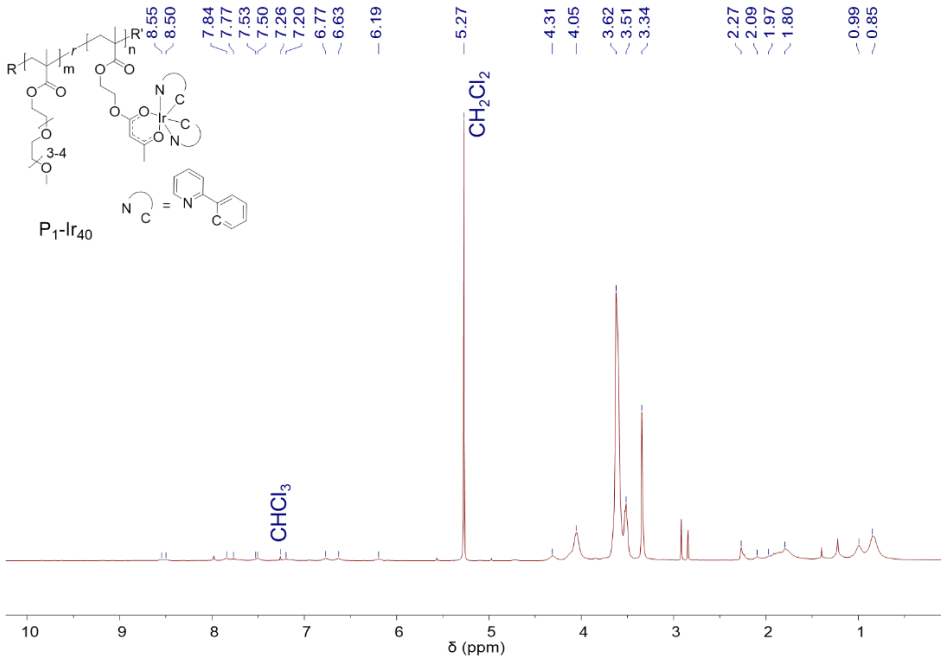

Figure A.III.20. ^{1}H NMR spectrum of **P_1-Ir_{10}.**

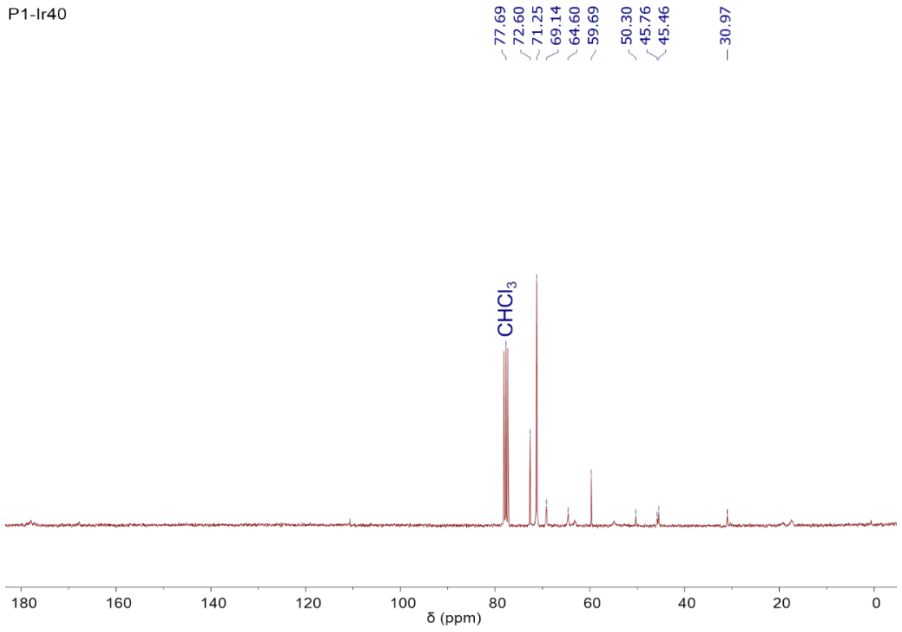

Figure A.III.21. ^{13}C NMR spectrum of **P_1-Ir_{10}.**

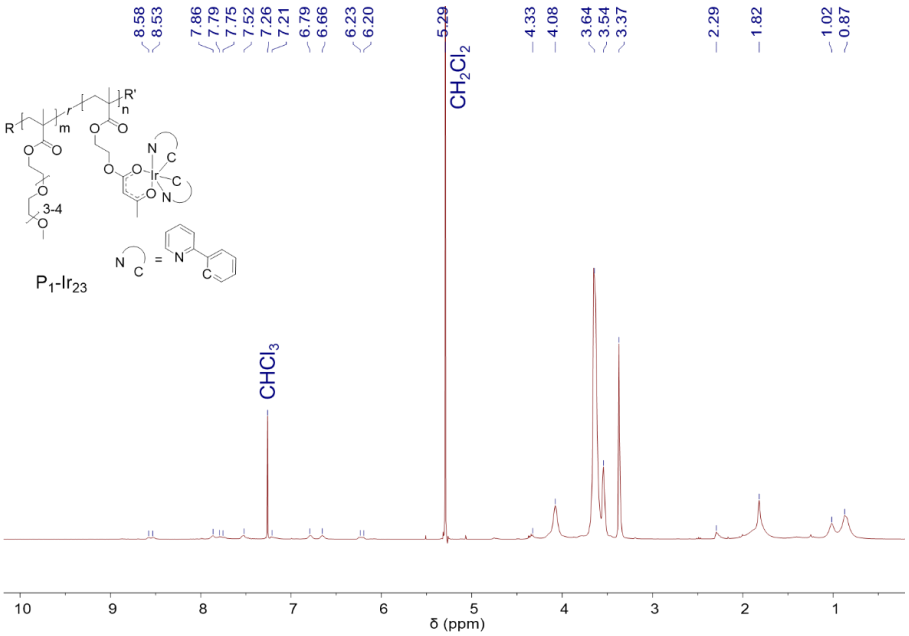

Figure A.III.22. ^{1}H NMR spectrum of **P_1-Ir_{23}**.

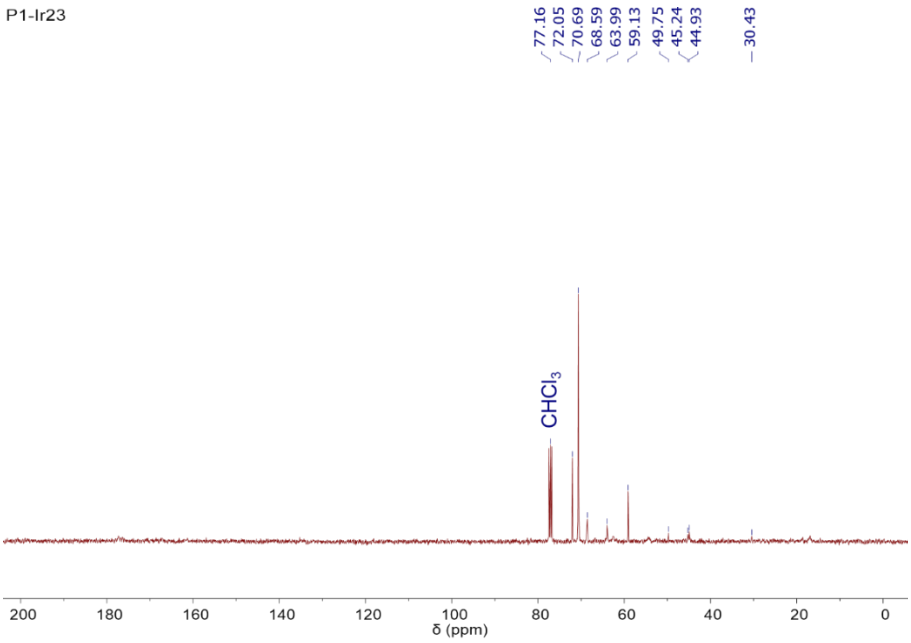

Figure A.III.23. ^{13}C NMR spectrum of **P_1-Ir_{23}**.

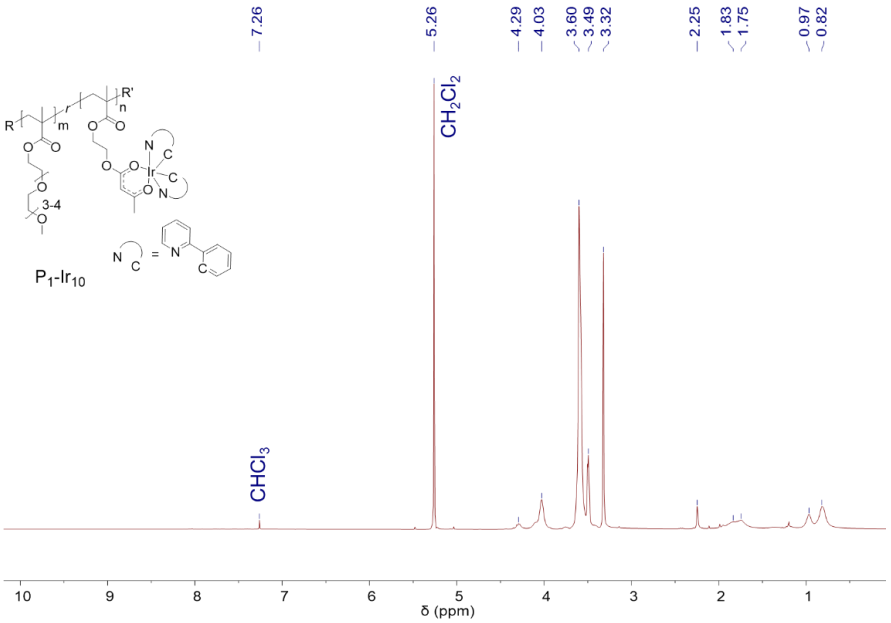

Figure A.III.24. ^{1}H NMR spectrum of **P_1-Ir_{40}**.

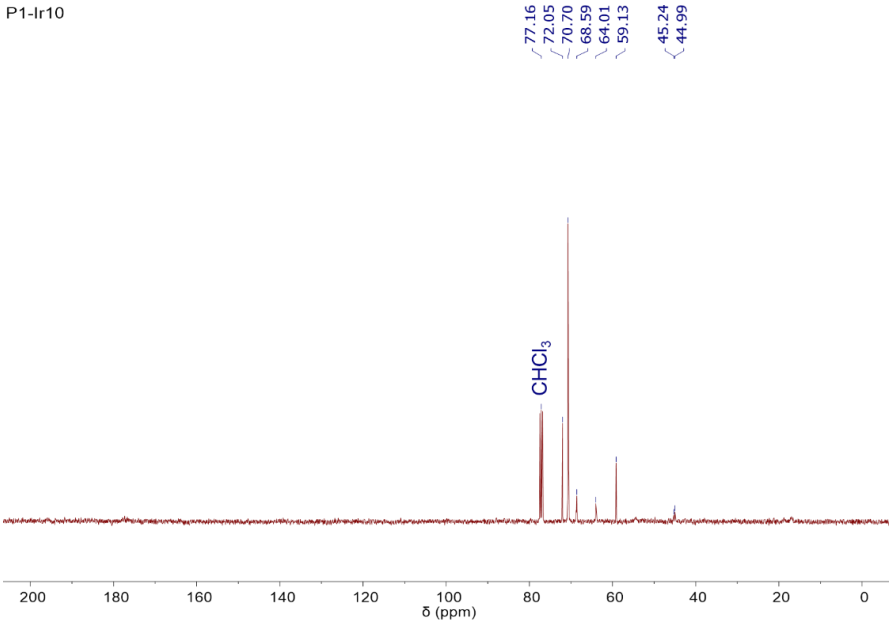

Figure A.III.25. ^{13}C NMR spectrum of **P_1-Ir_{40}**.

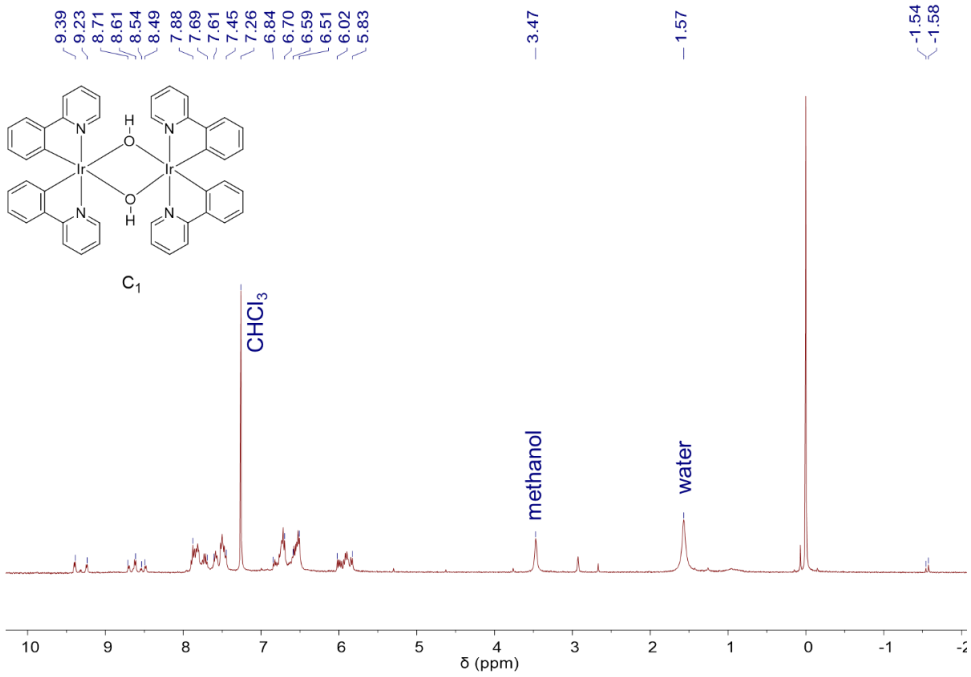

Figure A.III.26. ^{1}H NMR spectrum of **C$_1$**.

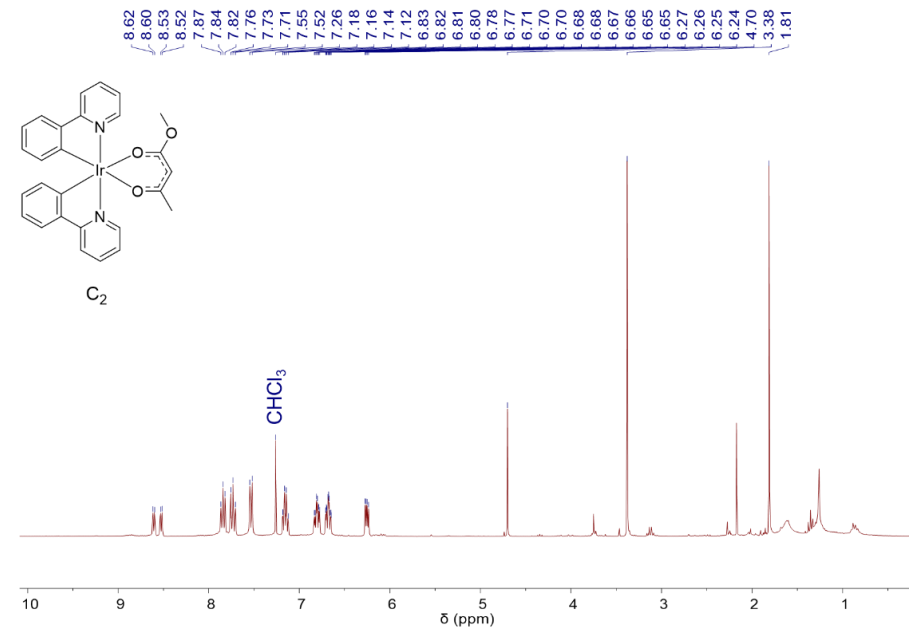

Figure A.III.27. ^{1}H NMR spectrum of **C$_2$**.

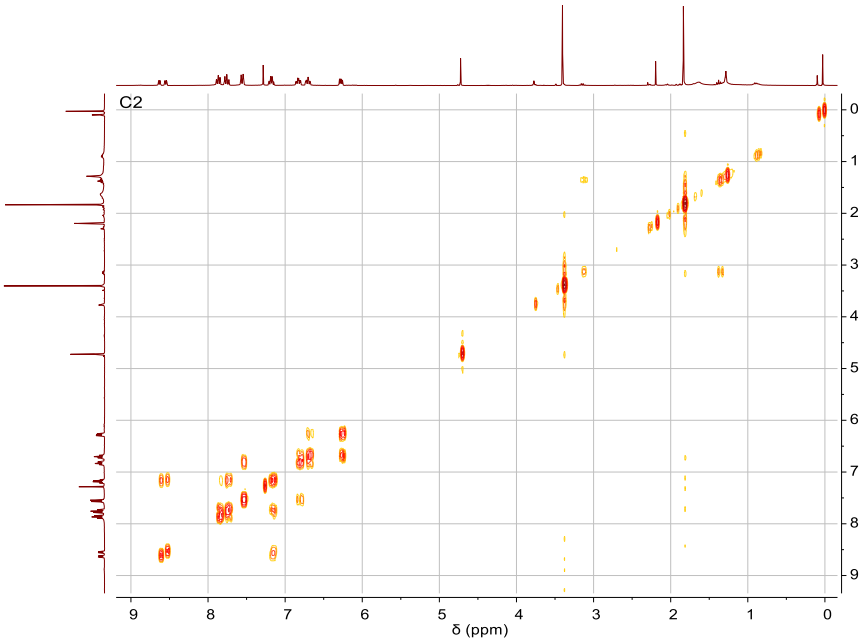

Figure A.III.28. ^{1}H COSY spectrum of **C$_2$**.

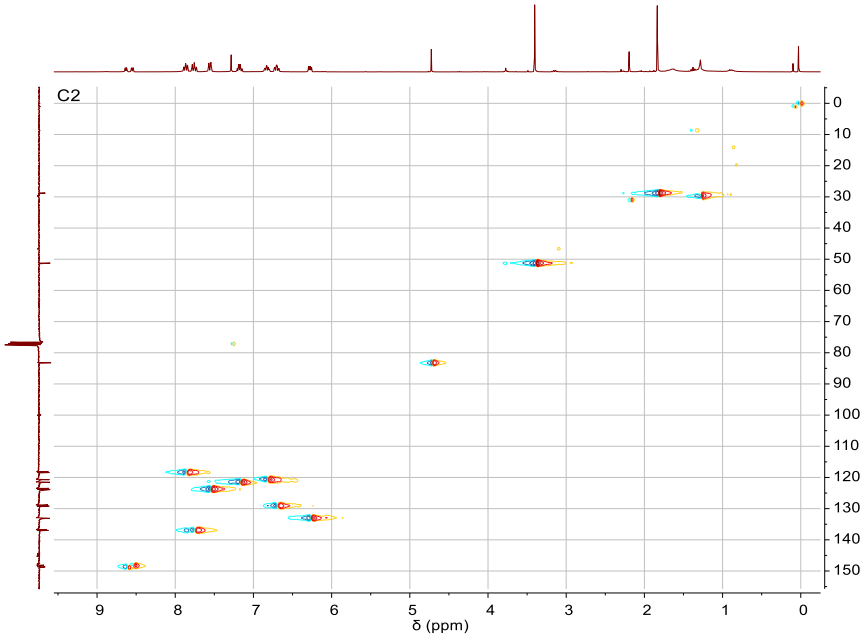

Figure A.III.29 ^{1}H-^{13}C HSQC spectrum of **C$_2$**.

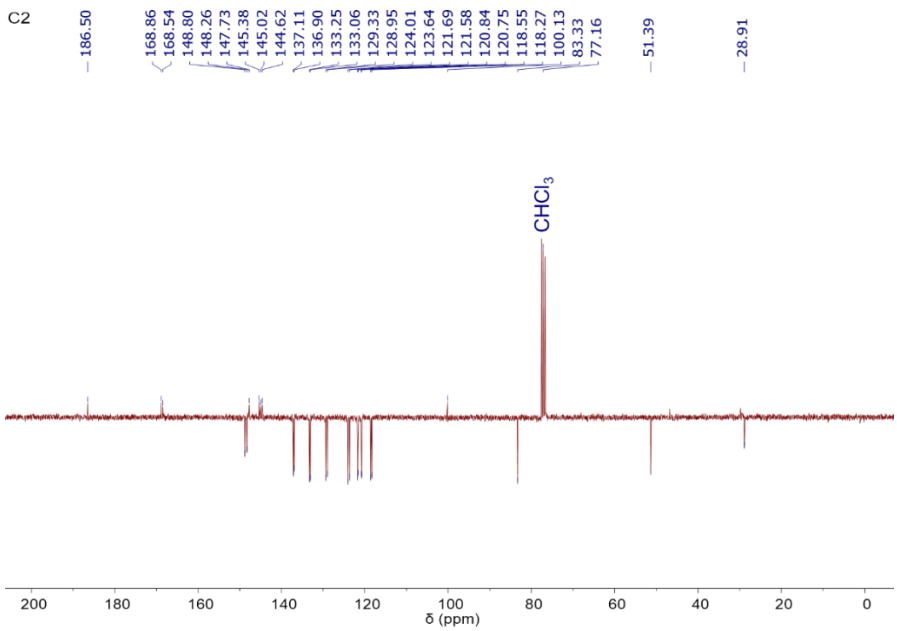

Figure A.III.30. ^{13}C DEPT spectrum of **C2**.

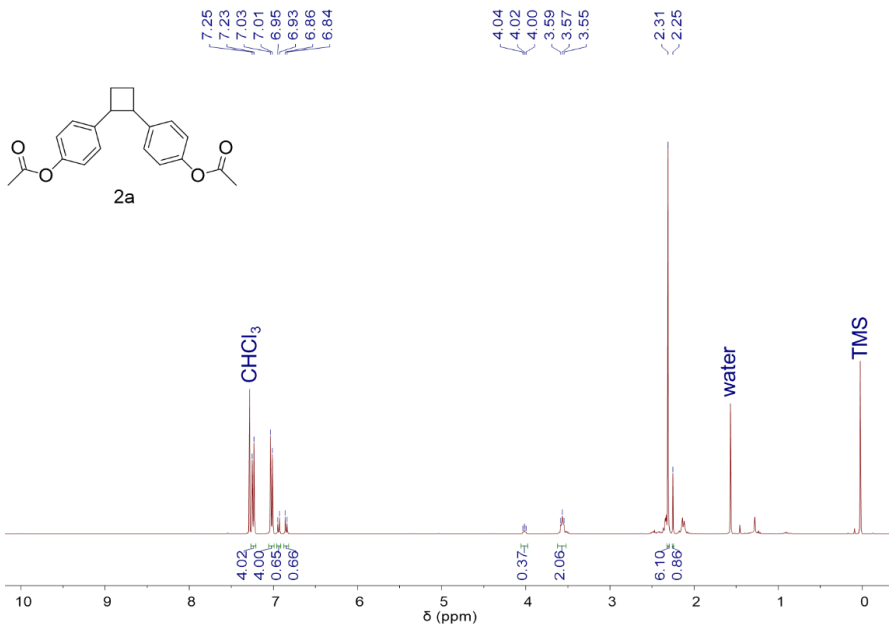

Figure A.III.31. ^{1}H NMR spectrum of **2a.**

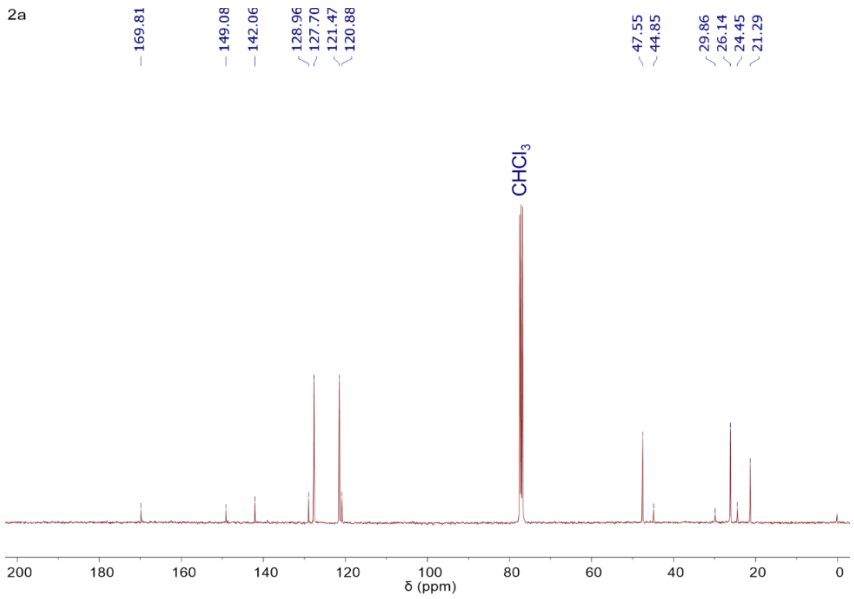

Figure A.III.32. ^{13}C NMR spectrum of **2a.**

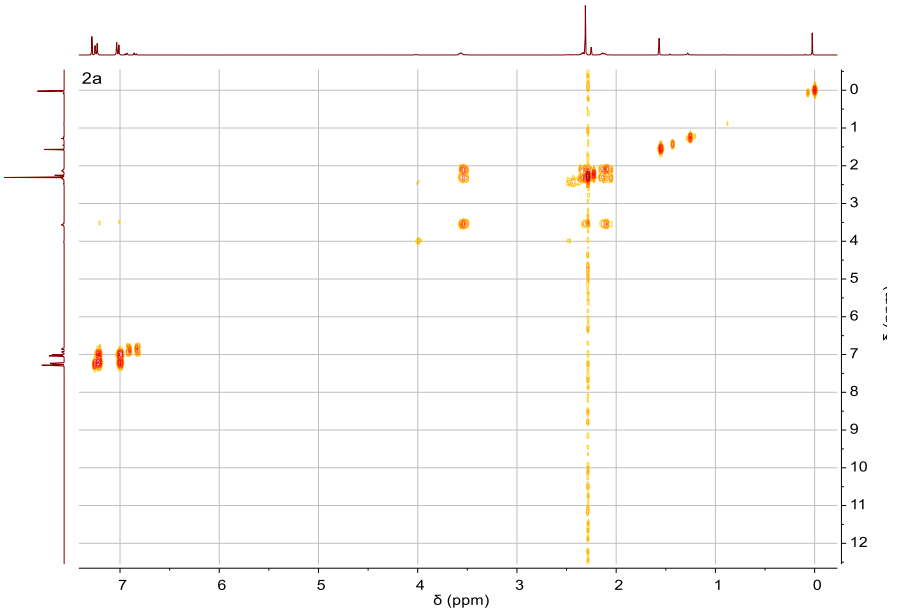

Figure A.III.33. ^{1}H COSY spectrum of **2a**.

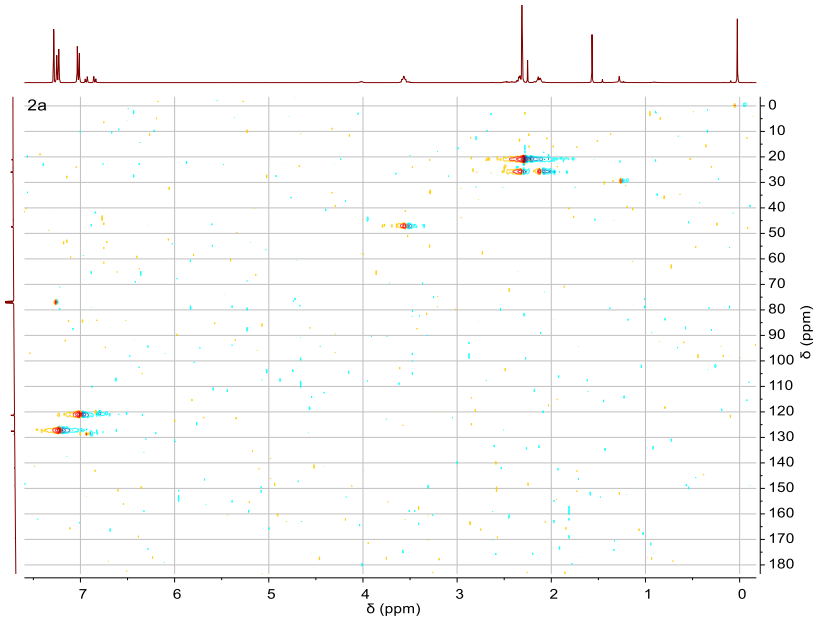

Figure A.III.34. ^{1}H-^{13}C HSQC spectrum of **2a.**

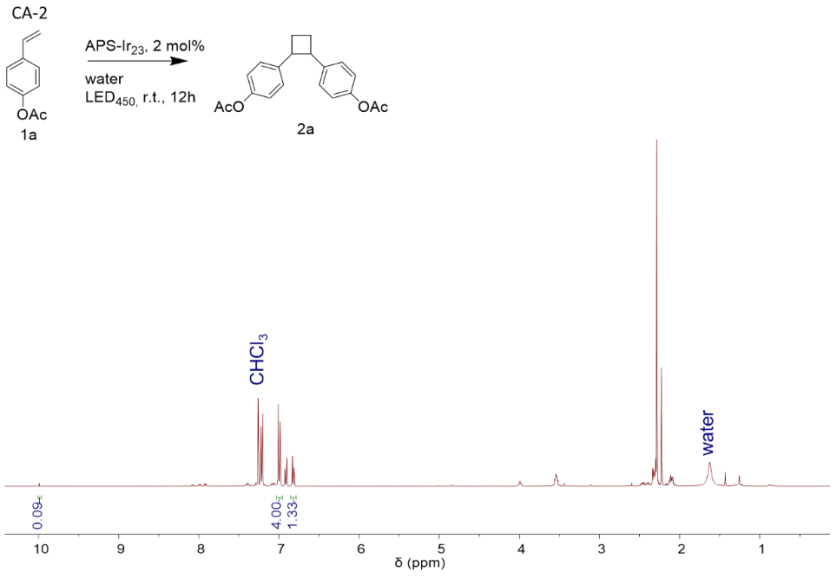

Figure A.III.35. [1]H NMR spectrum of the extracted crude from reaction **CA-2**.

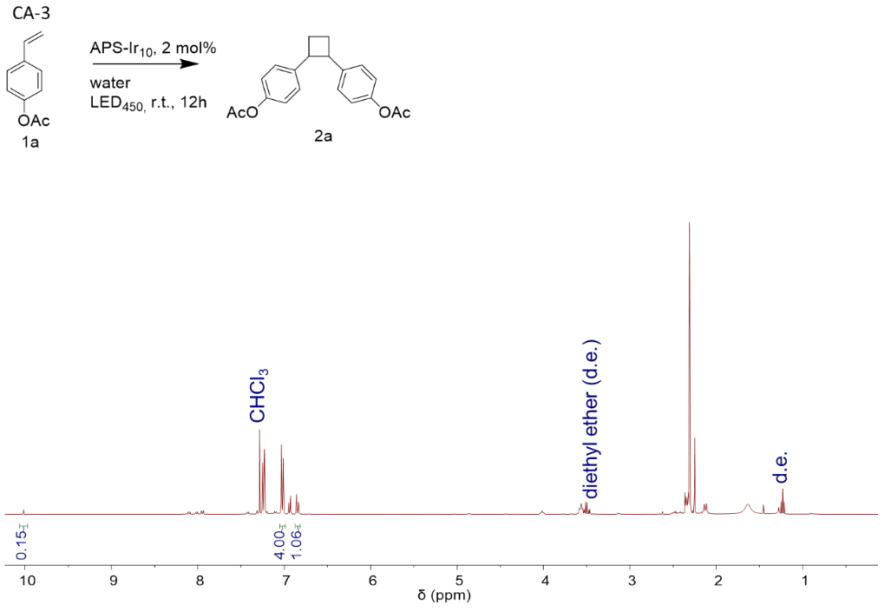

Figure A.III.36. [1]H NMR spectrum of the extracted crude from reaction **CA-3**.

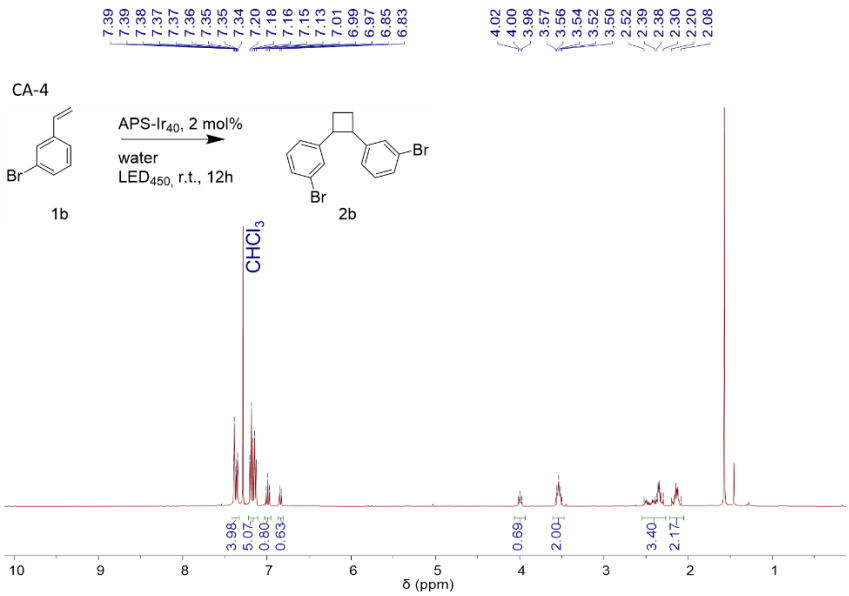

Figure A.III.37. ^{1}H NMR spectrum of the extracted crude from reaction **CA-4**.

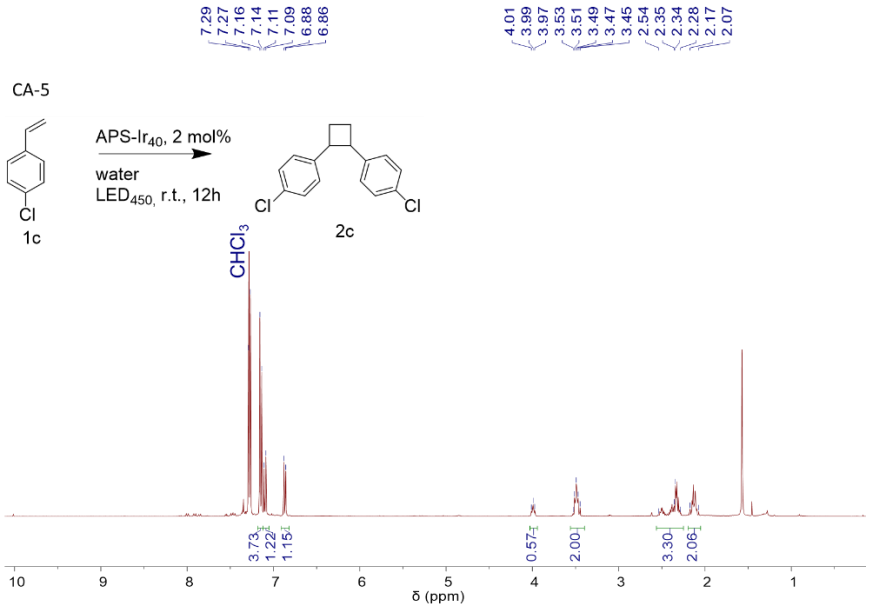

Figure A.III.38. ^{1}H NMR spectrum of the extracted crude from reaction **CA-5**.

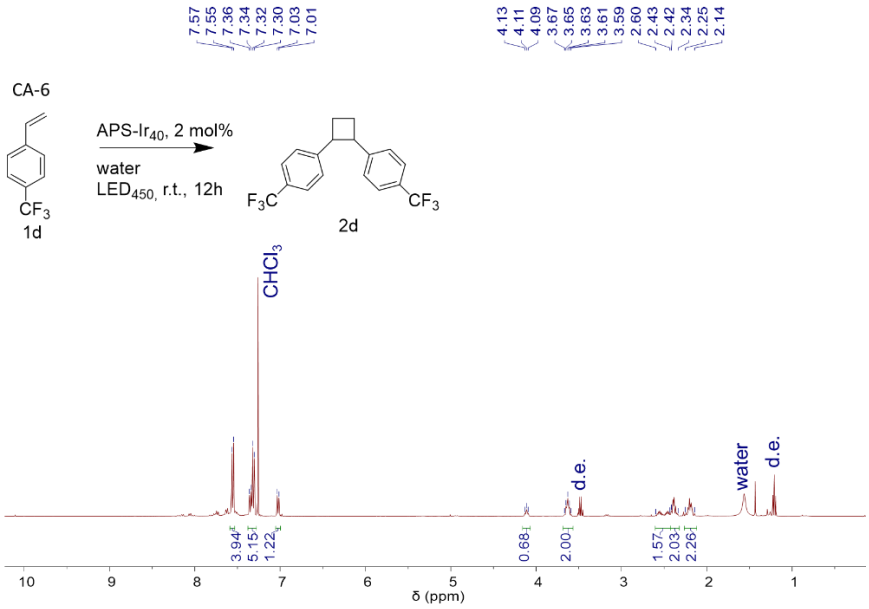

Figure A.III.39 [1]H NMR spectrum of the extracted crude from reaction **CA-6**.

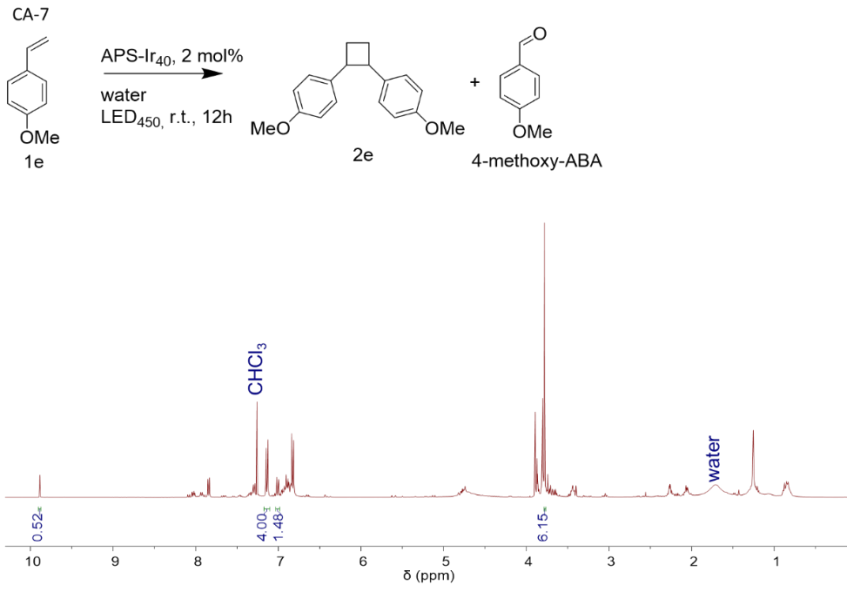

Figure A.III.40. [1]H NMR spectrum of the extracted crude from reaction **CA-7.**

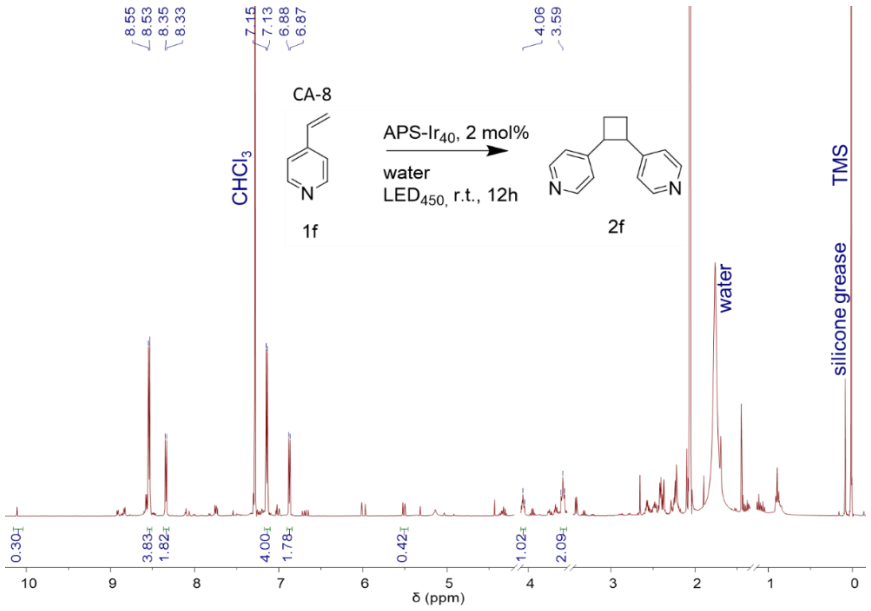

Figure A.III.41. [1]H NMR spectrum of the extracted crude from reaction **CA-8**.

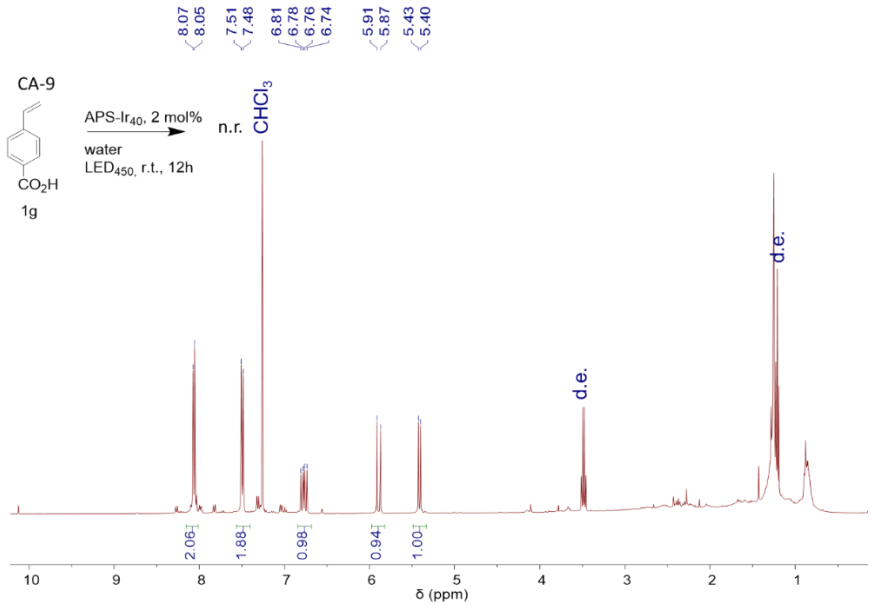

Figure A.III.42. [1]H NMR spectrum of the extracted crude from reaction **CA-9**.

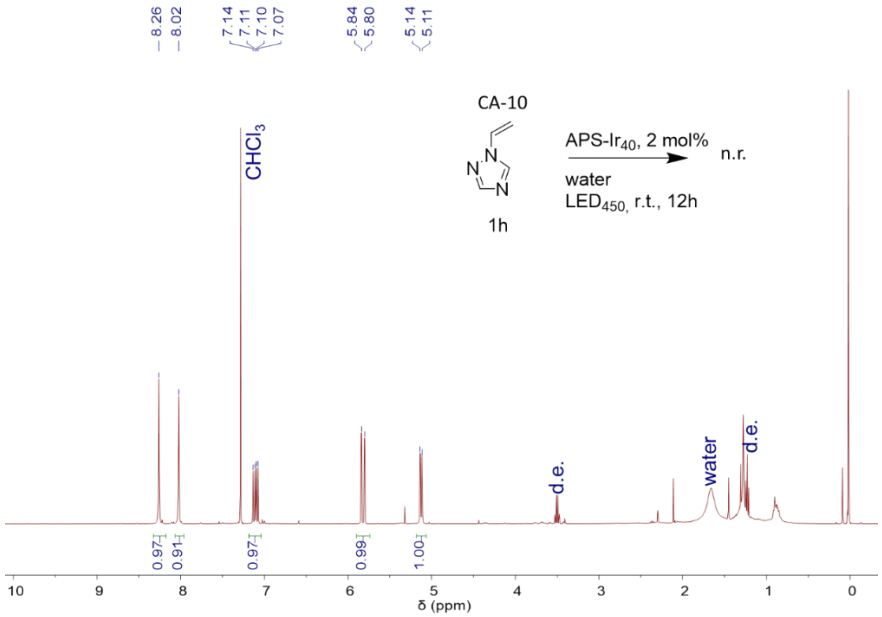

Figure A.III.43. [1]H NMR spectrum of the extracted crude from reaction **CA-10**.

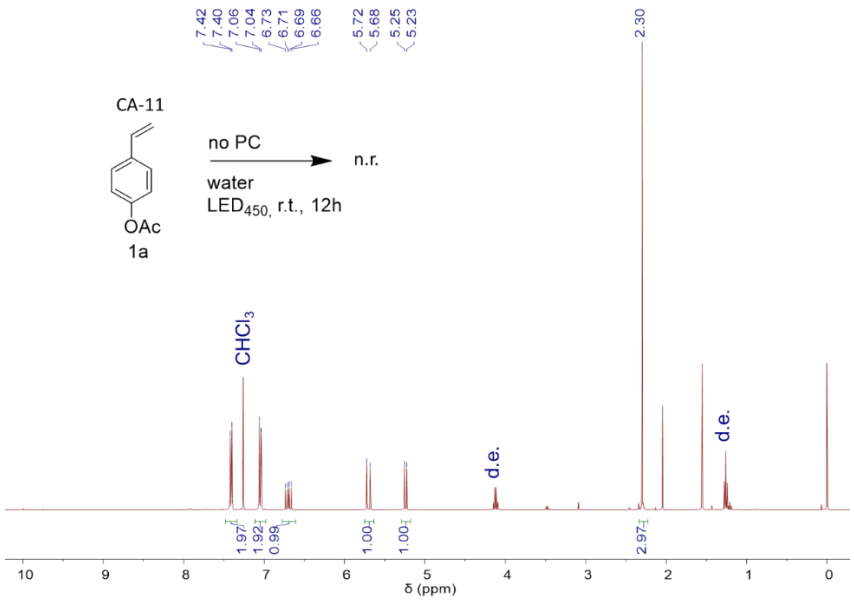

Figure A.III.44. [1]H NMR spectrum of the extracted crude from reaction **CA-11**.

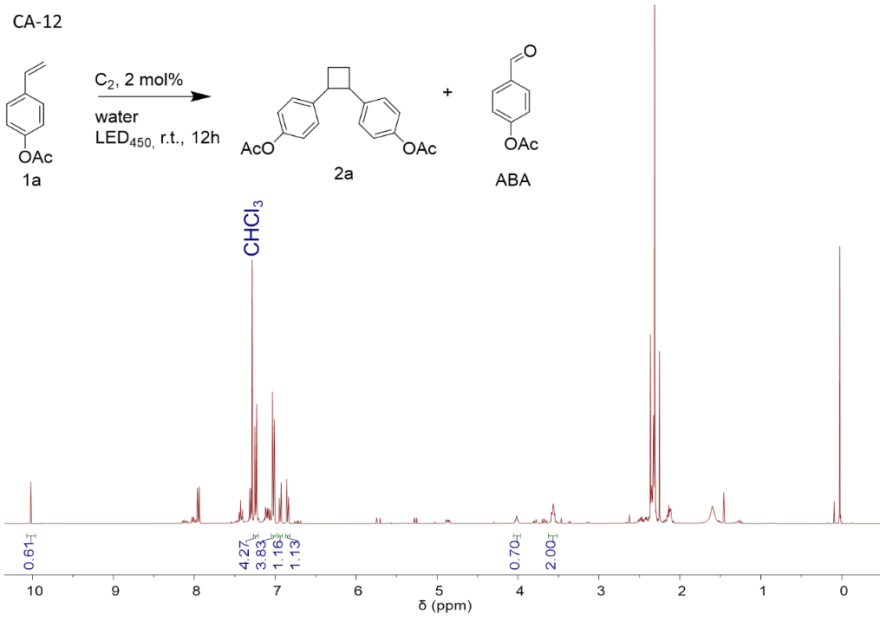

Figure A.III.45. ^{1}H NMR spectrum of the extracted crude from reaction **CA-12**.

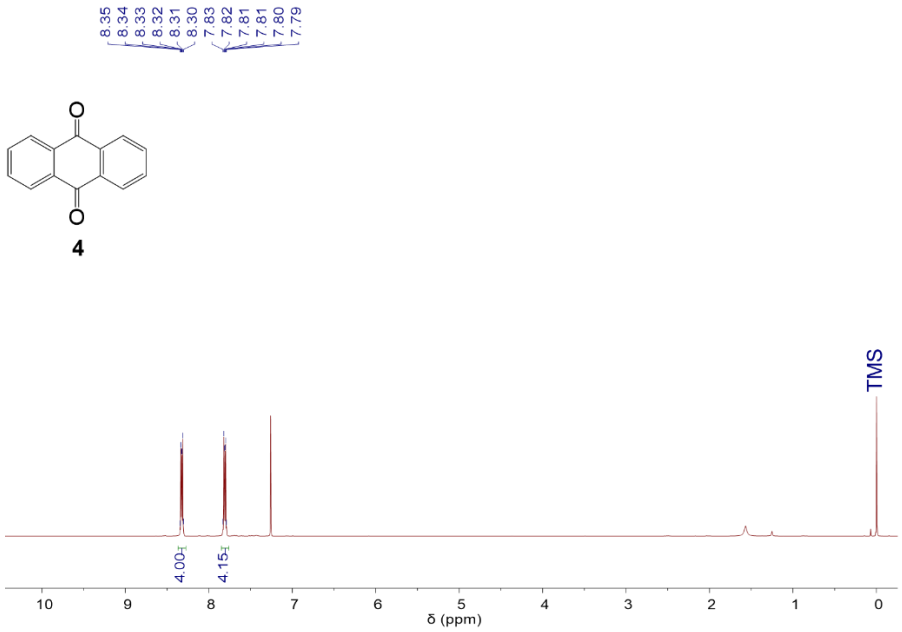

Figure A.III.46. ^{1}H NMR spectrum of **4**.

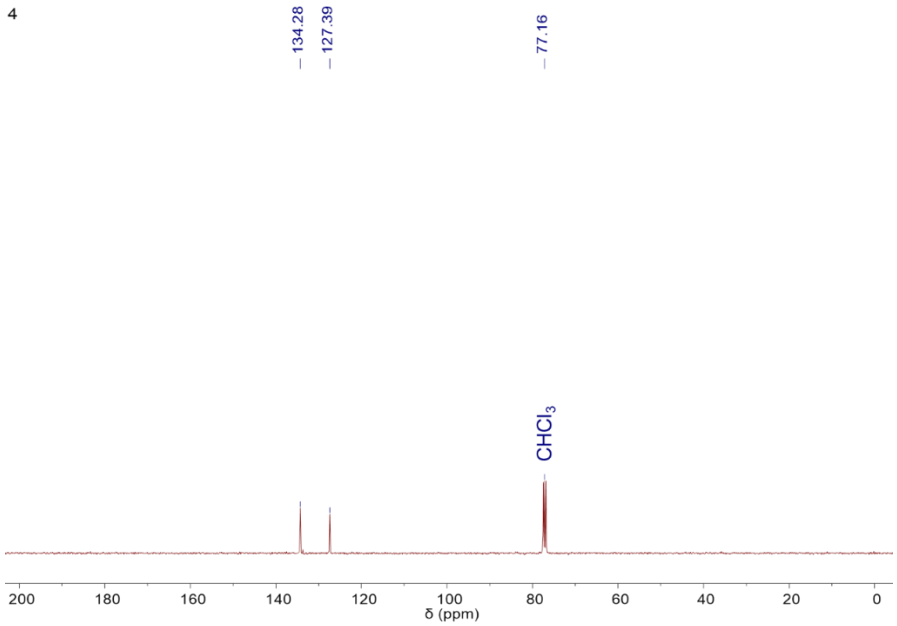

Figure A.III.47. ^{13}C NMR spectrum of **4**.

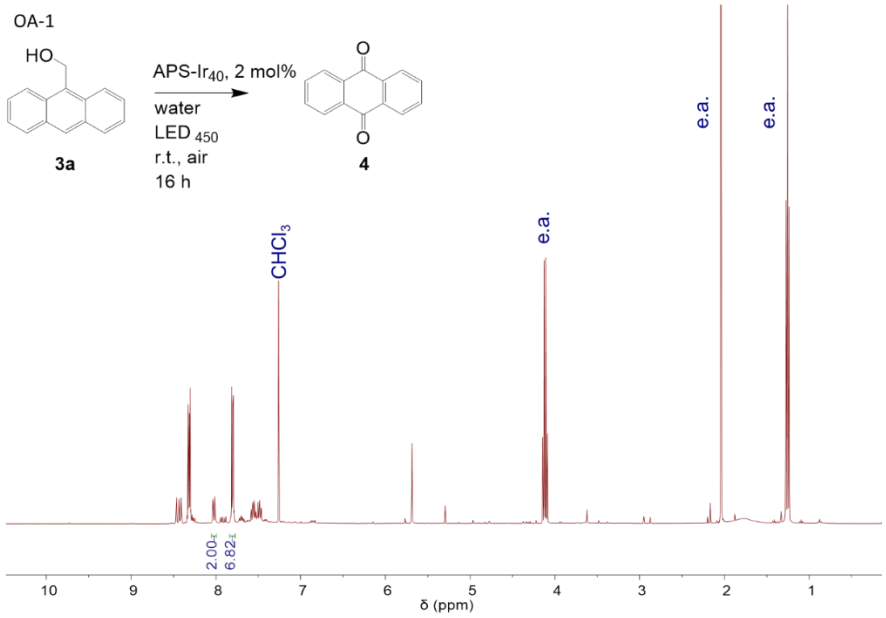

Figure A.III.48. [1]H NMR spectrum of the extracted crude from reaction **OA-1.**

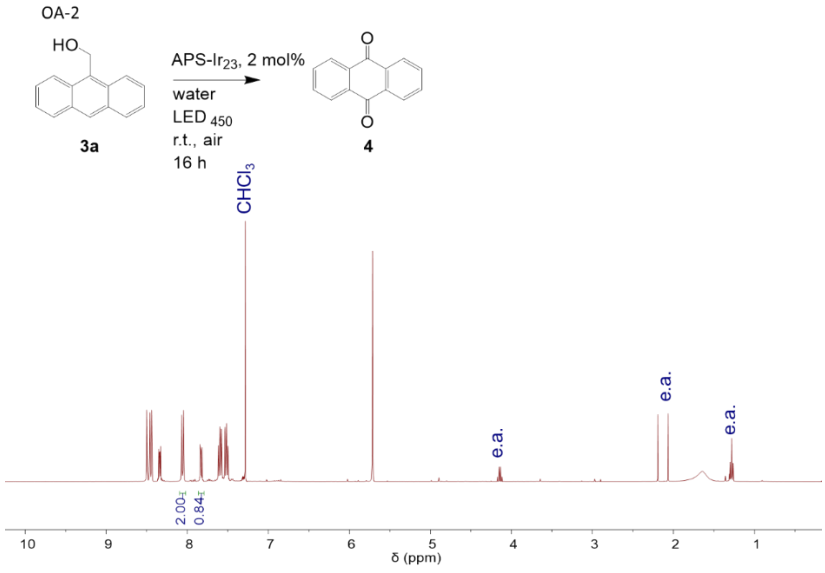

Figure A.III.49. [1]H NMR spectrum of the extracted crude from reaction **OA-2.**

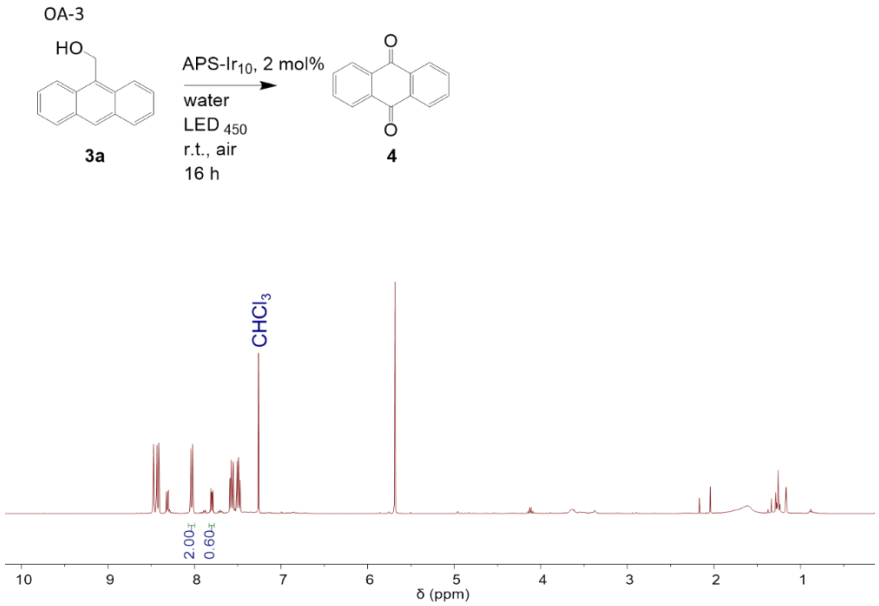

Figure A.III.50. ^{1}H NMR spectrum of the extracted crude from reaction **OA-3.**

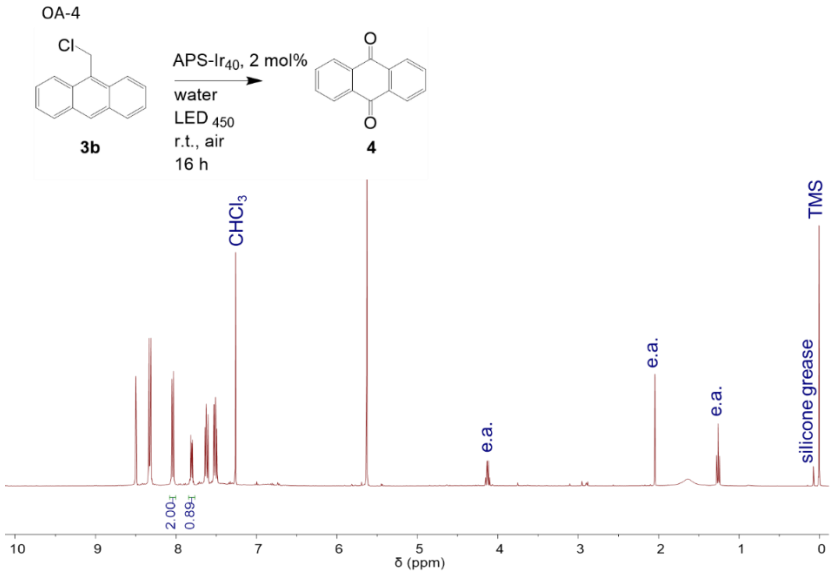

Figure A.III.51. ^{1}H NMR spectrum of the extracted crude from reaction **OA-4.**

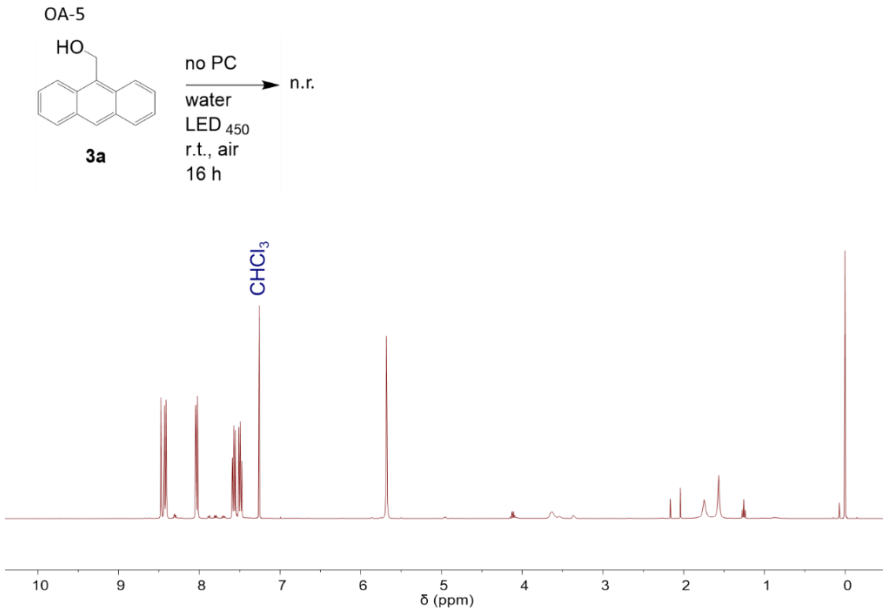

Figure A.III.52. ^{1}H NMR spectrum of the extracted crude from reaction **OA-5.**

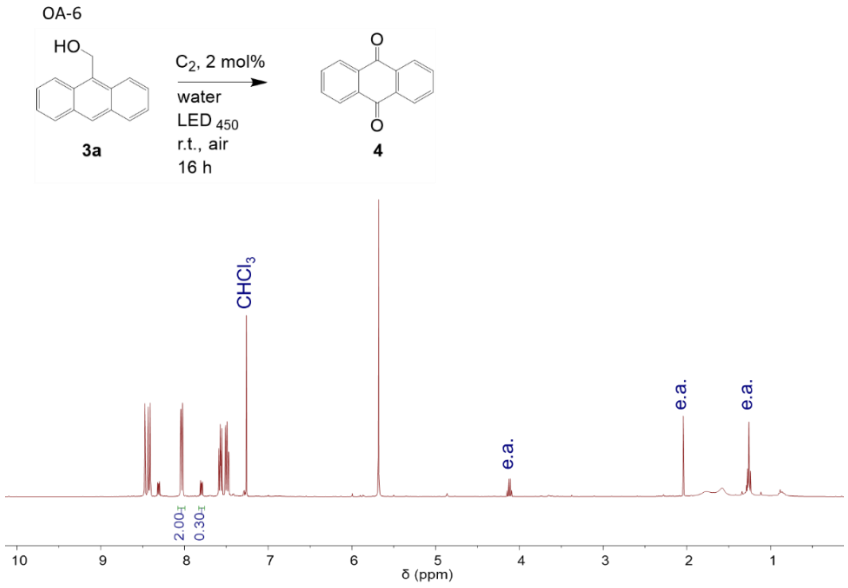

Figure A.III.53. ^{1}H NMR spectrum of the extracted crude from reaction **OA-6.**

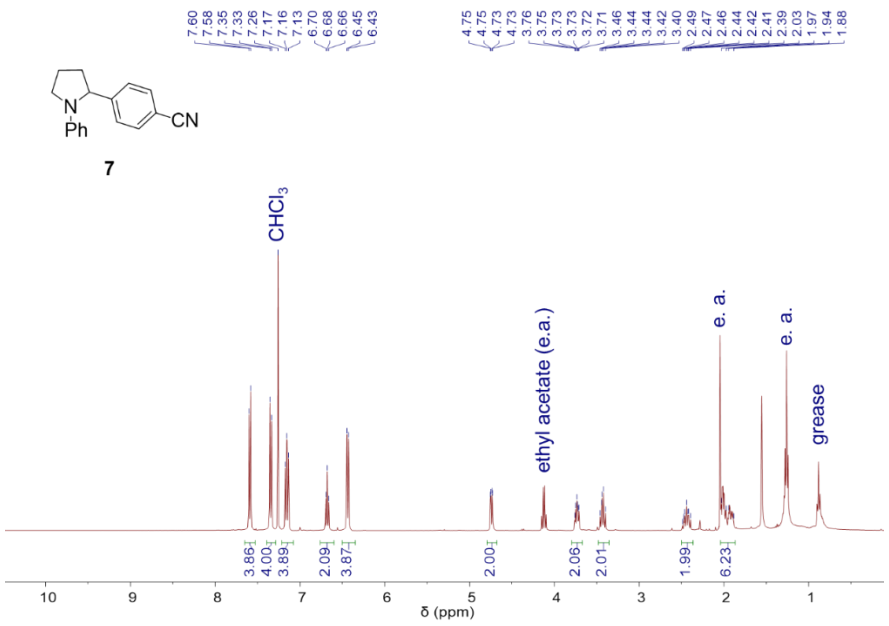

Figure A.III.54. ^{1}H NMR spectrum of **7.**

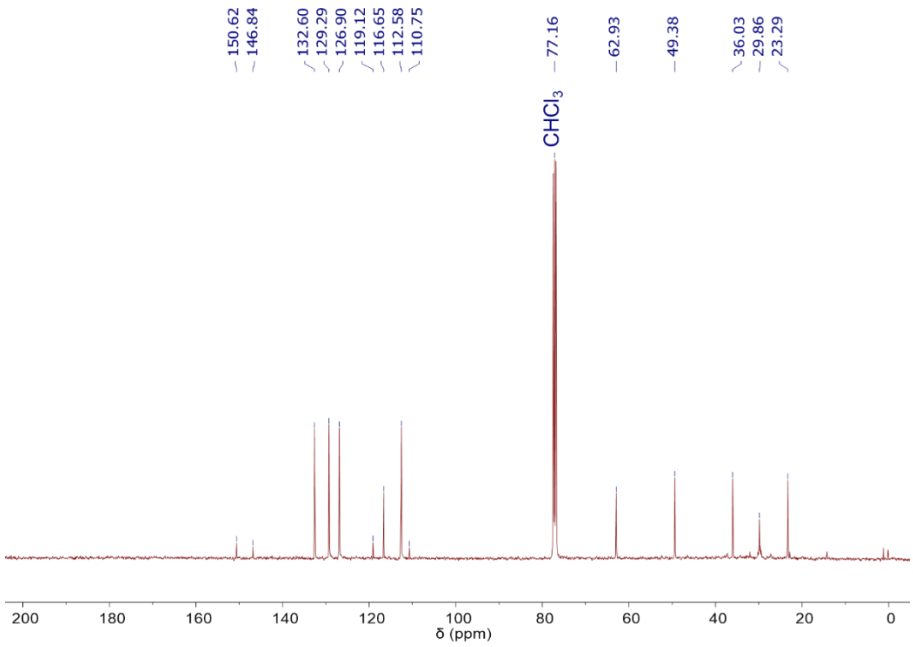

Figure A.III.55. ^{13}C NMR spectrum of **7.**

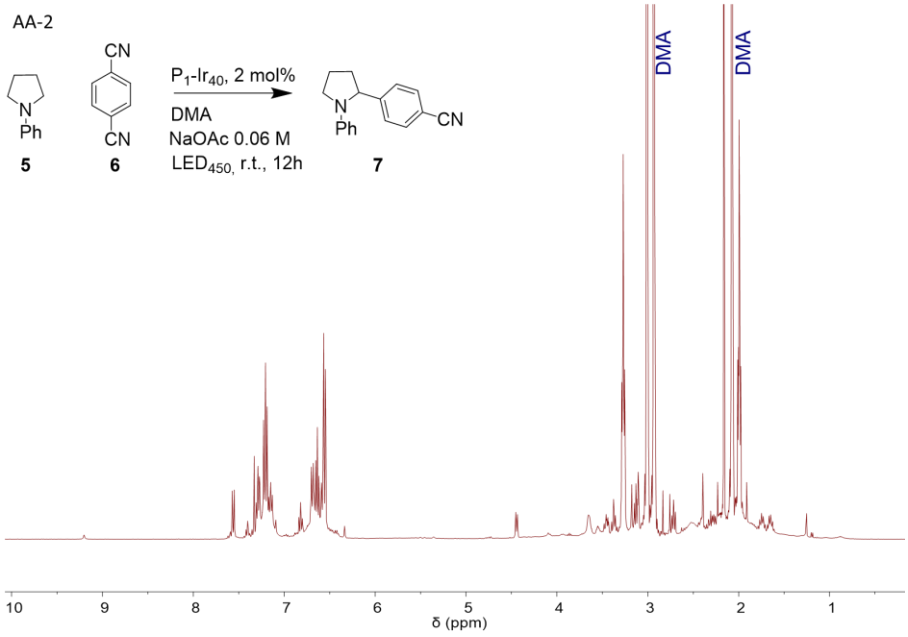

Figure A.III.56. [1]H NMR spectrum of the extracted crude from reaction **AA-2.**

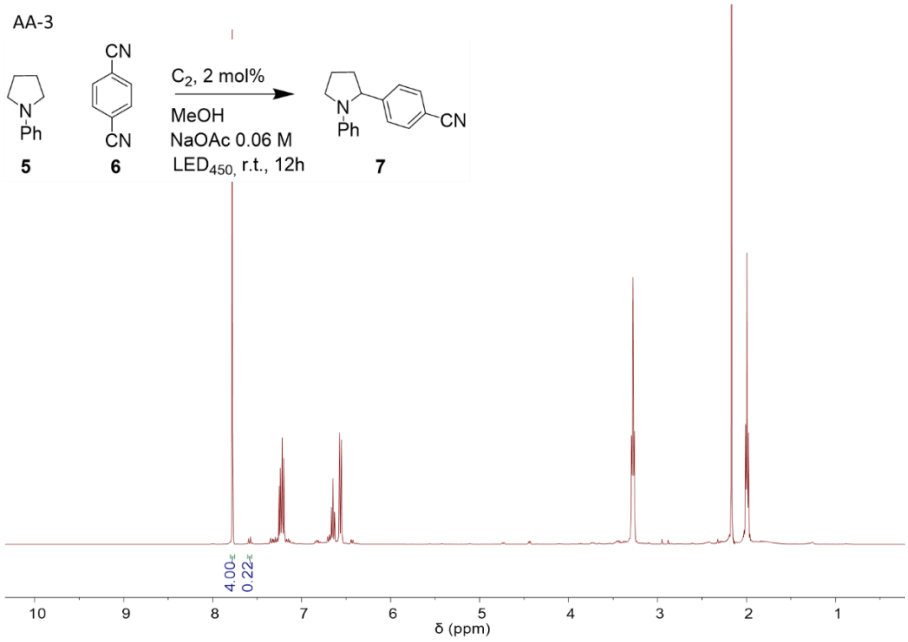

Figure A.III.57. [1]H NMR spectrum of the extracted crude from reaction **AA-3.**

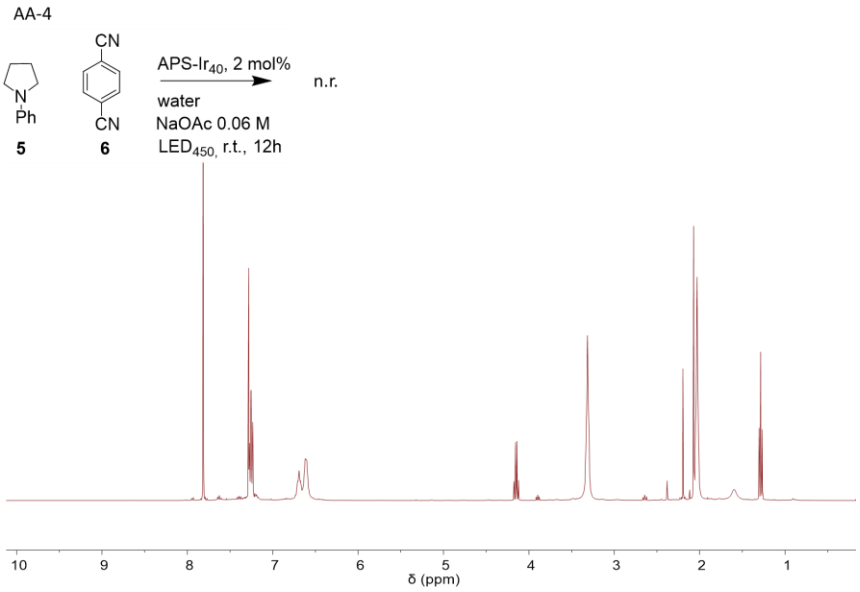

Figure A.III.58. ^{1}H NMR spectrum of the extracted crude from reaction **AA-4.**

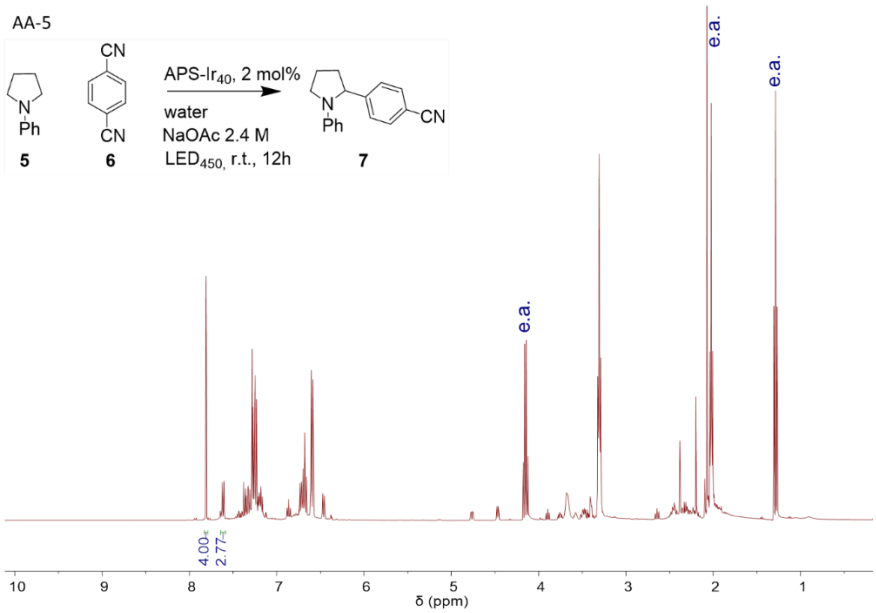

Figure A.III.59. ^{1}H NMR spectrum of the extracted crude from reaction **AA-5.**

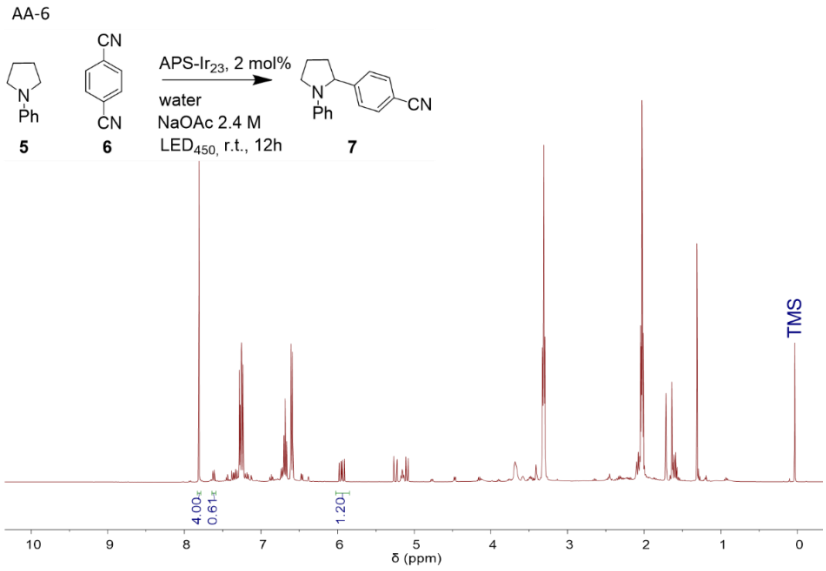

Figure A.III.60. [1]H NMR spectrum of the extracted crude from reaction **AA-6.**

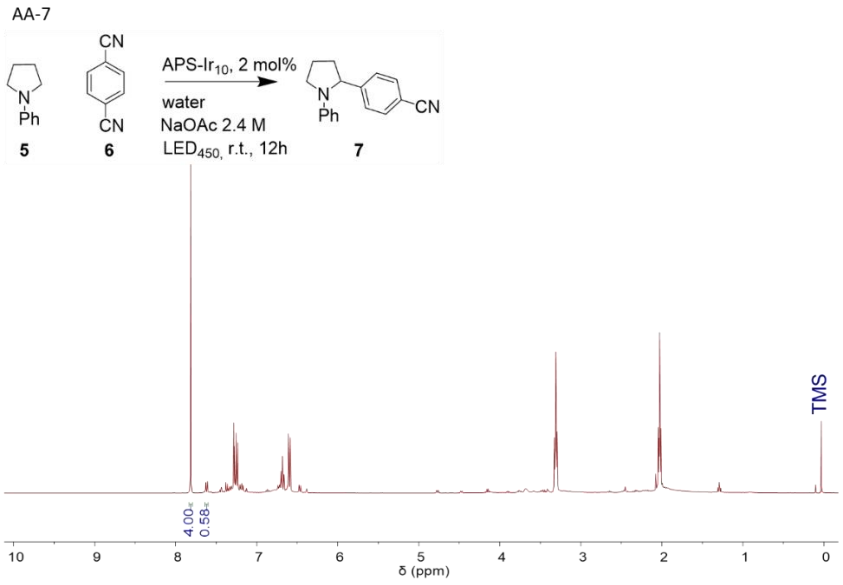

Figure A.III.61. [1]H NMR spectrum of the extracted crude from reaction **AA-7.**

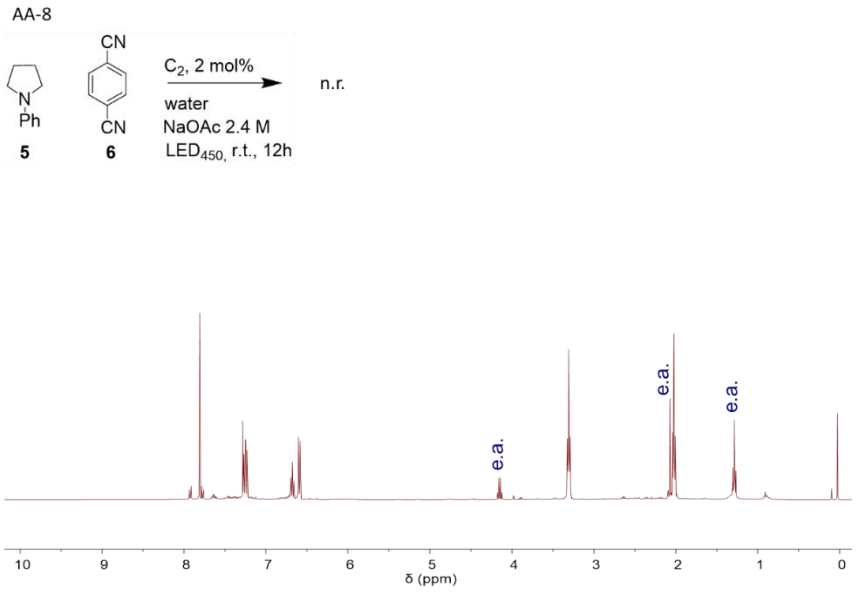

Figure A.III.62. ^{1}H NMR spectrum of the extracted crude from reaction **AA-8.**

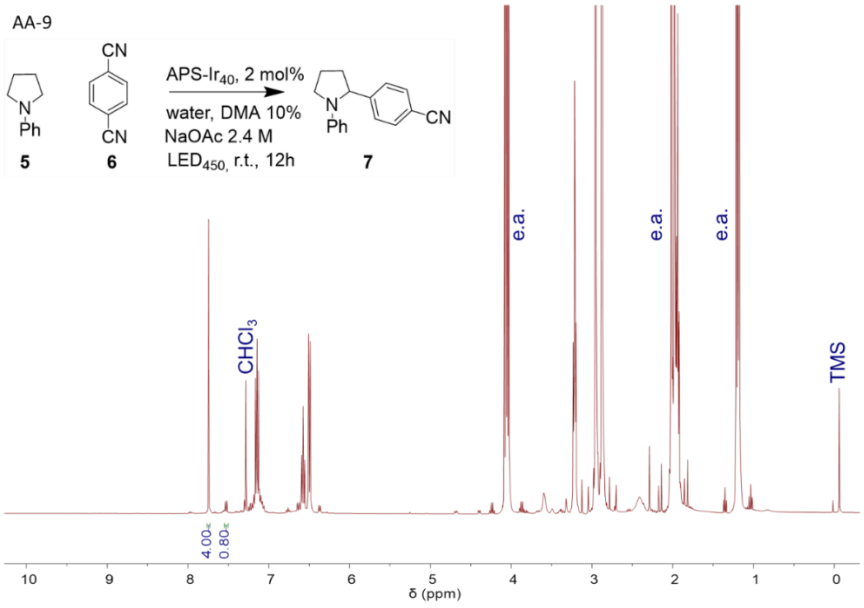

Figure A.III.63. ^{1}H NMR spectrum of the extracted crude from reaction **AA-9.**

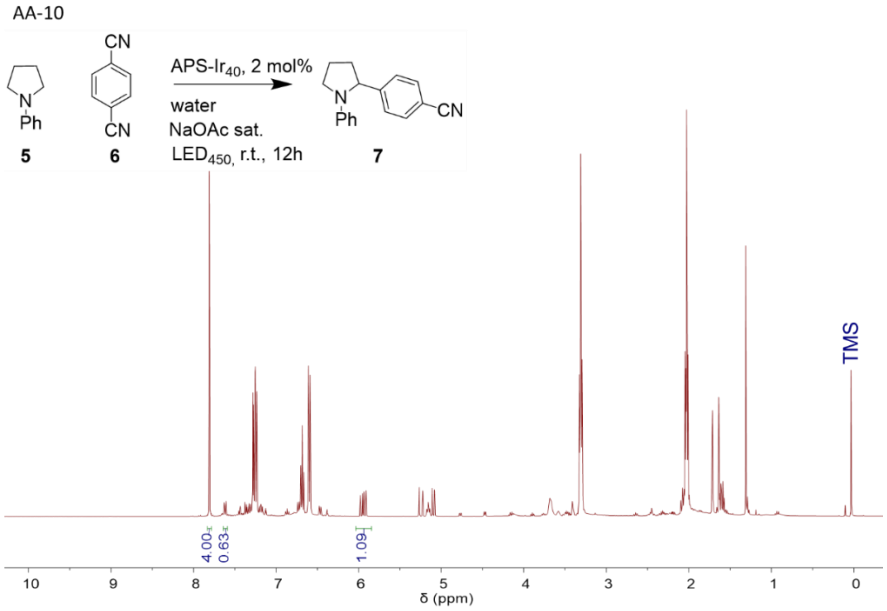

Figure A.III.64. ^{1}H NMR spectrum of the extracted crude from reaction **AA-10.**

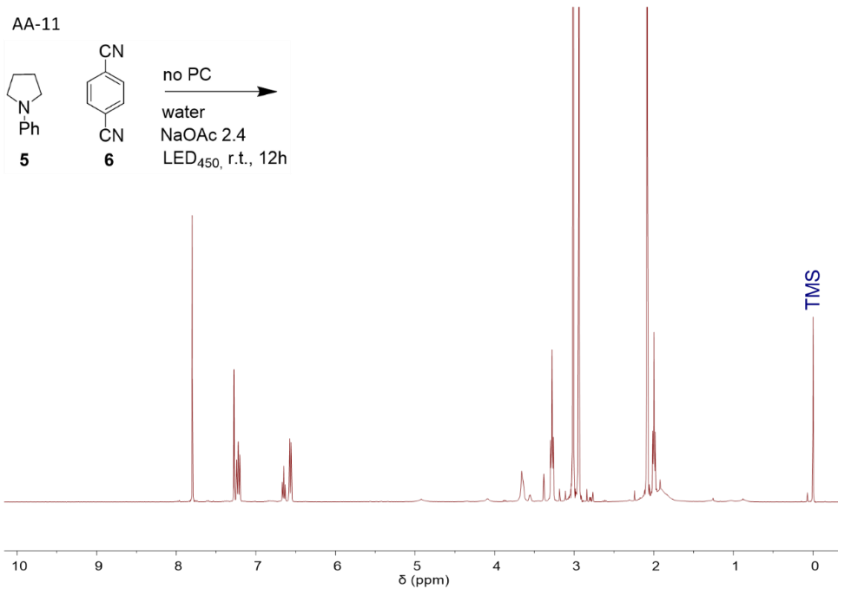

Figure A.III.65 ^{1}H NMR spectrum of the extracted crude from reaction **AA-11.**

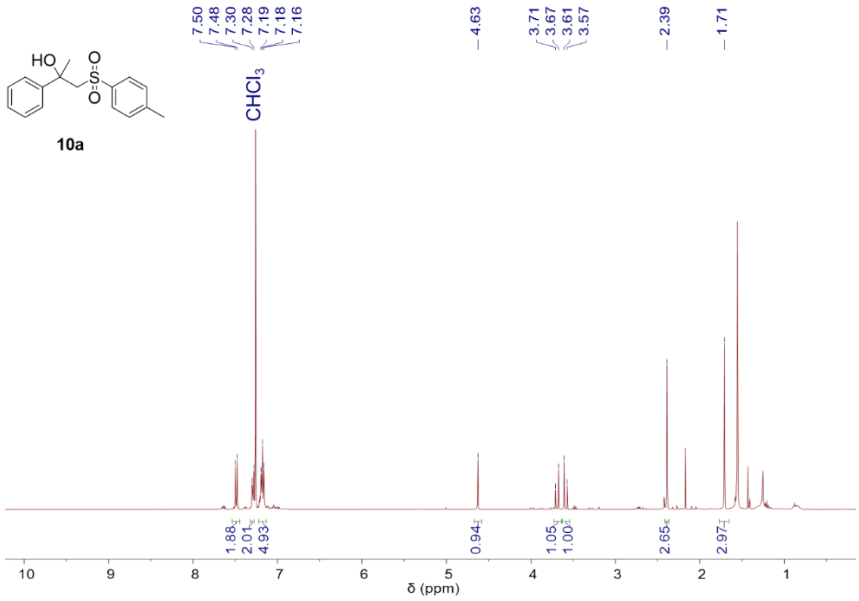

Figure A.III.66. [1]H NMR spectrum of **10a**.

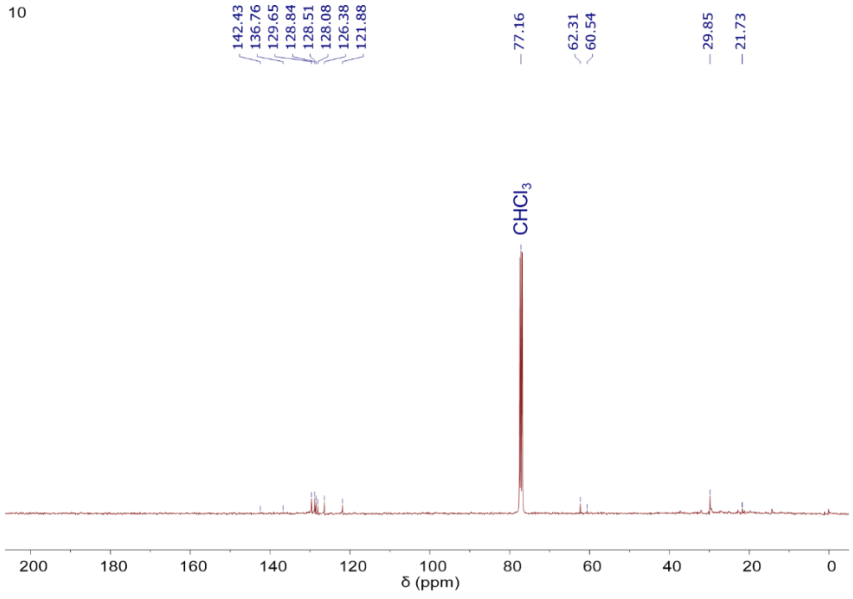

Figure A.III.67. [13]C NMR spectrum of **10a**.

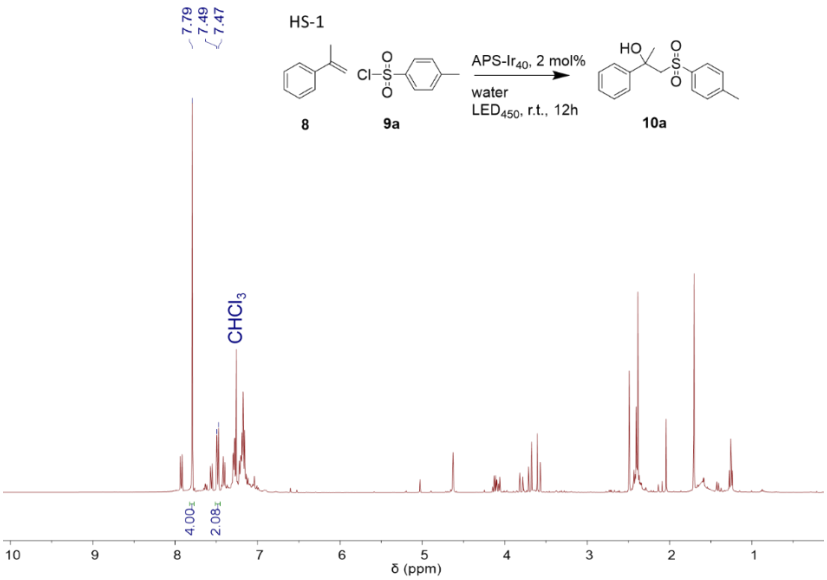

Figure A.III.68. ^{1}H NMR spectrum of the extracted crude from reaction **HS-1.**

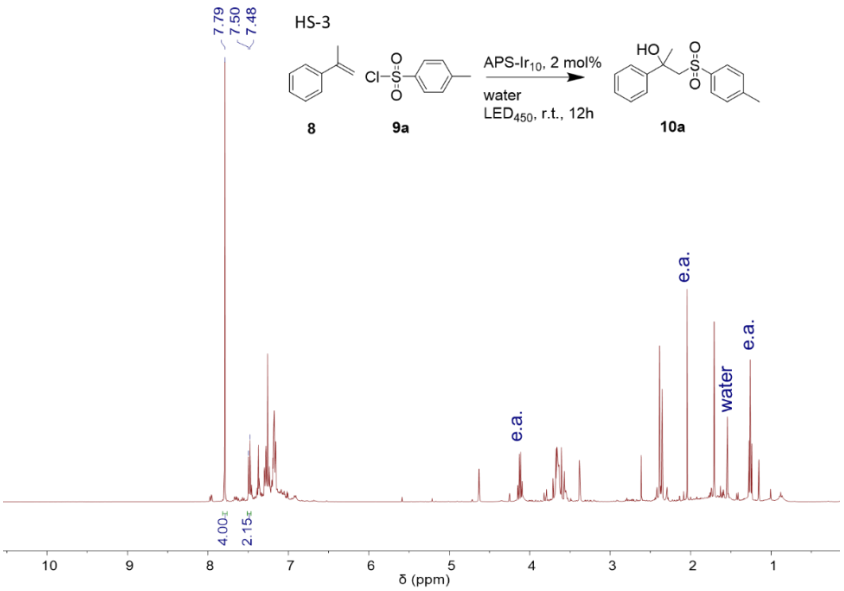

Figure A.III.69. ^{1}H NMR spectrum of the extracted crude from reaction **HS-3.**

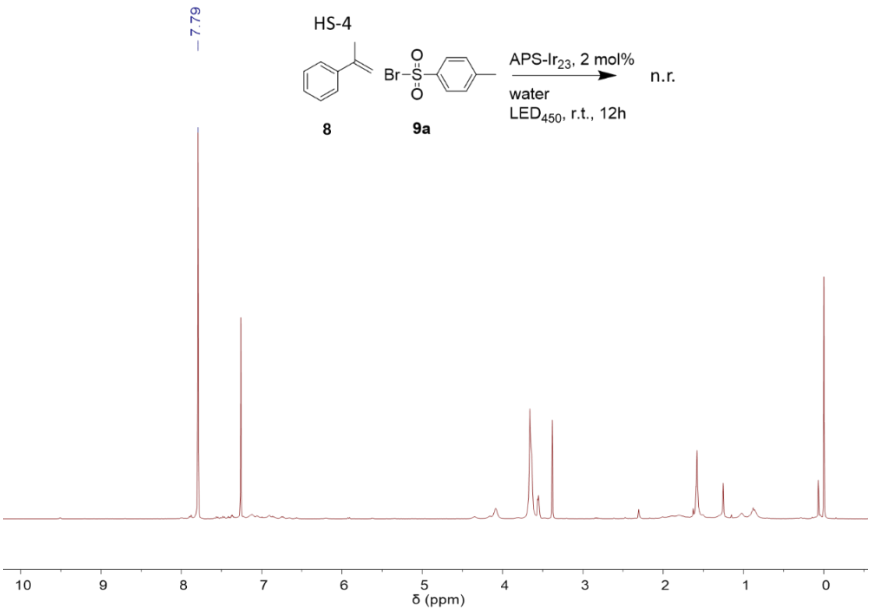

Figure A.III.70. [1]H NMR spectrum of the extracted crude from reaction **HS-4.**

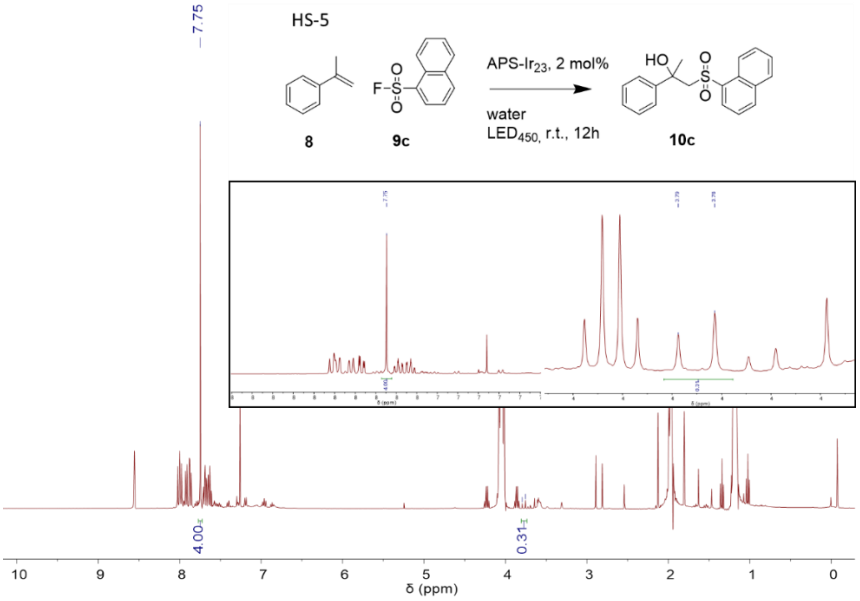

Figure A.III.71. [1]H NMR spectrum of the extracted crude from reaction **HS-5.**

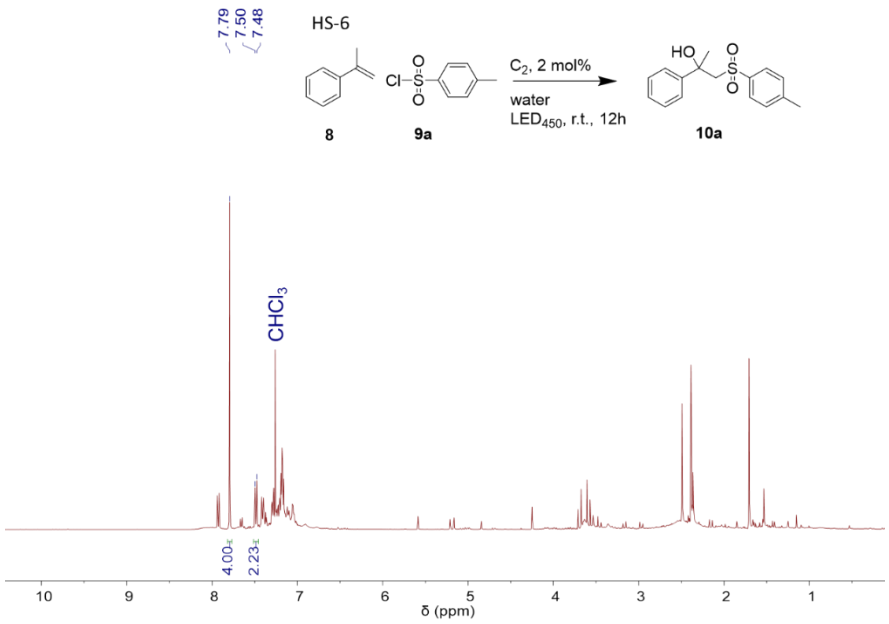

Figure A.III.72. [1]H NMR spectrum of the extracted crude from reaction **HS-6.**

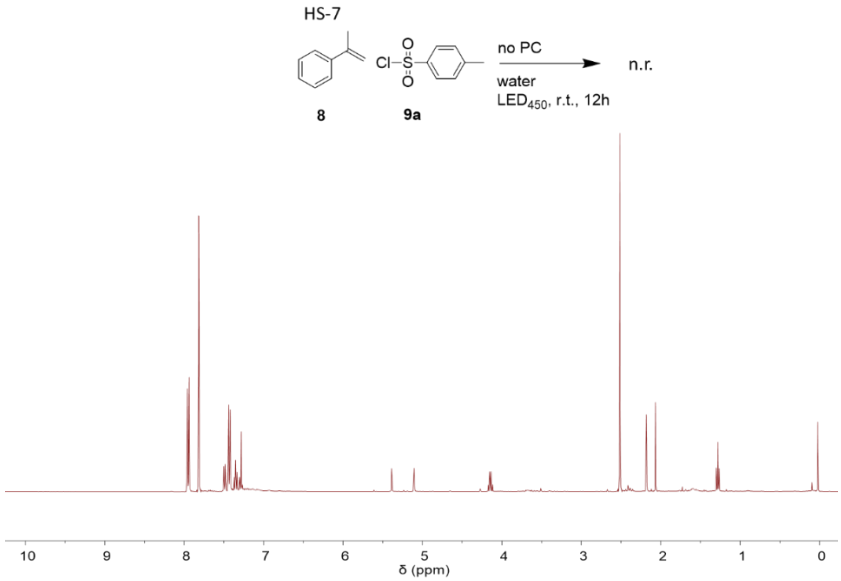

Figure A.III.73. [1]H NMR spectrum of the extracted crude from reaction **HS-7.**

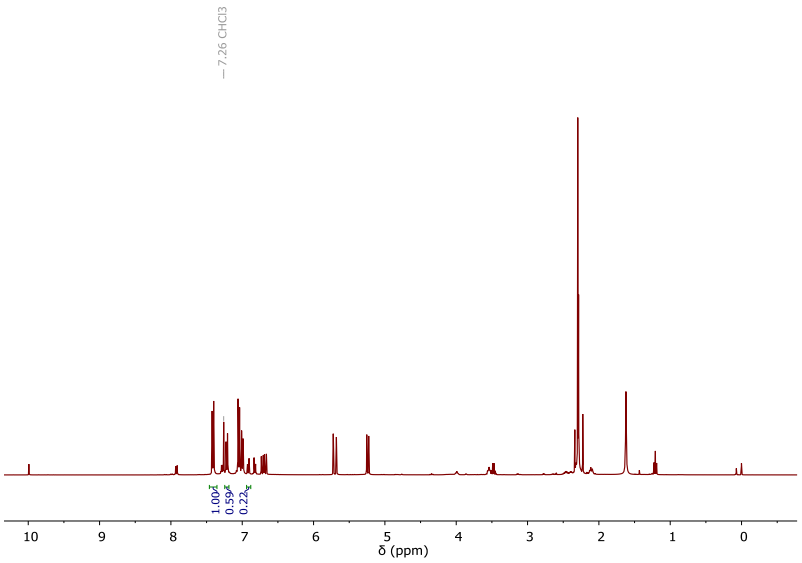

Figure A.III.74. ^{1}H NMR spectrum of the extracted crude of the second catalytic cycle performed by recycled **APS-Ir$_{40}$** for the "*in water*" [2+2] photocycloaddition of **1a** under title conditions.

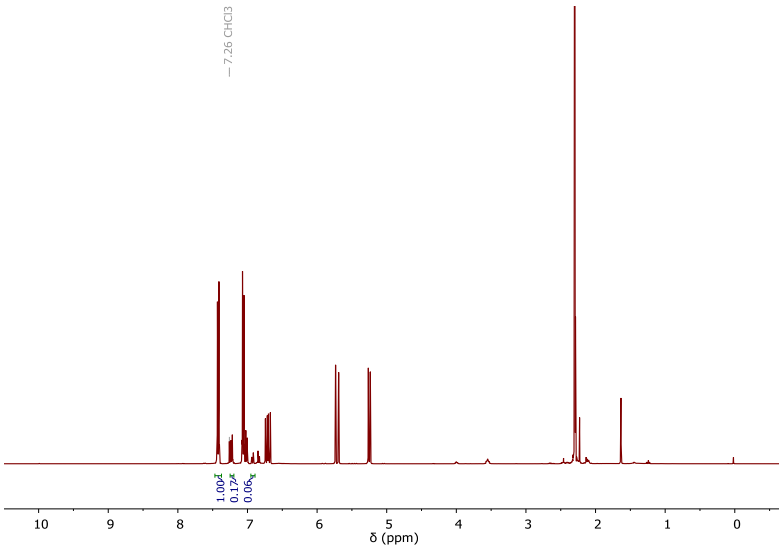

Figure A.III.75. ^{1}H NMR spectrum of the extracted crude of the third catalytic cycle performed by recycled **APS-Ir$_{40}$** for the "*in water*" [2+2] photocycloaddition of **1a** under title conditions.

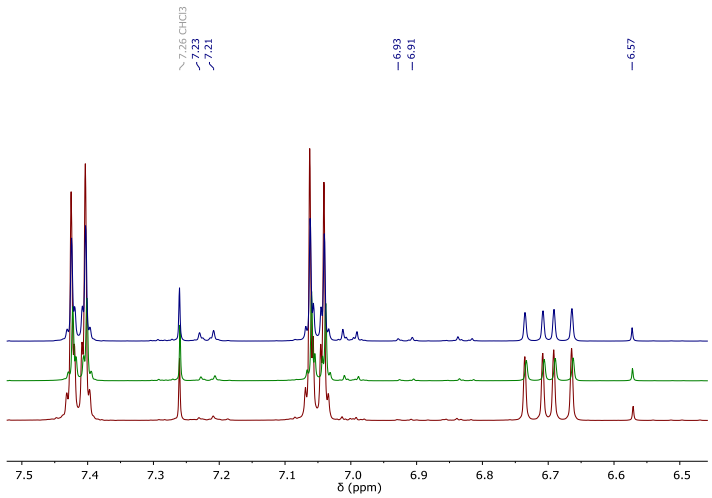

Figure A.III.76. ^{1}H NMR superimposed spectra of the extracted crudes of the **APS-Ir$_{40}$** -catalyzed "*in water*" [2+2] photocycloaddition of **1a** at [**1a**] = 235 mM. Dark green line, reaction quenched at 600 seconds, red line, 1200 seconds and blue line at 1800 seconds.

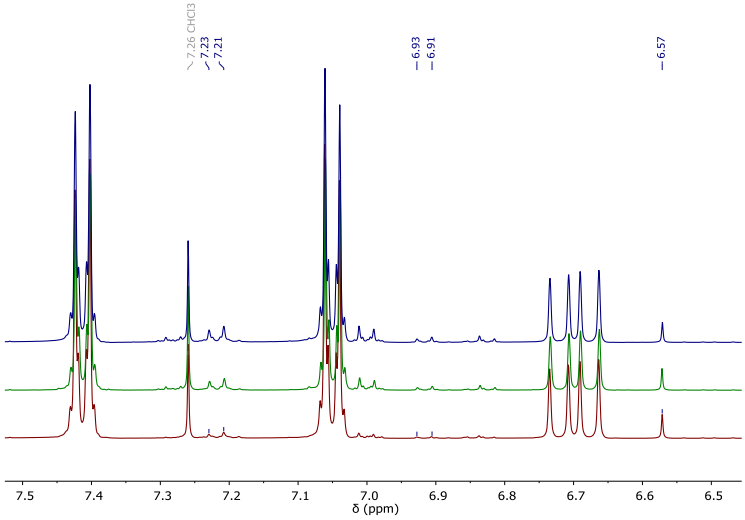

Figure A.III.77. ^{1}H NMR superimposed spectra of the extracted crudes of the **APS-Ir$_{40}$** -catalyzed "*in water*" [2+2] photocycloaddition of **1a** at [**1a**] = 175 mM. Dark green line, reaction quenched at 600 seconds, red line, 1200 seconds and blue line at 1800 seconds.

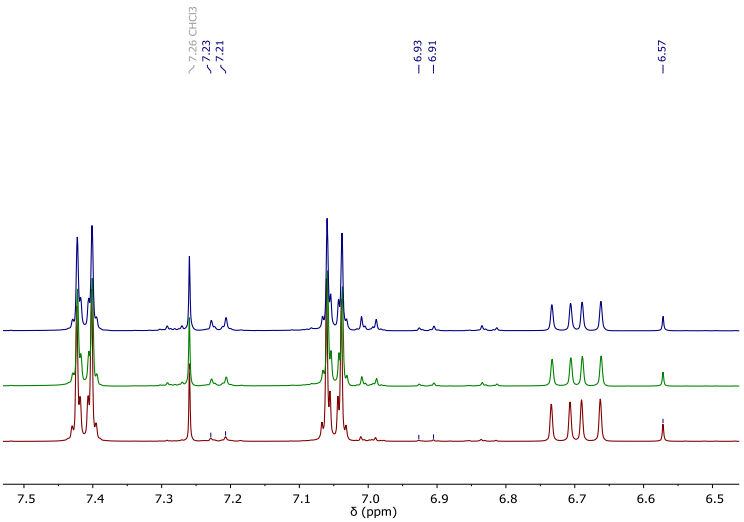

Figure A.III.78. [1]H NMR superimposed spectra of the extracted crudes of the **APS-Ir$_{40}$** -catalyzed "*in water*" [2+2] photocycloaddition of **1a** at [**1a**] = 120 mM. Dark green line, reaction quenched at 600 seconds, red line, 1200 seconds and blue line at 1800 seconds.

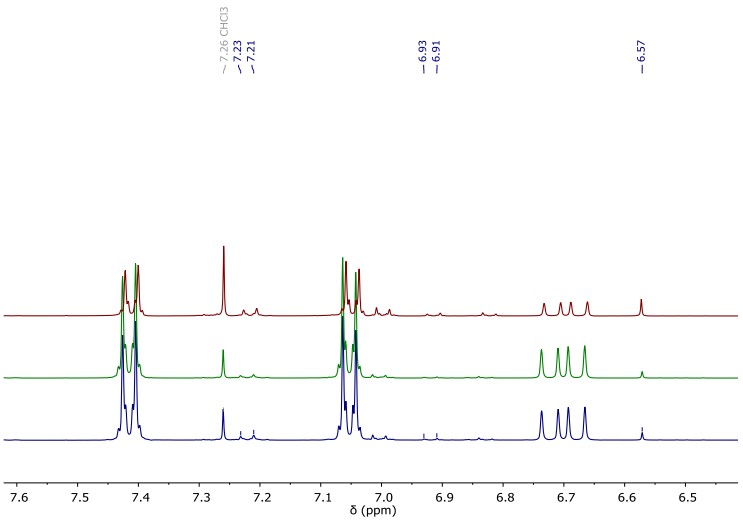

Figure A.III.79. [1]H NMR superimposed spectra of the extracted crudes of the **APS-Ir$_{40}$** -catalyzed "*in water*" [2+2] photocycloaddition of **1a** at [**1a**] = 58 mM. Dark green line, reaction quenched at 600 seconds, red line, 1200 seconds and blue line at 1800 seconds.

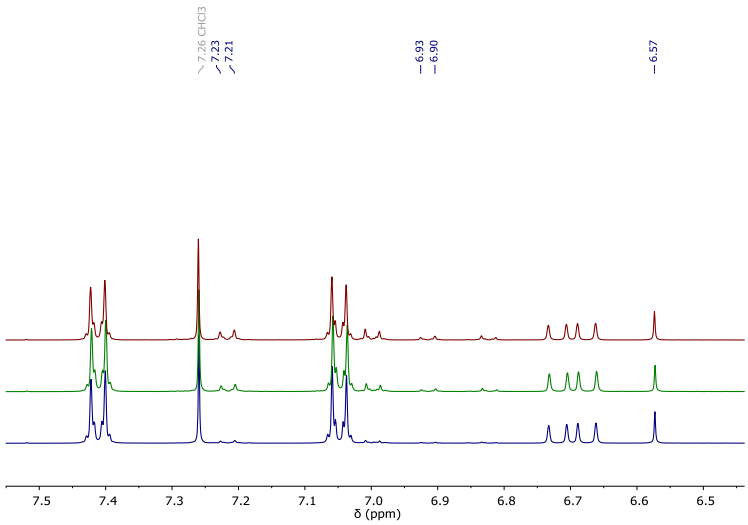

Figure A.III.80. ^{1}H NMR superimposed spectra of the extracted crudes of the **APS-Ir$_{40}$** -catalyzed "*in water*" [2+2] photocycloaddition of **1a** at [**1a**] = 15 mM. Dark green line, reaction quenched at 600 seconds, red line, 1200 seconds and blue line at 1800 seconds.

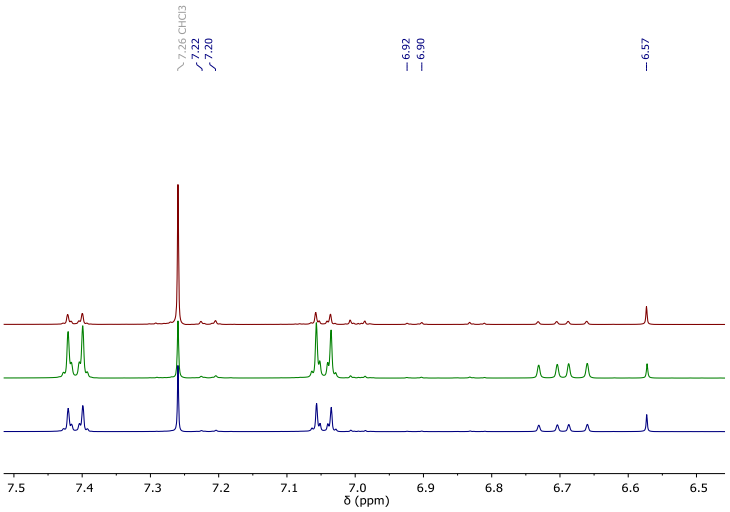

Figure A.III.81. ^{1}H NMR superimposed spectra of the extracted crudes of the **APS-Ir$_{40}$** -catalyzed "*in water*" [2+2] photocycloaddition of **1a** at [**1a**] = 8 mM. Dark green line, reaction quenched at 600 seconds, red line, 1200 seconds and blue line at 1800 seconds.

Appendix to Chapter IV

A.IV.1. Preparation of copolymers with higher anthracene content.

A.IV.1.1. Synthesis of the copolymer **P_4**

296 mg (1.07 mmol) of AnMA, 321 mg (1.07 mmol) of $OEGMA_{300}$, 1.51 mg (5.4 µmol) of CPADB, 0.34 mg (2.1 µmol) of AIBN and 1.07 ml of 1,4-dioxane were added to a dark, oven-dried vial, equipped of a magnetic stir bar. After purging the mixture with an argon flow for 10 min., the vial was sealed with a rubber septum, and the reaction was left stirring at 70 ºC and under inert atmosphere for 19 h. After this time, the crude was purified *via* four consecutive precipitations in *n*-hexane. After drying under dynamic vacuum for 24 h, the obtained product was analyzed *via* SEC and ^{1}H NMR. M_w (kDa) = 214.6, Đ = 1.28, AnMA (mol%) = 50. ^{1}H NMR (400 MHz, $CDCl_3$): **δ** (ppm) = 8.26-7.37 (m, 9H, H^{Ar}), 5.85 (b.s., 2H, $H_9C_{10}C\underline{H}_2$), 3.98 (m, 2H, $CH_2C\underline{H}_2O$), 3.57-3.48, (m, $(OCH_2CH_2)_n$), 3.32 (s, 3H, $OC\underline{H}_3$), 1.70 (m, $C\underline{H}_2CCH_3$), 0.73 (m, $CH_2CC\underline{H}_3$).

A.IV.1.2. Synthesis of the copolymer **P_5**

591 mg (2.14 mmol) of AnMA, 1.51 mg (5.4 µmol) CPADB, 0.34 mg (2.1 µmol) of AIBN and 1.07 mL of 1,4-dioxane were added to a dark, oven-dried vial, equipped of a magnetic stir bar. After purging the mixture with an argon flow for 10 min., the vial was sealed with a rubber septum, and the reaction was left stirring at 70ºC and under inert atmosphere for 19 h. After this time, the crude was purified *via* four consecutive precipitations in *n*-hexane. After drying under dynamic vacuum for 24 h, the obtained product was analyzed *via* SEC and ^{1}H NMR. M_w (kDa) = 235.8, Đ = 1.36.

^{1}H NMR (400 MHz, $CDCl_3$): **δ** (ppm) = 8.05-7.07 (m, 9H, H^{Ar}), 5.60 (b.s., 2H, $H_9C_{10}C\underline{H}_2$), 0.61 (m, $CH_2CC\underline{H}_3$)

A.IV.2. Room-light PDT experiment

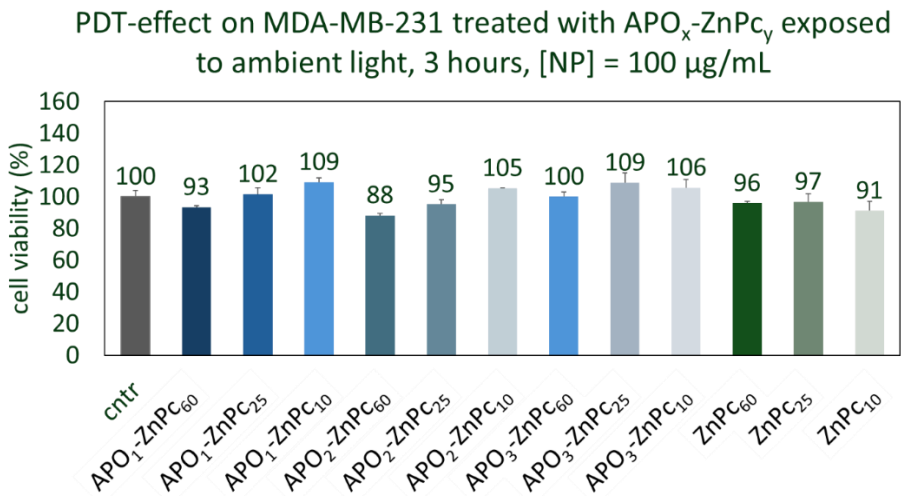

Figure A.V.1. No significant PDT-effect was observed when exposing treated MDA-MB-231 cells to ambient light for 3 hours. **Pc_x** (x → 60, 25, 10 = 1.2 µM, 0.5 µM, 0.2 µM, respectively).

A.IV.3. SEC chromatograms

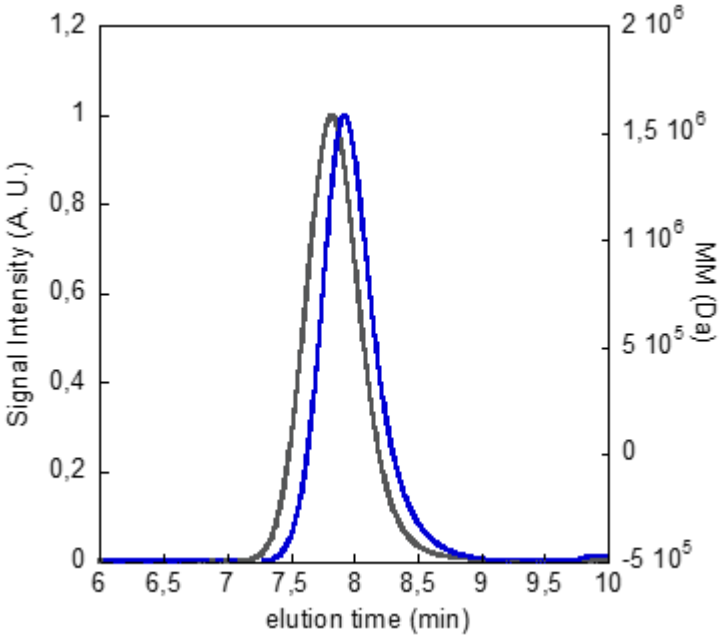

Figure A.IV.2. SEC chromatogram of copolymer $\mathbf{P_1}$ (dRI detector blue line, LS detector grey line, THF, 1 mL min^{-1}).

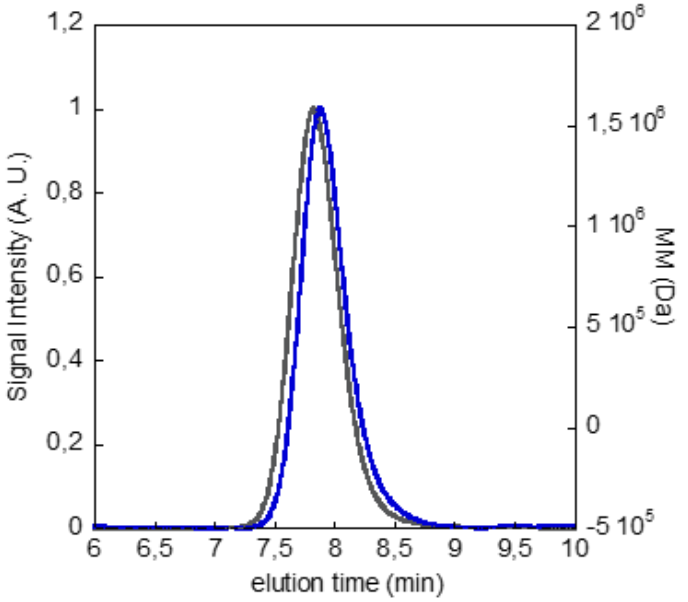

Figure A.IV.3. SEC chromatogram of copolymer $\mathbf{P_2}$ (dRI detector blue line, LS detector grey line, THF, 1 mL min^{-1}).

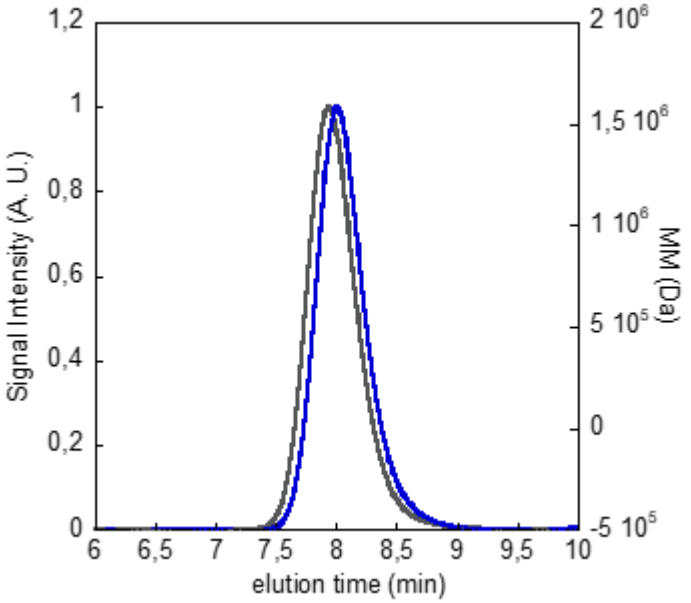

Figure A.IV.4. SEC chromatogram of copolymer **P$_3$** (dRI detector blue line, LS detector grey line, THF, 1 mL min^{-1}).

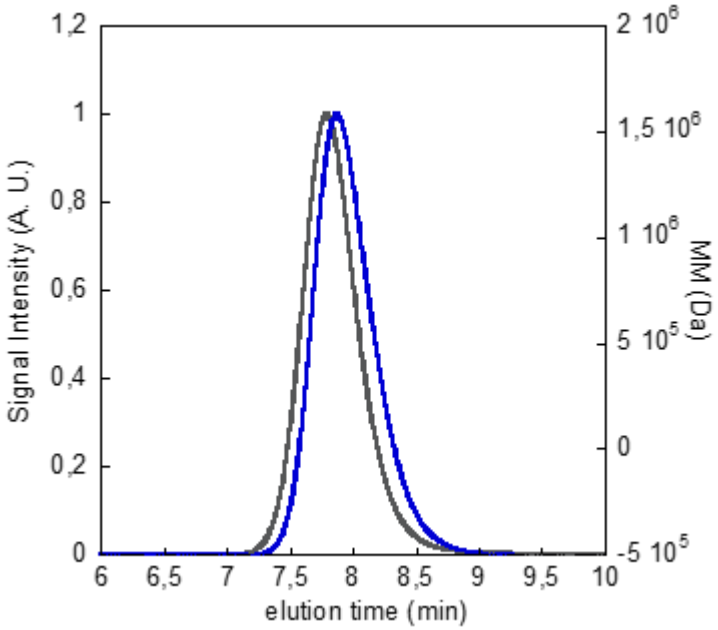

Figure A.IV.5. SEC chromatogram of copolymer **P$_4$** (dRI detector blue line, LS detector grey line, THF, 1 mL min^{-1}).

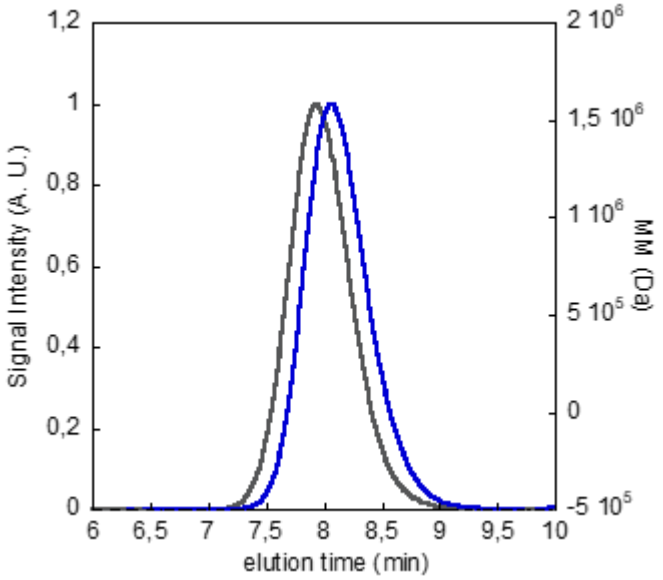

Figure A.IV.6. SEC chromatogram of copolymer **P**$_5$ (dRI detector blue line, LS detector grey line, THF, 1 mL min^{-1}).

A.IV.4. NMR spectra

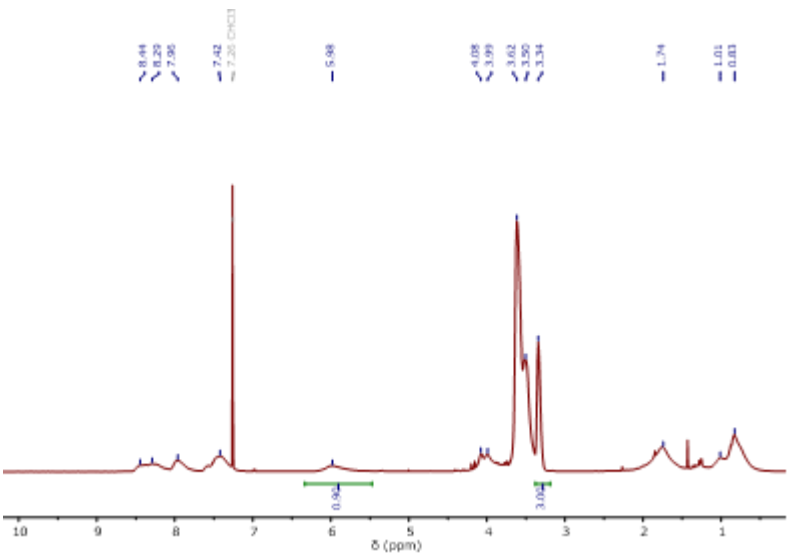

Figure A.IV.7. ^{1}H NMR spectrum of **P$_1$**.

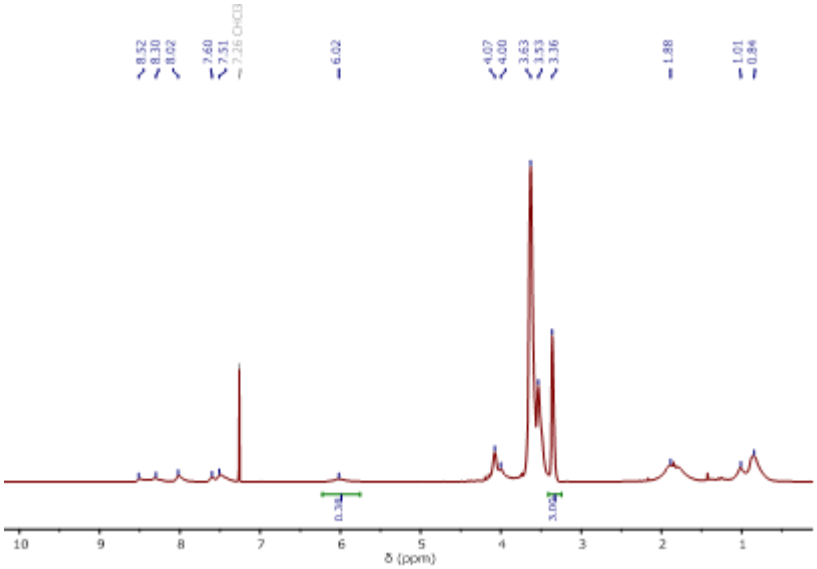

Figure A.IV.8. ^{1}H NMR spectrum of **P$_2$**.

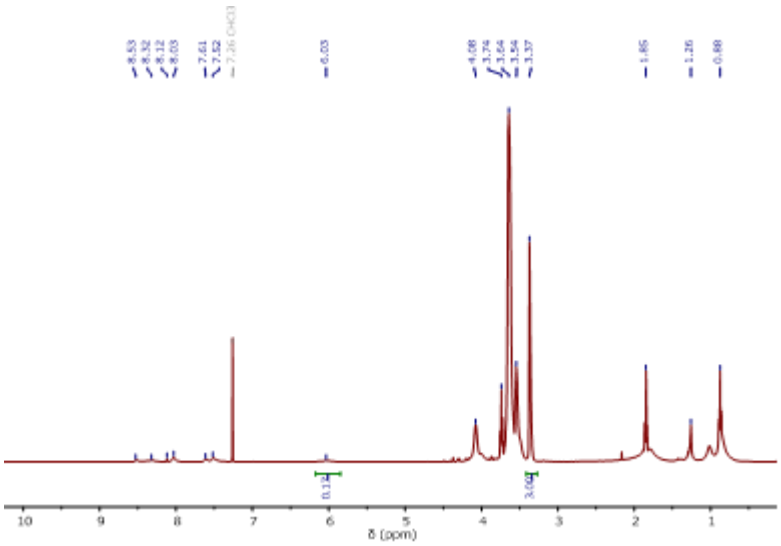

Figure A.IV.9. ^{1}H NMR spectrum of **P$_3$**.

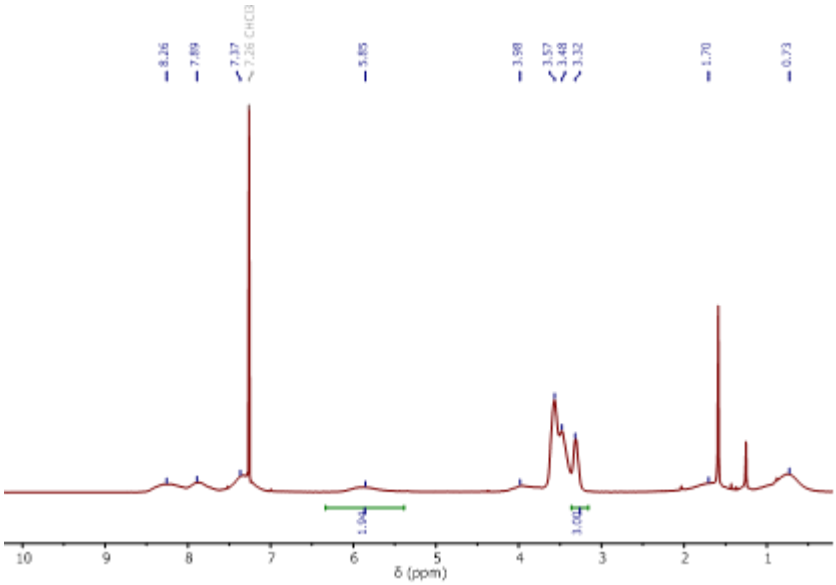

Figure A.IV.10. ^{1}H NMR spectrum of **P$_4$**.

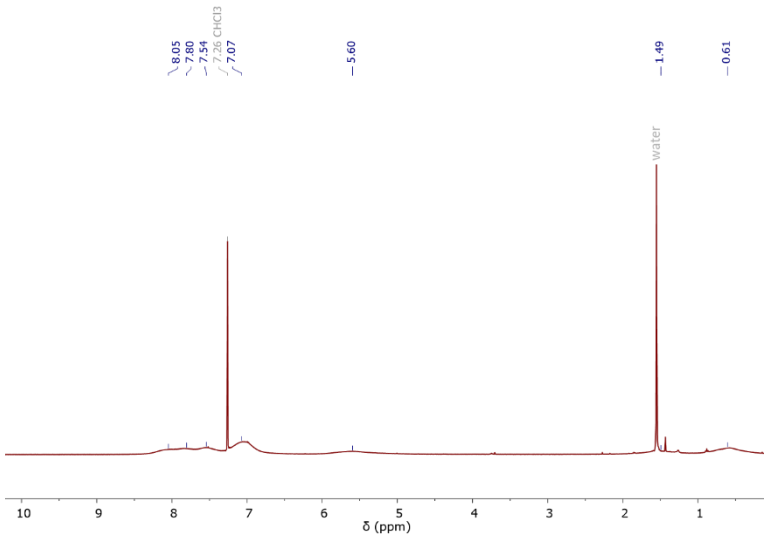

Figure A.IV.11. ^{1}H NMR spectrum of $\mathbf{P_5}$.

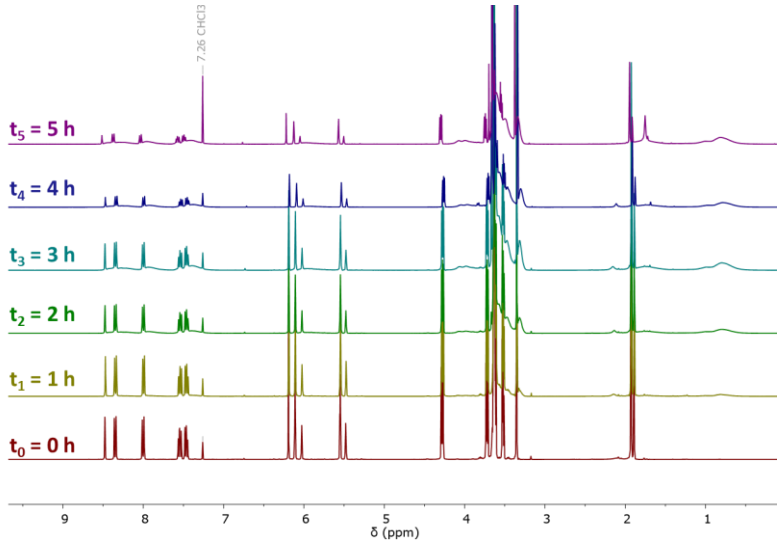

Figure A.IV.12. Superimposed ^{1}H NMR spectra for the RAFT copolymerization kinetics experiment for the preparation of the copolymers $\mathbf{P_x}$.

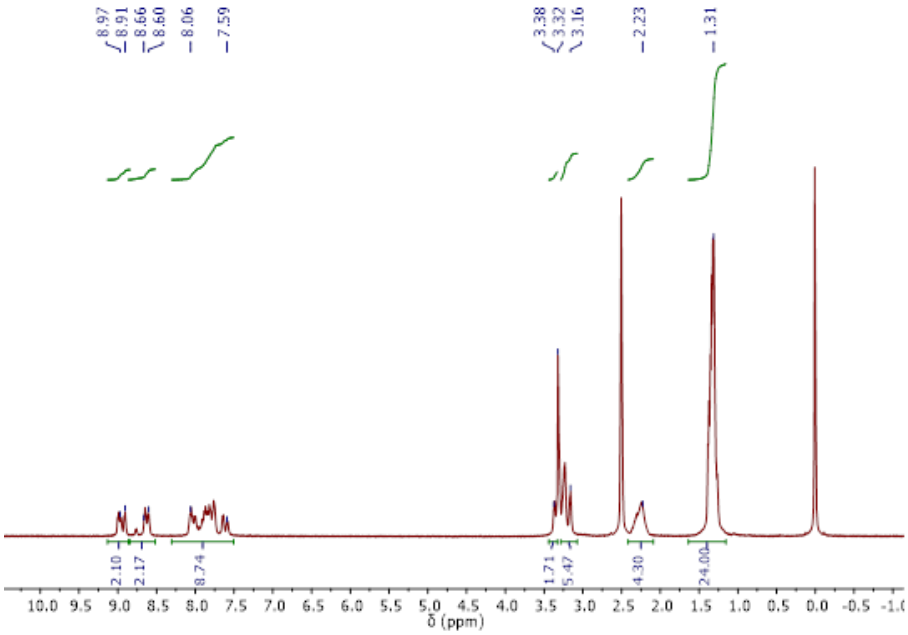

Figure A.IV.13. ^{1}H NMR spectrum in DMSO d_6 of **ZnPc.**

A.IV.5. Supplementary spectroscopy

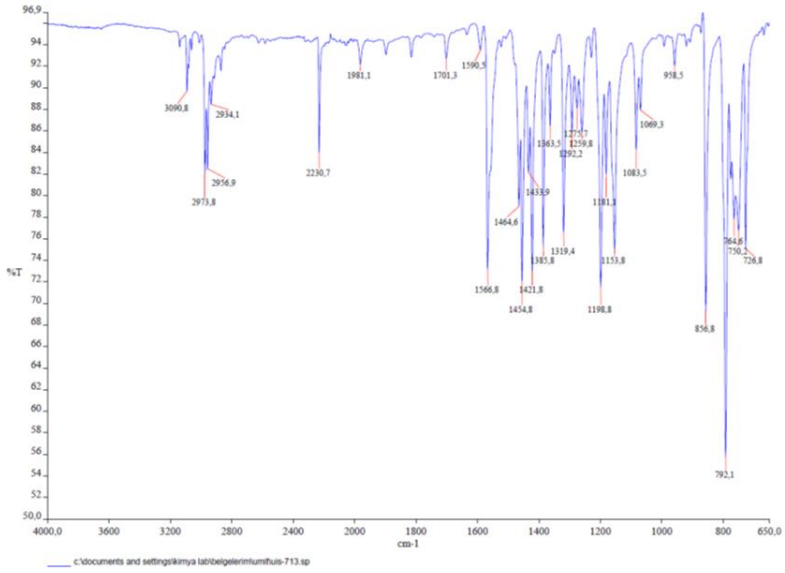

Figure A.IV.14. FT-IR spectrum of **(1)**.

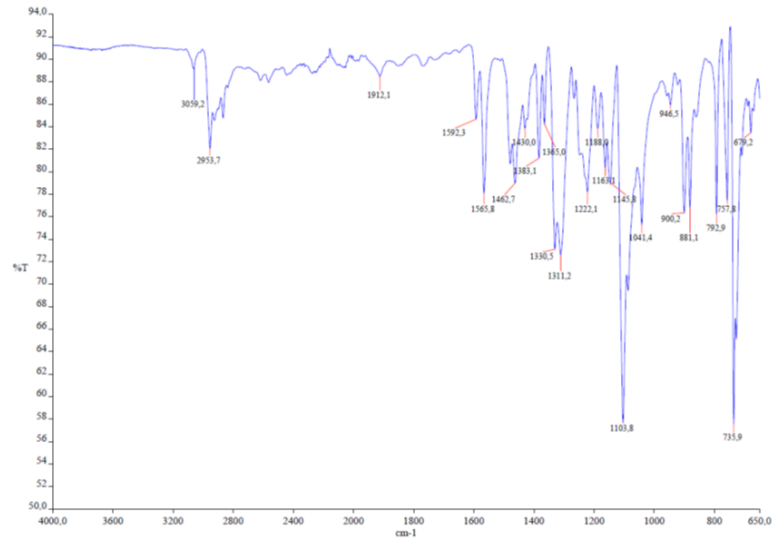

Figure A.IV.15. FT-IR spectrum of **ZnPc**.

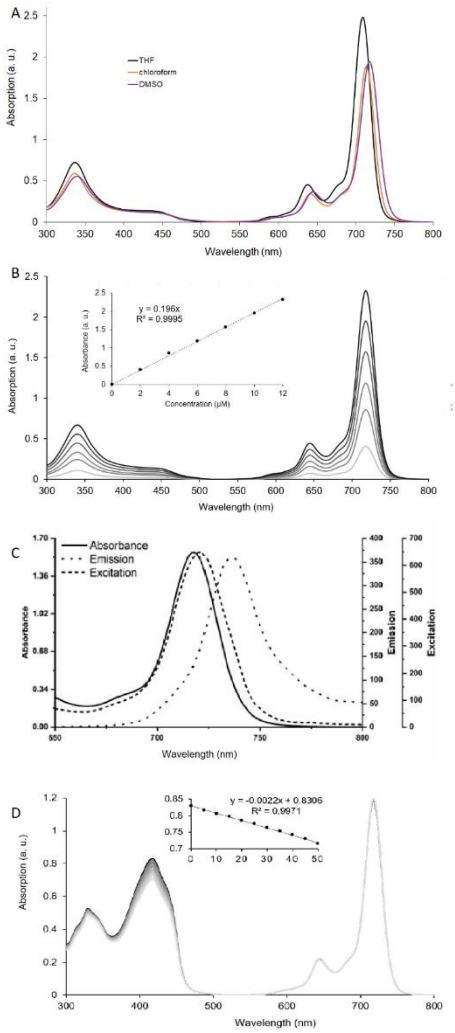

Figure A.IV.16. a) Superimposed UV-vis spectra of **ZnPc** in chloroform, DMSO and THF (10 μM). b) UV-vis absorption spectra of **ZnPc** in DMSO (2-12 μM). Inset: absorption *vs.* concentration. c) Absorbance, emission (irradiation: 640 nm), and excitation spectra of **ZnPc** in DMSO. d) Determination of singlet oxygen quantum yield of **ZnPc** in DMSO (6 μM). Inset: Plot of DPBF absorbance at 417 nm vs. time.

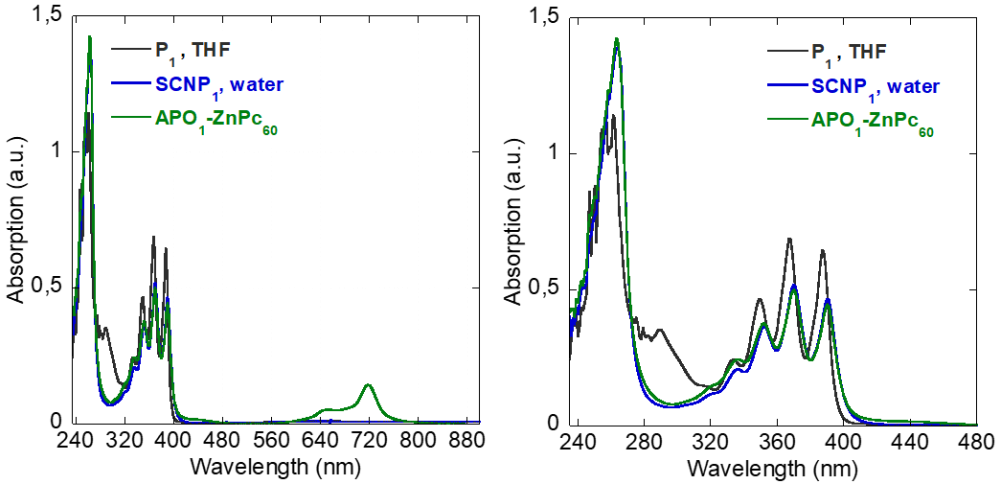

Figure S16. Superimposed UV-Vis absorption spectra of **P_1**, **$SCNP_1$** and **APO_1-$ZnPc_{60}$**, recorded at a [copolymer] = 0.1 mg mL^{-1}. On the rigth, ingrandment of the typical anthracene electronic transitions region.

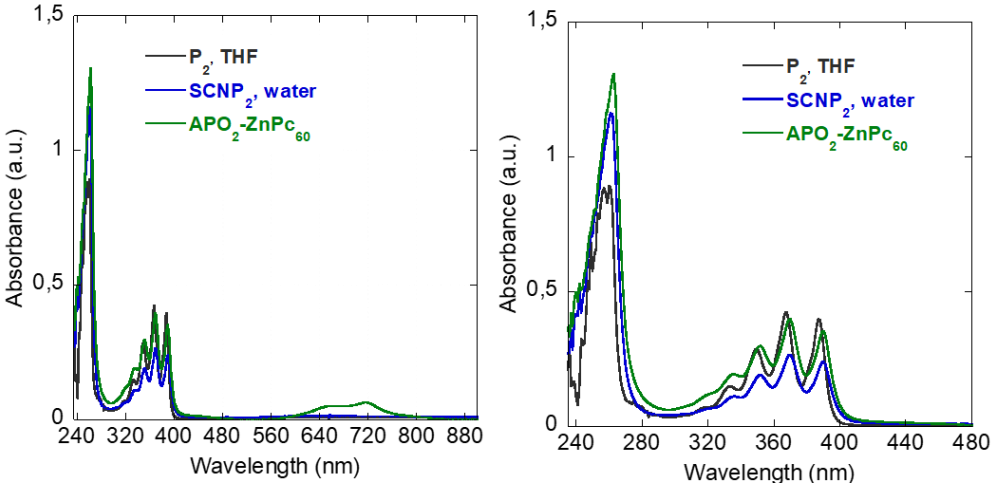

Figure S17. Superimposed UV-Vis absorption spectra of **P_2**, **$SCNP_2$** and **APO_2-$ZnPc_{60}$**, recorded at a [copolymer] = 0.1 mg mL^{-1}. On the rigth, ingrandment of the typical anthracene electronic transitions region.

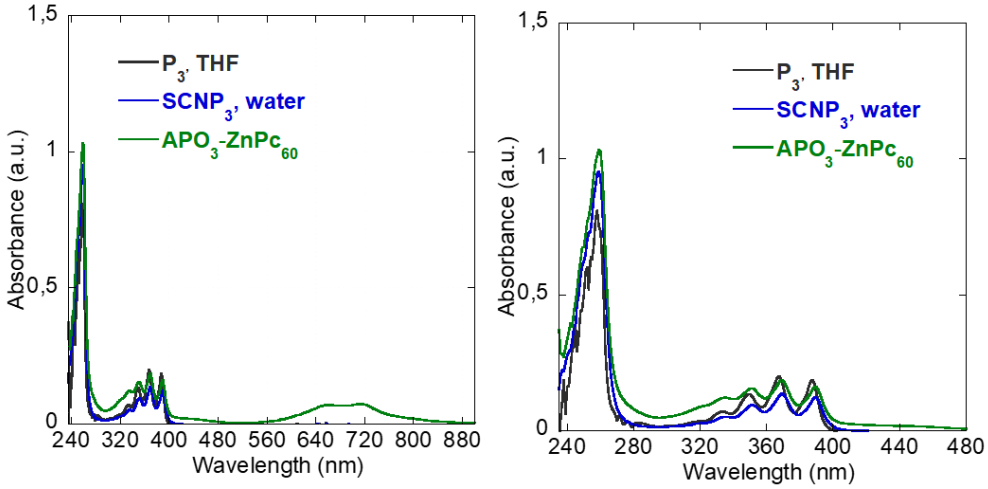

Figure S18. Superimposed UV-Vis absorption spectra of **P_3**, **$SCNP_3$** and **APO_3-$ZnPc_{60}$**, recorded at a [copolymer] = 0.1 mg mL^{-1}. On the rigth, ingrandment of the typical anthracene electronic transitions region.

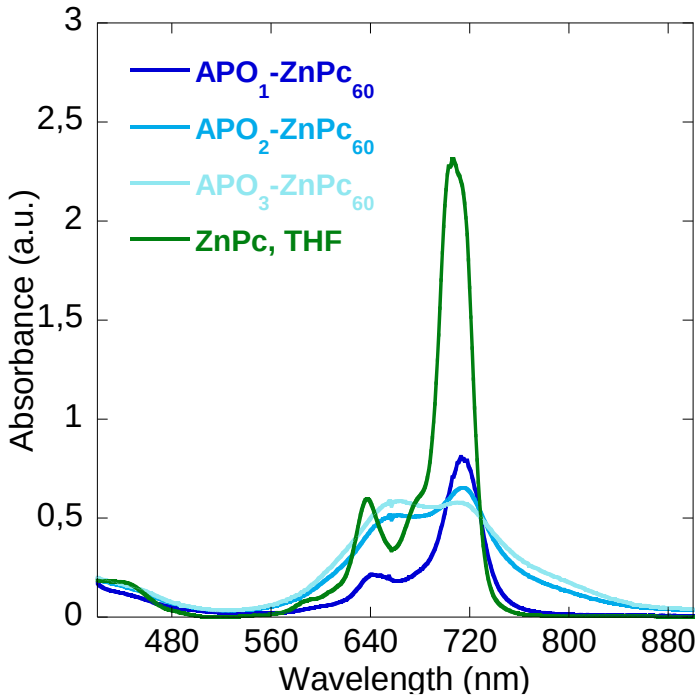

Figure S19. Superimposed spectra showing the red absoprtion of encapsulated **ZnPc** withing **APO_x-$ZnPc_{60}$** ([copolymer] = 1 mg mL^{-1}), compared with free **ZnPc** ([**ZnPc**] = 1.2 µM) in THF.